TASK-SPECIFIC UNCERTAINTY FOR INDUSTRIAL MEASUREMENTS

by

Mario Orlando Valdez

A dissertation submitted to the faculty of
The University of North Carolina at Charlotte
in partial fulfillment of the requirements
for the degree of Doctor of Philosophy in
Mechanical Engineering

Charlotte

2015

Approved by:

____
Dr. Edward Morse

____
Dr. Gert Goch

____
Dr. Jimmie Miller

____
Dr. Wesley Williams

____
Dr. Moutaz Khouja

ABSTRACT

MARIO ORLANDO VALDEZ. Task-specific uncertainty for industrial measurements. (Under the direction of DR. EDWARD MORSE)

The purpose of measurement is to provide information about a quantity of interest – a measurand. Since no measurands are exactly known, measurement uncertainty is estimated for common measuring tasks in order to quantify the result of a measuring process. Task-specific uncertainty estimation methods are performed to determine the measurement uncertainty for a specific scenario that is not addressed by the "standard" uncertainty budget. Often these situations are those in which a traditional sensitivity analysis, as recommended by the *Guide to the Expression of Measurement Uncertainty (GUM),* is not feasible or if the flexibility of the instrument allows the evaluation of many different measurands, making a ”generic” uncertainty budget impractical. For the traditional sensitivity analysis procedure, a mathematical model of the particular measurand must be developed in order to compute the sensitivity coefficients (partial derivatives) that are used in the *Law of Propagation of Uncertainty (LPU)* estimation for the combined standard uncertainty. Major drawbacks arise from this analysis method, in that the mathematical model for a measurand is often complex, resulting in problems of nonlinearity, non-analytical solutions, or solutions by numerical-approximates. A task-specific uncertainty estimation - as with any valid estimate - must take into account all the uncertainty sources associated with the details of the measurement process, hence is a function of the measurand. The difficulty in performing the uncertainty analysis will be related to the details of the measurand.

A series of ISO standards and ISO technical specifications exists today in support of task-specific uncertainty; these documents describe best-practices in determining the methodology, influence quantities, and analysis for the measurement uncertainty for a particular measurand. These ISO and ISO/TS documents cover everything from basic definitions of metrological characteristics to off-line uncertainty evaluation software (UES) packages used to simulate uncertainty sources numerically. It should be considered, however, that these documents are written for users of traditional, Cartesian Coordinate Measuring Machines (CMMs) that are utilized in controlled metrology lab environments. There has been minimal work done on shop floor CMMs and even less done on non-Cartesian CMMs (e.g. portable metrology technologies) that are built specifically for shop floor measurements.

Portable metrology technologies and non-Cartesian CMMs include laser trackers, articulating arm coordinate measuring machines (AACMMs), laser scanners and theodolites. In general, metrology equipment used mainly in large-scale applications where the instrumentation has to be taken to the work-piece being inspected. The standards for the performance evaluation of these technologies are still evolving and no standardized methods for task-specific measurement uncertainty evaluation, like that of the traditional Cartesian CMM, have been suggested. The research presented in this dissertation develops preliminary evaluation methods for task-specific uncertainty analysis of the available portable CMM technologies. These methods are based on existing methods, but consider the different construction of the instruments, the environments in which they operate, and the nature of the work-pieces they are used to inspect. Case studies of a typical industrial measurement processes using these portable CMM technologies are presented.

ACKNOWLEDGMENTS

First and foremost I would like to extend my deepest gratitude to Dr. Ed Morse who over the past few years has been a crucial in my development as a better precision engineer but even more so as a professional. With his insight and vast knowledge of dimensional metrology, I have developed new tools for critical thinking and professional judgment that will follow me throughout my professional life. The skill set I now possess is the result of his willingness and patience to guide me in the right direction. I will forever be in his debt.

I would like to thank Dr. Gert Goch and Dr. Jimmie Miller for assisting me in research. Dr. Goch for his willingness to assist me in tracking down relevant information for my research and reviewing it with a fine tooth comb. Dr. Miller for taking an active interest in my research, assisting me in a time of need and for the many conversations we has throughout the years.

I would like to thank Dr. Wesley William and Dr. Moutaz Khouja for graciously accepting to be part of my committee, I thank you for that.

I would like to thank Siemens Energy for the support and funding over the course of my research, specifically Mr. Mike Jones. I would also like to thank Mr. Ian Doran and Mr. Steven Gardner for their assistance on the Siemens Shop floor.

I would like to thank Mrs. Jennifer Chastain for being our school mom. From the treats she made us to the just being such a joy to be around. She really did brighten up my days.

Lastly I would like to thank my family and friends…especially the BasedGod Lil B, the Originator of all things based. #TYBG.

TABLE OF CONTENTS

LIST OF FIGURES

LIST OF TABLES

CHAPTER 1: INTRODUCTION

From the CIRP keynote paper by Wilhelm *et al.* [1], task-specific uncertainty is defined as *"the measurement uncertainty associated with the measurement of a specific feature using a specific measurement plan."* Measurements are usually of size, position, orientation or form of the specific part features, where each are made to evaluate the fidelity of the manufactured work-piece to the dimension and tolerance on the product specification [2]. An elementary example is the measurement uncertainty associated with the form of a spherical calibration artifact continuously-scanned using a fixed-bridge CMM in a temperature-controlled lab or the measurement uncertainty associated with the diameter of an engine block cylinder bank measured discretely using a moving-table CMM on the shop floor. These simple examples demonstrate a specific feature measured using a specific measurement plan, in specific, the measurand of interest, instrument, sampling strategy, etc.

Also important is traceability. The *International Vocabulary of Metrology* (VIM) [3] defines traceability as *"the property of the results or the value of a standard whereby it can be related to stated references, usually national or international standards, through an unbroken chain of comparisons all having stated uncertainties."* Traceability cannot be validated unless a measurement result has an associated uncertainty statement. To ensure traceability, the *Guide to the Expression of Uncertainty in Measurement* (GUM) [4] suggests guidelines and methods for the determination of uncertainty through a sensitivity analysis. Task-specific uncertainty is an alternative method in demonstrating traceability outside of a classical sensitivity analysis and still follows the guidelines set out by the GUM (similar references that follow the suggestions by the GUM are Frenkel and Kirkup, [5] and NIST Tech Note 1297, [6]) The work in this dissertation demonstrates task-specific measurement uncertainty methodologies on industrial measurements and assesses the results in accordance to the guidelines stated in the GUM.

1.1 Task-specific Uncertainty Error Sources

CMMs are versatile machines that have the capabilities to measure not only part dimensions but also part form, part feature location, and other features of interest all in a single or multiple setups [1], [7]. Because of this versatility, the sources of uncertainty are difficult to determine due in part of the variability in the task being performed, the environment, the operator, the chosen measurement methodologies, and other influencing quantities. With many possible sources, it is very complicated to perform a traditional sensitivity analysis suggested by the GUM. Determining a linear (or linearized) mathematical model for the measurand recommended by the GUM can be tedious and nearly impossible because of the numerous influence quantities. If a mathematical model can be fully-developed, additional difficulties may arise from the model not having a closed-form solution and can only therefore be numerically-approximated. The influence quantities are the most difficult aspect in modeling the measurand since it is near impossible to determine every one of them, even when opting to consider only the most apparent ones.

Task-specific measurement uncertainty specifically considers five main factors that encompasses all the possible sources of uncertainty: (1) hardware (2) work-piece (3) sampling strategy (4) fitting and evaluation algorithms and (5) extrinsic factors. It is not possible to capture every one of the possible influence quantities but it is possible to find the largest contributors, reduce them to manageable levels, and quantify them with sufficient fidelity. The following subsections will briefly detail how each the five main factors attributes to the uncertainty of the measurement.

1.1.1 Hardware

The sources of uncertainty that come from the hardware are associated with the errors of the CMM (e.g. design, scales, geometry, probing systems, machine dynamics, etc.) The biggest contributors from a traditional, Cartesian CMMs are the 21 parametric errors of a three-axis model where lots of published work has been done to identify these errors and test them [1], [7], [8]. Additional errors come from uncorrected systematic and random probing errors; probe changing and articulation errors [7]; probing parameters; and temperature (environmental/machine) [9]. There are other sources and many more resources that can be referenced from [1] that cover other specialized areas related to the sources listed and this is by no means an exhaustive list.

1.1.2 Work-piece

The sources of uncertainty related with the work-piece can be from the material properties of the work-piece, measurement interaction with the work-piece or a combination. A typical list of sources is traditionally compiled by part form deviations [10]; accessibility restrictions and sampling distributions; contact mechanics, surface finish and elastic deformation due to probing force [7]; and uncertainty in the datum reference frame. If the work-piece was manufactured from a valid engineering drawing with proper dimensioning and tolerancing, as well as under a controlled process, these sources can be minimized.

For the classical small-part-on-a-CMM work-piece measurements, minimizing the uncertainty of the work-piece can assist in negating other primary sources (e.g. part form deviation, stiffness, etc.) However, this is unlikely true for large, unorthodox work-pieces where the measurement types are now CMM-to-large-part and minimizing the uncertainty of the work-piece is a challenge. Manufacturers of large work-pieces have to consider gravitational effects on the machine and work-piece, deformation of the work-piece during machining, thermal deformation from non-uniformity, long machining cycles, and other situations that can have significant effect on the final outcome [11].

1.1.3 Sampling Strategy

Inadequate sampling is the main contributors to scale-dependent errors. This can be from sampling strategy interaction with the form error [12], sampling strategy interaction with complex form, error magnification from inadequate datums and error from comparison of calibrated work-pieces to real work-pieces. Depending on the feature of interest, there are known sampling criteria for the minimum number of points needed to define or characterize a part or part feature [13]. It is uncommon in Cartesian CMMs to develop random sampling strategies for regular, prismatic geometries as the quality of characterization of the geometry is dependent on point spacing and density. Most of the algorithms used to evaluate the profile are iteration-based. Linear features geometries (e.g. planes) are less stringent when it comes to characterization of the part geometry as the algorithms usually do not need an iteration technique to find the critical parameters (e.g. centroid of a plane).

1.1.4 Fitting and Evaluation Algorithms

Most sources of algorithm-based uncertainty arise from the suitability and selection of the algorithm used for the substitute-geometry fits, algorithm interaction with the sampling density and the actual algorithm implementation. References [14] and [15] have done work on some of these issues, however, the software package that comes with the CMM usually has gone through some quality assurance testing or can be tested using the National Institute of Standards and Technology's (NIST's) algorithm testing data [16]. For traditional Cartesian CMMs, the software is well-equipped with various fitting algorithms for substitute-geometry evaluations.

1.1.5 Extrinsic Factors

The sources of uncertainty of concern here are the ones that contribute to the reproducibility of the CMM measurements. Typically, this is caused by variations in the environment, machine/operator interaction, cleanliness of the work-piece and operator-selectable options. These error sources are hard to control and are typically out of the manufacturer's hands (often out of the user's hands as well). In a traditional metrology lab environment, all these influence quantities are minimized by ensuring proper procedures are in place when setting up for a measurement and followed thoroughly by the metrologists. Additionally, having an environmentally-controlled laboratory is the standard when it comes to minimizing the extrinsic effects on the dimensional measurements.

Overall, there are many sources that effect the uncertainty of measurements and is a tremendous task to quantify for all but the simplest measurements. For measurement tasks, task-specific uncertainty allows a metrologist to determine an uncertainty using standardized, experimental methodologies in compliance with the GUM and to ensure traceability. Wilhelm, *et al.* [1] demonstrates a process flow of the error components that attribute to the uncertainty of the measurement as seen in FIGURE 1 below, this is generalized and non-exhaustive but captures all the primary contributors to the task-specific uncertainty.

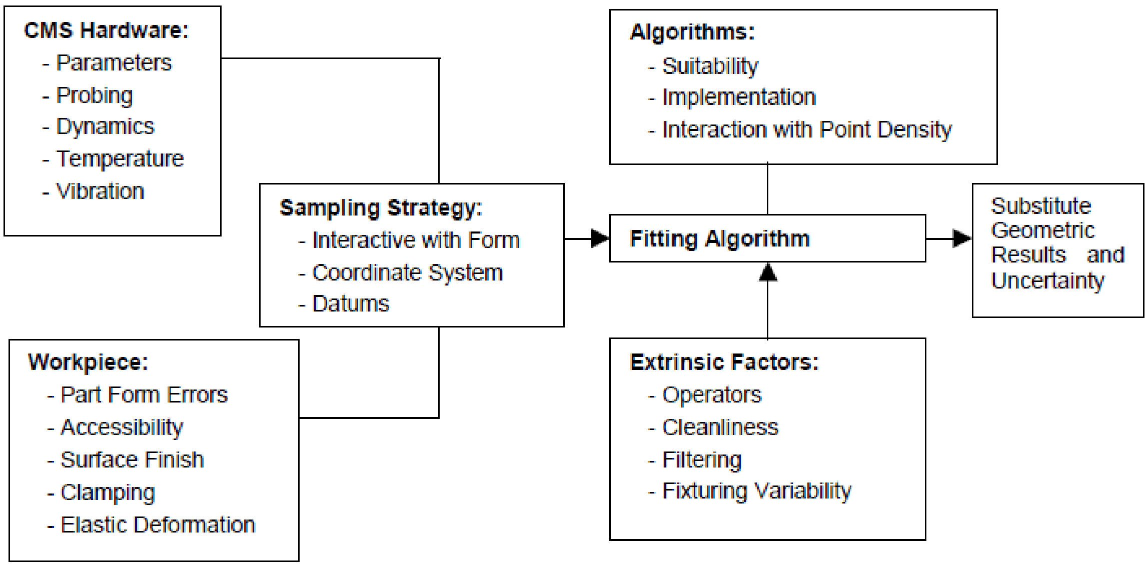

FIGURE 1: Task-specific error component flow chart, [1].

1.2 Task-specific Uncertainty Models

The CIRP keynote paper on task-specific uncertainty separates uncertainty methodologies into so-called uncertainty models. Each model adheres with the guidelines set out in the GUM and compliance is upheld to distinguish the difference between systematic and random error sources, which is often vague. Six different models exist: (1) sensitivity analysis, (2) expert judgment, (3) substitution method using calibrated work-pieces, (4) computer simulations, (5) statistical estimations and (6) hybrid methods. Each model will be described briefly as well as an explanation to some of the advantages and disadvantages of each model when used to determine measurement uncertainty.

1.2.1 Sensitivity Analysis

The method suggested and outlined in the GUM is what is considered the sensitivity analysis method. The experimental mathematical model of the measurand is represented with Eq. 1,

$$y = f(x_1, x_2, \ldots, x_n) \tag{1}$$

where x_i for $i = 1, 2, \ldots, n$ represent the influence quantities that define the measurand. Once the mathematical model of the measurand is defined, and all the standard uncertainties associated with each influence quantity, then the *Law of Propagation of Uncertainty* (LPU) is used to calculate the combined standard uncertainty. The general equation for the LPU is stated with Eq. 2, where the sensitivity coefficients $\partial f/\partial x_i$ determine how much influence each input quantity has on the measurand and overall combined standard uncertainty,

$$u_c^2(y) = \sum_{i=0}^{n} \left(\frac{\partial f}{\partial x_i}\right)^2 u^2(x_i) + 2\sum_{i=1}^{n-1} \sum_{j=i+1}^{n} \left(\frac{\partial f}{\partial x_i}\right)\left(\frac{\partial f}{\partial x_j}\right) u\left(x_i, x_j\right) \qquad (2).$$

For uncorrelated influence quantities, the covariance part of Eq. 2 is equal to zero and does not factor into the result. If the influence quantities are correlated, then the covariances must be evaluated. Additionally, the effective degrees of freedom must be determined when each sensitivity coefficient is estimated so a coverage factor can be estimated from a t-Test distribution. This can be done using the Welch-Satterthwaite equation or Eq. 3 below,

$$v_{eff} = \frac{u_c^4}{\sum_{i=1}^{N} \frac{u_i^4(y)}{v_i}} \tag{3}$$

One of the main advantages is that if one is able to determine a precise mathematical model of the measurand and its standard uncertainties, then a relatively straightforward measurement uncertainty analysis can be carried out. However, there are drawbacks like determining the measurand model for a complex measurement. Mostly, uncertainty determination using the sensitivity analysis is limited to simple point-to-point length measurements as other methods for complex models are preferred. Overall, the method is the suggested way of performing a traditional uncertainty analysis where the validity, complexity and precision is dependent on the metrologist knowledge and skill set when determining the model.

1.2.2 Expert Judgment

For the uncertainty evaluation using expert judgment, the basic idea is to perform what the GUM refers to as a Type-B evaluation of measurement uncertainty. From the VIM, a Type-B evaluation is defined as *"the evaluation of a component of measurement uncertainty determined by means other than a Type-A evaluation or other statistical analysis."* This requires a significant amount of knowledge about and experience with CMMs or a specific CMM (e.g. the Abbe offsets, geometric errors, irreproducibility, etc.) This method is often used when no other tools or techniques are available and a good-level of prior knowledge of statistical distributions can be reasonably justified [17]. It is obvious what the advantages are given the experience and knowledge of CMMs. Of course, the same can be said of the disadvantages. Preliminary work has begun on a new part of the ISO 15530 series to develop sets of guidelines and criteria for using expert judgment, as well as conformance decisions, in the determination of measurement uncertainty. As is the case when using expert judgment, it is reasonable to refer back to guidelines on Type-B evaluation in the GUM to determine adequate probability distributions for a specific value or range of values when performing the measurement uncertainty assessment.

1.2.3 Substitution Method using Calibrated Parts

The substitution method using calibrated parts is the most straightforward and practical method since it is essentially a comparison method. This method is essentially taking a calibrated work-piece that is very similar in geometry and composition to that of a real work-piece and comparing each geometrical parameter and uncertainty of interest. The determination of uncertainty is reduced to the evaluation of the instruments' ability to repeat each measurement (on the calibrated work-piece and the work-piece under test). This method has been around for decades and has been performed traditionally using touch-trigger probes, interferometers [18] and other methods of measurement. For this method to be successful, there is a similarity criteria that must be met in order to proceed with an uncertainty analysis. Another important aspect are the environmental conditions of the measurement, in specific, a stable temperature, humidity and pressure as well as a stable temperature gradient.

Advantages are that the actual uncertainty analysis is simple to evaluate once all the measurements have been performed, additionally, the variation of environmental scenarios and user influences are covered. Once programmed to measure the calibrated artifact, it only becomes an issue of setting up the part alignment for the next measurement run. The most obvious disadvantage is the calibrated work-piece itself, which must be ‘absolutely’ calibrated using calibration principles carried out in a traditional calibration laboratory as well as traceable. This can be very expensive to have done and for large work-pieces may not be feasible or practical. Other disadvantage are from the differences between calibrated work-pieces and the work-pieces themselves such as form deviations, differences in coefficients of thermal expansion (CTEs), uncertainties of CTEs, etc. Also, differences in mounting/fixturing and operator effects can add to the uncertainty. Ideally, both calibrated work-piece and work-piece should be in *identical* positions on the CMM when measured. Also, the calibrated feature of the work-piece must have lower uncertainty than that of the CMM used for measurement [7]. Overall, a very useful method but takes considerable requirements and costs to perform.

1.2.4 Computer Simulations

From the keynote paper by Wilhelm, et al. [1], there are four suggested simulation methods that have been reported in the literature: Virtual CMM (VCMM), Simulation by Constraints (SBC), the Expert CMM (ECMM) and traditional Monte Carlo approaches. Simulation methods estimate the measurement uncertainty by numerical simulation of the measuring process. The Uncertainty Evaluating Software (UES) is based on a computer-aided mathematical model of the measuring process where Monte Carlo algorithms typically represent the model. The influence quantities vary between possible or assumed ranges of values, where the measuring process is repeatedly simulated, using all possible combinations. For the VCMM, SBC, and ECMM UES packages, user inputs are entered into the appropriate interfaces that pertain to geometric errors of a certain machine configuration, probing strategies/setups, environmental conditions, performance evaluation standards and various other options unique to each package. Traditional Monte Carlo methods are programmed or developed by each individual metrologist in their preferred programming language (e.g. MATLAB, Excel, C++, FORTRAN, R, Python, etc.) Each of the four listed UES methods has its own unique requirements and explanation can be found in the literature [19], [20] and [21].

Advantages of the computer simulations are that a metrologist can perform uncertainty estimations prior to measuring a work-piece, therefore a comparison between the measurement uncertainty and the tolerance specification is now available. Additionally, with many of the influence quantities input into the UES, thousands of measuring processes can be simulated over the given ranges of values so a standard uncertainty can be quantified. Traceability can be ensured by inputting available performance evaluation data (e.g. B89, ISO, etc.) into the UES. One disadvantage of a UES is that most, if not all, extrinsic factors are not included into the assessment and therefore have to be evaluated using a Type-B evaluation. Then the results can be combined using the LPU. Furthermore, form deviation assessment is not included in the assessment. Also, each UES package does not give access to the programming architecture and mathematical models of the CMMs utilized so it is near-impossible to know exactly how these uncertainties are calculated. This can be remedied by the metrologist programming their own measurement uncertainty software but this task is likely to be very complicated.

1.2.5 Statistical Estimations

If a large set of measurement data is available and an uncertainty measurement estimation is needed, then well-known statistical methods can be applied via the GUM or any other like reference. This method can put an upper bound on the measurement uncertainty but is not a good method in determining if a bias exists. If the intention of the manufacturing plant is to produce high-volume parts then this is a valid way of making a more rapid determination on the uncertainty of the measurements. More rigorous statistical methods can be applied to determine control charting and risk analysis as well but are outside of the realm of what is useful for uncertainty estimation.

1.2.6 Hybrid Methods

Hybrid methods are a combination of the methods already mentioned above to determine measurement uncertainty. It seems traditionally that hybrid methods are used more frequently, an example being many people will make expert judgment on certain influence quantities and then perform one of the simulation methods. Of course, there is no standardization for hybrid methods so it is not commonly known as a hybridization.

There is a common theme in the current realm of task-specific uncertainty and that is the majority of research has only been done on traditional, Cartesian CMMs. Furthermore, most of the research has been done in stable work environments, such as a metrology lab, where issues with temperature, humidity, pressure, gradients, and any other environmental parameters are stabilized to minimize the influence on measurements. There is a large gap in the non-Cartesian CMM or portable CMM (e.g. laser trackers, articulating arm coordinate measuring machines (AACMMs), etc.) classification that are more commonly used in shop floor or industrial working conditions. It is of real interest in knowing how the measurement uncertainty is influenced when this particular class of CMMs is utilized in its commonly-used working environment which led to the motivation behind this dissertation.

1.3 Motivation for Work

Portable CMM technologies are proving to be widely used when it comes to most industrial measurement, especially in large-scale applications. The need for precision measurements on large-scale objects increases as tolerance specifications decrease. More often than not, the measurement results are presented without an uncertainty statement which brings the validity and traceability of the results into question. To ensure that traceability is not lost, it is critical that a statement of uncertainty accompany any measurement results. A common approach to measurement uncertainty analysis is done by task at hand, where a specific feature is measured with a specific measurement plan.

The motivation for performing task-specific uncertainty on industrial measurements stems from three years' worth of projects in collaboration with a large, industrial manufacturing plant. The focus of each project was to measure large components related to their steam turbines and generators using portable CMM technologies (e.g. laser trackers and AACMM) that are readily available, see FIGURE 2 below for an example of one the components. The main objective was to determine if the available portable CMMs would be feasible replacements to the current, machine tool and hand tool measurement processes. After determining that the results from the alternative portable CMM measurement processes had comparable accuracy to the current measurement process, a validation of the results was needed. To validate the measurement results, an uncertainty statement must be provided. In determining the measurement uncertainty, traceability can then be established. This led to the motivation of developing methodologies to determine the task-specific measurement uncertainty for these types of industrial measurements.

FIGURE 2: Steam turbine throttle valve.

As was mentioned previously, classical error budgeting is a very complex and difficult task to carry out on any CMM due to the complexity and flexibility of the measurement process. Therefore, task-specific uncertainty analysis seems a more reasonable route that still enables the establishment of an uncertainty statement therefore validating the measurement process results. The goal of this dissertation is to develop preliminary evaluation methods for task-specific measurement uncertainty analysis using the available portable CMM technologies and existing methods of assessment but also consider the different constructions of the instrument being used, the operational environment and the nature of inspected work-pieces.

CHAPTER 2: CURRENT STATE OF THE ART AND LITERATURE REVIEW

Standardized documentation exist in today's industry practices that aide in the determination of task-specific measurement uncertainty. The International Organization of Standardization (ISO) has a series of standards and technical specifications, namely the ISO 15530 series, dedicated for the evaluation of task-specific uncertainty. These documents outline methods used for the testing and analysis of pertinent influence quantities contributing to the measurement uncertainty of task-specific measurands. Though developed for Cartesian CMMs, they are applicable to non-Cartesian CMMs as well. Currently, the only available standards for non-Cartesian CMMs are for performance evaluation testing. These are only extended to laser trackers and AACMMs but do not provide detailed testing or analysis for the measurement uncertainty outside of simple length measurements. A review of the current state of the art and literature will be carried out in the following sections.

2.1 ISO/TS 15530 Series

The Geometric Product Specification (GPS) has been updated by the activity of the ISO/TC 213 working group to unify a model for design, manufacturing and verification. This is based on improved language and new concepts such as surface models, geometric features, characteristics, specification uncertainty and correlation uncertainty [22]. The ISO 15530 series was developed by the ISO/TC 213 working group to provide terminology, techniques and guidance for the determination of task-specific uncertainty of

CMM measurements in compliance with the GUM. The ISO 15530 series consists of 4 parts:

- Part 1: Overview of metrological characteristics
- Part 2: Use of multiple strategies in measurements of artifacts (*not released*)
- Part 3: Use of Calibrated work-pieces or measurement standards
- Part 4: Evaluating task-specific measurement uncertainty using simulation

Parts 2 was never approved for release but has been validated from an external source [23]. The following subsections will give a brief overview of each standard. (For a great overview of the ISO 15530 series, see NPL's Measurement Good Practice Guide No. 130: *Co-ordinate Measuring Machine Task-specific Measurement Uncertainties* by D. Flack, [24]).

2.1.1 15530-1: Overview of Metrological Characteristics

Part 1, [25], is an overview of the ISO 15530 series. It groups task-specific uncertainty into three categories of error sources: intrinsic factors, measurement plan factors, and extrinsic factors. For intrinsic factors, all CMM technologies have geometric errors that affect the accuracy of a measured point (i.e. the CMM inaccurately measures a point in space.) Additionally, probing error, sensor error and software errors all contribute to the measurement uncertainty in this category. Measurement plan factors take into account the errors that are related to the work-piece location/orientation, probe selection, styli selection, sampling strategies and the quantity being measured. Finally, the extrinsic factors contribute to the measurement uncertainty in a variety of ways such as the environmental effects, non-ideal work-pieces, fixturing and operator-influences which are commonly random in nature and difficult to control. FIGURE 3 below shows the general sources of uncertainty that are considered when performing a task-specific uncertainty analysis suggested by the ISO 15530 series, this list is non-exhaustive.

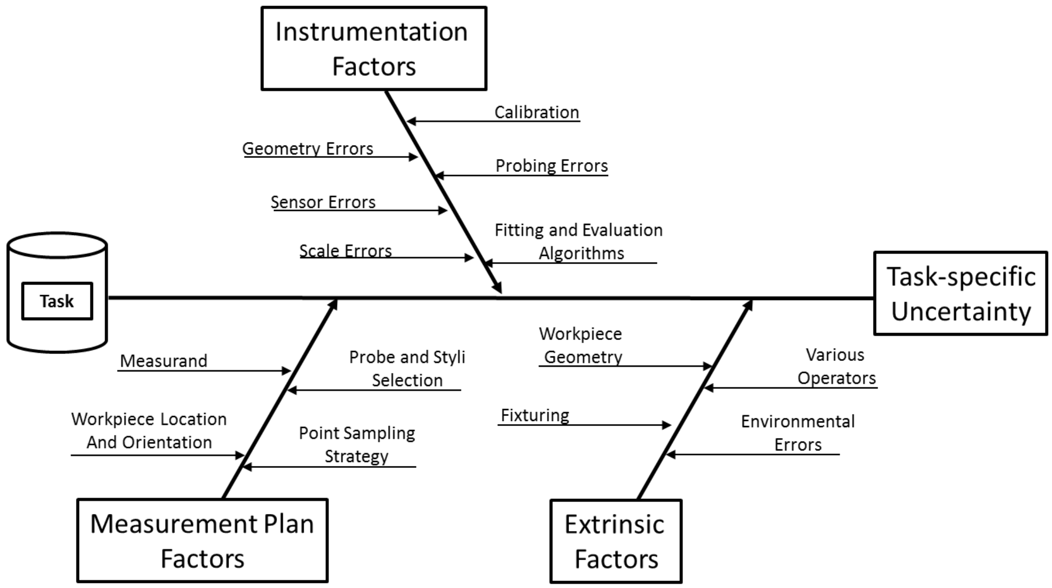

FIGURE 3: Ishikawa diagram for task-specific uncertainty.

2.1.2 15530-2: Use of Multiple Measurement Strategies

Part 2, [26], introduces a technique where multiple measurements strategies are performed on the same work-piece in multiple orientations to determine the task-specific uncertainty of the CMM measurements. The idea behind Part 2 is to develop a method using uncalibrated work-pieces so most, if not all, CMM users can determine the measurement uncertainty. The principle behind this method is to randomly vary the uncertainty contributions from measurement to measurement, changing the measurement point distribution and work-piece orientation, assuming that the uncertainty contributions are all independent in each measurement. It is also assumed that biases due to the different measurements will cancel out one another, resulting in a distribution of errors that has near-zero mean. The primary uncertainty contributions that cannot be estimated are the average length measurement error and the probing error. Both can remedied by measuring a calibrated feature of length and a calibrated feature of size, respectively. By measuring these calibrated standards of length and size, traceability can be established in the measurement. Other significant contributors (i.e. thermal, etc.) not accounted for in these measurements can be assessed as Type-B contributors.

The standard was never released, however, the methodology was experimentally validated by the completion of the EASYTRAC project by Trapet, *et al*. [23] in 2004. The techniques from ISO/TS 15530-2 have been used in the advancement of traceability of CMMs for industrial, dimensional measurements [27] and free-form artifacts [28], [29] with comparable results to what is achievable via alternative methods (i.e. sensitivity analysis, simulation, etc.) The scientific community involved in the development of this part of the series opted to broaden the investigation of the principle as well as organize several additional data collecting projects, therefore leading to a non-release of the standard.

2.1.3 15530-3: Use of Calibrated Work-pieces or Measurement Standards

Part 3, [30], introduces the use of calibrated work-pieces for a very straightforward approach to uncertainty analysis in CMM measurements. Most of the uncertainty sources are evaluated through the repeated measurement approach developed in the ISO/TS 15530-2 document, but in this case the measurements are performed on calibrated work-pieces. By repeatedly measuring the calibrated work-piece, instrumentation factors, measurement plan factors and some extrinsic factors can be incorporated in the measurements. The technique applies to specific measurement tasks and CMM results obtained from both uncorrected and corrected measurements. For uncorrected measurements, there is a non-substitution method where the CMM indication results are not corrected for a systematic bias. For corrected measurements, a substitution measurement is used to determine the measurement uncertainty where the CMM indication has been corrected for systematic errors by measuring both the work-piece and calibrated work-piece. A similarity criteria must be met for both the work-piece and calibrated work-piece if the substitution method is used, which is detailed below in TABLE 1.

TABLE 1: Similarity requirements for ISO 15530-3, [30].

Subject	Requirements	
Dimensional Characteristics	Dimensions	Identical within: - 10% beyond 250 mm - 25 mm below 250 mm
	Angles	Identical within ± 5°
Form Error and Surface Texture	Similar due to functional properties	
Material (e.g. CTE, elasticity, hardness)	Similar due to functional properties	
Measuring Strategy	Identical	
Probe Configuration	Identical	

Estimating the task-specific uncertainty using this method assesses four main uncertainty contributors: the standard uncertainty of the measurement process, u_P; the standard uncertainty of the calibrated work-piece, u_{cal}; the standard uncertainty of the residual bias contribution, u_b; and the standard uncertainty of the manufacturing process, u_W.

TABLE **2** details the contributions and how each is assessed in compliance with the GUM. For the expanded uncertainty, Eq. 4 is used to estimate using quadrature and multiplied by a coverage factor of *k* (for 95% confidence, *k* = *2*).

$$U = k \times \sqrt{u_p^2 + u_{cal}^2 + u_b^2 + u_w^2} \tag{4}$$

TABLE 2: Uncertainty components from ISO 15530-3, [30].

Uncertainty Component	Method of Evaluation (GUM)	Designation
Geometrical errors of CMM	A	Assessed in a sum u_P
Temperature of CMM		
Drift of CMM		
Systematic error of CMM		
Repeatability of CMM		
Scale resolution of CMM		
Temperature gradients of CMM		
Random errors of probing		
Probe changing uncertainty		
Errors induced by the procedure		
Errors induced by dirt		
Errors induced by measurement strategy		
Calibration uncertainty of calibrated work-piece	B	u_{cal}
All the factors contributing to u_P and the thermal environment during the assessment of the calibrated work-piece	B	u_b
Differences among work-pieces and the calibrated work-piece • Roughness, form, CTE, elasticity, etc.	A or B	u_w
NOTE: The list of uncertainty contributions may not be exhaustive.		

The EASYTRAC project [23] was successful in demonstrating the methods for free-form profiles [28], [29] and thread calibration [31] with encouraging results. Of the 15530 series, this is the most widely used and applicable approach.

2.1.4 15530-4: Evaluating Task-specific Uncertainty using Simulation

Part 4, [32], provides guidelines for estimating the task-specific uncertainty using computer simulation methods. ISO/TS 15530-4 is broken down into 3 sections: Uncertainty Evaluating Software (UES), UES model and UES validation. The UES software is used to estimate a measurement uncertainty by simulating the overall CMM measuring process of a work-piece. UES software can be either on-line (VCMM, [19]) or off-line (PUNDIT/CMM, [20]) however both are similar and consider the metrological characteristics (i.e. geometric errors, environmental, probing, probing strategy, etc.) but differ slightly in what is simulated. For the UES model, Monte Carlo techniques are usually the algorithm of choice because of the repeating nature and randomization. It is important to detail as many influence quantitates as inputs into the model to achieve the most accurate results. Validation of the UES is performed by testing on a calibrated artifact with uncertainty statements. This is done in most cases on point-to-point length measurements where the main influence quantities could be the error map, the probing (if known) or the scale errors. An output of the results should be less than or equal to 1 for validation. FIGURE 4 below details a typical flow process of UES.

Simulation methods have been used in numerous applications such as industrial work-piece tolerance verification [33], feature form deviations [34] and evaluation of different methods of uncertainty assessment [35]. Simulation is the most practical route to estimating task-specific uncertainty and preferred by most metrologists when the measurement model is sufficiently complex. If one is able to determine many of the influence quantities, the range of the influence quantities and probability density functions then an accurate uncertainty estimated can be obtained.

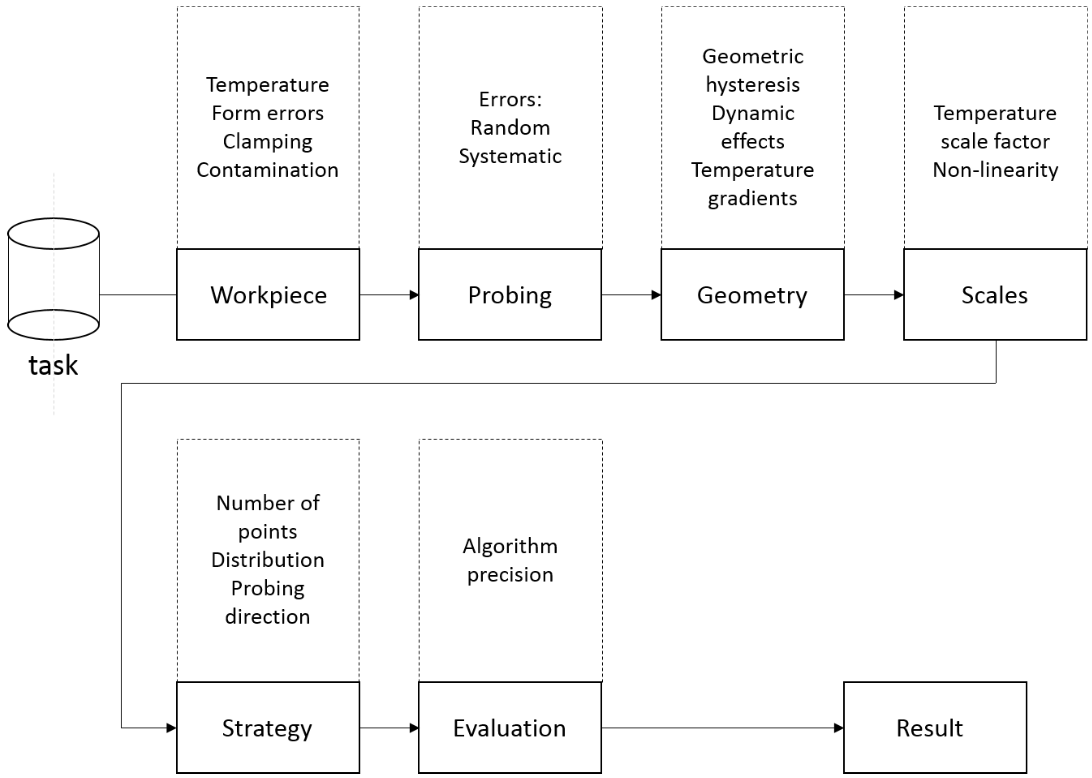

FIGURE 4: UES flow chart of error sources that affect final result, [32].

ISO 15530 is the only series of standards that is currently available for task-specific uncertainty of CMM measurements and was validated using traditional, Cartesian CMMs at the time of development. However, the same principles and methods can be applied to the class of portable CMMs with considerations to the specific influence quantities that affect the accuracy of measurements.

2.2 Performance Evaluation and Error Assessment of Portable CMMs

Performance evaluation is the assessment of whether or not a CMM is compliant with the manufacture's specifications within the recommended operating conditions. This includes environmental requirements and testing methods. The class of portable CMM technologies currently has minimal standardization available overall but has some for performance evaluation. The ASME B89 standards committee has developed the ASME

B89.4.19 for laser trackers [36] and the ASME B89.4.22 for AACMMs [37]. American standards, as well as international (VDI/VIN [38], [39]), have steadily included uncertainty assessments of certain influence quantities into non-mandatory appendices.

2.2.1 Laser Trackers

Laser trackers are considered by most practicing metrologists and researchers the most accurate of the available portable CMM technologies. Each laser tracker is equipped with an interferometric laser source that adds to its accuracy and the influence of the operator is only in the placement of the spherically mounted retroreflector (SMR). In any case, there are numerous sources of error that contribute to the overall uncertainty in the measurement data. The likeliest influences are those of the geometric misalignment errors and environmental errors. First a look at the standard available for performance evaluation and then onto what has been done in the literature for uncertainty assessment.

2.2.1.1 Performance Evaluation - B89.4.19 Standard

ASME B89.4.19, [36], establishes requirements and methods for specifying and testing the performance of laser trackers. The tests in the standard are specified and designed to evaluate the point-to-point length measurements capabilities of the laser trackers. The sets of test are divided up into two types: *system tests* and *ranging tests*. *System tests* are designed to evaluate the performance of a laser tracker in the measurement of a set of point-to-point lengths. The tests consists of comparing the length measured with a known value or *reference length*. The test length measurements are carried-out at multiple locations and orientations that are sensitive to known geometric error sources of a typical laser tracker. Additionally, *two-face* measurements are also performed at multiple locations and orientations which highlights the fact that the geometric errors “reverse” (frontsight/backsight). *Ranging tests* are designed to evaluate a laser trackers displacement (IFM) and distance (ADM) measuring devices that are built in to the system.

The system length tests consist of five measurement setups: *horizontal*, *vertical*, *right diagonal*, *left diagonal* and *user-defined* (see FIGURE 5). Since a laser tracker measures the distance between points, these different setups will be sensitive to the geometric errors of the laser tracker, therefore taking the known systematic errors into account. The errors in the measurements are identified in the form of a bias when compared to a traceable reference. In regards to the reference length, there are some specifications that need to be met. A minimum reference length of 2.3 m is required and an expanded uncertainty of the realized reference length should not exceed a fractions (1/4th) of the Maximum Permissible Error (MPE) of the performance tests. This relationship is captured by the measurement capability index, C_{m}.

The system two-face test is sensitive to the angular misalignments (geometric errors) of the laser tracker that reverse in sign when measured in frontsight and backsight, therefore it is an excellent diagnostic test. FIGURE 6 details the setup used when performing the two-face test. Each of the system tests has required approximate distances, heights and orientations to be utilized when performing the measurements which are covered in detail in the standard. Additionally, there are also user-defined requirements for the testing that is left to the metrologist to determine what is most adequate for their measurement purposes.

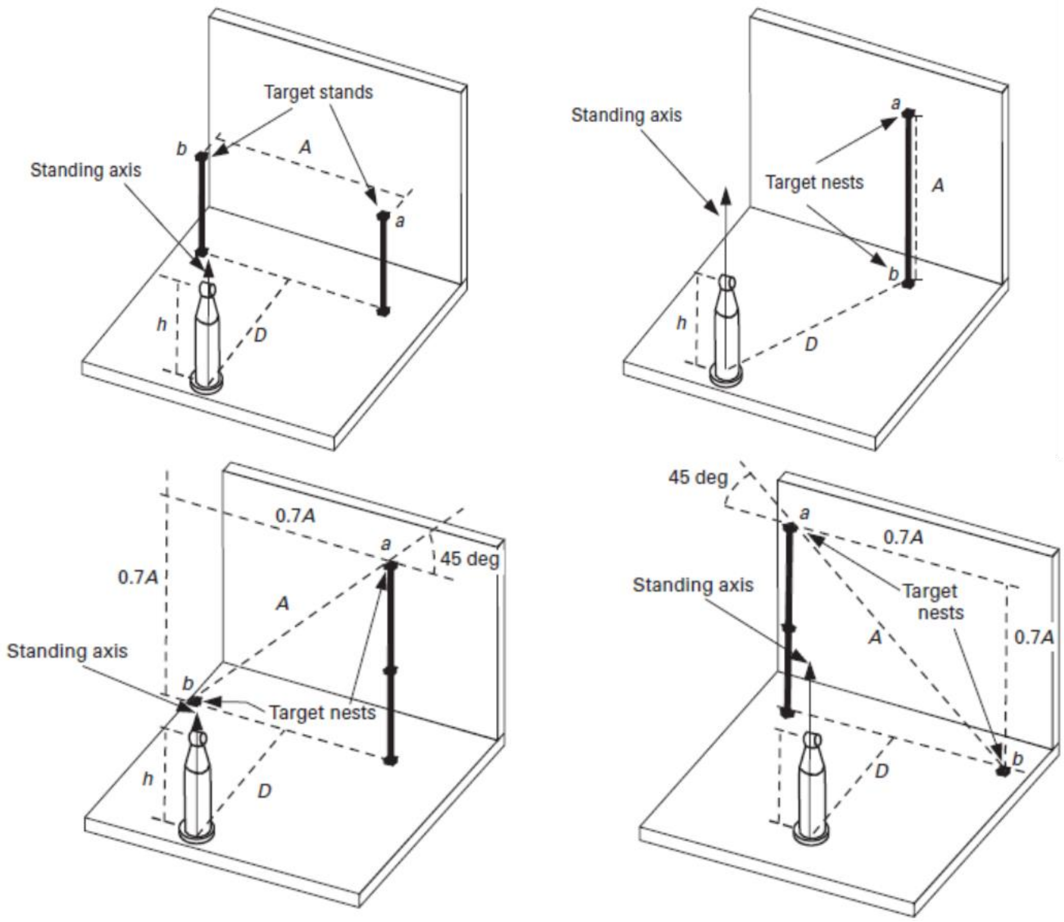

FIGURE 5: System length test setups, [36].

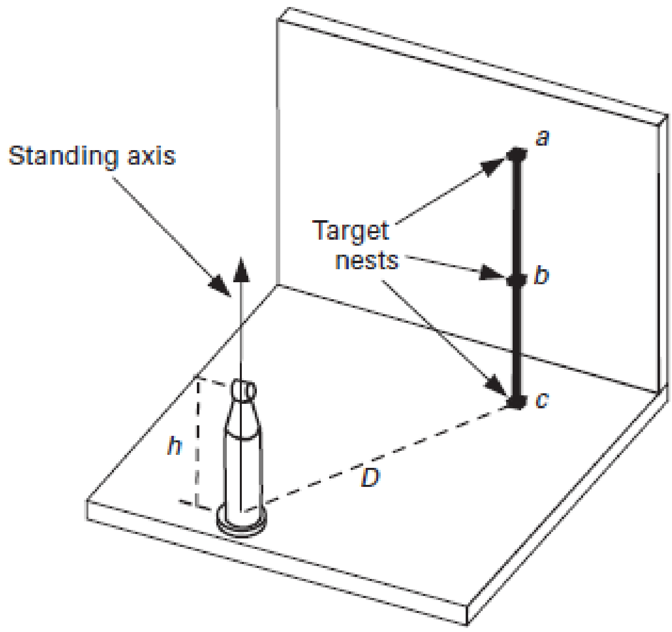

FIGURE 6: Two-face system test, [36].

Ranging tests are used to determine the performance of the IFM and ADM ranging capabilities of the laser tracker. The IFM range testing, in particular, tests the length-dependent errors, which commonly scale linearly with increasing length, and the proper counting of the interferometric fringes. As for the ADM range testing, a similar approach is performed to look at the time-of-flight. FIGURE 7 details the setup for the ranging tests and the standards details the required conditions to carry-out the measurements.

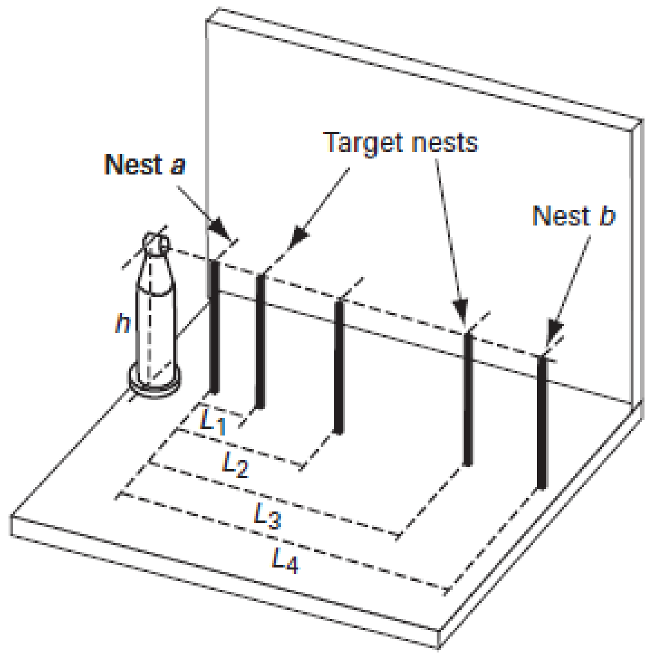

FIGURE 7: Ranging test, [36].

After all the testing has been completed and the data analyzed in accordance with ASME B89.4.19, instruments that have passed the performance tests of the standard are considered capable of traceable point-to-point length measurements for the required stated conditions. The drawbacks are that these test only test simple point-to-point length test, do not evaluate work-piece thermal compensation capabilities and are not sensitive to SMR imperfections. All these additional error sources that influence the measurement uncertainty must be evaluated by other means. Applications to specific work-pieces or measurement tasks require additional testing and analysis in order to establish metrological traceability.

2.2.1.2 Laser Tracker Error and Uncertainty Assessment

An abundance of work in the literature has been done on assessing the geometric errors and developing error models outside of performance evaluation, originally by Tullar, *et al*. [40], where they developed the preliminary error modeling and testing on the first generation of laser trackers. Loser and Kyle developed and tested the error models specifically for a laser tracker with a beam source in the column [41] and an assortment of field testing experiments to assess the uncertainty. Muralikrishnan, *et al.* [42] at NIST modified Loser and Kyle's model for a model with the beam source in the head. They identified, developed, tested the sensitivity and suggested improved sensitivity testing using the ASME B89.4.19 performance evaluation standard. Hughes, *et al.* [43] at NPL developed a new method to determine the geometric misalignments without having to use calibrated reference lengths, instead measuring a network of target locations (compensation off) from multiple laser tracker locations, thus determining the uncertainties and correlations. This was done using what is termed a *bundle adjustment*, where specific error source inherent in the laser tracker are "weighted" differently (e.g. the angular errors are given less weight than the range errors since the laser tracker is more accurate at range measurements.)

Like all CMMs, an error model for all the geometry errors is important when determining measurement uncertainty contributions from the instrument. An error model for a system using a mirror mounted on a two-axis gimbal mechanism was developed by Loser and Kyle [41], where it was determined that 15 misalignment parameters contribute to the systematic error in the measurements. The misalignment sources originate from the laser beams, mirrors, rotational axes, motors and encoders. They classify the 15 parameters into 3 different categories: offsets, tilt deviations and eccentricity/vertical offset index (See TABLE 3.)

The error model is shown below using Eq.s 5, 6 and 7 that represent the range, horizontal (azimuth) and vertical (zenith).

$$R_C = R_M - 2\sin\left(\frac{V_M}{2}\right)\left[\mathrm{e}\cdot\cos\left(\frac{V_M}{2}\right) + f\right] \tag{5}$$

$$H_C = H_M + \frac{1}{\sin(V_M)}\left[\alpha + \frac{\beta}{R_M}\right] - \frac{i\cdot\sin\left(\frac{V_M}{2}\right) + c}{\cos\left(\frac{V_M}{2}\right)} + E_y\sin(H_M) - E_x\cos(H_M) \tag{6}$$

$$V_C = V_M - \gamma - \frac{\delta}{R_M} - \cos\left(\frac{V_M}{2}\right)\left[\frac{2}{R_M}\left(\mathrm{e}\cdot\cos\left(\frac{V_M}{2}\right) + f\right) + K_x\right] + K_y\sin\left(\frac{V_M}{2}\right) \tag{7}$$

where for convenience and clarity the following parameters are used: $\alpha = I_x\cos(H_M) - I_y\sin(H_M)$, $\beta = O_{1x}\cos(H_M) - O_{1y}\sin(H_M) + O_{2x} + H_{off}$, $\gamma = I_y\cos(H_M) + I_x\sin(H_M)$ and $\delta = O_{1x}\sin(H_M) - O_{1x}\cos(H_M) + O_{2y} + V_{off}$.

TABLE 3: Error parameters for the mirror mounted laser tracker, [41].

Parameter	Description
R_C, H_C, V_C	The corrected laser tracker measurements (range, horizontal, vertical)
R_M, H_M, V_M	The measured laser tracker measurements (range, horizontal, vertical)
e	Transit axis offset
f	Mirror offset
O_{1x}, O_{1y}	Beam offset
O_{2x}, O_{2y}	Cover plate offset
c	Mirror tilt
i	Transit axis tilt
I_x, I_y	Beam axis tilt
E_x, E_y	Horizontal encoder eccentricity
K_x, K_y	Vertical encoder eccentricity
j	Vertical index offset
H_{off}, V_{off}	Offset from internally corrected PSD measurement

The error model for the beam source in the rotating head was developed by Muralikrishnan, *et al.* [42] at NIST where they performed a detailed analysis on the geometric misalignments using the performance evaluation testing of the ASME B89.4.19 standard. A modification of Loser and Kyle's model (see TABLE 4) was developed. Muralikrishnan, *et al.* understood that incorrect compensation or misalignments after compensation were possible so thoroughly performed a sensitivity analysis on the ASME B89.4.19 standard performance test, namely the two-face system test and the length measurement system test. Eq.s 8, 9 and 10 are the model for frontsight only but minor changes can be applied for the backsight error model,

$$R_C = R_M + x_2 \sin(V_M) + x_8 \tag{8}$$

$$\begin{aligned} H_C = H_M + \frac{x_{1t}}{R_M \sin(V_M)} + \frac{x_{4t}}{\sin(V_M)} + \frac{x_5}{\tan(V_M)} + x_{6x} \cos(H_M) \\ - x_{6x} \sin(H_m) + x_{9a} \sin(2H_m) + x_{9a} \cos(2H_m) \end{aligned} \tag{9}$$

$$\begin{aligned} V_C = V_M - \frac{x_{1m}}{R_M} + \frac{x_2 \cos(V_M)}{R_M} + x_3 + x_{7n} \cos(V_M) - x_{7z} \sin(V_M) \\ + x_{10a} \sin(2V_M) + x_{10b} \cos(2V_M) \end{aligned} \tag{10}$$

After a thorough treatment of describing the effect each misalignment has on the two-face and length measurement system tests, the model was used in numerically simulating the performance evaluation tests from ASME B89.4.19 and the sensitivity analysis of each. Additionally, new length system tests were proposed to demonstrate improved sensitivity to the misalignments that were previously undetected.

TABLE 4: Error parameters for source in head laser tracker model, [42].

Parameter	Description
R_C, H_C, V_C	The corrected laser tracker measurements (range, horizontal, vertical)
R_M, H_M, V_M	The measured laser tracker measurements (range, horizontal, vertical)
x_1	Beam offset
x_2	Transit offset
x_3	Vertical index offset
x_4	Beam tilt
x_5	Transit tilt
x_6,x_7	Encoder eccentricity
x_8	Bird bath error
x_9,x_{10}	Scale errors in the encoder

The geometric errors of a laser tracker are well established and can be determined performing some well-established alignment or calibration procedures. Hughes, *et al.* [43] developed a method of determining the geometric errors using a network measurement. By placing SMR nests at different locations and measuring the points with the instrument in different locations, the error model parameters were determined and no calibrated artifacts were needed. Furthermore, they were able to determine the uncertainties and correlations associated with the error model parameters. A series of repeated measurements is obtained from the network setup and a mathematical error model is fitted to the data where the parameters and uncertainties are estimated using rigorous, statistical methods. *Spatial Analyzer* has a similar bundle adjustment option built-in that determines the instruments uncertainty contributions from the point data. Other researchers have gone on to look at the errors of the laser tracker kinematically by using three dimensional matrices [44], but similarly use a known error model of the tracker. A simple, common correction method of the geometric misalignment errors would be to measure a calibrated, traceable reference artifact with a minimal uncertainty and then correcting the measurement data for any bias in the measurements.

A large gap exists when it comes to the task-specific uncertainty assessment of laser tracker measurement. Yang, *et al.* [45] compared the results from the GUM, Monte Carlo and a hybrid method for determining the task-specific uncertainty for cylinder measurements using a network of instruments. Both experimental and model-based approaches were exploited. An uncertainty budget was outlined in accordance to the ISO 15530 series where instrumentation factors, measurement plan factors and extrinsic factors were considered. The instrumentation factors were determined using the method outlined and developed by Hughes, *et al.* [43]. They showed good comparison between all three methods but the Monte Carlo method was deemed more feasible because of the rigor in determining an analytical model for the GUM methodology but the other methods also had their positives.

2.2.1.3 Environmental and Extrinsic Error Sources

Laser trackers are commonly used in shop floor environments where stability issues are almost the norm. Temperature is the largest contributor in these shop floor environments, therefore, laser trackers are equipped with environmental-compensation capabilities. These capabilities are able to correct the laser readings for the current working environment (i.e. temperature, pressure, and humidity), which can be setup in the software to monitor for a specified time duration. Part sensors can be setup on the work-piece to monitor and correct for the change in temperature but the temperature is likely different throughout the work-piece as these sensors only check localized areas. The atmospheric conditions on the laser beam do have an effect regardless, especially at long distances that can contribute to the uncertainty significantly.

Puttock [46] and Estler, *et al.* [47] show that for a laser beam source coming out of the laser tracker, effects from the temperature, turbulence and gradients (thermal and spatial) can cause refraction and retardation. As an example, FIGURE 8 is a simple schematic of how a beam is potentially affected at a far distance. The beam path *AB* would be straight in vacuum but in a shop floor, it would look similar to that of the curved path and if uncorrected, the endpoint of the line might be up to point *B'*. This being the case, the error is modelled as, ***e*** = *B'* - *B*. Most of the error is from three causes: refraction errors, variation of the speed of light and turbulence.

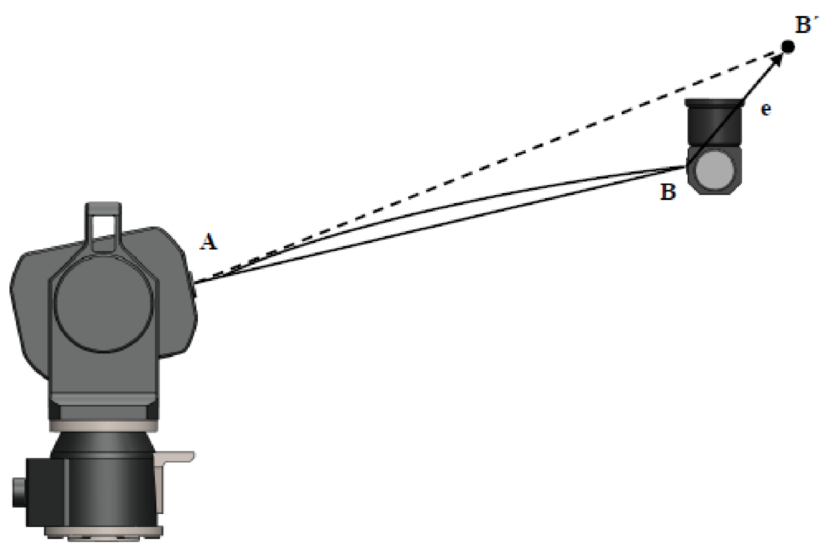

FIGURE 8: Effects of atmospheric refraction (courtesy: M. Rubeo, [48]).

Both papers go on to say that the effects from humidity are negligible on the state of the air density, however, the pressure and temperature components might have significant effects and must be considered. As height increases, air pressure will decrease causing the beam to bend horizontally. To account for both, Eq.s 11 and 12, where L is in meters and β is the lapse time rate in *K/m*), are used:

$$h_P = (1.58 \times 10^{-8})L^2 \quad (11)$$

$$h_T = (46.4 \times 10^{-8})\beta L^2 \quad (12)$$

Historically, significant errors usually only occur at distance of 50 m or further where errors range anywhere from a few hundred micrometers to a few millimeters [47].

ASME B89.4.19 has non-mandatory appendices that aide in determining the effects on the refractive index of air and air temperature on the laser tracker measurements. Edlen's or Ciddor's equation is the traditional way of correcting for the effect on the refractive index of air and the laser tracker software compensation has them built-in. The appendix for testing the effects from air temperature is only concerned with one particular error – the one caused by refraction and retardation along the beam path. The standard goes on split the error into radial and traverse errors. The appendix elaborates in much more detail on the descriptions and calculations [36].

Sandwith [49] evaluated the uncompensated thermo-mechanical errors in the calibration of a laser tracker's IFM, to determine the difference from compensation in a temperature-controlled laboratory and shop floor environments. Sandwith hypothesized that compensation in a shop floor environment does not adversely affect and may actually improve the uncertainty. It was determined that the hypothesis was in fact proved and thus is the result from thermo-mechanical errors having a lower uncertainty in a shop floor environment which lead to smaller uncertainty in the measurements. However, calibration in a temperature-controlled environment is standard and what is accepted throughout industry.

2.2.2 Articulated Arm CMMs

AACMMs are the most common portable CMM technology when it comes to industrial measurement capabilities. AACMMs are able to provide accurate results, depending on the application, while allowing the metrologist to conveniently setup on or near the part. With the versatility of the AACMM comes the error associated with that versatility, where the accuracy is highly-dependent on the experience of the operator. This tends to lead to varied ranges of accuracy and precision, especially if multiple operators are used in during the measurement cycles. A look at the current state of the in performance evaluation and uncertainty assessment will be detailed in the following sections.

2.2.2.1 Performance Evaluation - B89.4.22 Standard

ASME B89.4.22, [37], establishes requirements and methods for specifying and testing the performance of AACMMs. Furthermore, the standard is intended to test AACMMs with contact probes only as non-contact, optical probes are specifically excluded. It is broken up into three sections: machine classification, machine environmental requirements and machine performance tests. Machine classification and environmental requirements are well documented in the standard. The performance tests are used to test for probe error, articulation error and volumetric error. Within the standard, performance values are reported as the maximum deviation, the range and the standard deviation. The purpose is to bring the standard more in-line with existing national and international standards.

Machine performance tests for AACMMs are broken up into three parts: the effective diameter test, the single point articulation test and volumetric test. The effective diameter test is validated by measuring a calibrated sphere using nine probing points, which is repeated three times and the largest test deviation from the calibrated value is reported. The test provides results that in effect harmonize with respect to a bi-directional length measurement test common in Cartesian CMM testing. The single-point articulation performance test is intended to assess the AACMM's ability to provide similar values of a point coordinate when the instrument is articulated through the maximum possible range of motion for that single point, FIGURE 9. By design, the test incorporates aspects of both repeatability and reproducibility of the system's combined ability to reproduce the coordinate of a fixed point in space.

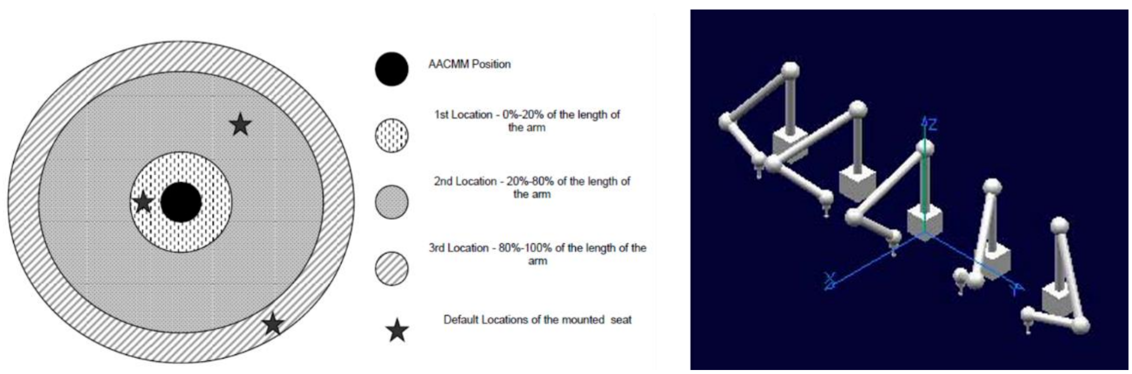

FIGURE 9: Single-point articulation tests, [37].

The volumetric test is used to assess the AACMM's performance throughout its working volume. Since the AACMM is unlike a traditional, Cartesian CMM, there is an infinite number of arm orientations that can result in the same location of the probe. As a consequence, a linear displacement accuracy test will not reveal much information about the instrument. To account for the linear displacement and volumetric testing, a calibrated length artifact is measured in multiple orientations throughout the measurement volume.

The volumetric assessment test is designed to be sensitive to the geometric errors of the AACMM so any systematic biases from the errors can be identified. This is similar to the volumetric testing of a Cartesian CMM when a calibration is performed. FIGURE 10 below shows the suggested orientations and positions of the calibrated length artifact for the volumetric performance test.

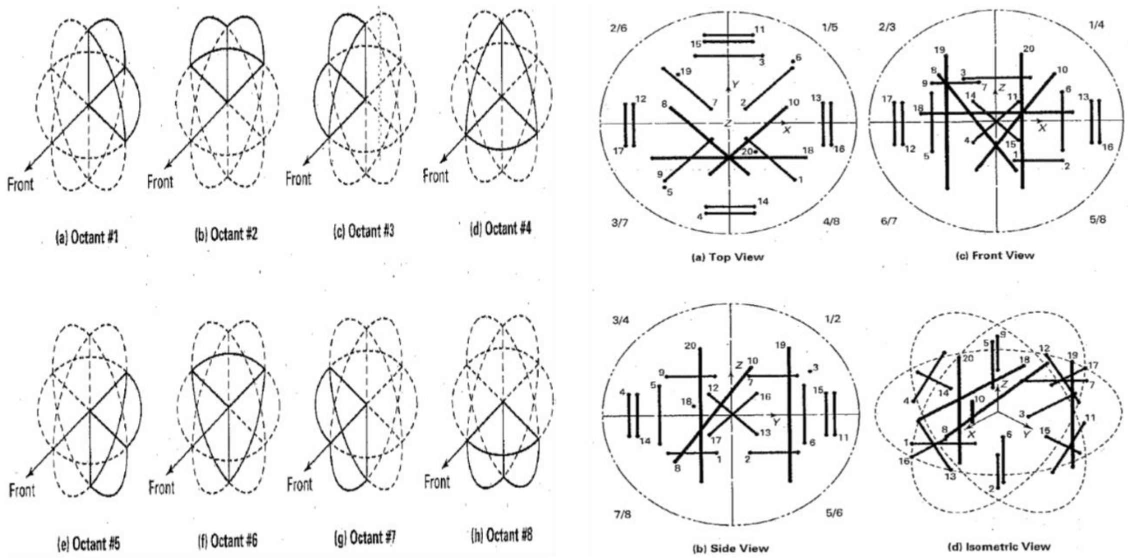

FIGURE 10: Volumetric test orientations, [37].

Overall, the ASME B89.4.22 is only intended to evaluate the performance of the AACMM and to verify if it meets the manufacturer’s specifications for the recommended testing conditions. Appendices in the standard detail some specific methods to estimate the uncertainty but for simple point-to-point measurements only. Mutilba, *et al.* [50] carried out the tests from ASME B89.4.19 and determined the uncertainty associated with each test. However, the uncertainty results seem underestimated (e.g. $U_{95} = 3.6\ \mu m$ for the volumetric tests) and very few error sources were considered in the estimations.

2.2.2.2 AACMM Geometric Errors and Uncertainty Assessment

AACMMs configurations are based on the rotating joints that connect the linkage-arms to the probe tip where the ASME B89.4.22 standard describes each of the possible configurations for commercial AACMMs. Mathematically the AACMM can be modelled by a generalized vector form of a CMM with *n* linkage arms, where the position of the probe can be modelled using Eq. 13 below. For the machine configuration in FIGURE 11, there are $n = 2$ linkage arms but mathematically the model is still very complex as each rotational matrix, $\boldsymbol{R}_i$ and length vector $\boldsymbol{L}_i$ in each linkage arm can rotate in the three directions.

$$\boldsymbol{P} = \boldsymbol{R}_1^{-1}\left(\boldsymbol{L}_1 + \boldsymbol{R}_2^{-1}\left(\boldsymbol{L}_2 + \cdots + \boldsymbol{R}_i^{-1}\left(\boldsymbol{L}_i + \cdots + \boldsymbol{R}_n(\boldsymbol{L}_n)\right)\ldots\right)\right) \qquad (13)$$

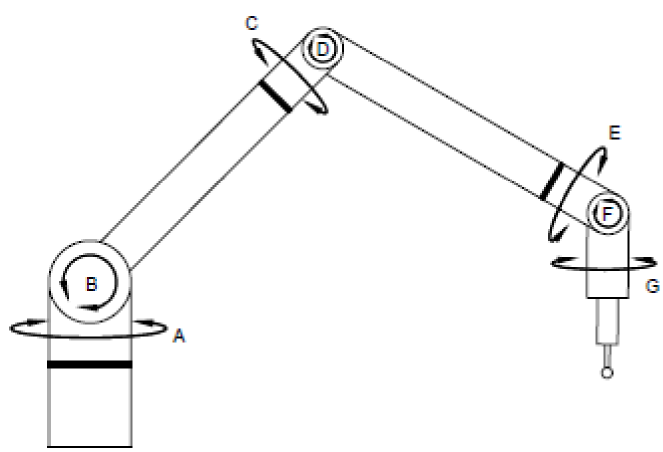

FIGURE 11: AACMM 2-2-3 configuration, [37].

The major geometric error sources that contribute to the uncertainty of the measurements are usually from the errors of the angular encoders inside the joints, squareness between the rotational axes, error motion of the arm articulation, elastic deformation of the linkage arms, probing error and calibration error [7]. The most difficult uncertainties to quantify are those associated with the dimensional stability of the composite materials used, stresses/strains and variations in the distortion levels of the flexible coupling. Mathematically, these error sources are incorporated into rotation matrices and length vectors that describe the AACMM geometrically in Eq. 13 and compensated in the software. Error models for the AACMM are difficult to model since they are manually-operated but there are numerous papers in the literature that have worked on some error modeling for AACMMs.

Error modeling has been performed using the geometrical parameters of the AACMM. Santaloria, *et al.* [51], [52] developed a kinematic model (Eq. 14) that optimizes the geometry parameters and characterized the repeatability errors of measurements in different orientations and distances,

$$T_6^0 = A_1^0 A_2^1 A_3^2 A_4^3 A_5^4 A_5^6, \qquad \bar{X}_{AACMM} = T_6^0 \bar{X}_{AACMM} \tag{14}$$

where, A_i^{i-1} is the homogenous transformation matrix between frames i and $i-1$, Eq. 15

$$A_i^{i-1} = \begin{bmatrix} \cos(\theta_i) & -\cos(\alpha_i)\cdot\sin(\theta_i) & \sin(\alpha_i)\cdot\sin(\theta_i) & a_i\cos(\theta_i) \\ \sin(\theta_i) & \cos(\alpha_i)\cdot\cos(\theta_i) & -\sin(\alpha_i)\cdot\cos(\theta_i) & a_i\sin(\theta_i) \\ 0 & \sin(\alpha_i) & \cos(\alpha_i) & d_i \\ 0 & 0 & 0 & 1 \end{bmatrix} \quad (15).$$

Sladek, *et al.* [53] attempted to theoretically model the errors of the AACMM, where they approached with an online assessment (e.g. a type of virtual AACMM) based on simulation which allows for a correction based on a compensation matrix. Furutani *et al.* [54] described an identification method for AACMMs to approximate the uncertainty using artifacts and a minimum number of different articulations. However, this work did not specify the procedure to obtain the parameters of the model, the type of model implemented nor any experimental results. Ye, *et al.* [55] developed a simple parameter identification procedure based on arm positions captured for a specific point in space.

Other works have looked at influence from the deformation of various parts of the AACMM. Li, *et al.* [56] considered an integrated model that took into account the bending deformation and torsions generated by gravity. However, the deflections were measured with a level which in turn led to limitations in the model. Hamana, *et al.* [57] integrated the bending deformation in their theoretical model but coupled the extremity of the AACMM with a traditional CMM where they showed low distortion but a complicated procedure. Romdhani, *et al.* [58] developed a Monte Carlo measurement model to assess the uncertainties of the AACMM measurements. The geometric parameters, errors of the angular encoders' position, dimensional variation and distortion of the AACMM were accounted for in the model of the measurement process.

2.2.2.3 Environmental and Extrinsic Error Sources

Commercial AACMMs have temperature compensation built into the controller which enables correction of the measured data from the effect of the environmental conditions. AACMMs are manually operated so thermal effects from the operator are additional contribution factors that contribute to the uncertainty in the measurements. ASME B89.4.22 has a dedicated appendices for thermal environment testing which specifies procedures and responsibilities in the event that the machine does not meet the requirements of the performance evaluation. Testing includes the mean ambient temperature, frequency and amplitude of temperature variation and thermal gradients. Additionally, an appendix exists for the determination of the *thermal error index* for AACMMs, basically to assess the thermal effects on the AACMM performance tests and/or work-piece measurements.

Santolaria, *et al.* [59] took on the task to development an empirical correction model for the thermal errors in an AACMM with a focus on the non-geometrical and temperature influences only. First they tested the thermal influences at 5 different temperatures by measuring a calibrated artifact with spheres at known distances. From the results of the calibrated artifact measurements taken over the stated range of temperatures, a thermal error correction model was developed. Lastly, a comparison between before and after thermal compensation showed improved accuracy for temperatures different from 20°C.

2.2.3 Laser Scanners

Laser scanner technology has been primarily used for the rapid acquisition of 3D data information of a surface. Most applications are large-scale such as scanning cars, buildings and those that are ordinarily not possible to "fully-measure" using traditional methods. Not known for precision measurements, laser scanners have the advantage of gathering large quantities of measurement data to reconstruct geometries easily. One of the main features of a laser scanner is its range where common usage is anywhere from less than a meter up to 250 m, depending on what type of laser scanner is used. The accuracy of the range is limited to around sub-millimeter to sub-centimeter, with a scan rate of around 10,000 points per second (http://www.faro.com).

2.2.3.1 Performance Evaluation

In the present, no standardization exists for testing the performance evaluation of laser scanners. Efforts in determining testing for the volumetric performance have been ongoing with a recent publication by Muralkrishnan, *et al.* [60]. In their work, a geometric error model was developed for a laser scanner with a laser source and a spinning prism mirror rotating about the vertical axis. Furthermore, they go on to use the error model for determining suitable positions/orientations of targets and reference artifacts in order to reveal the sensitivity of the systematic errors. Performing point-to-point length and two-face measurements were used to assess the sensitivities. This work is very similar to the work previously done by the NIST large-scale metrology group for sensitivity of laser tracker geometric errors, as the geometric error model is derived similarly to that of the laser tracker.

2.2.3.2 Geometric Errors and Uncertainty Assessment

Like all other instruments in metrology, laser scanner measurements are affected by error sources which lead to measurement uncertainty. Many of the geometric errors of a laser scanner are similar to those of laser trackers and share a similar geometric error model. These errors result from offsets, tilts, eccentricities and scale errors in the laser scanner due to the fact that any assembly of components will never be perfectly aligned. Muralkrishnan, *et al.* [60], realized this and developed an error model in the same manner as their model for a laser tracker. Therefore, to determine the parameters of the error model and sensitivity, similar artifacts and testing methods to that of the ASME B89.4.22 standard (laser trackers) were exploited in addition to specifically designed conditions for some of the unique geometric errors of a laser scanner (e.g. zero-offset).

Self-calibration is a common method when it comes correcting for the systematic effects in laser scanners. Self-calibration can be described as procedures or techniques used to minimize the effects of systematic errors on measurements by correcting the actual measurement with the estimated bias when taking redundant measurements and introducing the unit of length. Litchi [61] rigorously performed a self-calibration over a span of 13 months by utilizing a network of points and determined a systematic error model for the range, zenith and azimuth of a specific model of laser scanner. Chow *et al*. [62] performed a self-calibration of a terrestrial laser scanner (LTS) to remove the systematic defects without hardware modifications or specialized equipment. The self-calibration was performed on both point-based and planar-based measurements of a large quantity of signalized targets. The targets, measured with the LTS in different positions and orientations, were used to register point clouds. Both the point-based and the planar-based self-calibrations were based on 3D, rigid body transformation and least-square fits. It was seen that systematic errors were linear, highly-correlated before the self-calibrations were performed. Once the self-calibrations were performed, data showed randomness which implies that noise was the largest contributor. Abbas *et al.* [63] investigated the minimum requirement for network configurations to determine an on-site self-calibration. They considered three criteria for their analysis: (1) minimum number of scan station placements, (2) minimum number of planes for target distribution and (3) minimum number of point targets per plane. It was determined that a minimum configuration of two scan stations, two planes and sixteen point targets was suitable for on-site calibration.

Many papers in the literature have discussed the accuracy and precision of laser scanners with most of the research in the behavior of the laser scanner. There is very little on estimating the uncertainty in the measurements. Polo *et al.* [64] proposed a method to determine the uncertainty in measurement in terms of repeatability. A grid of near-symmetrical, uncalibrated contrast targets was fixed to a rigid structure and measured at multiple ranges. The center of the contrast targets were treated as vectors from the centroid of the entire data set to each individual measure. Repeatability uncertainties ranges from 1-4 mm.

2.2.3.3 Environmental and Extrinsic Error Sources

Nguyen and Liu [65] fundamentally determined and analyzed the geometric errors of a laser scanner by grouping the error sources into four areas: instrumental, object-related, environmental and scanning geometry-related. The instrumental errors are the errors associated with the laser rangefinder, axes, angular measurement system and edge effects. For the object-related (work-piece) errors, these are surface reflectance and multi-path reflection. Environmentally, the error sources arise from the laser beam propagation in the atmosphere, influence from atmospheric conditions, weather conditions on the laser scanner measurements, interfering radiation and laser scanner instability from vibration. Finally, they also relate errors to scanning-geometry most notably the incident-angle. The errors in these categories are similar to those in laser tracker measurements.

2.3 Structure of Work in Dissertation

The work in this dissertation will look to develop preliminary evaluation methods used to determine the task-specific measurement uncertainty analysis for industrial measurements. Primarily, the development of methods for assessment of the measurement uncertainty but consider the different construction of the instrument, operational environments and nature of the inspected work-pieces. Of particular interest is the separation of predictable biases introduced by the environment and work-piece from the quantifiable, but random, errors introduced by the same.

A procedural view of the experimental evaluations will be performed on multiple large-scale work-pieces, which are calibrated with a large-scale, high accuracy CMM. Next, each calibrated work-piece will be re-measured using the available portable CMMs in shop floor, industrial environments and conditions. The measurement uncertainty will then be evaluated in compliance with the GUM for both the reference measurements and industrial measurements for the particular task at hand. With experimental data available, simulations of the measurement process will be performed to compare both experimental and simulated uncertainties. Additionally, a conformity assessment will be carried-out by calculating a performance statistic to determine if the comparison between the reference measurements and industrial measurements are satisfactory and deemed acceptable or unsatisfactory, which in turn signals that the measurement process or uncertainty estimates may not be suitable for the measurand in question. Then, a few industrial case studies will be used as applications of the methodologies described. Finally, conclusions on the final results will be made and considerations for future work.

CHAPTER 3: EXPERIMENTAL APPROACH

In this chapter, detailed explanations will be provided on the experimental approach in determining the task-specific measurement uncertainty for industrial measurements. Firstly, a detailed explanation will be given on the instrument used to calibrate the available work-pieces and how to determine the measurement uncertainty of the reference measurements. Next, descriptions of the available work-pieces will be provided including the measurands of interests. Followed by the details of the measurement methods and how to assess the measurement uncertainty both experimentally and by simulation. Lastly, an error normalization will be estimated using the E_N performance statistic to compare the measured result against the referenced results as a form of conformance assessment.

3.1 Calibration Instrument and Calibration Uncertainty Assessment

The work-pieces used varied in size, volume, complexity, and other physical characteristics which were taken into consideration when determining the type of instrument used for calibration. By default, the work-pieces available for the project were large so a large-capacity instrument was needed. A Leitz PMM-F 30.20.16 (3m x 2m x 1.6m), gantry-type CMM located at UNC-Charlotte's Large Manufacturing Solutions Laboratory, was the instrument used in the calibration of the available work-pieces. Given the size of the Leitz PMM-F, the versatility and volume, FIGURE 12, the capability of measuring large-scale parts accurately is now possible to perform in-house.

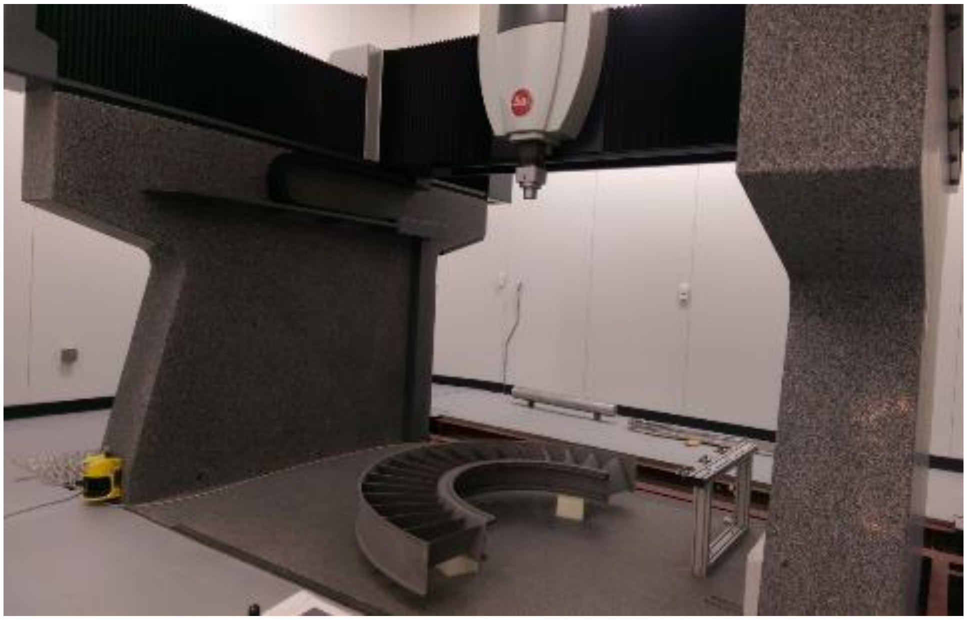

FIGURE 12: UNC-Charlotte's Leitz PMM-F 30.20.16.

The PMM-F is housed in a laboratory designed with a temperature specification of 20°±0.5℃, a temperature stability of ±0.5℃ per 8 hours and a maximum air velocity of 0.0508 m/s (10 ft/min). During the calibration, the maximum permissible error for length, MPE_E, was determined to be $2.3+0.0025\times L$ (µm) was verified, a maximum permissible error for probing (multi), MPE_P, of 1.7 µm and a maximum permissible error for scanning according to, MPE_S, of 2.2 µm. The entire calibration was done according to the ISO 10360 series for length measurements [66], continuous scanning [67] and single and multi-stylus probing systems [68].

Determining the reference uncertainty can be a challenge and since the measurements are task-specific, other options maybe more adequate [20], [35]. Most often than not, measurement corrections to consider in CMM measurements are variability of the multiple measurement cycles, the CMM geometry errors, the CMM resolution, the probing error and the thermal errors of the scale and work-piece [69]. Hocken and Pereira [7] suggested similar corrections to determine the measurement uncertainty for CMM measurements of length and size. In their approach, they considered the machine uncertainty, sampling uncertainty, thermally-induced uncertainty and datum uncertainty as a task-specific estimation. For the purpose of the work in this dissertation, their suggested approach will be used with the exception of the datum uncertainty. The datum uncertainty contribution will not be considered for two reasons: it does not influence features of length or size and it is unclear how to estimate the influence from each of the three datums (primary, secondary, tertiary) that construct the datum reference frame. Measurands different from length and size will be addressed separately with emphasis on angles, form error and location (position).

3.1.1 Machine Uncertainty

The main uncertainty contribution from the CMM during the measurement of specified surface points on the work-pieces are the geometric errors. After calibration of the CMM, a specification is given that represents the volumetric accuracy of the CMM. This is the maximum permissible error. This value designates a range by which the measured distance between two points is allowed to deviate from a known, reference distance, which is specified as $MPE_E = A + B \times L$ where A is the variance resulting from the repeated sampling of the same surface point on a final dimension, B is the length-dependent component of the length measurement deviation and L is the length measurement in millimeters.

To determine the uncertainty contribution from the measuring instrument for measurements of length (or size), assuming that all the values are equally probable within the maximum permissible error, the standard uncertainty can be modelled assuming a uniform probability distribution. Hence, this is modelled with Eq. 16

$$u_{CMM} = \frac{MPE_E}{\sqrt{3}} = \frac{A + B \times L}{\sqrt{3}} \qquad (16).$$

This is a moderate estimate of the contribution from the measurement instrument but as was mentioned previously, performing a classical error budget on a CMM is a formidable task. The variety of measurements a CMM is capable of determining just adds to the complexity. However, for this particular CMM, the measurements determined using the PMM-F had high repeatability with no indication of a significant change in the results occurring over the time frame that each of the work-pieces were measured.

3.1.2 Sampling Uncertainty

Uncertainty from sampling is due to the measurement of a limited number of points from an infinite number of possible points that constitute a feature. Because of the infinite possibility of point distributions, a Type-A approach is used to quantify the contribution in the form of a sample standard deviation of the mean. The larger the sample size, the smaller the uncertainty, assuming that the points were adequately distributed and not bunched together which would be less-sensitive to error in the geometry of the feature itself.

To estimate this contribution, Eq. 17 is utilized, where the contribution from sampling strategy uncertainty is dependent on the point coordinate error, σ_{pc}; the number of points, *n*; and the mathematical minimum number of points to define a given feature, *x*,

$$u_{sampling} = \frac{\sigma_{PC}}{\sqrt{n-x}} = \frac{\sqrt{\sigma^2{}_{MPE_P} + \sigma^2{}_{Stylus}}}{\sqrt{n-x}} \qquad (17).$$

The point coordinate error is the RSS of the maximum permissible error for probing, σ_{MPE_P}, which was determined during the machine calibration, and the stylus error, σ_{Stylus}. It is unlikely that the stylus used in the calibration of the instrument (small probe-tip diameter, short stylus-length) is the stylus used when measuring so the stylus error term accounts for this. This can usually be determined from the probe qualification routine performed before measurement of the work-piece.

3.1.3 Thermally-Induced Uncertainty

The temperatures of the measuring environment, measuring instrument and work-piece should all ideally be 20℃, which would result in no uncertainty from thermal errors. That is never the case, even in temperature-controlled environments. The overall measurement uncertainty must account for these thermally-induced errors. Thermally-induced errors can be quantified according to the ISO/TR 16015 [70] where the total thermal uncertainty is determined from the uncertainty of the nominal expansion (UNE_i) of scale or work-piece CTE, the uncertainty of the temperature measuring device and the variation in ambient temperature. Additionally, the dimensional uncertainty due to the temperature measurement ($DUTM_i$) is considered for both the scale and work-piece. The total thermal uncertainty can be modelled as the RSS of the four different contributors, which is modelled with Eq. 18,

$$u_T = \sqrt{UNE_s^2 + UNE_{wp}^2 + DUTM_s^2 + DUTM_{wp}^2} \tag{18}$$

The UNE and DUTM will be detailed in a later section as it applies for both the reference measurements and the industrial measurements. Minimizing this contribution can be done with a highly stable temperature-controlled lab. Furthermore, the contribution from the scale of the measuring instrument is negligible if numerical compensation is applied to the measurements. The same may not be true for the work-piece, particularly in poorly-controlled environments, as numerical compensation for the work-piece is based on a localized, surface temperature measurement that assumes a uniform distribution throughout the work-piece.

3.1.4 Expanded Uncertainty of Reference Measurements

Once all these contributions are estimated, the sources are assumed to be independent, therefore, summing up the parameters in quadrature and multiplying by a coverage factor 2 for 95% confidence yields the expanded uncertainty for the reference measurements of length and size. Eq. 19 below models this,

$$U_{Reference} = 2 \cdot \sqrt{u_{CMM}^2 + u_{sampling}^2 + u_T^2} \tag{19}$$

These reference uncertainties will be important for two reasons: comparison purposes to the industrial measurement results; and for calculating the performance statistic E_N.

3.1.5 Special Considerations: Angles, Form Errors and Tolerances

In dimensional metrology, not all measurands are features of length or size. More often than not, measurands are angles, form errors and locations. Depending on how each measurand is described, assessing the measurement uncertainty may not always be the same as assessing those for measurands of length or size. Statistical-approaches in determining the measurement uncertainty are viable alternatives whether it is specific distributions or Monte Carlo simulations. The following subsections will attempt to identify what types of error sources likely contribute to the measurement uncertainty as well as how to estimate the expanded uncertainty.

3.1.5.1 Angles

Angle measurements are often an important feature in dimensional metrology whether it is determining a simple angle on a sine bar or a more complicated feature like the slot angles in a generator rotor shaft. Angles are usually determined two-dimensionally such as the angle between two lines, three-dimensionally such as the angle between two planes, or a combination (i.e. the angle between a line and plane). When assessing the measurement uncertainty, there are multiple error sources but repeatability and CMM geometry errors are generally considered the two largest sources.

The contribution from the CMM geometry errors is the same as Eq. 16, but estimates are given in units of length, not angular units. Therefore a conversion factor or sensitivity coefficient is needed. For 2D cases where the angles are defined between two lines, an analytical form of the uncertainty can be calculated, where each line is the distance between two points. However, following a similar approach for 3D cases is not so easy. Descriptions on both will be presented below.

For the 2D case, the Laws of Cosine are used to determine the angle between two lines. Suppose that FIGURE 13 represents the angle between the centers of two holes where a line from the center hole to each respective hole is determined as the length between two points. To calculate the angle, φ, lengths L_1, L_2 and L_3 are needed, where the angle is calculated using Eq. 20,

$$\varphi = \cos^{-1}\left(\frac{{L_1}^2 + {L_2}^2 - {L_3}^2}{2L_1L_2}\right) \qquad (20).$$

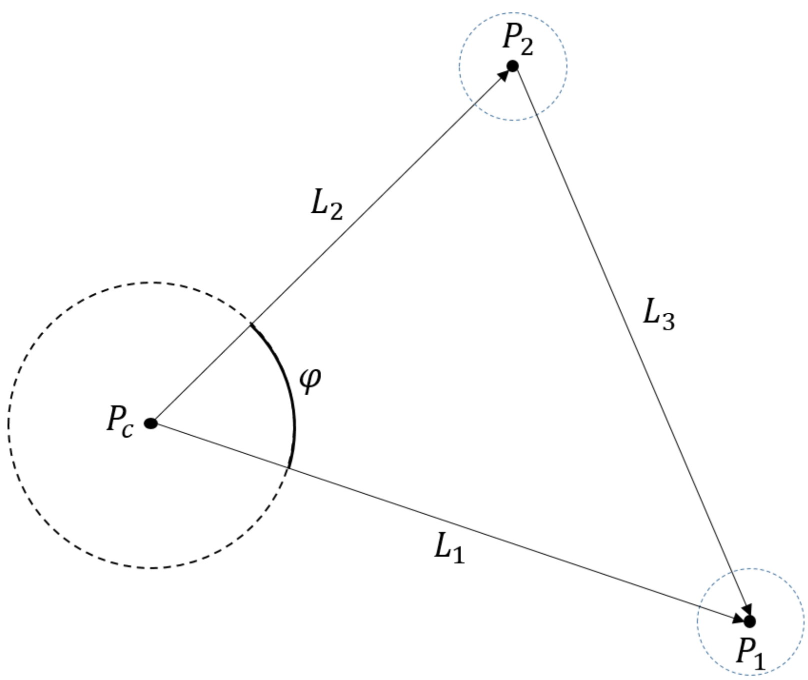

FIGURE 13: Angle between two lines.

With the equation of the measurand determined, sensitivity coefficients can be calculated for each of the influence quantities in the model. To calculate them, Eq.s 21, 22, and 23 describe the partial derivative of φ with respect to each of the respective lengths, per the GUM,

$$\frac{\partial\varphi}{\partial L_1} = -\frac{{L_1}^2 - {L_2}^2 + {L_3}^2}{2{L_1}^2 L_2\sqrt{1 - \frac{\left({L_1}^2 + {L_2}^2 - {L_3}^2\right)^2}{4{L_1}^2{L_2}^2}}} = -\frac{{L_1}^2 - {L_2}^2 + {L_3}^2}{2{L_1}^2 L_2 \sin(\varphi)} \tag{21}$$

$$\frac{\partial\varphi}{\partial L_2} = -\frac{{L_1}^2 + {L_2}^2 + {L_3}^2}{2L_1{L_2}^2\sqrt{1 - \frac{\left({L_1}^2 + {L_2}^2 - {L_3}^2\right)^2}{4{L_1}^2{L_2}^2}}} = -\frac{{L_1}^2 + {L_2}^2 + {L_3}^2}{2L_1{L_2}^2 \sin(\varphi)} \tag{22}$$

$$\frac{\partial\varphi}{\partial L_3} = \frac{L_3}{L_1 L_2\sqrt{1 - \frac{\left({L_1}^2 + {L_2}^2 - {L_3}^2\right)^2}{4{L_1}^2{L_2}^2}}} = \frac{L_3}{L_1 L_2 \sin(\varphi)} \tag{23}$$.

This results gives radians per unit length so multiplying by the proper conversion from radians to degrees is necessary. Therefore, one can estimate the expanded uncertainty of the angle between two lines using Eq. 24,

$$U_{angle} = 2\cdot\sqrt{u_{rep}^2 + \left(\frac{\partial\varphi}{\partial L_1}\cdot u_{L_1}\right)^2 + \left(\frac{\partial\varphi}{\partial L_2}\cdot u_{L_2}\right)^2 + \left(\frac{\partial\varphi}{\partial L_3}\cdot u_{L_3}\right)^2} \tag{24}$$

where u_L is the standard uncertainty of length, $u_L = 1.3\ \mu m + 1.4\ \mu m/m$, where a uniform distribution is assumed. A coverage factor of 2 is assumed for a 95% confidence in the estimation of the uncertainty.

For the 3D case, such as the angle between two planes seen in FIGURE 14, the error sources are not only those from the 2D case but additional error sources are present with the introduction of an additional dimension. These additional error sources are mostly geometry-related because the angles are now in 3D. To calculate the angle between the planes, the geometric definition of the scalar (dot) product can be used where the two Euclidean (normal) vectors of the planes are known. This can be modelled using Eq. 25, where the two normal vectors are $\hat{n}_1$ and $\hat{n}_2$,

$$\varphi = \cos^{-1}\left(\frac{\hat{n}_1 \cdot \hat{n}_2}{|\hat{n}_1||\hat{n}_2|}\right) \qquad (25).$$

Estimating the standard uncertainty via the GUM principles is non-trivial and the sensitivity coefficients cannot be calculated analytically. To resolve this dilemma, a Monte Carlo simulation is the ideal evaluation method where the uncertainty in the plane-fitting parameters (i.e., $f(a_1, b_1, c_1)$ for plane 1 and $f(a_2, b_2, c_2)$ for plane 2) that are used to determine the normal vectors, can be utilized to estimate the uncertainty.

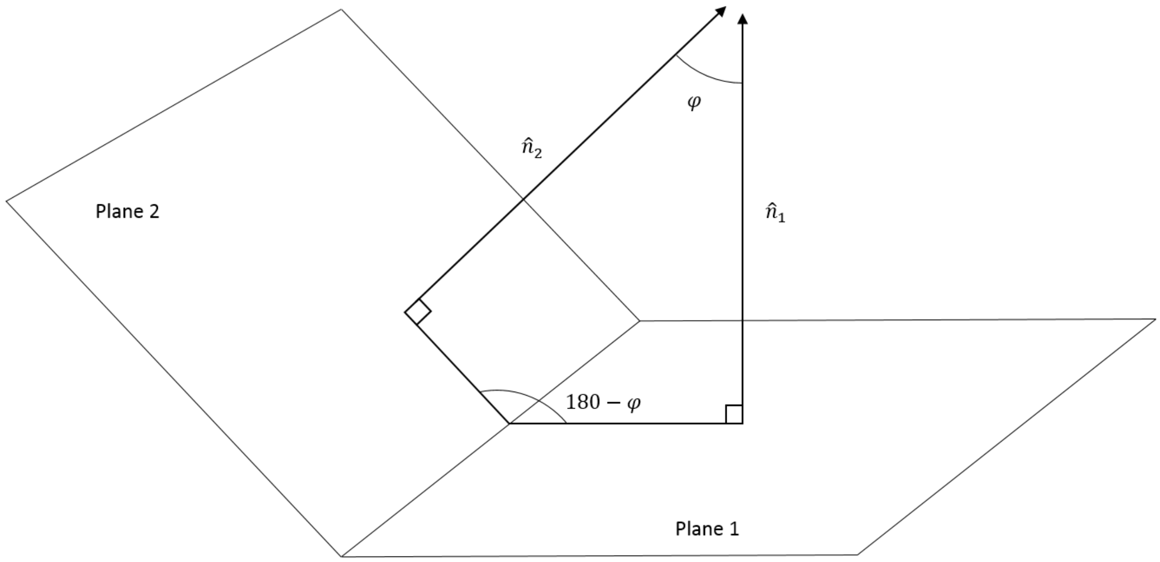

FIGURE 14: Angle between two planes.

3.1.5.2 Form Error

Form errors are the result of calculating the range of deviations from a substitute-geometry element (e.g. least-squares, minimum zone, etc.) Since range values have no sign and there is a possibility, although minute, of calculating the same results from a different measurement strategy, evaluating the uncertainty is non-trivial. A moderate approach to determining the uncertainty would be to consider error contributions from the repeatability of the measurements, the sampling strategy, the CMM geometry errors and thermal effects.

For the sampling strategy uncertainty, Eq. 17 is used. Since the contribution is statistically determined, ensuring that a large number of points are collected will reduce its contribution to the overall uncertainty. Caution should be taken however in estimating the uncertainty as the formula is insensitive to individual point locations where two different results can occur from the different point sampling strategies as is seen in FIGURE 15 below. A poor sampling strategy, like Strategy 2 in the figure, will amplify the errors hence a large uncertainty in the compute result. Ensuring an adequate sampling strategy will remedy this problem.

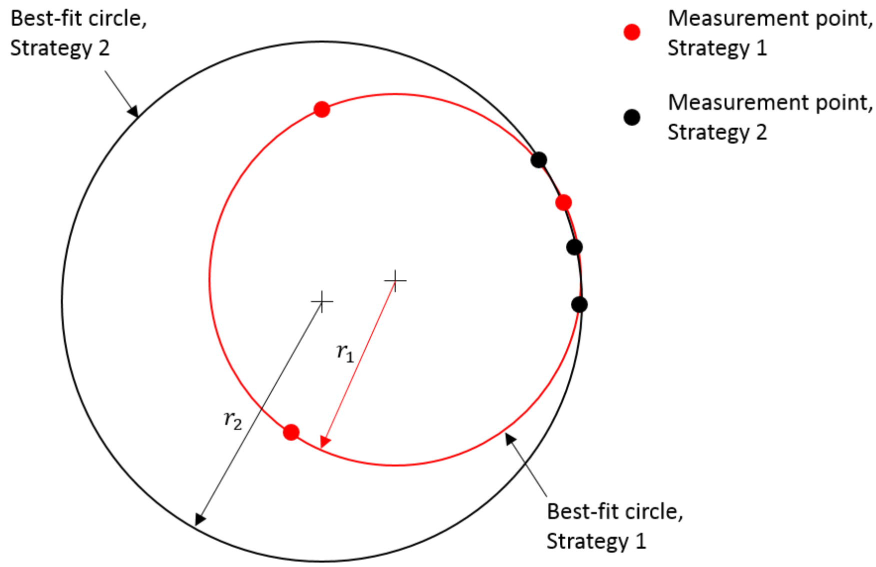

FIGURE 15: Substitute-geometry fits from different sampling strategy, [7].

The geometry errors of the CMM can possibly contribute to the form error assessment but depends on the work-piece itself. If a reference standard such as a calibrated ring gauge is measured then the geometry errors of the CMM can show up in the measurements [71], [72]. FIGURE 16 shows the elliptic pattern that a specific CMM geometry error will exhibit on the nominal radius in the 0°, 180° direction for the X-scale error; 90°, 270° direction for the Y-scale error; and the 45°, 135°, 225°, 315° directions for the XY-squareness error. However, if the work-piece is a casting or something to that nature then the effect from the CMM errors will be outweighed the errors in the work-piece itself.

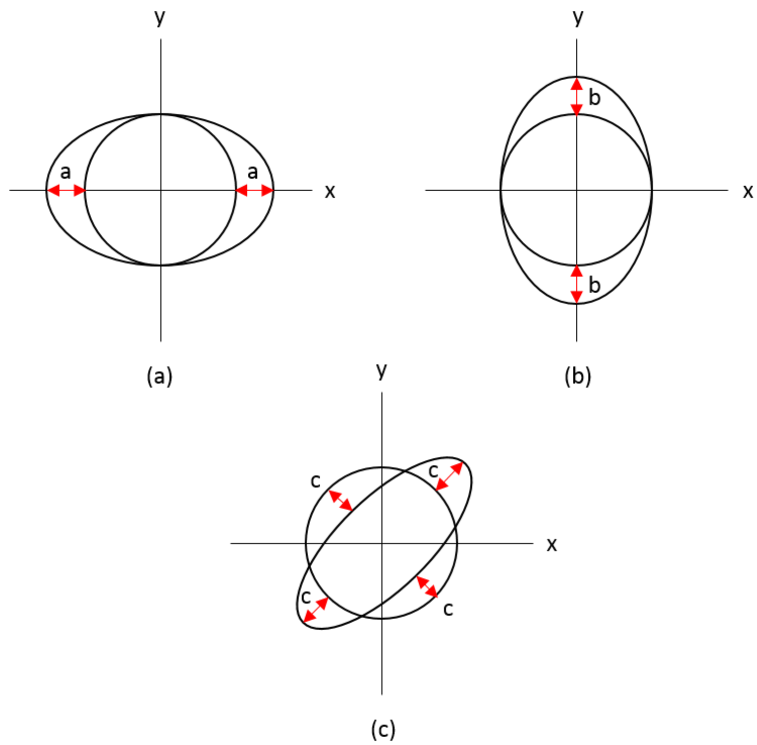

FIGURE 16: CMM errors: (a) X-scale; (b) Y-scale; (c) XY-squareness, [72].

Thermal errors such as thermal drift and thermal deformation can affect the measurements of form error. Changes in the CMM and work-piece are typically the most influenced by these factors. If the CMM is numerically-compensated, then the thermal effects on the measurements from the CMM are corrected and need not be considered. The work-piece temperature uncertainty will contribute to the uncertainty but can be minimized if measured in a temperature-controlled environment and was adequately soaked-out before measured.

A moderate approach to estimating the expanded uncertainty for form error measurements is detailed below in Eq. 26,

$$U_{form} = 2 \times \sqrt{u_{rep}^2 + u_{CMM}^2 + u_{sampling}^2 + u_T^2} \qquad (26)$$

where u_{rep} is the sample standard deviation of the measurements, and the three other contributors are estimated using Eq.s 16, 17 and 18 respectively.

3.1.5.3 Location (Position) Tolerances

Position tolerancing is used for locating features of size such as center points, axes and median planes [2]. It defines a zone within which the feature center or axis must lie. The tolerance zone size is equal to the allowable amount of variation from the theoretically exact position (i.e. true position). True position of a feature is initially determined from the reference point (i.e. center of a machined hole), then compared to any datum surfaces to determine how far off the true center of the feature is, see FIGURE 17. Location tolerance measurements are similar to form errors as both are ranges, however, are always greater than zero (i.e. $r \geq 0$). If true position is the measurand of interest, effectively, the measurand is then considered to be the radial deviation.

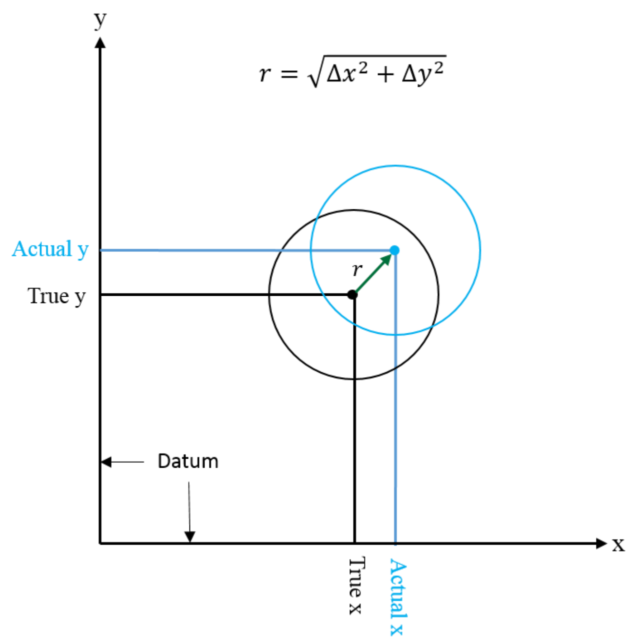

FIGURE 17: True position - location of a feature.

To evaluate the uncertainty of true position, it is common practice to use a check standard. The error sources are the repeatability of the check standard measurements and the calibration uncertainty of the check standard [7]. If a check standard is unavailable, error sources to consider would be the repeatability of the measurements and the CMM geometry errors, which are assumed uncorrelated. Adding these in quadrature then gives a standard uncertainty in each of the orthogonal measurement directions. If the measurements give independent, normal distributions with zero mean for uncertainty in the *x*- and *y*-directions (i.e. $\Delta x = \Delta y$), they can be combined to give a Rayleigh distribution for uncertainty in the radial direction [73]. The probability distribution function is then modelled using Eq. 27,

$$p(r) = \frac{re^{-r^2/2\sigma^2}}{\sigma^2}, \qquad r \geq 0 \tag{27}$$

where the mean of the Rayleigh distribution is calculated with Eq. 28,

$$\mu_r = \sigma\sqrt{\frac{\pi}{2}} \quad (28).$$

and the standard deviation gives the combined standard uncertainty as Eq. 29

$$\sigma_r = \sigma\sqrt{2 - \frac{\pi}{2}} \quad (29).$$

A conservative estimate of the expanded uncertainty at 95% confidence is to add two standard uncertainties to the mean value (i.e. Eq. 28). This assumes that the true position is centered or having zero offset which the Rayleigh distribution is only valid for.

If there exist a non-zero offset, that is the distance between the reference point and center of the bivariate distribution, then the probability distribution function is generalized to Eq. 30,

$$p(r) = \frac{re^{-(r^2+A^2)/2\sigma^2}}{\sigma^2} I_0\left(\frac{rA}{\sigma^2}\right), \qquad r \geq 0 \quad (30)$$

where A is the offset and I_0 is a modified Bessel function of the first kind, order zero. This is known as the Rice distribution [74]. This probability distribution represents the magnitude of a circular, bivariate normal random variable with the possibility of having a non-zero mean. What makes this distribution unique is when the offset A is zero, the Rice distribution is exactly the Rayleigh distribution. However, when $A > 0$, the distribution tends towards a normal distribution which can be seen in FIGURE 18.

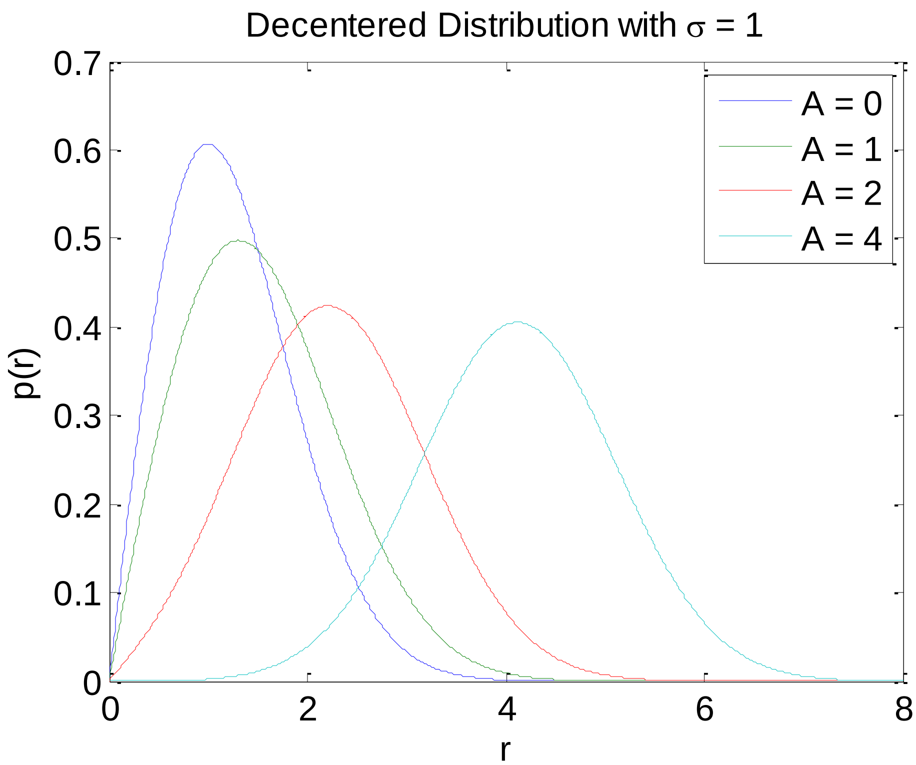

FIGURE 18: Decentering effects when using Rice distribution.

If the true position is un-biased (i.e. centered) then the expanded uncertainty can be evaluates with using the Rayleigh distributions. If the true position is biased (i.e. decentered) then the analysis using the Rice distribution is used where the mean is modelled using Eq. 31,

$$\mu_r = \sigma\sqrt{\frac{\pi}{2}}L_{1/2}\left(\frac{-A^2}{2\sigma^2}\right) \tag{31}$$

where $L_{1/2}$ is a Laguerre polynomial and the variance as Eq. 32,

$$\sigma_r^2 = 2\sigma^2 + A^2 - \frac{\pi\sigma^2}{2} L_{1/2}^2\left(\frac{-A^2}{2\sigma^2}\right) \tag{32}$$

Taking the square-root of Eq. 32 will give an estimate of the combined standard uncertainty for a biased true position measurement.

3.2 Work-pieces

The available work-pieces were donated from industry partners and range from different materials, geometries, wear conditions, etc. which will give a range of potential conditions commonly seen in industrial settings. The work-pieces being used for experimental evaluation are an aluminum cylinder used in steam turbines, a steel exhaust muffler for a steam turbine, an invar ball-bar length gauge used in CMM calibration, a titanium helicopter rotor yoke and a steel ‘flexible’ artifact made from bar stock rods. Detailed descriptions are provided in the following subsections of each.

3.2.1 Aluminum Cylinder

The aluminum cylinder (FIGURE 19) is a work-piece donated to UNC-Charlotte from Siemens Energy as part of a large-scale metrology collaboration. The material is 6061 aluminum which has a high CTE. A high CTE lends itself to be very sensitive to changes in environmental conditions, in particular temperature. As a result of the sensitivity to environmental changes, the work-piece is ideal for testing the thermal effects of measurements collected in industrial conditions. One particular thermal effect of interest is the non-uniformity of the work-piece temperature, which makes this work-piece ideal for investigating the effect it would have on the measurement results. A detailed discussion will be carried-out in a later section. For completeness of the physical characteristics, the approximate weight of the part is 50 kg (~ 110 lbs) which will contribute a gravitational sag effect if not properly supported.

FIGURE 19: Steam turbine “pry-bar” aluminum cylinder.

3.2.2 Exhaust Muffler

Donated from a previous project, the exhaust muffler (FIGURE 20) is a component on the steam turbine with tight tolerance specifications on a number of the internal features. The work-piece is no longer a service part and shows obvious signs of wear from years of use, thus the work-piece has defects on it, most notably pockets on some of the internal features which are the result of steam pressure and high temperature. However, there was adequate surface area to discretely probe and characterize the measurands, thus making the work-piece purposeful. The approximate weight of the part is 100 kg (~ 220 lbs). This work-piece is a good representation of the typical, physical condition that industrial parts are sometimes measured in, specifically in the turbine and generator industry.

FIGURE 20: Steam turbine exhaust muffler.

3.2.3 Ball-bar Length Gauge

The ball-bar (FIGURE 21) is a NIST-traceable, calibration gauge made of a low-CTE material, invar, which is part of the CPM's CMM calibration equipment. It consists of 8 stainless steel spheres nominally spaced 100 mm apart, center-to-center with each sphere having negligible form error. Invar is a low-CTE material, ideal for high dimensional stability and thus minimizing (or near-elimination of) all thermal effects that affect dimensional measurements. Measuring the ball-bar artifact with the portable CMM's is ideal for checking the accuracy of the instrument in a type of interim check. This is good practice particularly when a portable CMM is used in poorly-controlled environments that can have large variations in temperature and/or the possibility of significant influence from other extrinsic factors.

FIGURE 21: Invar ball-bar length gauge.

3.2.4 Rotor Yoke

A titanium (Ti-6Al-4V) helicopter rotor yoke (FIGURE 22) was donated to the UNC-Charlotte's Mechanical Engineering and Engineering Sciences (MEES) department and was used for high-speed machining applications. The curved nature of the work-piece, the lone planar surface and not having an engineering drawing left minimal options in determining the work-piece coordinate system or any of the specific features. Therefore, the outer-hole locations were not considered because of the curvature in the geometry and focus was solely on the central geometry of the work-piece, in particular the center hole and bolt-hole pattern. A length of approximately 1.5 m and a mass of approximately 60 kg (~130 lbs.) so gravitational sag may effect some of the parameters depending on the setup.

FIGURE 22: Helicopter rotor yoke.

3.2.5 Flexible Length Artifact

Gravitational sag effects can be a significant extrinsic contributor to the measurement uncertainty. It is important to identify those geometry-dependent errors and determine their contribution to the overall measurement uncertainty. The idea behind manufacturing a long, flexible work-piece (FIGURE 23) is to setup the work-piece in a position/orientation that would exploit gravitational sag or "bending". It was determined that a long, thin rod would be an ideal candidate for evaluation of the gravitational sag. The work-piece has approximate dimensions of 1.8 m (72") in length and 25.4 mm (1") in diameter. Flats were machined at dimensions of approximately 75 mm (3") in length and 5 mm (0.2") in depth with a center-hole of diameter approximately 6.5 mm (0.25"). Two of the four flats were manufactured at approximately 90° for testing as well.

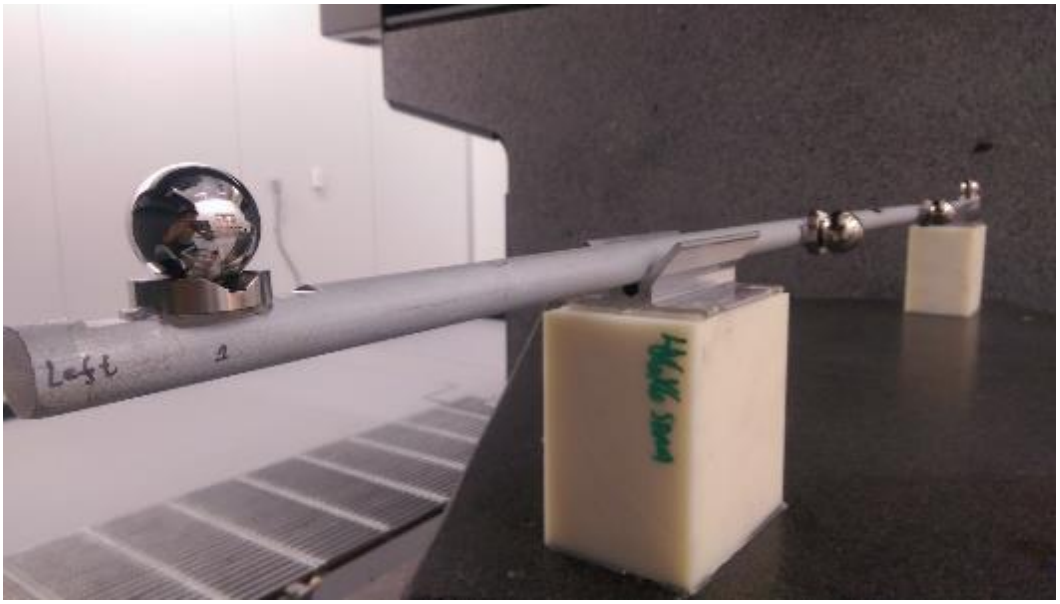

FIGURE 23: Flexible artifact.

3.3 Industrial Measurement Process

From the literature, applications of the ISO 15530 standards have been performed with success in demonstrating viable uncertainty estimations and traceability [23], [27], [28], [29], [35], [75], [76]. In truth, all but [76] were carried out using a tactile Cartesian CMM, or in an environmentally-controlled laboratory to minimized the effects from the environment. In large-scale, industrial environments, there are many reasons as to why it may not always be feasible. Costs of having an environmentally-controlled laboratory large enough would be profound. Given that portable CMM metrology is more adequate for large-scale applications, measurement techniques need to be developed that can be used specifically to assess the measurement uncertainty. The following subsections describe in detail the measurement strategy used for measuring each of the available work-pieces with the available portable CMMs.

3.3.1 Measurement Strategy

The measurement strategy is comprised of the necessary factors involved in executing the measurement. This includes the work-piece position/orientation, the probes for the measurement and the sampling strategy. Additionally, the measurand needs to be specified without any ambiguity to ensure the proper fitting analysis is calculated on the measurement data (i.e. least-squares, minimum-zone, etc.) A multiple measurement strategy will be utilized which is ideal for large-scale measurements. The instrument will be re-located instead of the work-piece, further demonstrating the portability and versatility of the instrument. The sampling strategy is dependent on the feature being measured but the minimum requirement is that there must be more points than the mathematical minimum used to define a specific feature. Each measurement data set will be analyzed using a least-squares algorithm for the substitute-geometry.

3.3.1.1 Multiple Measurement Strategy

Measurement uncertainty is usually dominated by systematic errors, in most cases unknown systematic errors. There is a need to identify, eliminate and/or reduce these errors. Using a single measurement strategy repeatedly cannot adequately identify these systematic errors other than revealing a systematic bias over the entire measurement sample. To account for these systematic errors, the use of multiple measurement strategies is performed.

The principle behind the multiple measurement strategies is to take repeated measurements after varying the measurement conditions, as in FIGURE 24, where it is assumed that correlation between errors sources is eliminated from the measurements. In doing so, the systematic errors (known and unknown) are randomized thus allowing for statistical averaging where the measurement uncertainty is evaluated using Type-A analysis. ISO/TS 15530-1 states that *"task-specific measurement uncertainty takes into account all uncertainty sources associated with the details of the measurement process, including the CMM, probing system, sampling strategy, work-piece location/orientation, fixturing contamination, thermal environment."* [25], where a significant amount are covered when using the multiple measurements strategies. Some extrinsic error sources must be determined by other means (Type-B) as they are not covered under this experimental approach. If the principle is carried-out properly (i.e. measurement setups are sufficiently altered), this will result in a general reduction of the measurement uncertainty for the measured geometrical features compared to a single measurement and the knowledge of the task-specific uncertainty for each geometrical feature.

FIGURE 24: Multiple measurement strategy.

It should be noted that this experimental approach does not strictly apply to Cartesian CMMs but its principles are derived from experimental measurements taken with a Cartesian CMM where the work-piece is placed in the working volume (i.e. part-to-CMM). Portable CMMs are the opposite in that the instrument *can* be placed in a work-piece's working volume (i.e. CMM-to-part) and thus have arbitrary, though still limited, working volumes which leads to a vast number of possible positions/orientations. The physical aspects of the work-pieces makes it inefficient in trying to position/orientate in multiple setups thus an alteration in the measurement strategy is needed. Additionally, the accessibility of all the measurands of interest may be limited from a single position of the instrument.

The new approach is to use multiple measurement strategies where the position of the *instrument*, not the *work-piece*, is altered. Therefore, by randomizing the placement of the instrument (FIGURE 25), variation of the systematic errors and their influences on the measurements will be included in the uncertainty assessment. Instrumentation factors such as geometry errors, instrument temperature errors, drift errors, repeatability, probing errors, instrument scale errors and the various errors of the CMM will be covered. Measurement plan errors and some extrinsic factors will also be covered from this new approach.

FIGURE 25: Multiple positions of instrument.

One important observation to note is that the multiple measurement strategy technique that is used in this work to performed with a single instrument every time by “linking together” the multiple instrument locations using a network of reference points. This allows one to complete multiple measurements from different locations. Therefore, the uncertainty from moving the instrument is related to how well the reference points are re-measured and the location of the instrument in relation to the network of points. When using portable CMMs, it is possible to link together several instruments to collect a single measurement with the use of a network of reference points as well where a bundle adjust is used by bringing the multiple instruments together into a common coordinate system.

The uncertainty in the measurements from linking multiple instruments is related to how well the software calculates the positions of each instrument in a global coordinate system.

3.3.1.2 Instrument Probing and Sampling Strategy

The laser tracker uses a spherically-mounted retroreflector (SMR) to probe the measurand surface. The principle behind the SMR is the use of a cube corner target. The cube corner is made of three mutually-perpendicular mirrors attached together to make a reflecting surface for the laser beam of the laser tracker. The beam is reflected parallel to the incoming beam, at an equal (and opposite) distance to the vertex of the mirrors. Because the laser tracker measures the range and two angles with the distance meter and angular encoders respectively, the center of the SMR can be calculated very accurately. Additionally, with the spherical design of the SMR, its center is always at a fixed, radial offset distance, R_{SMR}, with respect to any surface being measured, so the coordinates of the surfaces or points measured with the SMR are readily obtained. FIGURE 26 details a 2D schematic of the "probing" for a laser tracker measurement.

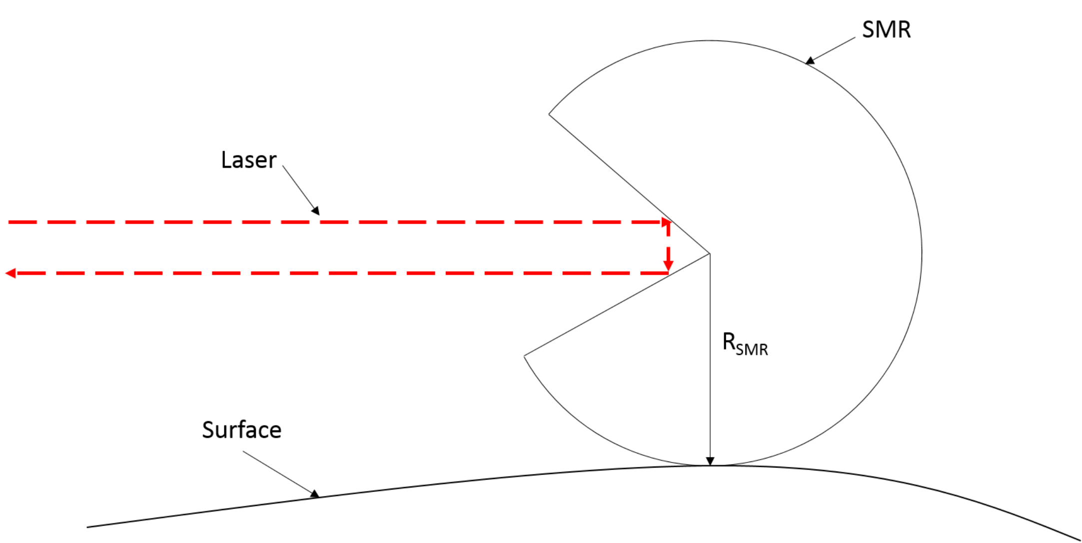

FIGURE 26: SMR probing of surface.

Controlling a uniform, discrete sampling strategy is possible when using a laser tracker but, since these are manual machines in terms of probe placement, any uniformity would have to be managed by the software by using a spatial or temporal scanning measurement profile. That alone will not guarantee very good point-to-point repeatability and will only add to the dynamic error effect from continuous-scanning. Good judgement should be practiced when taking the measurements to ensure points are sampled thoroughly throughout the measurand. Clustered or closely-spaced points will be less-sensitive to errors that arise from the sampling strategy which will affect the accuracy of the measurement results.

AACMMs use a traditional hard-probe but do have the option of attaching a laser-line scanner for non-contact measurements but was not considered in this work. The probing of an AACMM is like any traditional CMM probing where first the probe needs to be qualified (or calibrated) to determine the center and radius of the probe. This is either done using a known, calibrated sphere where the AACMM probes points on the sphere or a kinematic seat where the AACMM is articulated in three-dimensions (120° apart) to determine the point. With the articulation of the AACMM and the geometry of the probe, the coordinate location on the probe center is known for multiple articulations in all three-dimensions. This is the result of the known lengths of the linkage arms and angular encoders. FIGURE 27 below show a 2D-schematic of the probing with an AACMM.

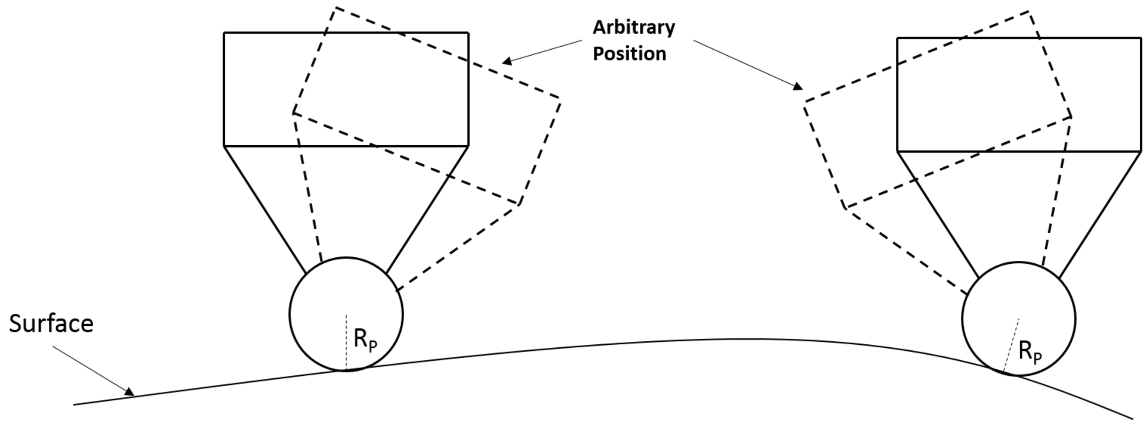

FIGURE 27: AACMM probing on a surface.

The same issues with the sampling strategy of the laser trackers measurements are true as well for an AACMM, with the addition of large operator-dependence. Due to the arm length restrictions, measurements are taken within the suggested 20-80% working volume suggested by the performance evaluation standard, FIGURE 9. Overexertion or pinch-points in the arms will likely result in faulty data or no data collection at all.

The laser scanner is a non-contact technology, which “probes” a work-piece by illuminating the work-piece with light. This is done using an infrared laser beam that is emitted to the center of the rotating mirror. The mirror then deflects the beam on a vertical rotation around the environment being scanned. Scattered light from the surrounding surfaces reflects back to the instrument. Similar to a laser tracker, time-of-flight (ADM), is applied when determining the point coordinate, and FIGURE 28, respectively.

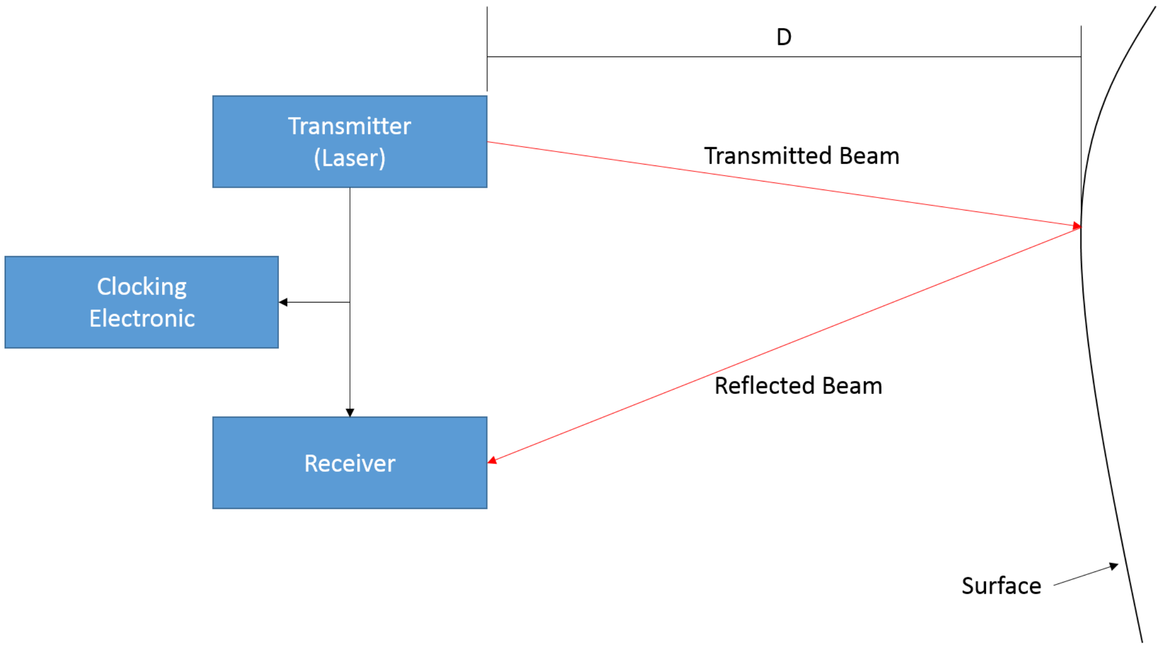

FIGURE 28: Laser scanner time-of-flight measurement.

Unlike the laser tracker and AACMM which generate a single-point from probing, laser scanning generates point clouds of objects, which are made up of high-density, single points with individual 3D coordinates. The sampling strategy is dependent on the density of the point-cloud which is input into the software and uniform over the surface. With such a high-density data acquisition, post-processing, such as filtering, is usually required for analysis.

3.3.2 Data Fusion

Portable CMM metrology is similar to traditional CMM metrology where the need for features of reference (e.g. points, holes, etc.) are essential to locate the work-piece relative to the CMM's reference frame. The obvious difference between the two technologies is how the reference features are used. Cartesian CMMs have a finite, rectangular working volume (FIGURE 29) where the work-piece must be in a position/orientation that all the reference features can be accessed for alignment between coordinate systems. All features can then be measured without having to re-position/orientate the work-piece, unless the working volume is too small to accommodate the work-piece. If so, re-measurement of the reference features has to be performed to locate the new position/orientation of the work-piece relative to the CMMs reference frame.

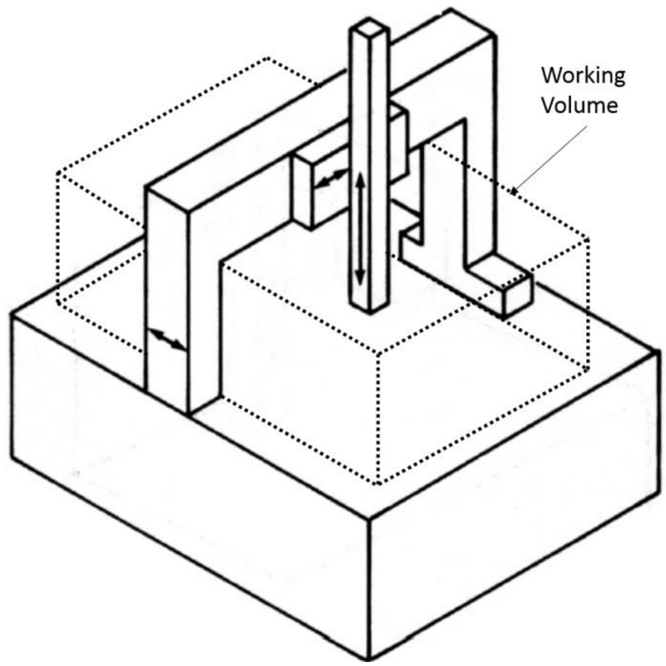

FIGURE 29: Cartesian CMM working volume (Courtesy: Hocken).

Working volumes for portable CMMs are finite but their ranges depend on the type of technology being used. Laser trackers and laser scanners have long ranges anywhere from 25-200 meters but the distance contributes to the measurement uncertainty so self-imposed restrictions are up to the discretion of the operator. AACMMs working volumes range from 1-4 meters which is the result of the limitation of the linkage arms. However, all these CMMs have roughly spherical working volumes and can access 360° azimuthally. For large or complex work-pieces, not all the features may be accessible from one single position/orientation therefore, reference features must be measured and re-located after the instrument is moved (FIGURE 30), which will be referred to as data fusion.

Depending on the instrument used, data fusion can be determined using reference targets, spheres, planes or any feature that can repeatability be measured. All, if not most, CMM software's have this capability built-in and can easily provide the error from the data fusion transformation. A minimum of three reference points are needed but six or more is recommended to provide more rigorous alignment, significantly improve repeatability and accuracy as well as helping identify errors. The distribution of points to encompass the object is important to ensure that the best-fit transformation is not biased and to reduce further measurement and alignment errors across the measurement volume.

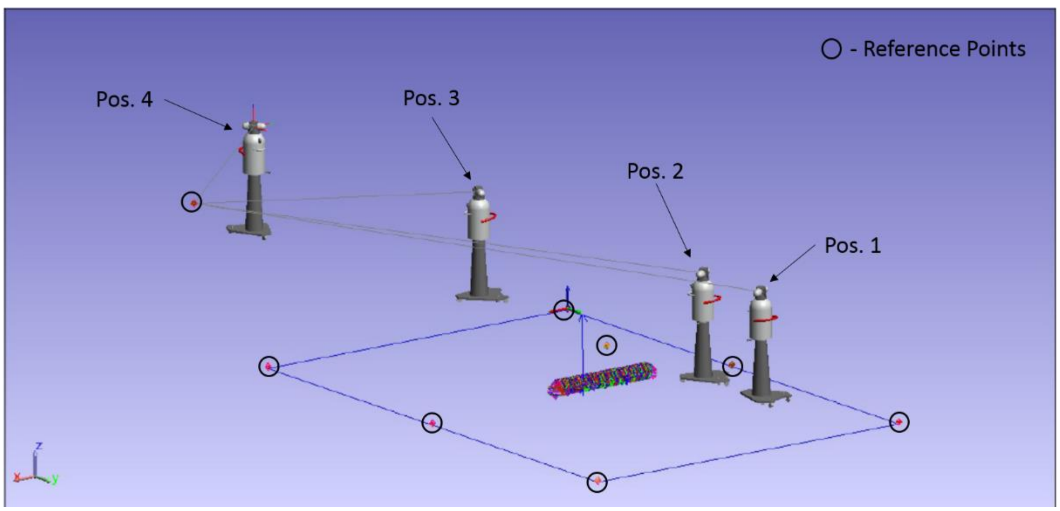

FIGURE 30: Portable CMM data fusion example.

Consequently, the transformation errors contribute to the measurement uncertainty and must be taken into account. The errors in the measurements are dependent on the type of network used when linking the instrument positions together. If a single instrument is used, then a best-fit is calculated in the software via a homogenous spatial transformation. Since the multiple measurement strategy principle is used, the best-fit transformation might introduce error stack-up and can be significant. FIGURE 31 shows what happens when stack-up error is introduced every time the instrument re-locates to a new location. Commonly, this is going to be the case if only a single instrument is available for measurement.

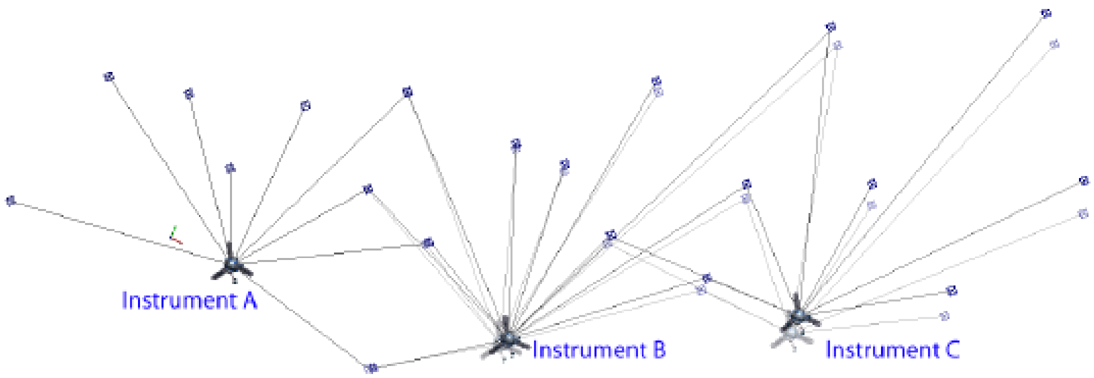

FIGURE 31: Instrument stack-up error (source: SA user's manual.)

3.4 Uncertainty Evaluation Methods

Estimating the task-specific measurement uncertainty can be done in a number of ways as was described in the introductory chapter, with the importance that the uncertainty is determined in compliance with the GUM. For the uncertainty determination in this dissertation, both experimental statistical evaluations (Type-A) and non-statistical evaluations (Type-B) will be developed to estimate the combined standard uncertainty. For the simulation approach, Monte Carlo techniques are utilized to simulate the measurement process, thus establishing correlation to the experimental approach. Given the industrial nature of the measurements, additional extrinsic contributions are also be considered

3.4.1 Experimental Uncertainty Evaluations

As was briefly explained, estimating the task-specific uncertainty when using the substitution method (i.e. ISO 15530-3) is a straightforward and reliable method. Four contribution are considered in the uncertainty budget where the expanded uncertainty is expressed by Eq. 4, namely the standard uncertainties of the calibrated work-piece, measurement process, manufacturing process, and bias. To evaluate the task-specific measurement uncertainty in this work, a similar approach is exploited where additional contributors will be considered such as thermally-induced and data fusion. Additional extrinsic factors will also be evaluated if deemed to have a significant contribution to the measurement uncertainty.

3.4.1.1 Uncertainty Contribution from the Measurement Process

To estimate the uncertainty contribution from the measurement process, a sample standard deviation. This is related to the multiple measurement strategy principle which allows the use of statistical averaging and Type-A evaluation in quantifying the standard uncertainty which can be estimated by Eq. 33, where n is the number of measurements. This is assuming that the randomization associated with the multiple measurement strategy will have a normal distribution trend. Statistically, a sample size of $n \geq 30$ is suggested to adequately use a normal distribution according to the Central Limit Theorem for modelling the standard uncertainty, but that depends on the accuracy requirements [77]. The ISO 15530 series suggests a minimum of 10 measurement cycles and a total sample size of 20 to obtain a sufficient standard uncertainty.

$$u_P = \sqrt{\frac{1}{(n-1)} \sum_{i=0}^{n} (y_i - \bar{y})^2} \tag{33}$$

Influence quantities covered by u_P are the geometry errors of the CMM, systematic and random probing error, repeatability of the CMM, scale resolution of the CMM and sampling strategy errors. Some of the environmental conditions are said to also be covered but this is likely to be underestimated if the measurements are made in poorly-controlled measurement environment.

3.4.1.2 Uncertainty Contribution from the Work-piece

Errors from the manufacturing process of the work-piece can attribute to the overall uncertainty. Such errors are from the CTE, form errors, elasticity, roughness and other physical characteristics that may be the result of manufacturing errors, wear, etc. If a calibrated work-piece is utilized, some of the contributions can be reduced to negligible values. If the work-piece errors cannot be neglected, then how they influence the measurement uncertainty must be determined. For work-piece in industrial environments, the conditions of the work-piece vary and therefore closer evaluations of some of the physical characteristics may be necessary. Form error, elasticity and roughness will be investigated further. The variation of the work-piece CTE may have an effect such as the difference among work-pieces and the calibrated work-piece however this is typically covered in the estimation of the thermally-induced errors (Eq. 18).

The contribution from form errors are only considered if they are substantial. If so, expert judgement is a viable option. Since form error is not considered the measurand of interest, unlike what was described in an earlier subsection, but does contribute to the uncertainty, the mathematical definition of the specific from error (e.g. flatness, roundness, etc.) can be propagated via the GUM principles. This is very cumbersome so most often than not a probability distribution is assumed. Given the mathematical-nature of estimating form error as the difference between the maximum and minimum variations from a substitute-geometry feature, all other values are contained within these limits. Therefore, it is logical to assume a uniform distribution with the best-estimate being the midpoint, that is $\delta_{form} = (\varepsilon_{max-}\varepsilon_{min})/2$. This is modelled using Eq. 34,

$$u_{form} = \frac{\delta_{form}}{\sqrt{3}} = \frac{\varepsilon_{max-}\varepsilon_{min}}{\sqrt{12}} \tag{34}$$

If the work-piece is rigid (i.e. stiff) then the elasticity contribution can be considered negligible. Of course, this depends on such physical properties as the weight and size of the work-piece itself as well as how the work-piece is supported. To estimate the uncertainty from the elasticity, experimental assessment can be utilized by applying potential loads from probing, gravity or any force that may cause a deflection or a sensitivity analysis approach.

Due to the physical nature of some of the work-pieces being used, the roughness may influence the measurement uncertainty in the form of the “probe tip” interaction with the surface roughness. The surface roughness is determined by the parameter *Ra,* where over a finite sampling length of the work-piece surface, *Ra* is given as the arithmetic average of the absolute values of the height deviations or Eq. 35

$$Ra = \frac{1}{N}\sum_{i=1}^{N}|z_i| \tag{35}$$

where the standard uncertainty is simply the sum of the individual uncertainties divided by the number of samples [78], or average uncertainty (Eq. 36),

$$u_{Ra} = \sqrt{\frac{1}{N}\sum_{i=1}^{N} u^2(z_i)} \qquad (36).$$

To model the uncertainty of the work-piece for the influence quantities mentioned, the LPU can be performed or Eq. 37,

$$u_{WP} = \sqrt{u_{form}^2 + u_E^2 + u_{Ra}^2} \qquad (37)$$

where it is assumed that the sources are independent of one another.

3.4.1.3 Uncertainty Contribution from the Bias

Every measurement process that uses a reference work-piece has a systematic bias that encompasses unknown systematic errors. The systematic bias is estimated as the difference of the arithmetic mean of the measurements and the conventionally known reference value of the measurand. Specifically, the difference between the industrial measurements and the environmentally-controlled measurements. For the standard uncertainty of the bias, a systematic uniform distribution is assumed as identifying each of the influences that contribute to the bias is an impossible task. To estimate the contribution, Eq. 38 below is used,

$$u_B = \frac{s_b}{\sqrt{3}} = \frac{\left|\bar{x} - x_{reference}\right|}{\sqrt{3}} \quad (38).$$

If the bias itself is considered a contribution instead the residual effects then it is recommended that a measurement sample-size of $n > 15$ be performed [79]. This also is the case when the measurement results are uncorrected.

3.4.1.4 Uncertainty Contribution from the Data Fusion

As was previously mentioned, instrument registration is defined as the alignment and transformation of data to a common coordinate system, which is a defining feature of portable CMM technologies. Like all instrument registrations or alignments, transformation errors occur when the measurement instrument is moved to a new location and has been studied before [80]. Influences that contribute to this error are the drift of the CMM, the known and unknown systematic effects of the CMM, the machine precision of the software when mathematically calculating the transformation matrices, the systematic and random probing errors as well as environmental contributions.

When re-establishing the new location of the instrument using a best-fit transformation, the sensitivity of the reference points to the measurand will be greater if the reference points are placed poorly in relation to the measurand. In other words, if the network of reference points "surround" the measurand (e.g. the work-piece is placed inside the "measuring volume"), then the errors in the point stitching will have a smaller effect on the measurement result. If the opposite is true, then the influence on the results will be greater, where it is predicted that the angular and translational errors of the transformation will affect the results, where the angular errors are assumed most-sensitive.

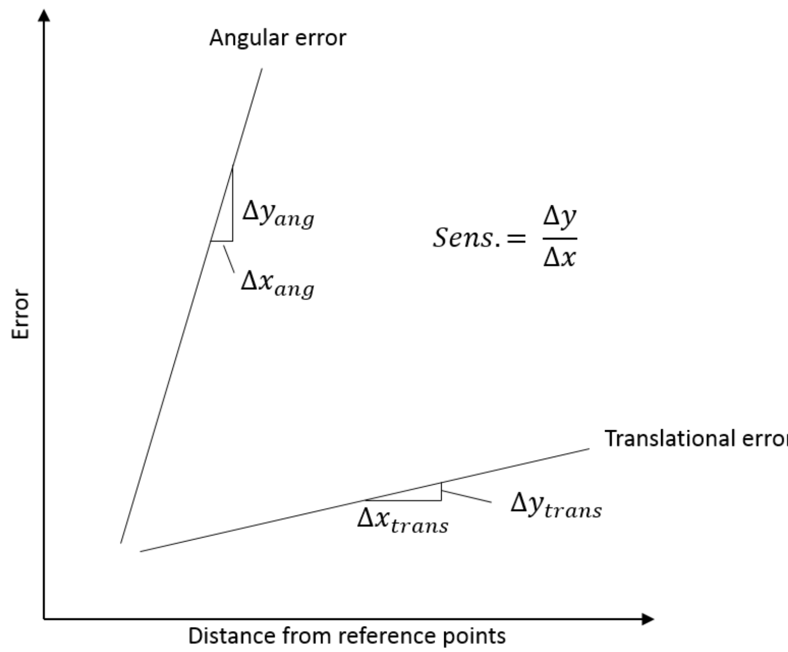

FIGURE 32: Sensitivity of point stitching in relation to the measurand.

Estimating the standard uncertainty from the point stitching is done via the GUM principles where the sensitivity coefficients is calculated as the slope of the lines. For example, FIGURE 32 shows the error of the angular and translational results from the transformation results. The sensitivity of the angular errors is greater than the translational errors, which is directly correlated to the instrument. Therefore, Eq. 39 is the general expression of the uncertainty in the point stitching for a laser tracker,

$$u_{ps} = \sqrt{\left(\frac{\Delta y_{ang}}{\Delta x_{ang}}\right)^2 u^2(x_{ang}) + \left(\frac{\Delta y_{trans}}{\Delta x_{trans}}\right)^2 u^2(x_{trans})} \qquad (39).$$

If the reference points “surround” the measurand, then the uncertainty contribution from the point stitching can be estimated as the standard deviation from the best-fit transformation results of all the reference points (these results can be determined in all, if not most, advanced coordinate metrology software packages via homogenous spatial transformations.)

To determine the drift in the measurements, the reference location points are measured pre- and post-measurement procedure where the drift in the measurements is determined as the maximum error between the measurements of the reference points. The standard uncertainty can be modelled assuming a uniform distribution, which is Eq. 40

$$u_{drift} = \frac{\sigma_{max}}{\sqrt{3}} = \frac{max\left|x_i - x_f\right|}{\sqrt{3}} \quad (40),$$

where x_i is the pre-measurement and x_f is the post-measurement. Therefore, the standard uncertainty contribution for the data fusion is shown below in Eq. 41, which is assuming that they are independent of one another

$$u_{DF} = \sqrt{u_{ps}^2 + u_{drift}^2} \quad (41).$$

3.4.2 Uncertainty Contribution from the Thermal Errors

Thermal errors are the largest single source of non-repeatability and inaccuracy in most CMMs and work-pieces, which poses a challenge to minimize their effect on the uncertainty of measurements [7]. Of the thermal errors, temperature variation is the most complicated to deal with. Compensation of the CMM for temperature has been thoroughly investigated and basic numerical compensations are built-in to most commercial CMMs with sensors distributed throughout the instruments temperature-sensitive components (i.e. scales). These sensors interact with the software packages to provide corrections to measurement data [7], [9]. The real problem arises from thermal issues in the thermal variation of the work-piece, particularly when measurements are made at nonstandard temperatures (i.e. T ≠ 20°C). Therein lies the challenge in identifying how to determine the contributions from the work-piece to the overall thermal error uncertainty. Traditionally, thermally-induced errors are quantified into an uncertainty contribution by accounting for the effects of both the scale of the CMM and work-piece itself. As was eluded to in an earlier section, a detailed explanation will be given on the contribution and how they contribute to the uncertainty.

3.4.2.1 Uncertainty Due to Thermal Expansion

In dimensional metrology, work-pieces change with temperature due to thermal expansion. To overcome this issue and correct for it, industrial lengths have been defined as the size at a temperature of 20 °C since 1931 [81]. Correcting for temperatures outside of 20°C allows one to correct for a known systematic effect. Contributions to uncertainty in measurements for temperatures outside of 20 °C are a function of the dimension being measured, the work-piece CTE, the temperature of the work-piece and their respective uncertainties. The CTE of the material, α, is defined by Eq. 42 and a function of temperature,

$$\alpha(T) = \left(\frac{dL}{L}\right) \cdot \left(\frac{1}{dT}\right) \tag{42}$$

where dL/L is the fractional change in a characteristic linear dimension and dT is the change in temperature. For dimension L_0 at a reference temperature T_0, L can be found at a different temperature T by integration of Eq. 42 which yields Eq. 43, the general case for thermal expansion,

$$L = L_0 \cdot \exp\left[\int_{T_0}^{T} \alpha(T)dT\right] \tag{43}$$

It is common practice to assume that $\alpha(T)$ does note vary significantly over small temperature range. Additionally, for changes in temperature from room temperature to their melting points, Eq. 43 can be approximated by Eq. 44 to within less than 1% [82],

$$L = L_0[1 + \alpha(T - T_0)] \tag{44}$$

Eq. 44 is the standard expression used to correct dimensional measurements taken at temperatures other than the reference temperature. Estimating the uncertainty contribution from thermal expansion is done using the LPU or Eq. 2 from the GUM. The uncertainty from the dimension, $u(L_0)$, is omitted as it is second-order thus making it insignificant, the uncertainty from the reference temperature is $u(T_0) = 0$, therefore the only considered parameters are the CTE and its uncertainty of the material, α and $u(\alpha)$; the average temperature and its uncertainty, T and $u(T)$; and the dimension L_0, where after calculating the partial derivatives and simplification yields Eq. 45 below,

$$u_{TE} = L_0 \cdot \sqrt{(T - T_0)^2 \cdot u^2(\alpha) + \alpha^2 \cdot u^2(T)} \tag{45}$$

It is assumed that no correlation between the variation in temperature and the variation in CTE exists. Eq. 45 is the general case for thermal expansion but in dimensional metrology, determining the uncertainty contribution of the thermal variation for both the scale of the measuring instrument and the work-piece are considered thus evaluated as the nominal expansion.

3.4.2.2 Uncertainty of the Nominal Expansion

For measurement instruments, the thermal expansion manifests itself in the form of the expansion of the work-piece and the expansion of the instrument's scale. The results of these two contribution is usually known as the nominal expansion (NE). It is expressed using Eq. 46 below,

$$NE = L \cdot \left[\alpha_{wp}(T_{wp} - 20°\text{C}) - \alpha_s(T_s - 20°\text{C})\right] \qquad (46).$$

From the NE, both the UNE and DUTM can be estimated to determine the overall thermal variation contribution for the measurement, which was stated earlier by Eq. 18. The UNE is the estimate of the overall uncertainty contribution from the CTE of the scale or the work-piece. Assuming that the CTE's of the work-piece and scale are uncorrelated, the UNE can be estimated by Eq. 47, where *i* is either the scale (s) or work-piece (wp),

$$UNE_i = L \times \sqrt{u^2(\alpha_i) \times (\bar{T}_i - 20)^2} \qquad (47).$$

Common work-piece materials can have large ranges of CTE values (i.e. cast iron can vary between 8.1-19.3 ppm/°C, depending on the alloy) which leads to larger uncertainties whereas scale materials are restricted to thermally-stable materials or materials with small CTE's. Research on the effects of non-standard thermal conditions is nothing new [82], [83]. Measurements of actual CTE values can vary significantly from different chemical contributions, different microstructures with the physical processing, difference in temperature ranges at which the CTE was stated and the homogeneity of the material. Estimating the uncertainty contribution from the CTE can be done by measurements of the work-piece/scale and the uncertainties of these measurements are used, estimating based on distributions found among the results of actual experiments conducted on similar objects, or those found among published data [70].

Frequently, uncertainty estimations are determined by assuming that the CTE values are accurate to within ±10%. It is usually left to expert judgment in determining what percentage is adequate. Gauge block steel is usually accurate between ±10% for a temperature range of 15°C to 30°C [82] and most aluminum alloys are ±20% [7]. Therefore, if the material has a small range of possible CTE values, the uncertainty can be estimated using Eq. 48, assuming a uniform distribution,

$$u(\alpha_i) = \frac{\alpha_i \cdot (\%\, Value)}{\sqrt{3}} \qquad (48).$$

This model can be used for both the scale and work-piece contributions. Contribution to the overall thermal variation uncertainty from the influence of the CTE will yield minimal variation as the typical industrial temperature ranges for dimensional measurements are limited [82].

3.4.2.3 Dimensional Uncertainty due to Temperature Measurements

The DUTM is the contribution from the temperature uncertainty in dimensional measurements affected by both the variation of temperature of the work-piece/scale and the uncertainty of the temperature-measuring device (i.e. sensor(s)). By only considering the temperature effects of Eq. 46 and carrying-out the LPU, the DUTM can be estimated using Eq. 49, where α_{wp} and α_s are the CTEs of the work-piece and scale, respectively; and $u(\alpha_{wp})$ and $u(\alpha_s)$ are the standard uncertainties of the CTEs of the work-piece and scale, respectively

$$DUTM_i = \alpha_i \times L \times \sqrt{u^2(T_i) + u^2(T_{sensor})} \quad (49).$$

The uncertainty contribution from temperature can be determined in different ways such as measuring the temperatures of multiple, similar work-pieces/scales using the same sensors and measurement procedure to identify variations. More commonly, it is determined by assuming that the range of the ambient temperature is cyclic in nature (U-distribution) and the sensor accuracy are the largest contributors in work-piece and scale temperature measurements. Therefore, the temperature uncertainty can be modelled using Eq. 50. This is a good estimate for temperature-controlled labs as it is assumed an adequate soak-out time of the work-piece is reached so the temperature is nearly-uniform,

$$u(T) = \sqrt{\left(\frac{T_{max} - T_{min}}{\sqrt{2}}\right)^2 + u(T_{sensor})^2} \quad (50).$$

In reality, estimating the contribution from the temperature of the work-piece can be a challenge to quantify and usually has the larger influence of the two. Work-piece temperature can be affected by combinations of radiation, convection and conduction within the measurement environment, therefore producing differential heating or cooling [84], [85]. As a result of these heat transfer mechanisms, the work-piece temperature as a whole is not necessarily the same at any one point. Besides uncertainty from the non-uniformity of the temperature distribution over the work-piece, non-equilibrium of the work-piece with the environment is just as significant. For larger work-pieces, it is nearly impossible to model the thermal behavior as interactions from material differences, clamping forces, work-piece geometries, and surface finish can change instantaneously for all but the simplest of geometries. Shop floor environments typically have cyclical, ambient temperature-conditions so the work-piece temperature varies and lags by an amplitude-ratio [86]. Additionally, transient effects may have to be considered as a result of this lag. It is inefficient to place numerous temperature sensors on a work-piece and compensate within the software. Minimizing this effect is critical and can be achieved by allowing the part to thermally-stabilize where the steady-state effects are dominate over the transient. There are ways to minimize the uncertainty of the temperature on the work-piece, one common way is to practice ‘soaking-out’ the work-piece.

Soak-out time is defined as the time required for the work-piece temperature to heat up/cool down to within an acceptably small range of the environmental temperature. Or more commonly, the amount of time needed to reach thermal equilibrium. During this soak-out time, the work-piece is changing size and shape which causes significant errors if the work-piece if measured before thermal equilibrium. By allowing the work-piece to come to thermal equilibrium, temperature effects on the work-piece will be minimized thus minimizing the uncertainty contribution from temperature. If the temperature variation and work-piece temperature never stabilize to within an acceptable range, then it becomes difficult to quantify the temperature uncertainty. This can lead to having to determine the contribution by other means such as FEA or other numerical simulation techniques.

3.4.3 Uncertainty Contribution from Additional Extrinsic Factors

Extrinsic factors may be major contributors to the expanded uncertainties but also can be complicated in assessing. When it comes to determining the standard uncertainty of extrinsic factors, expert judgement is commonly used but extensive testing just as well. Influence sources can be attributed from gravity/sag of the work-piece, non-uniform temperature distributions in the work-piece, operator experience, additional errors that are not covered by measurement process contribution, u_P, additional environmental errors, and mostly those that contribute to the reproducibility.

The contributions that are of the most concern here are the errors of the work-piece, specifically due to the size. For example, some of the artifacts used are sensitive to gravitational effects, however these geometry-dependent errors can be approximately-modelled using well-known methods [87], [88]. Another such example is that of the non-uniformity of the temperature distribution in a work-piece. These two contributions will be investigated in detail with an attempt at quantifying an estimate of the contribution to a specific work-piece with a symmetric axis.

3.4.3.1 Gravitational Sag

Gravitational acceleration can have significant effects on long or large work-pieces that bend under their own weight, thus contributing to the overall uncertainty of measurements if not corrected. In large-scale industrial environments (i.e. the shipping industry, the aviation industry, the energy industry, etc.), this error often is corrected using indicators and hydraulic lifts for the simplest of cases (i.e. simply-supported) However, it is most often uncorrected (or ignored) as there is no straightforward methodology to combat this issue. For common geometries, such as rods and beams, fundamental engineering principles can be utilized to develop predictive models for the testing of gravitational sag effects. Two applications of these principles are the sag (deflection) of a beam centerline and length-shortening error.

Sag from gravitational acceleration is nonlinear in its complete form but is very complex to model analytically so numerical methods are suggested for all but the simplest of geometries [89]. However, gravitational sag can be modelled to a first-order approximation where the weight and stiffness of the work-piece are used, and are mathematically proportional, as Eq. 51 below describes

$$Sag \propto \frac{W}{K} \qquad (51).$$

Mathematically, this implies that if either of the quantities changes, an effect on the other quantity occurs (i.e. as the weight of the work-piece increases, the stiffness decreases, and vice-versa). This is a generalized approximation, so it is possible to approximate the sag if both parameters can be determined either analytically or numerically. For the work in this dissertation, a task-specific experimental approach will be exploited in predicting and measuring the sag of a work-piece as well as estimating the uncertainty. The flexible artifact is an ideal candidate to setup and model as a beam. In determining the gravitational sag, a predictive model of the flexible artifact’s centerline is developed using Euler-Bernoulli beam theory [90], [91]. This is a conservative approach but is reasonable to assume that the centerline mimics an elastic curve.

The predictive models are broken up into multiple parts, one for the uniform loading and one for the concentrated point load anywhere. To start, the simply-supported model with uniform loading consists of two equations: the deflection at any point, that is for the deflection between the support point and the outer end (i.e., distance a in FIGURE 33); and the deflection between the supports. The deflection for the outer end is shown below in Eq. 52

$$y_{SS-end} = -\frac{W_1 u}{24EIL}[6c^2(b+u) - u^2(4a-u) - b^3] \tag{52}$$

and for between the supports Eq. 53

$$y_{SS-between} = -\frac{W_1 x(l-x)}{24EIL}[x(b-x) + b^2 - 6b^2] \tag{53}$$.

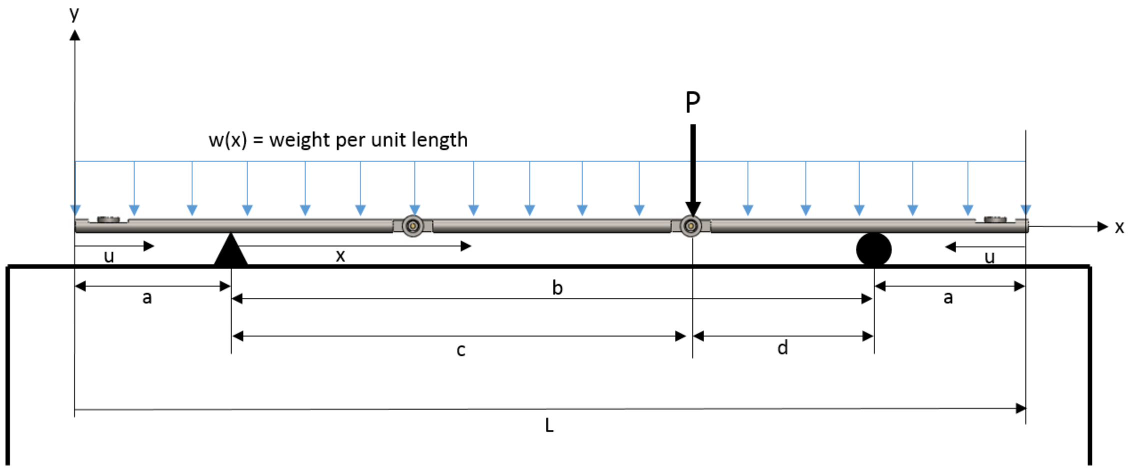

FIGURE 33: Flexible artifact setups: simply-supported.

The model for a concentrated point load at any location has three different segments to model which are as follows: deflection between outer edge and support (i.e. distance *a* in FIGURE 33); deflection for segment of length *c*; and deflection for segment of length *d*. For the overhang or distance *a*, Eq. 54

$$y_{SS-a} = -\frac{W_2 cdu}{6EIb}(b+d) \tag{54}$$,

for the length segment *c* Eq. 55, and for length segment *d* Eq. 56

$$y_{SS-c} = -\frac{W_2 dx}{6EIb}[b^2 - x^2 - d^2] \tag{55}$$

$$y_{SS-d} = -\frac{W_2 d}{6EIb}\left[\frac{b}{d}(x-c)^2 + (b^2 - d^2)x - x^3\right] \tag{56}$$.

For the second setup, FIGURE 34 shows the cantilever setup and superposition of a uniform loading with a concentrated point load. Modelling the deflection is done in a similar fashion to that of the simply-supported. For the uniform loading, the model is shown below in Eq. 57,

$$y_{C-w} = -\frac{W_1 x^2}{24EIL}(x^2 - 4Lx + 6L^2) \tag{57}$$

and for the concentrated load at any point at length segments *a* and *b*, Eq. 58 and Eq. 59 are the models for the two different segments,

$$y_{C-P} = -\frac{W_2 x^2}{6EI}(3a - x), \quad (0 < x < a) \tag{58}$$

$$y_{C-P} = -\frac{W_2 a^2}{6EI}(3x - a), \qquad (a < x < L) \tag{59}.$$

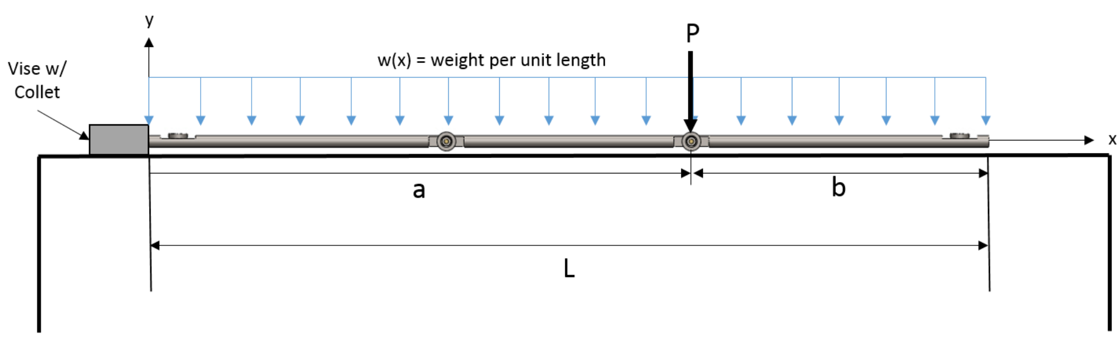

FIGURE 34: Flexible artifact setups: cantilever.

To determine the centerline of the experimental measurements a straightforward reversal [92] technique will be applied after the measurements are collected. The mathematical model for the centerline determination when performing a reversal is shown below in Eq. 60,

$$y_{centerline} = R(x) - M_0(x) \tag{60}$$

where $R(x) = [(M_0(x) - M_{180}(x)]/2$ is the result of the measurement reversal and $M_0(x)$ is the measurement in the 0° position (measurement in the 180° position can be used as well). All systematic errors, such as tilts in the measurement from setting up on an uneven surface, should be corrected for in the experimental measurements.

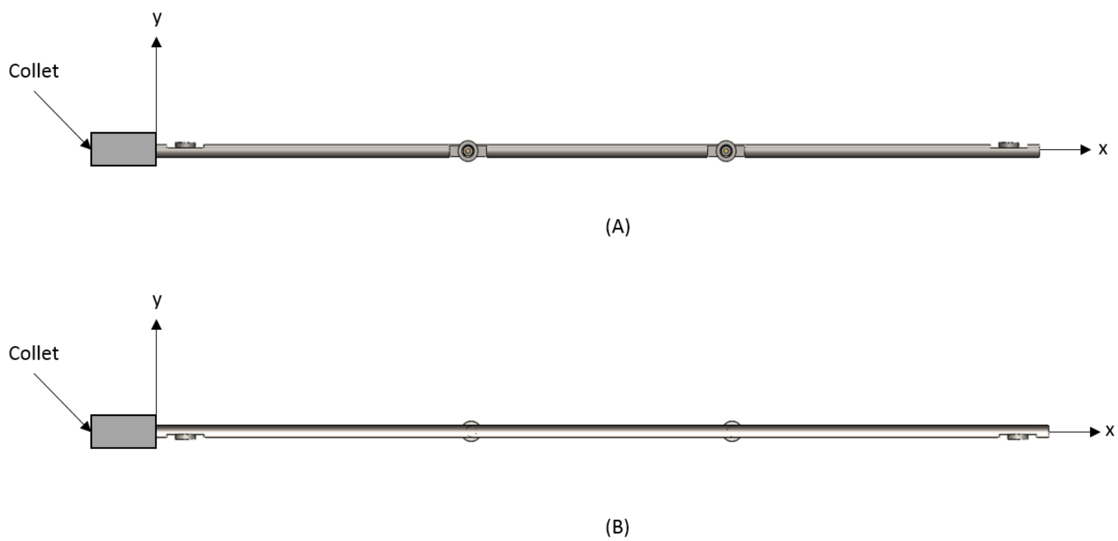

FIGURE 35: Reversal measurement: (A) $M_0\ (x)$; and (B) $M_{180}\ (x)$.

Next, to determine the error in the predictive model, the difference in the experimental measurement and predictive model is calculated, that is using Eq. 61,

$$\epsilon(y_{model}) = y_{measured}(x) - y_{model}(x) \tag{61}$$

where $y_{model}(x)$ is either the model for the simply-supported measurements or cantilever measurements. For clarity, the error in the predictive model is not the uncertainty in the measurements. It is only a metric for determining how well the centerline was modelled. If the model is strong, the estimated centerline errors will be close to zero along the *x*-axis. If the model is weak, then there is likely to be obvious indications in the errors such as the linear trending or another systematic influence.

To determine the uncertainty in the measurement an experimental sensitivity analysis is performed. Since the predictive models are a function of multiple parameters each one can contribute to the sensitivity of the measurements. However, the predictive models are likely to see minute influence from most of the parameters with the exception of the modulus of elasticity. The stiffness of the work-piece is directly related to the work-piece sag, hence the importance of the modulus of elasticity. By varying the value of the modulus of elasticity, the sensitivity in the measurements can be identified in the form of variations in the deflection at specific points along the centerline. Additionally, the error in the measurement process will also be considered in the uncertainty determination.

3.4.3.2 Length Shortening Error due to Gravity

Another gravitational distortion that occurs when the work-piece is orientated horizontally is that of the apparent shortening of the work-piece due to bending (i.e. the difference between its original length and the horizontal projection of the elastic curve.) FIGURE 36 shows an example of this potential length shortening error. Generally, a model of this error is given by Eq. 62,

$$\Delta L = -\frac{1}{2}\int_0^L \left(\frac{dy}{dx}\right)^2 dx \tag{62}$$

where the vertical deflection (upward positive) is equal to $y(x)$. To demonstrate this effect, the flexible artifact is measured in a cantilever setup, FIGURE 33, as it is most sensitive to this error. For the entire derivation of the length shortening error, refer to Appendix A. The final result in Eq. 63 below,

$$\begin{aligned}\Delta L = \frac{-L}{5040E^2I^2}\Big[&L^4(507W_1^2 + 497W_1W_2 + 126W_2^2)\\ &- aL^3(1302W_1W_2 + 630W_2^2) - a^2L^2(945W_1W_2 - 420W_2^2)\\ &+ a^3W_2^2(1260L + 630a)\Big]\end{aligned} \tag{63}.$$

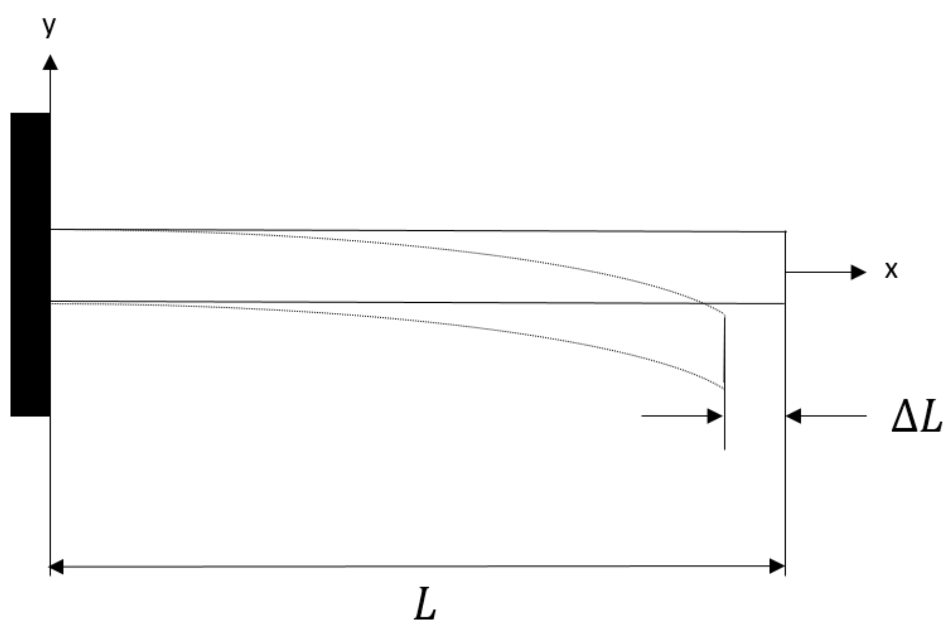

FIGURE 36: Cantilever length shortening error example.

Estimating the uncertainty via the GUM principles is a possibility with the length shortening error model derived but the model is complicated. Additionally, the model has six different influence quantities where the sensitivity coefficient for each also needs to be calculated. A more realistic method in determining the uncertainty is numerically by either an experimental sensitivity analysis or using Monte Carlo techniques. Since a model has been derived, a Monte Carlo simulation is developed to estimate the measurement uncertainty of the experimental results.

3.4.3.3 Non-uniform Work-piece Temperature

Of the heat transfer mechanisms, conduction and convection are the two mechanisms considered when looking at the effects on large work-pieces. For large work-pieces, conduction can be difficult to quantify as the temperature in specific regions of the work-piece may be significantly warmer/cooler from the rest of the work-piece. Therefore, modelling the temperature distribution is an arduous task analytically. As for convection, if the work environment is inadequately controlled (i.e. poorly-controlled shop floor) then the changing temperature contributes to the non-uniformity of the work-piece temperature, which results in additional complexities of modelling the temperature distribution throughout the work-piece. However, one way to test the effects of a non-uniform temperature distribution is a simplified case where the work-piece can be treated as a beam, assuming that the work-piece geometry resembles one.

Modelling the thermal stresses in a beam is done using Euler-Bernoulli theory assuming that the plane section remains plane under lateral deformation and the transverse shear stress is consequently ignored [93]. The general equation for modelling the deflection from thermal stresses is shown below Eq. 64,

$$\frac{d^2y}{dx^2} = -\frac{M_T + M_M}{EI} \tag{64}$$

where M_T is the moment due to the thermal gradient and M_M is the mechanical moment. However, analytically modelling for a geometry other than a beam with a rectangular cross-section is mathematically complex. Furthermore, assuming non-uniformity of a heat source for a specific surface area is more complicated to model without the use of FEA. Therefore, to predict the deflection of the centerline when applying a heat source over a finite surface area, an FEA analysis is conducted followed by the experimental measurements using a setup similar to that shown in FIGURE 37. To estimate the uncertainty in the results, the difference between the measured centerline and the centerline when measured at T = 20°C will be used, or the bias, where a uniform distribution is assumed for each point in the experimental measurements.

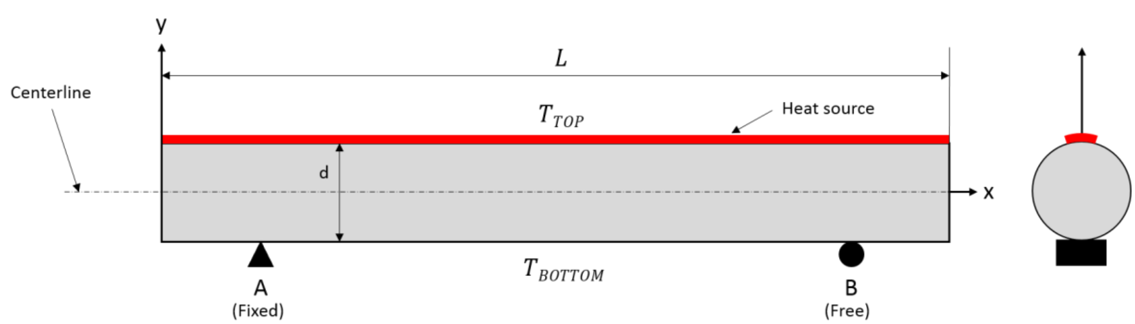

FIGURE 37: Schematic of thermal testing on aluminum cylinder.

3.4.4 Expanded Uncertainty

After all uncertainty contributions have been determined, combining the contributions in quadrature and multiplying by a coverage factor *k* estimates the expanded uncertainty, or Eq. 65. For most engineering applications, a coverage factor of 2 is the de facto choice which suggest a 95% confidence in the estimation of the measurement uncertainty. If a more accurate assessment of the confidence interval is needed, then the degrees of freedom from each contributor can be determined. Once determined, Eq. 3 can be used to estimate the effective degrees of freedom.

$$U = k \times \sqrt{u_P^2 + u_{WP}^2 + u_B^2 + u_{DF}^2 + u_T^2 + u_{EXT}^2} \tag{65}$$

According to the GUM, it is recommended that the full measurement results be stated once the expanded uncertainty calculated. Measurement results should be corrected for all the systematic effects.

$$Y = y \pm U \qquad (66).$$

The parameters in Eq. 66 are the estimated value of the measurand *y*, and the estimated expanded uncertainty of the measurement results, *U*.

3.4.5 Simulated Uncertainty Evaluations

For comparison, simulation of the measurement process are performed to determine the task-specific measurement uncertainty. Monte Carlo techniques are the algorithms of choice. In general, the Monte Carlo technique can be carried out as follows [94]: (i) model the uncertainties of the input quantities with pseudo-random generators; (ii) model the calculation of the output quantities from the input quantities using the measurement equation; and (iii) in a loop, generate a set of pseudo-random input quantities, calculate its output quantity, increment a histogram bin where the loop is repeated for *n* trials (commonly ≥ 10^5). The International Bureau of Weights and Measures (BIPM) developed a supplemental document [95] for the GUM where suggested guidelines are described as to how the technique works as well as how to determine the PDFs for each contributor. Supplement 1 lists four relatively straightforward steps in determining the measurement uncertainty and is detailed in FIGURE 38 below.

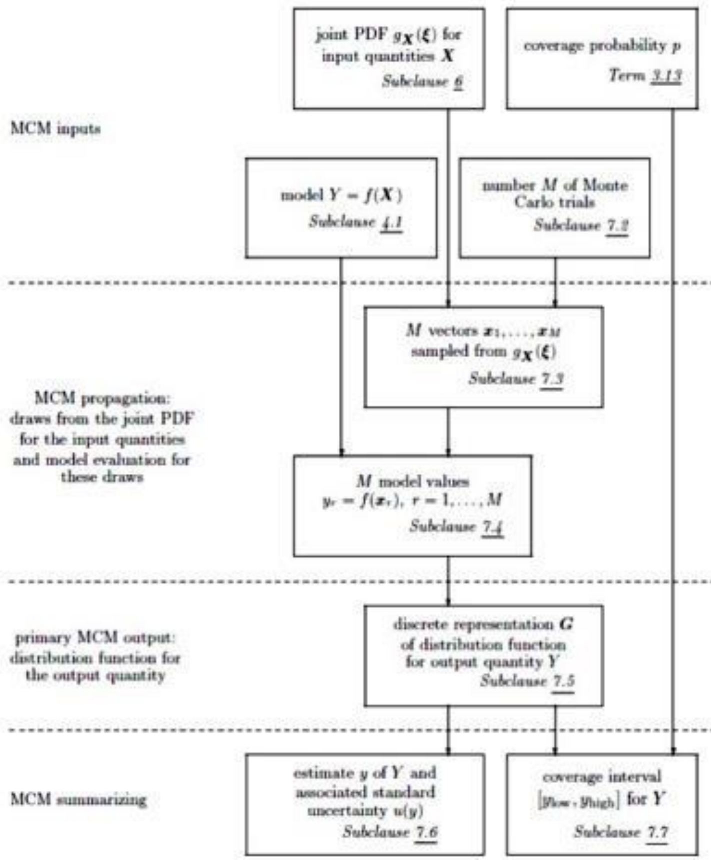

FIGURE 38: Uncertainty evaluation using MCM from Supplement 1, [95].

For the purpose of this dissertation, a straightforward linear measurement error model will be used and assigned PDFs accordingly. Using Eq. 1, the measurement process can be modelled as Eq. 67 below,

$$y = f\left(x_{mp}, x_{wp}, x_b, x_{ps}, x_{thermal,} x_{ext}\right) \tag{67}$$

where the best-estimate of *y* and associated standard uncertainty are then given as the sample statistics.

3.5 Performance Statistic

Interlaboratory comparisons are widely used for a number of purposes such as the establishment of the effectiveness and comparability of test or measurement methods, identification of interlaboratory differences, validation of uncertainty claims and the like. ISO has developed the ISO/IEC 17043 standard *"Conformity assessment – General requirements for proficiency testing"* for this reason [96]. Proficiency testing is defined as *"the evaluation of participant performance against pre-established criteria by means of interlaboratory comparisons"* where the interlaboratory comparison in this dissertation is between an environmentally-controlled laboratory and industrial environment. ISO/IEC 17043 defines and describes suggested criteria for testing. To interpret the proficiency testing results between the two laboratories, calculating a performance statistic is the suggested method.

The purpose of the performance statistic is to measure the deviation from the assigned value in a manner that allows comparison with performance criteria. Numerous performance statistics can be calculated but each should be appropriate for the relevant test and be well understood within a particular field. Since the uncertainty from both laboratories is determined in accordance to the principles of the GUM (ISO/IEC 98-3), two performance statistics are recommended: the ζ-score and E_N-number. The only difference between the two is the ζ-score uses standard uncertainties where the E_N-number uses expanded uncertainties. For our purpose, the E_N -number will be used. E_N can be calculated using Eq. 68 below,

$$E_N = \frac{x_{lab} - x_{ref}}{\sqrt{U_{lab}^2 + U_{ref}^2}} \tag{68}$$

where x_{lab} is the industrial measurand value, x_{ref} is the environmentally-controlled measurand value, U_{lab} is the industrial measurand expanded uncertainty and U_{ref} is the environmentally-controlled measurand expanded uncertainty. The E_N-number is known as a normalization error which will evaluate the metrological compatibility of the two different measurement results. If $|E_N| \leq 1$, then there is satisfactory agreement between the measurement results. If $|E_N| \geq 1$, then there is unsatisfactory agreement between the measurement results and action should be taken to determine cause. Let it be noted that if U_{lab} is grossly-overestimated, then this will yield a small E_N value and thus affecting the validity of the performance statistic.

CHAPTER 4: EXPERIMENTAL TESTING, EVALUATION, AND RESULTS

The following chapter describes in detail the testing and results of the experimental approach from the previous chapter. First the assessment of the best-estimate and expanded uncertainty for of each of the work-pieces calibrated with the Leitz PMM-F for reference measurements. Secondly the assessment of the industrial measurements. Third, a comparison between the PMM-F reference measurements and industrial measurements. Then, a normalization of the results by calculating the performance statistic E_N between the reference measurements and industrial measurements. Finally, the experimental testing and results of the gravitational effects on the work-piece and non-uniformity of the work-piece temperature.

4.1 Reference Measurements and Evaluations

For each of the work-pieces used, all the work-pieces soaked-out in the temperature-controlled environment for more than a few days before they were measured to ensure that each was in thermal-equilibrium with the measurements environment. Then each work-piece was measured once a day over the course of 3-5 days to capture the variations from the measurement environment. Each measurand was evaluated using the Quindos 7 software and a report was generated.

4.1.1 Aluminum Cylinder PMM-F Measurements

The measurands of the aluminum cylinder were the diameter, length and form error (cylindricity) as seen below in FIGURE 39. The work-piece material is 6061 aluminum with an estimated CTE of 24 ppm/°C. For the measurement setup, the aluminum cylinder was place on V-blocks with 5-DOFs constrained, where a translational movement is allowed to accommodate for thermal expansion of the work-piece. The work-piece is rigid but as a precaution, the V-blocks were placed near the Airy points. Measuring the work-piece with supports near the Airy points forces the opposing ends of the aluminum cylinder to be parallel with one another, this is important since the two end-faces where used to determine the length, L. Additionally, with supports at the Airy points, the effect of gravity on the centerline (axis) of the aluminum cylinder is minimized which then minimizes the out-of-straightness error of the work-piece centerline.

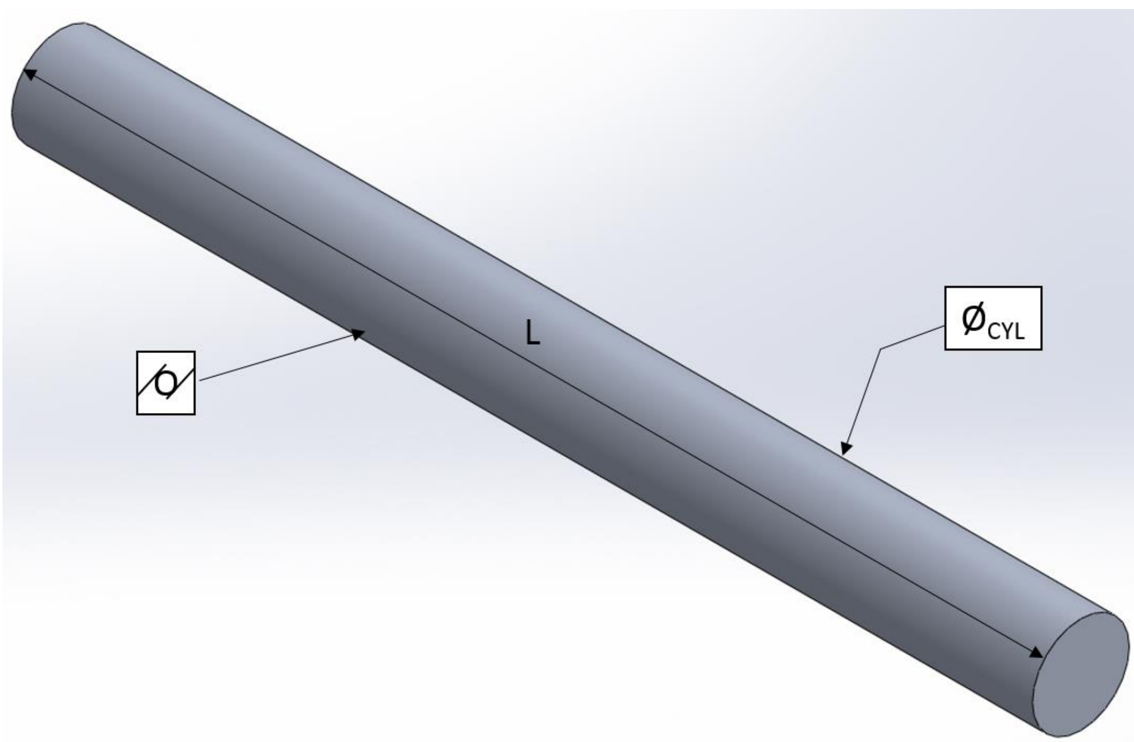

FIGURE 39: Aluminum cylinder measurands.

A sampling strategy of 10 points at 20 different levels was used to determine the cylinder diameter, cylindricity and centerline. Points were probed within an angular range of 5° to 175° at each level since the work-piece was measured in a horizontal orientation. The form error was determine from the diameter measurements as the range of deviations from the substitute-geometry (i.e. the difference between the maximum value of all the deviations and the minimum value of all the deviations.) For the length measurement, each opposing face was probed with 10 points.

To estimate the sampling strategy uncertainty contribution, the mathematical minimum number of points for a specific geometric feature is required in the formula (Eq. 17). For the cylindrical diameter measurement, $x_{cylinder} = 5$ and for the length measurement $x_{line} = 2$. All the estimated results are listed in TABLE 5 for the best-estimate of the reference measurements and the expanded uncertainty at 95% confidence.

TABLE 5: PMM-F aluminum cylinder results (in mm).

Measurand	**Best-Estimate**		**Expanded Uncertainty**
Diameter	120.4950	±	0.0041
Length	1270.2860	±	0.0244
Cylindricity	0.0433	±	0.0029

4.1.2 Exhaust Muffler PMM-F Measurements

The measurands of interest are the muffler exhaust outside diameter (OD), Datum C form error (flatness), the muffler exhaust inside diameter (ID) and the internal cylinder diameter, as seen below in FIGURE 40. The material of the work-piece is a common carbon alloy tool steel which has a CTE of approximately 12 ppm/°C. The muffler was setup in a vertical position on the PMM-F with Datum C facing upwards. This is not the usual measurement setup as the exhaust muffler is typically in a horizontal position which as it is usually measured as part of a larger assembly. With the vertical setup, no additional tooling is necessary for measurement, probing error from horizontal styli configurations is minimized to negligible error or eliminated completely. Additionally, gravitational effects on the work-piece are negligible since the work piece is resting on the granite surface of the PMM-F.

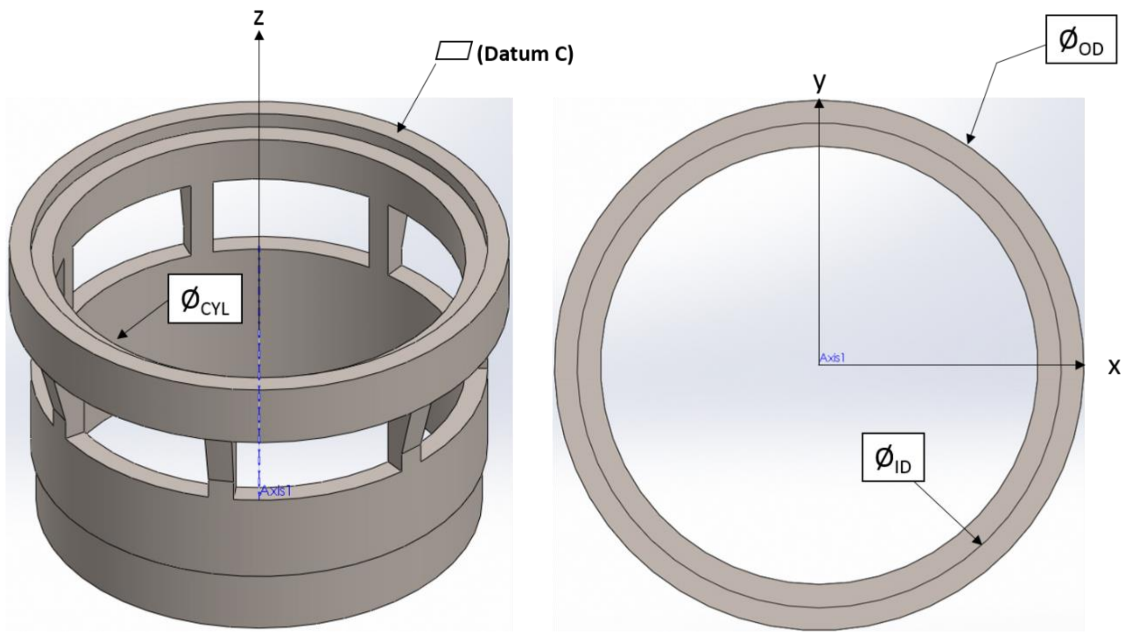

FIGURE 40: Exhaust muffler measurands and coordinate system.

The sampling strategy used for the muffler OD and Datum C flatness measurements were 20 evenly-space points, discretely probed. For the internal cylindrical feature of the muffler, a sampling strategy of 20 discretely probed points, evenly-space, at 3 levels was used in the calibration. Due to the irregularities on the ID of the exhaust muffler, 20 carefully-determined yet randomly-spaced points were discretely probed on the area of the surface that had no effects from steam (e.g. voids or chips). Since the sampling uncertainty is statistically-determined, the randomness of the points will not in effect contribute any more or any less to the overall sampling contribution. Additionally, since the number of sampled size of the points is large, the randomness of the points should affect the results minimally. The mathematical number of points for each feature are $x_{circle} = 3$ for all diameters and $x_{cylinder} = 5$ for the cylinder. Datum C was sampled every 20° (18 evenly-spaced points) in a circular pattern. The form error of Datum C was determined as the range of deviations from the substitute-geometry (least-squares fit) that was fitted to the Datum C. TABLE 6 lists the PMM-F results for the best-estimate of the reference measurements and the expanded uncertainty at 95% confidence.

TABLE 6: PMM-F exhaust muffler results (in mm).

Measurand	**Best-Estimate**		**Expanded Uncertainty**
Outside Diameter	592.1544	±	0.0077
Datum C Flatness	0.0483	±	0.0031
Inside Diameter	542.0995	±	0.0071
Cylinder Diameter	489.6491	±	0.0066

4.1.3 Ball-bar Length Gauge PMM-F Measurements

The measurands are those seen below in FIGURE 41, where d_i is the center-to-center distance for Sphere 1 (s_1) to Sphere i (s_i), and $SØ$ is the spherical diameter of each sphere. The nominal lengths are 100 mm apart and a total length of 800 mm. The ball-bar length gauge is invar, which is a low-CTE material that has a value of approximately 1.2 ppm/°C and the spheres are 302 stainless steel which has an approximate CTE value of 17.2 ppm/°C. The work-piece was setup horizontally with 5-DOFs constrained where only a single translation for expansion allowed (see FIGURE 21), however, due to the low CTE of the artifact (not including the spheres), any expansion would be insignificant.

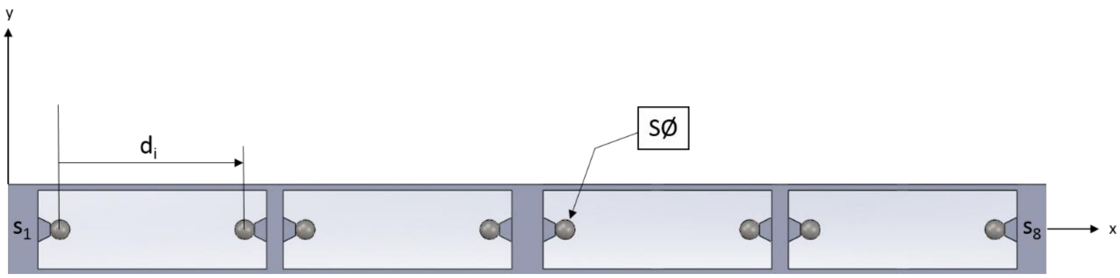

FIGURE 41: Ball-bar length gauge measurands.

For the measurement strategy, each sphere was discretely probed with 5 points total, 4 at the equator and 1 at the pole. After all the spheres were measured, least-squares fits were used to calculated the sphere radius and centers in the CMM's software. From each sphere center, the distance from center-to-center was calculated. The sequence went as follows: d_1 was the distance from Sphere 1 to Sphere 2, d_2 was the distance from Sphere 1 to Sphere 3, and so on until the last distance was calculated, that is d_7 (i.e. distance from Sphere 1 to Sphere 8.) The mathematical minimum number of points for the features were $x_{line} = 2$ and $x_{sphere} = 4$.

TABLE 7: PMM-F ball-ball results, lengths (in mm).

Measurand	Best Estimate		Expanded Uncertainty
Length 1	100.0108	±	0.0038
Length 2	199.9956	±	0.0041
Length 3	300.0088	±	0.0046
Length 4	399.9962	±	0.0050
Length 5	500.0148	±	0.0056
Length 6	600.0338	±	0.0061
Length 7	700.0589	±	0.0067

TABLE 7 and TABLE 8 show the results for the best-estimate of the reference measurements and the expanded uncertainty at 95% confidence. In comparison to the original NIST calibration certificate, which was calibrated using a Moore M48 CMM which has a 1D uncertainty of $U_{95} = 0.4 + 0.4 \times L\ \mu m$, the greatest difference was 1.5 μm for the length measurements and 0.9 μm for the diameter measurements.

TABLE 8: PMM-F ball-bar results, diameters (in mm).

Measurand	**Best Estimate**		**Expanded Uncertainty**
Diameter 1	15.8754	±	0.0039
Diameter 2	15.8757	±	0.0039
Diameter 3	15.8759	±	0.0039
Diameter 4	15.8752	±	0.0039
Diameter 5	15.8755	±	0.0039
Diameter 6	15.8749	±	0.0039
Diameter 7	15.8750	±	0.0039
Diameter 8	15.8749	±	0.0039

4.1.4 Rotor Yoke PMM-F Measurements

The measurands of interest on this particular work-piece are the hole diameters, the true position and the angular locations between each of the holes in the bolt-hole pattern, as shown in FIGURE 42. The work-piece is asymmetric, curved and has many free-form surfaces which makes it challenging to setup a reference coordinate system, with the addition of not having an engineering drawing. However, the center of the work-piece does have some reference features that were utilized. It is important that the coordinate system is known, specifically the datums, since the true position of the holes are measurands. Arbitrarily setting up a different coordinate system each measurement cycle is not ideal, since each hole center position is needed to be known very accurately. For the temperature effects, the CTE is approximately 8.6 ppm/°C, which is low so effects from the temperature will be small.

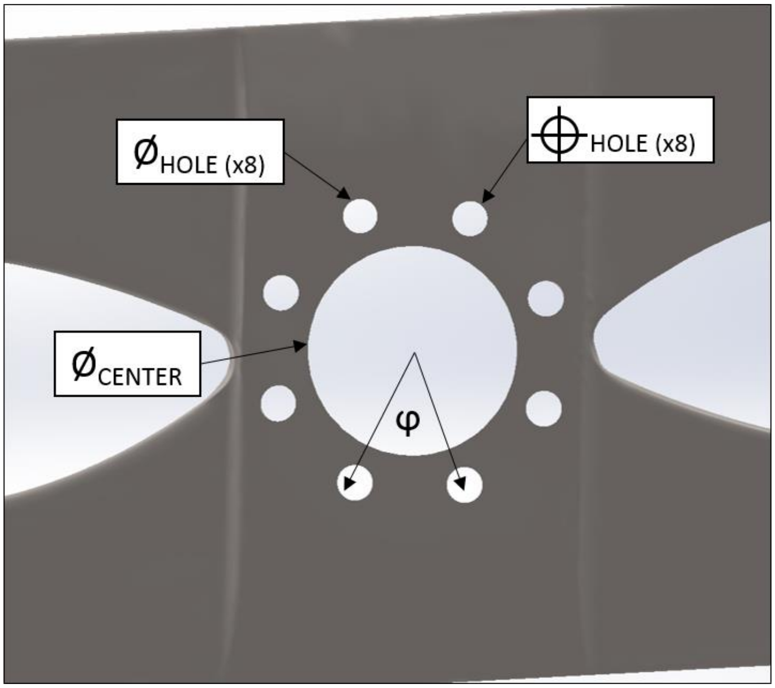

FIGURE 42: Rotor yoke measurands.

The setup and coordinate system used for calibrating the rotor yoke is shown in FIGURE 43. For the work-piece coordinate system, the flat surface where the center-hole and bolt-hole pattern are located was used as a primary planar surface (plane in the figure). Next, the center point of the center-hole will provide an origin location point. For the clocking point, two of the holes, in this case Hole 2 and Hole 3 of the bolt-hole pattern, were measured and the center point of each was determined. Then, a line was calculated between the hole where a midpoint could be determined on the line. This midpoint was then used as the clocking point of the work-piece coordinate system, which is the positive *y*-direction shown in the figure below.

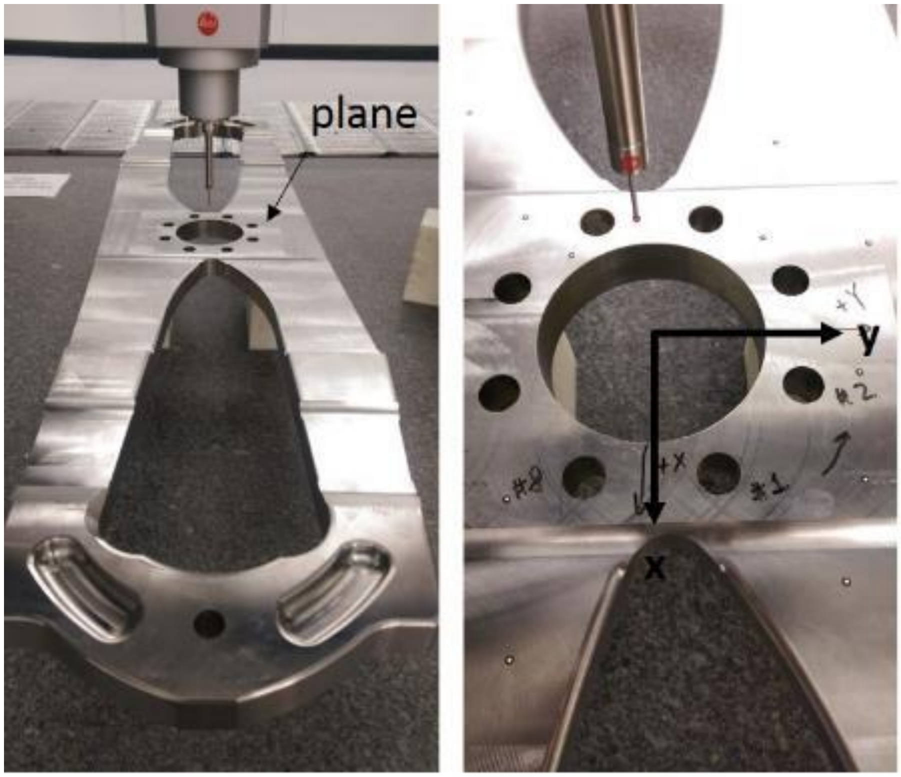

(A) (B)

FIGURE 43: (A) PMM-F measurement setup, (B) coordinate system.

TABLE 9: PMM-F rotor yoke results, diameters (in mm).

Measurand	**Best Estimate**		**Expanded Uncertainty**
Center Hole	111.1581	±	0.0033
Hole 1	19.0988	±	0.0031
Hole 2	19.1622	±	0.0031
Hole 3	19.0735	±	0.0031
Hole 4	19.1550	±	0.0031
Hole 5	19.0590	±	0.0031
Hole 6	19.0646	±	0.0031
Hole 7	19.0701	±	0.0031
Hole 8	19.0728	±	0.0031

The measurement strategy on the center-hole was 20 evenly-spaced points and each hole of the bolt-hole pattern was 10 evenly-spaced points. This was repeated for 3 measurement cycles. Each of the hole parameters were estimated using least-squares fits to determine the radii and centers of each. TABLE 9 lists the PMM-F results for the best-estimate of the reference measurements and the expanded uncertainty at 95% confidence.

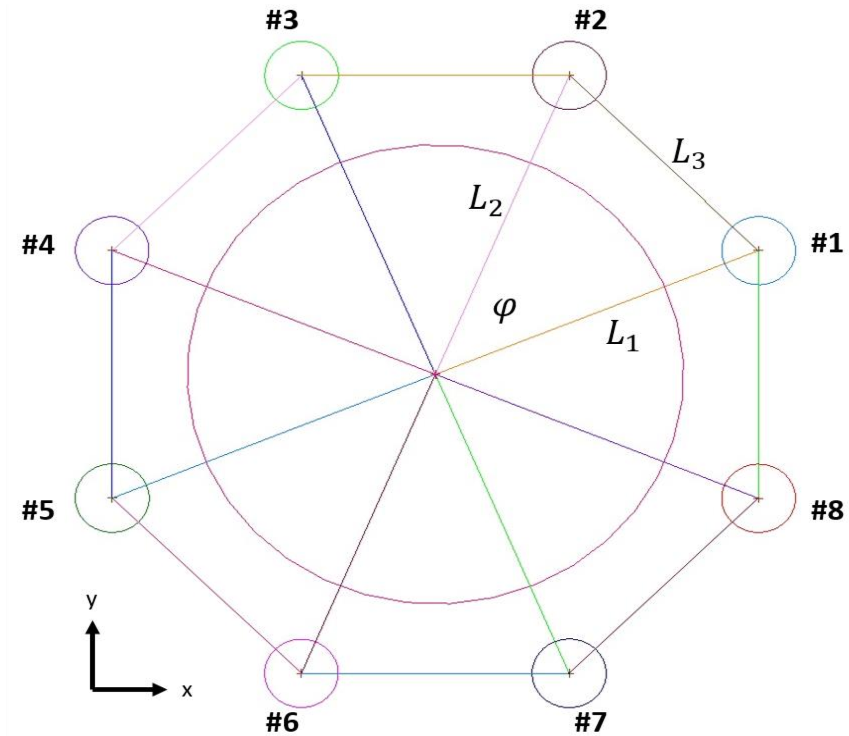

FIGURE 44: Angular location determination.

To determine the angle between each hole, a line from the origin (center point of the center hole) to the center of each individual hole in the bolt-hole patters was determined. Next, a line from each hole center point to a sequential hole center (i.e. the distance from Hole 1 to Hole 2 or L_3 in FIGURE 44) was calculated. L_3 is needed for estimating the uncertainty of the angular measurements per Eq. 24, since the angle between the two lines L_1 and L_2 is sensitive to this length. This same procedure was done for all the holes. The measurement uncertainty at 95% confidence was determined and the results are listed in TABLE 10 below.

TABLE 10: PMM-F rotor yoke results, angles (in degrees).

Measurand	Best Estimate		Expanded Uncertainty
Hole 1-to-2	45.0058	±	0.0002
Hole 2-to-3	44.9895	±	0.0005
Hole 3-to-4	45.0061	±	0.0004
Hole 4-to-5	44.9952	±	0.0002
Hole 5-to-6	44.9961	±	0.0002
Hole 6-to-7	44.9959	±	0.0002
Hole 7-to-8	45.0010	±	0.0002
Hole 8-to-1	45.0104	±	0.0006

Without having a work-piece drawing and not knowing the exact location of each hole center in the bolt-hole pattern, the center locations were then determined as the average of the multiple center measurements. Since each hole has a non-zero mean, the uncertainty is estimated using the Rice distribution statistics, which accounts for the decentering. A MATLAB routine was written for this purpose. The results are list below in TABLE 11.

TABLE 11: PMM-F rotor yoke results, location (in mm).

Measurand	Best Estimate		Expanded Uncertainty
Center Hole	0.0096	±	0.0014
Hole 1	0.0112	±	0.0022
Hole 2	0.0101	±	0.0019
Hole 3	0.0048	±	0.0016
Hole 4	0.0084	±	0.0019
Hole 5	0.0124	±	0.0020
Hole 6	0.0138	±	0.0018
Hole 7	0.0152	±	0.0017
Hole 8	0.0146	±	0.0020

4.1.5 Flexible Artifact PMM-F Measurements

The parameters of interest are the center-to-center distances of four manufactured holes, the overall length of the work-piece, the angles between the machined flats and end-faces. The shape of the centerline (axis) is also considered for gravitational sag evaluations in a later section. To calibrate the hole-to-hole distances, four magnetic 1.5” (38.1 mm)

SMR pin nests, each with a 0.25” (6.35 mm) shank, are fixtured inside each of the manufactured holes. A 1.5” (38.1 mm) stainless steel sphere is then placed onto each pin nest. By measuring the spheres, the centers can be calculated, therefore the center of the hole which is used in determining the distances from each center. FIGURE 23 shows the calibration setup. Each nylon block is estimated to be centered on the Airy points of the artifact to minimize any of the gravitational sag effects. The artifact is made out low-carbon, 1018 steel where the CTE of the material is approximately 12 ppm/°C.

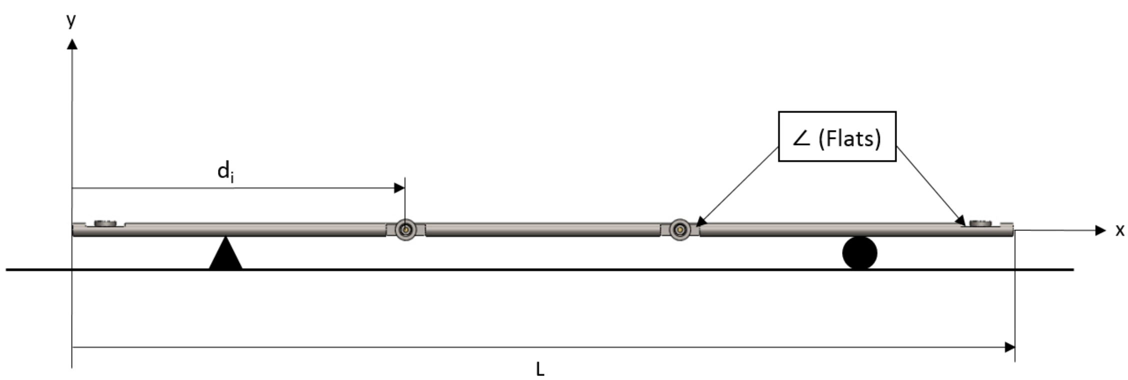

FIGURE 45: Flexible artifact measurands.

The centerline of the flexible artifact was determined by measuring 10 arcs (similar to the aluminum cylinder measurement strategy) with 5 points at each arc to calculate the axis. For the locations of the SMR drift nests, 9 discrete points were probed on the equator (8) and pole (1) of each sphere to determine the center and radius. With the sphere centers, the center-to-center distances were evaluated. TABLE 12 shows the results for the distance measurements and TABLE 13 are the results for the point-to-point lengths.

TABLE 12: PMM-F flexible artifact results, distances (in mm).

Measurand	Best Estimate		Expanded Uncertainty
d_1	53.4659	±	0.0032
d_2	647.6597	±	0.0084
d_3	1179.7233	±	0.0140
d_4	1773.9106	±	0.0205
L	1827.3765	±	0.0210

TABLE 13: PMM-F flexible artifact results, lengths (in mm).

Measurand	Best Estimate		Expanded Uncertainty
Hole 1-to-2	594.1939	±	0.0078
Hole 1-to-3	1126.2575	±	0.0134
Hole 1-to-4	1720.4448	±	0.0199
Hole 2-to-3	532.0636	±	0.0072
Hole 2-to-4	1126.2509	±	0.0134
Hole 3-to-4	594.1873	±	0.0078

Finally, each of the machined flats was probed with 8 points, where a plane was fit to each. Then, the angle between each plane was calculated in the software. Estimating the uncertainty in the measurements analytically is complex so Monte Carlo simulations were performed. Given the analytical definition for an angle between two planes (Eq. 25), errors from the plane fitting parameters were used to determine ranges of possible values for each. An example of the simulated angle is depicted in FIGURE 46. Because the work-piece was measured multiple times over the course of a work-week, variations from extrinsic factors would inherently be manifested in the measurement data. The full results are shown below in TABLE 14.

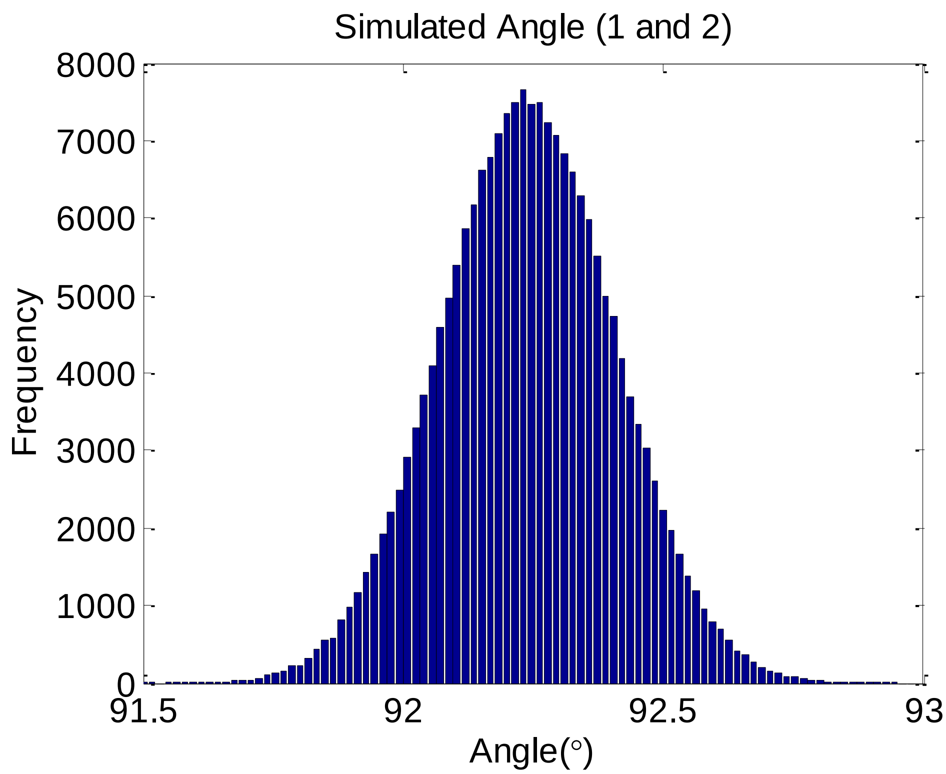

FIGURE 46: Example of simulated angle between planes.

TABLE 14: PMM-F flexible artifact results, angles (in degrees).

Measurand	**Best Estimate**		**Expanded Uncertainty**
Flat 1-to-2	92.24	±	0.34
Flat 1-to-3	90.44	±	0.77
Flat 2-to-4	91.80	±	0.94
Flat 3-to-4	90.01	±	1.16
End-to-End	178.40	±	0.65

4.2 Industrial Measurements and Evaluations

The following section details measurements of the work-piece using the available portable CMMs. Measurements were collected in a variety of locations ranging from a motorsports shop to a large-scale turbine and generator manufacturing plant. The available portable CMMs used were laser trackers belong to UNC-Charlotte's Center for Precision Metrology, an AACMM belonging to the UNC-Charlotte's motorsports department, and a laser tracker and AACMM belonging to a large-scale turbine and generator manufacturing plant. The laser scanner belonging to EPIC was unavailable due to the heavy usage

4.2.1 Aluminum Cylinder Industrial Measurements

Measurement of the aluminum cylinder was carried-out in two locations, the Siemens Large-scale Solutions laboratory with a laser tracker and on the shop floor of a motorsports laboratory with an AACMM. The temperature range in the Large-scale Solutions laboratory was 21°±2°C and is relatively-stable. A network of reference points were setup to create a “measurement volume” around the work-piece for the laser tracker measurements (FIGURE 47) and the part coordinate system was determined in the exact manner as the reference measurements. The sampling strategy for the diameter (and cylindricity) was 5 points at 5 different levels where the work-piece was measured with the laser tracker in different locations. For the length measurements, 10 probing points were collected on each end of the work-piece to create a planes. The distance between these planes is the calculated length of the work-piece. A total of 15 measurement cycles were performed over the course of a week where the work-piece temperatures were collected pre- and post-measurement, for every cycle with a temperature sensor having ±0.5°C accuracy.

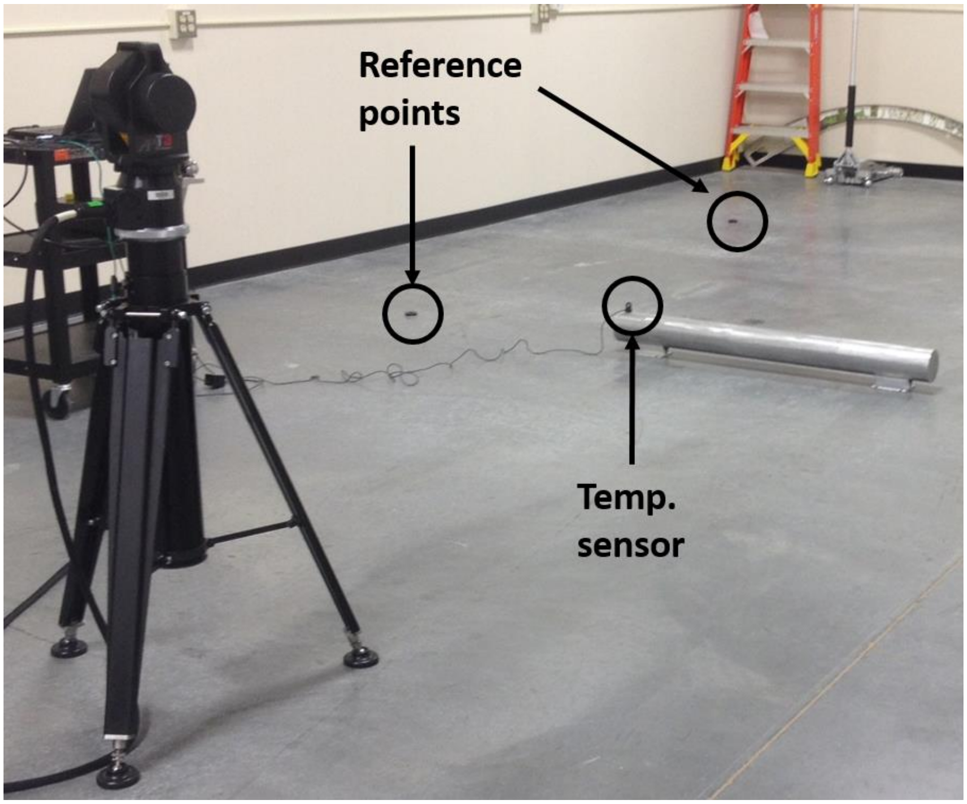

FIGURE 47: Aluminum cylinder measurement using a laser tracker.

For the motorsports shop, the temperature range was estimated at 25°±5°C during the measurement cycles. Since the shop had no temperature control other than industrial ceiling fans, work-piece temperature readings were collected approximately every 2 minutes with a portable temperature that had a stated accuracy of ±1°C. The workbench used to mount the work-piece had location holes throughout, therefore multiple holes were measured to determine center locations as reference points when moving the AACMM to a new location. A similar sampling strategy to that of the laser tracker measurements was used to determine the parameters. A total of 9 measurement cycles were performed over the course of a few days.

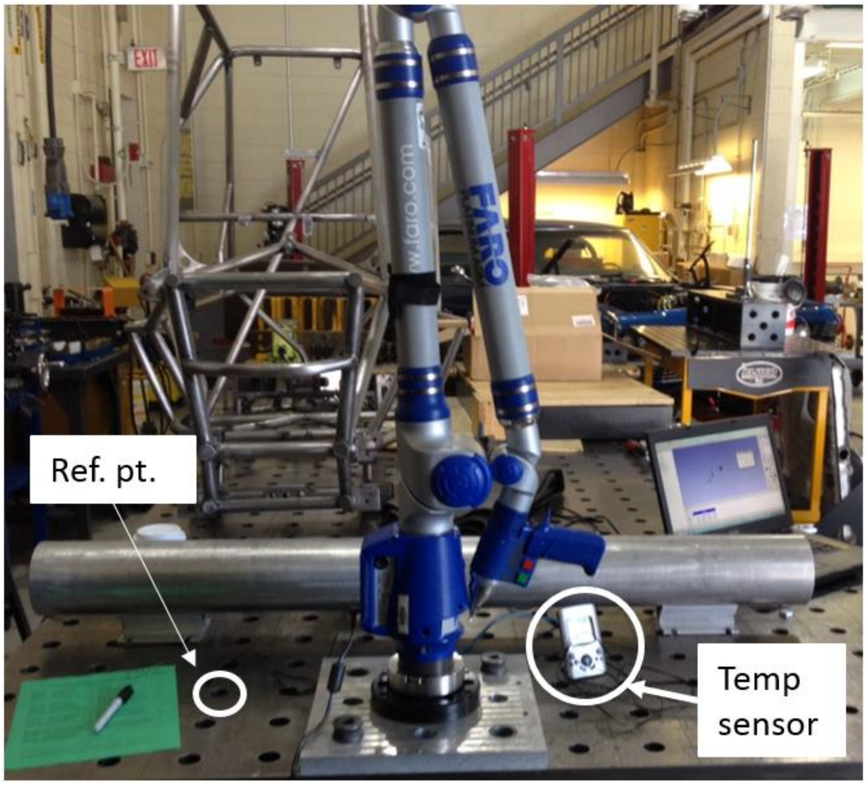

FIGURE 48: Aluminum cylinder measurement using an AACMM.

After completion of all the measurements, the results were calculated and the measurement uncertainties were estimated. Comparisons in the form of bar graphs and error bars representing the expanded uncertainty at 95% confidence are presented for each of the measurands. Additionally, simulation of the measurement results were provided as another comparison and application. As an example, the results for the diameter measurements of the work-piece are shown below in FIGURE 49. The measurement results from the laser tracker were closer to the PMM-F measurements than those of the AACMM. The bias in the laser tracker results was 22.2 μm and 62.2 μm for the AACMM measurements. The laser tracker's expanded uncertainty was ±42.5 μm as where the AACMM's was ±81.4 μm. The simulated results and uncertainty for the laser tracker and AACMM measurement were close to the measured values where small differences were seen. These results seem reasonable, as both biases for the laser tracker and AACMM are near each manufactures claims in accuracy. For the remainder of the results of the cylindricity and length, refer to FIGURE 97 and FIGURE 98 in Appendix B.

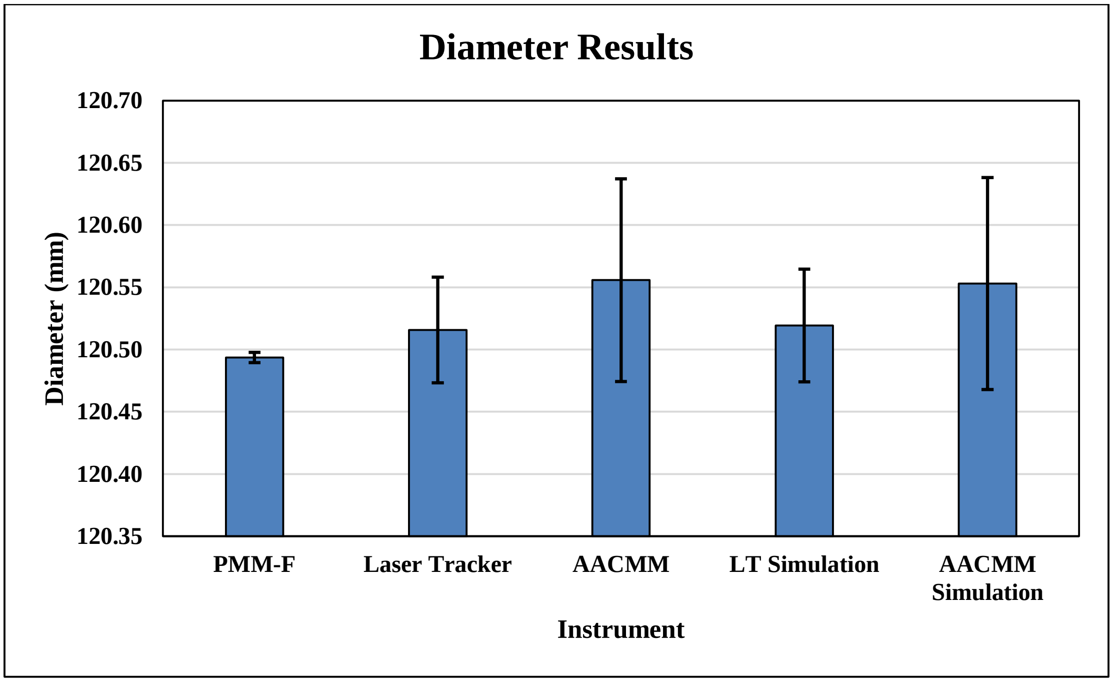

FIGURE 49: Measurement results for the aluminum cylinder diameter.

The normalization comparison between the reference measurements and the industrial measurements are shown in FIGURE 50. All of the measurement comparisons are less than 1, which makes all of the industrial measurements satisfactory or acceptable. The results from the cylindricity were all on the higher end of the threshold criteria but this is the result of the industrial measurement results and uncertainty estimations being significantly larger than the reference measurements, where the biases ranged from 13 – 20 µm.

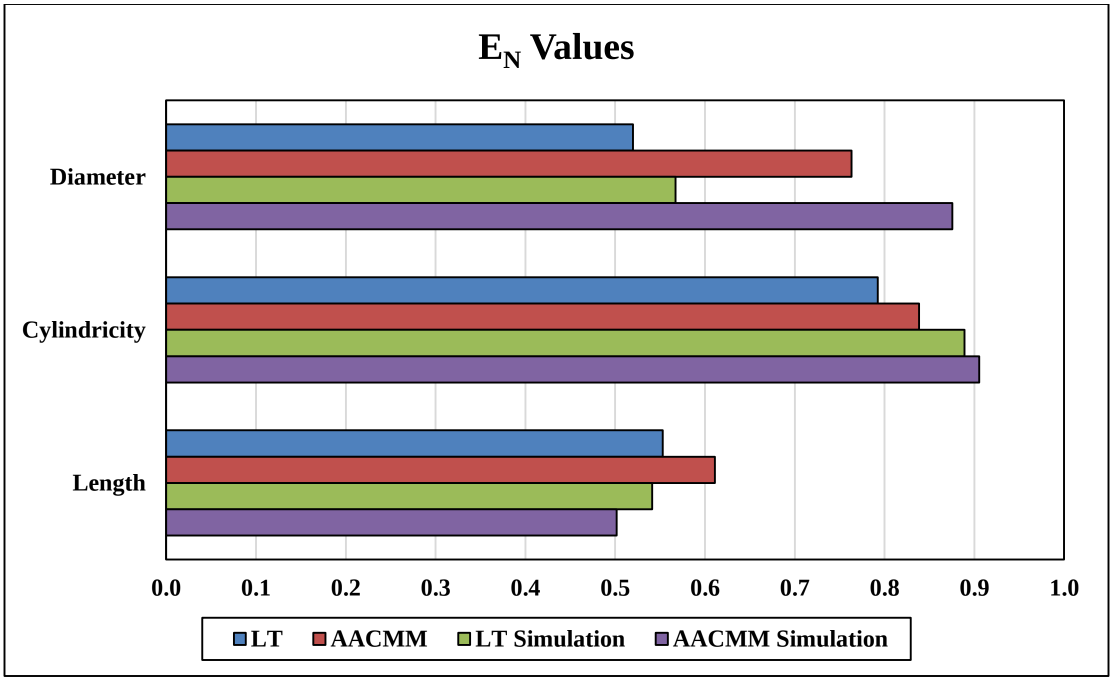

FIGURE 50: Aluminum cylinder E_N values.

4.2.2 Exhaust Muffler Industrial Measurements

To take measurements of the work-piece using a laser tracker, a horizontal orientation was necessary so the internal measurands could be accessed. FIGURE 51 shows the work-piece mounted and fixtured horizontally on an optical table in the line-of-sight of the laser tracker. One obvious issue is the inability to measure a 180° from the clocking point but there is still adequate surface area for sufficient point sampling. The sampling strategies are as follows: 20-30 points on each of the circular features at approximately 2° apart with 3 levels for the internal cylinder measurements and 20-30 points on Datum C. A total of 15 measurement cycles were performed over the course of a day where the work-piece temperatures were collected pre- and post-measurement, for every cycle with a temperature sensor having ±0.5°C accuracy. The laboratory temperature was approximately at 22°±1°C throughout the day.

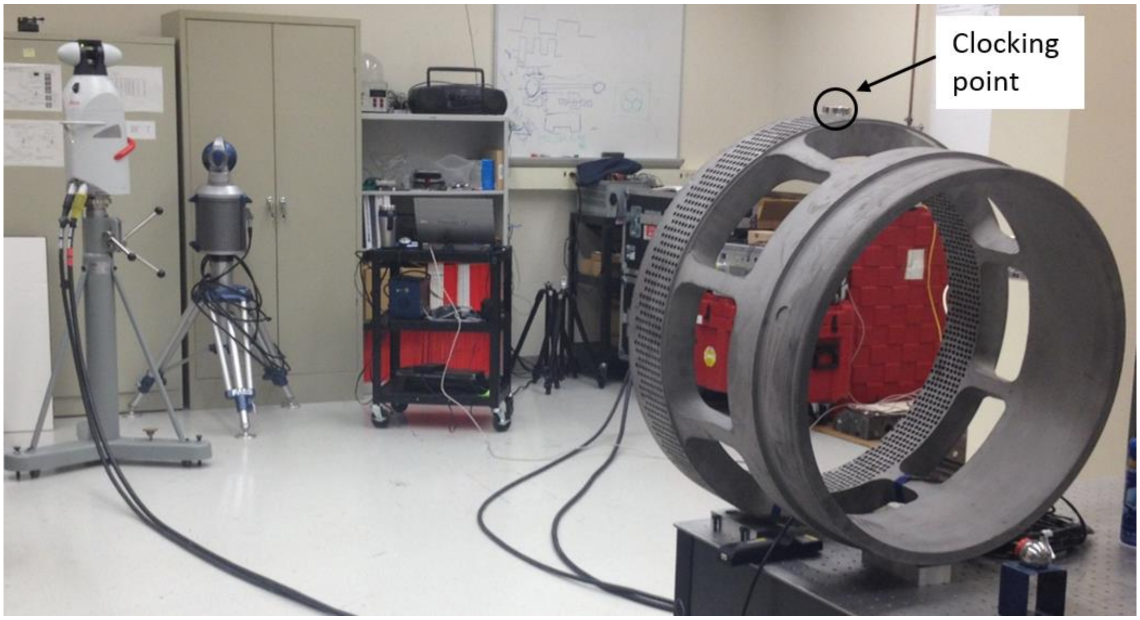

FIGURE 51: Exhaust measurement using a laser tracker.

The AACMM measurements in the motorsports lab were performed in the same manner as the aluminum cylinder measurements, FIGURE 52. The shop temperatures were at 25°±5°C during the measurement cycles so the work-piece temperature readings were collected frequently with a portable temperature that had an accuracy of ±1°C. Again, the workbench used to mount the work-piece had holes throughout, therefore multiple holes were measured to determine center locations as reference points when moving the AACMM to a new location. A similar sampling strategy to that of the laser tracker measurements was used to determine the parameters. A total of 9 measurement cycles were performed over the course of a few days.

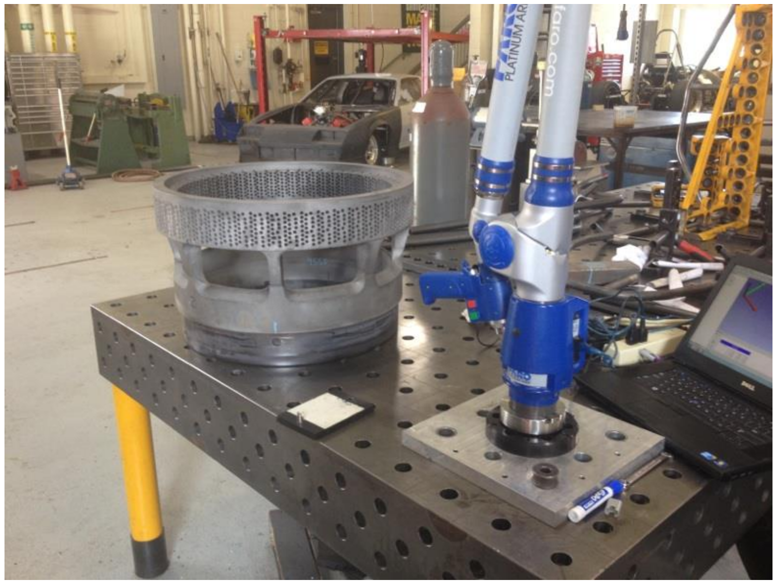

FIGURE 52: Exhaust measurement using an AACMM.

A comparison of the results for the outside diameter are shown in FIGURE 53 below. As expected, the laser tracker measurements were more accurate than the AACMM and has a smaller uncertainty but the AACMM measurements were also acceptable. The laser tracker measurements had a bias of 24.3 µm with an expanded uncertainty of ±40.5 µm, where the AACMM had a bias of 50.2 µm and expanded uncertainty of ±96.7 µm. The large uncertainty in the AACMM measurements was the result of a large error in the re-location of the instrument when moved which occurred from Position 1 to Position 2. From this error, the uncertainty in the measurement process also increased which was expected. Simulation of the industrial measurements showed comparable results to the experimental measurements with differences of less than 1% for each portable instrument. The results of the rest of the measurands are found in Appendix B, FIGURE 99, FIGURE 100, and FIGURE 101.

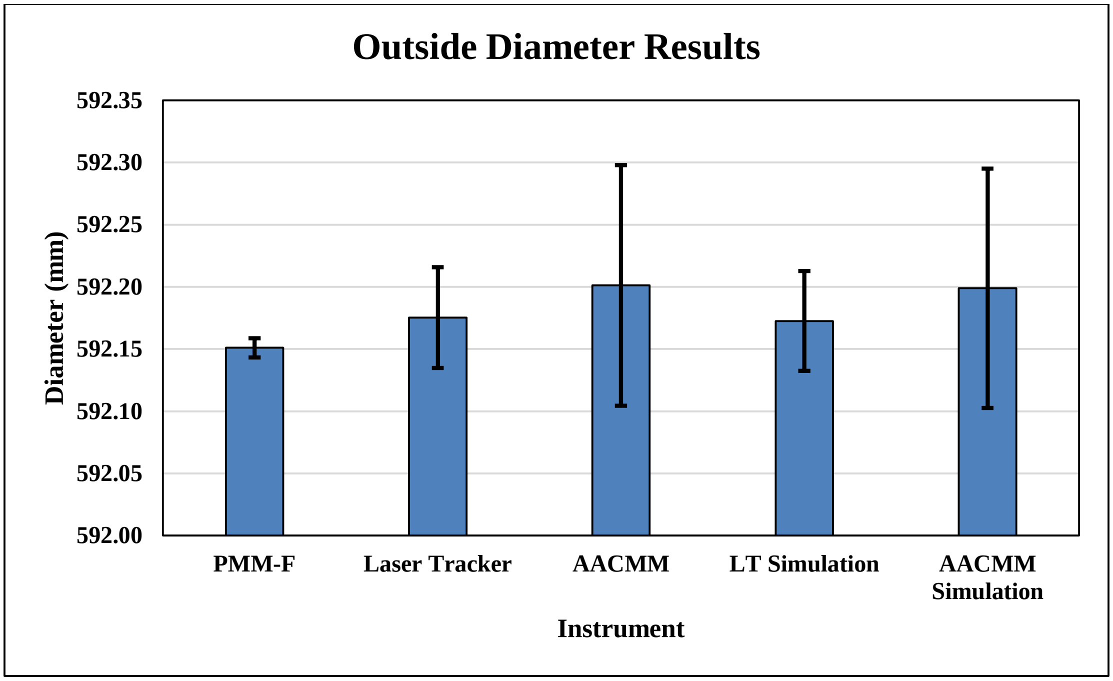

FIGURE 53: Measurement results for the muffler outside diameter.

Looking at the E_N-values, all but the AACMM measurements of the Datum C flatness were deemed satisfactory. The AACMM measurements have values just above the cut-off criteria which could be from possible under-estimation of the measurement uncertainty or poor estimate of the measurand, in fact, the laser tracker measurement results were just under the cut-off criteria of 1, as seen in FIGURE 54. Bias in the measurement results was 12.9 µm for the laser tracker results which is approximately 27% of the reference value. Worse, the bias in the AACMM measurement results was 25 µm which resulted in more than 50% of the reference value. These are likely related to the large errors in the re-location of the instrument, as was explained earlier. Overall, all the other measurands should satisfactory agreement and are acceptable measurement results.

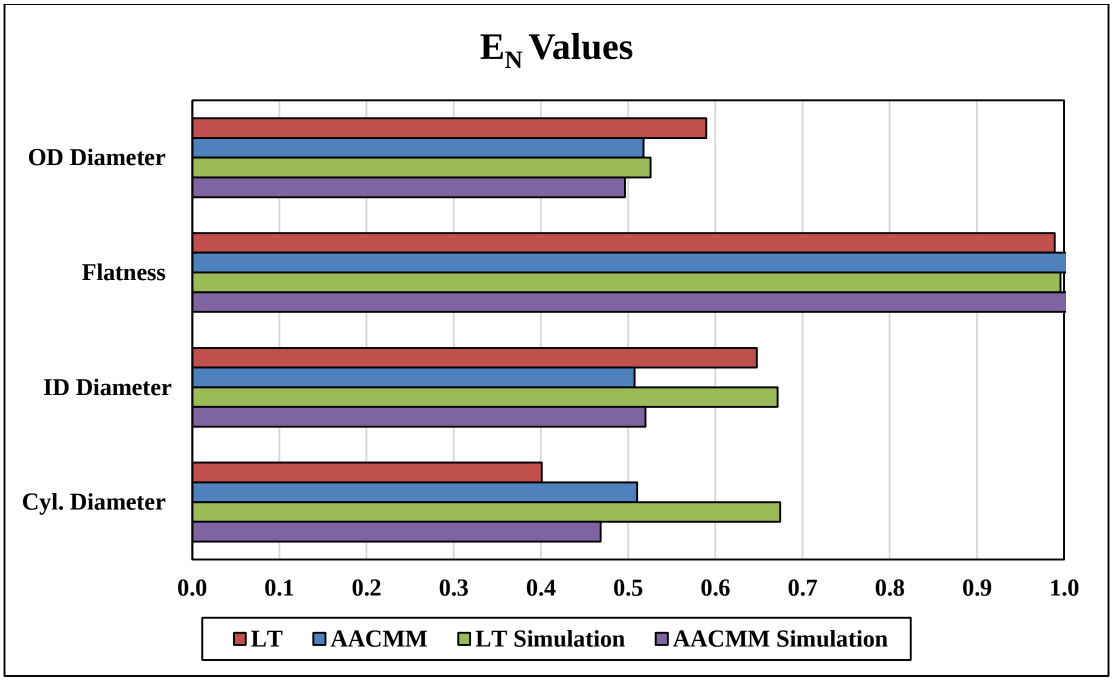

FIGURE 54: Exhaust muffler E_N values.

4.2.3 Ball-bar Length Gauge Industrial Measurements

Measurement of the ball-bar was carried-out in two locations, the Siemens Large-scale Solutions laboratory with a laser tracker and on the shop floor of a motorsports laboratory with an AACMM. Since the work-piece is made out of invar, with the exception of the spheres, temperature variations will have minimal effects on the measurement results but also lends itself to having high dimensional stability. Therefore, errors in the measurements are likely to result from the instrument and operator. The sampling strategy for the lengths (and diameters) were 5 points with 1 pole and 4 equator points. The distance between the centers represented the lengths (see FIGURE 41). A total of 9 measurement cycles were performed over the course of a few days for both the instruments.

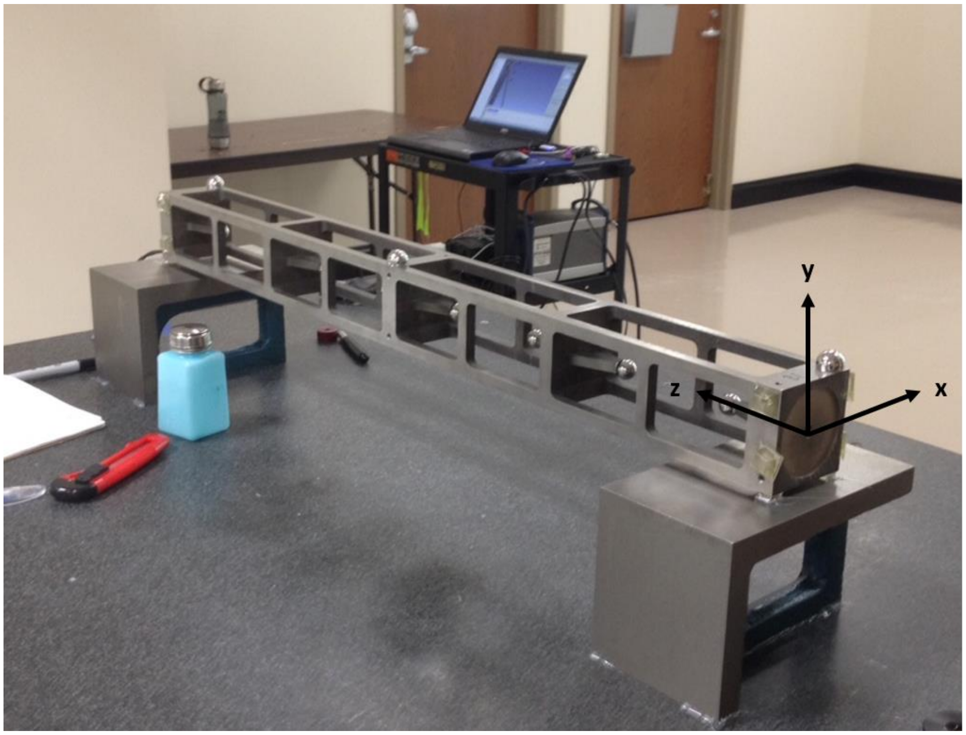

FIGURE 55: Ball-bar measurement setup.

Upon comparison of the reference measurements and the industrial measurements, both the laser tracker and AACMM had comparable results with the PMM-F measurements. For example, the first measurement length (FIGURE 56) had a bias of 20 μm for the laser tracker measurements and a bias of 37 μm for the AACMM. The simulated measurements were very nearly the same as the measured results for both the laser tracker and AACMM, given the fact that the measurements were unaffected by most extrinsic error sources, these can be assumed reasonable results. Estimation of the measurement uncertainty in the laser tracker measurements resulted in an expanded uncertainty of ±28.6 μm at 95% confidence where the AACMM expanded uncertainty resulted in ±55.1 μm. As for the simulated results, small differences of a few micrometers were calculated. The rest of the length results are found in Appendix B, in FIGURE 102, FIGURE 103, and FIGURE 104.

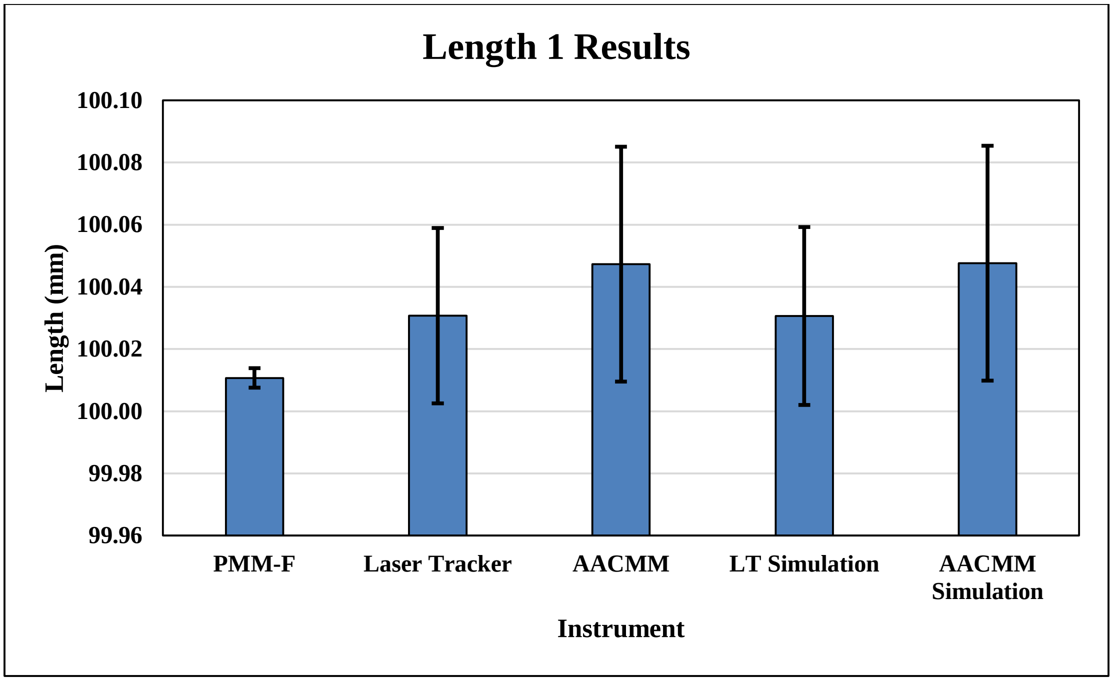

FIGURE 56: Measurement results for the ball-bar, L_1.

When comparing the measurement results, all the E_N values are shown in FIGURE 57. None of the measurement results were greater than the 1, even though some were approaching the threshold. The E_N values for both the industrial instruments were mixed in one being higher than the other. All the laser tracker measurements were closer to the reference values and had smaller uncertainty estimations than those of the AACMM measurement results. The estimated uncertainty values for the AACMM measurements were almost all twice as much as the laser tracker estimates which would cause the E_N values to be *smaller*. Overall, both sets of industrial measurements are acceptable.

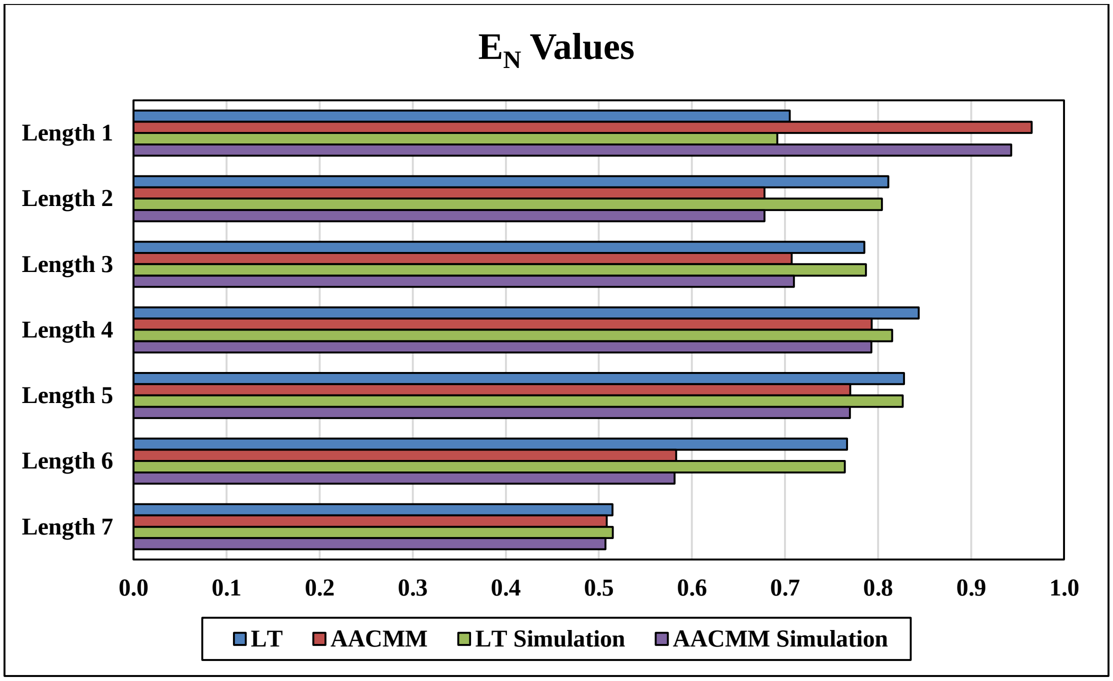

FIGURE 57: Ball-bar muffler E_N values, length.

An example of the sphere diameters is shown below in FIGURE 58. The laser tracker measurement results had a bias of 11.6 µm, and an expanded uncertainty of ±29.8 µm. As for the AACMM measurements, a bias of 35.6 µm was seen and an expanded uncertainty of ±42.3 µm was estimated. These are very good results and due to the high dimensional stability of the work-piece, most of the influence is likely influenced from the instrument and operator. Therefore, the measurement error could have been significantly different with an inexperienced operator performing the measurements. The work-piece is specifically designed for maintaining that dimensional stability by limiting the possibility of damaging the spheres by having a sort of "protective skeleton." If an operator with limited to no experience, possibly even more important, no patience, then it would be highly unlikely to see good repeatability in the measurement results. The remainder of the results for the additional sphere diameters are found in Appendix B, FIGURE 105, FIGURE 106 and FIGURE 107.

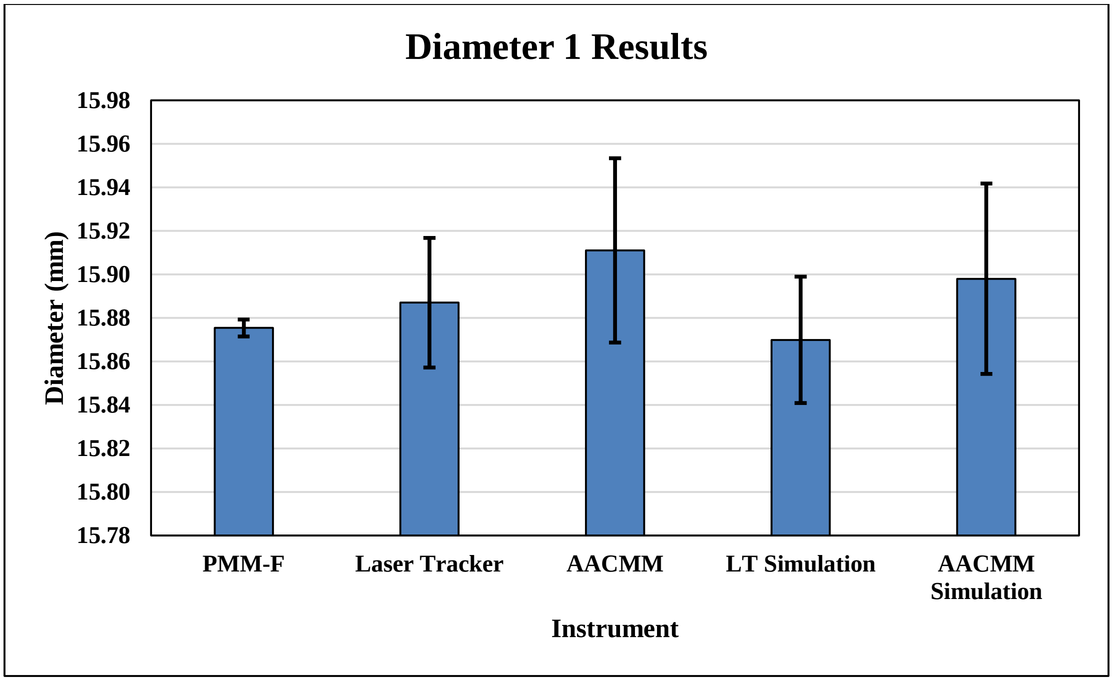

FIGURE 58: Measurement results for the ball-bar, D_1.

In comparing the results of the first sphere diameter, all of the E_N values are under 1 which makes are them acceptable, FIGURE 59. The laser tracker measurement results did not shown any indication of poor comparison as for the AACMM, the E_N values are all on the higher-end of the threshold but none exceed it. This could be the result on the difficulty in measuring each sphere and trying not to have a part of the instrument resting on the work-piece itself. However, the biases in the measurements were all near what is claimed in the manufacture specifications for the instrument accuracy so this may not be a surprising result but more as further proof of the accuracy of AACMMs.

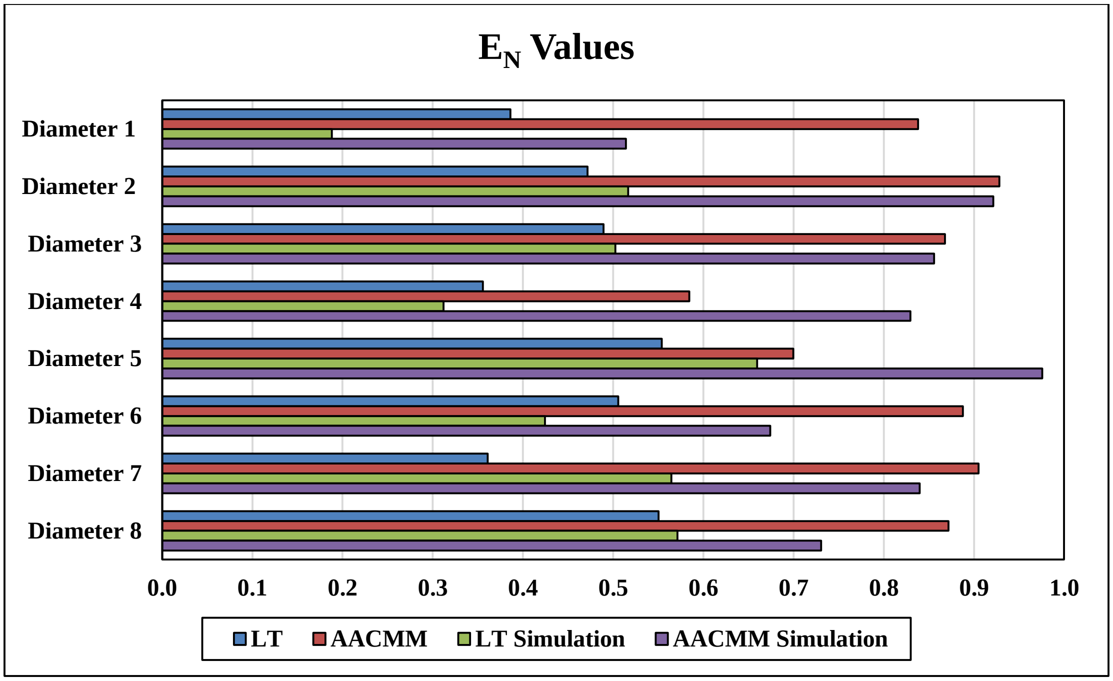

FIGURE 59: Ball-bar muffler E_N values, diameter.

4.2.4 Rotor Yoke Industrial Measurements

Measurements of the helicopter rotor yoke were collected in two locations, the Siemens Large-scale Solutions laboratory with a laser tracker and on the shop floor of a motorsports laboratory with an AACMM. The temperature range in the Large-scale Solutions laboratory was 21°±2°C and is relatively-stable. A network of reference points were setup to create a “measurement volume” around the work-piece for the laser tracker measurements (FIGURE 60) and the part coordinate system was determined in the exact manner as the reference measurements. The sampling strategy for the holes was 36 points per hole, where a spatial scan measurement profile was chosen in Spatial Analyzer. The angles and positions were calculated after each center point was estimated in the software. A total of 9 measurement cycles were performed over the course of a few days where the work-piece temperatures were collected pre- and post-measurement, for every cycle with a temperature sensor having ±0.5°C accuracy.

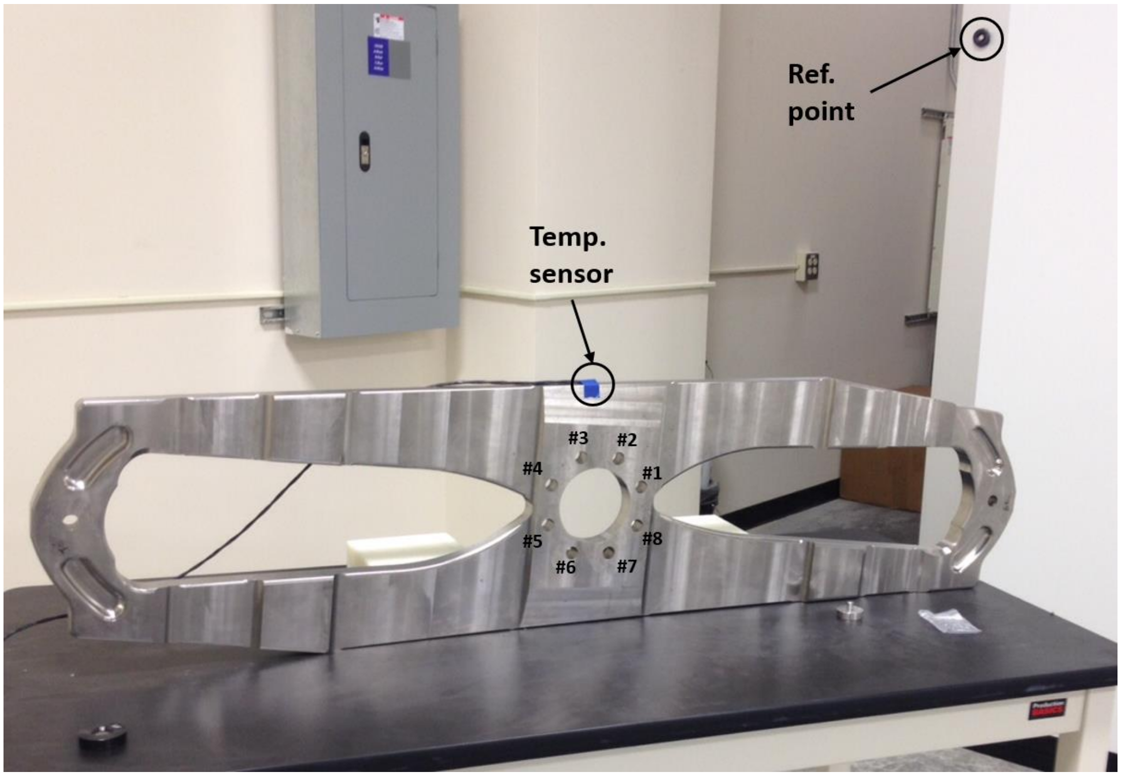

FIGURE 60: Yoke measurement setup for laser tracker and AACMM.

After completion of the measurements, FIGURE 61 below shows the measurement results and expanded measurement uncertainty for the center hole. The measurements from the laser tracker showed a bias of 20.4 μm with an expanded uncertainty of ±32.8 μm. As for the AACMM measurement results, a bias was determined to be 44.5 μm with an expanded uncertainty of ±64 μm. The simulated results had minimal difference but for both the laser tracker and AACMM measurements, the expanded uncertainty for each was estimated to be smaller than those of the actual measurements. The complete set of measurement results and associated expanded uncertainties are located in Appendix B, FIGURE 108, FIGURE 109, FIGURE 110, and FIGURE 111.

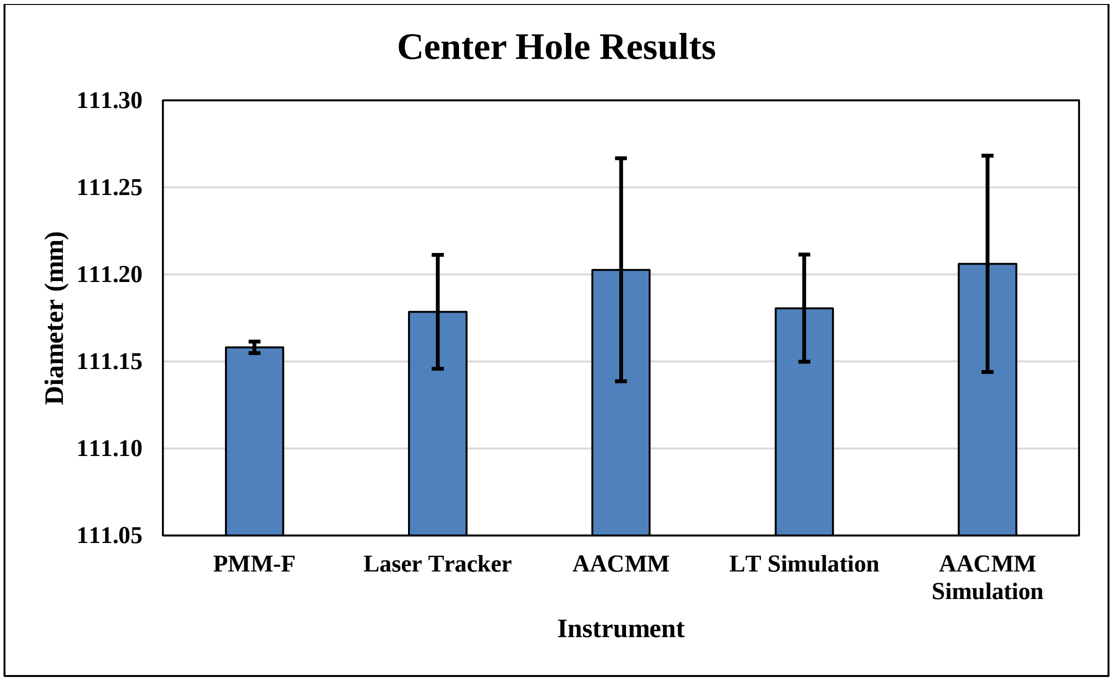

FIGURE 61: Measurement results for yoke center hole diameter, D_C.

After processing the measurement results and associated uncertainties, the E_N values in FIGURE 62 were calculated for the diameters of the center hole and bolt-holes. All of the measurement results from the laser tracker and AACMM met the criteria to be considered satisfactory. A few of the simulated results, namely the AACMM simulated results, were large but nothing to concerning.

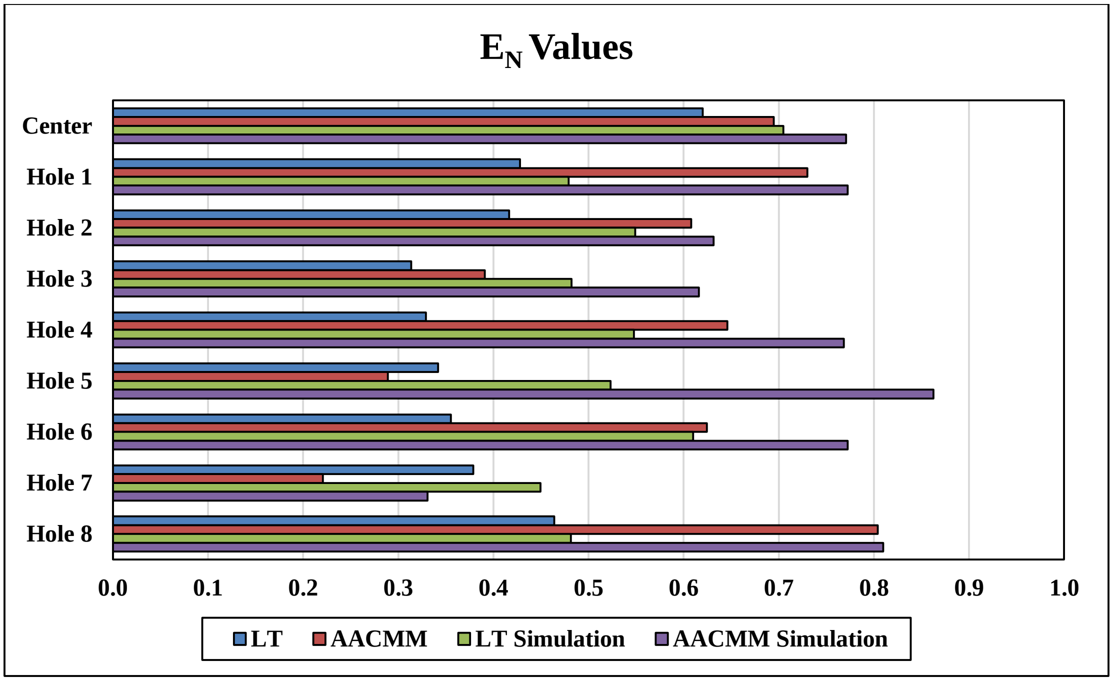

FIGURE 62: Rotor yoke E_N values, diameters.

When comparing the laser tracker results to the PMM-F results, a bias of 0.013° was determined. The expanded uncertainty of the laser tracker measurement results was estimated to be ±0.099° at 95% confidence. For the rest of the angles between the holes, similar biased and uncertainty values were determined and can be found in Appendix B, For the AACMM, the estimated result was smaller than those of the reference measurements with a value of 0.123° with an expanded uncertainty of ±0.136° at 95% confidence. The E_N values showed satisfactory results between the reference measurements and the industrial measurements as shown in FIGURE 64. The largest values were seen in the AACMM comparisons, likely from the large biases in the measurement results.

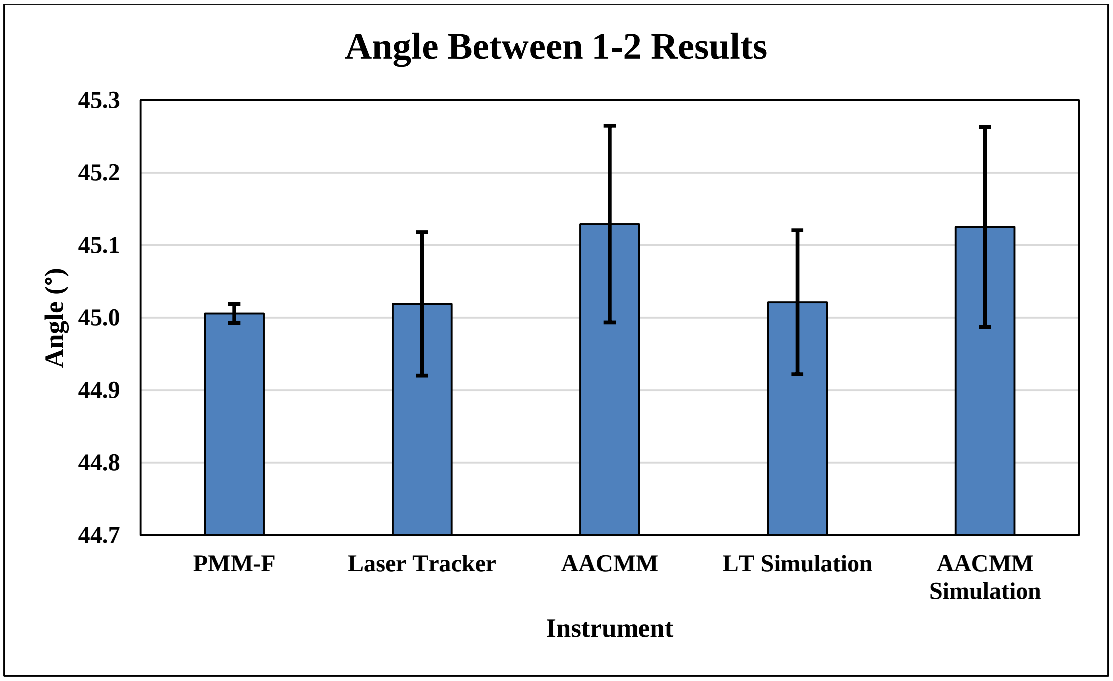

FIGURE 63: Measurement results for yoke angle, $\boldsymbol{\varphi_{12}}$.

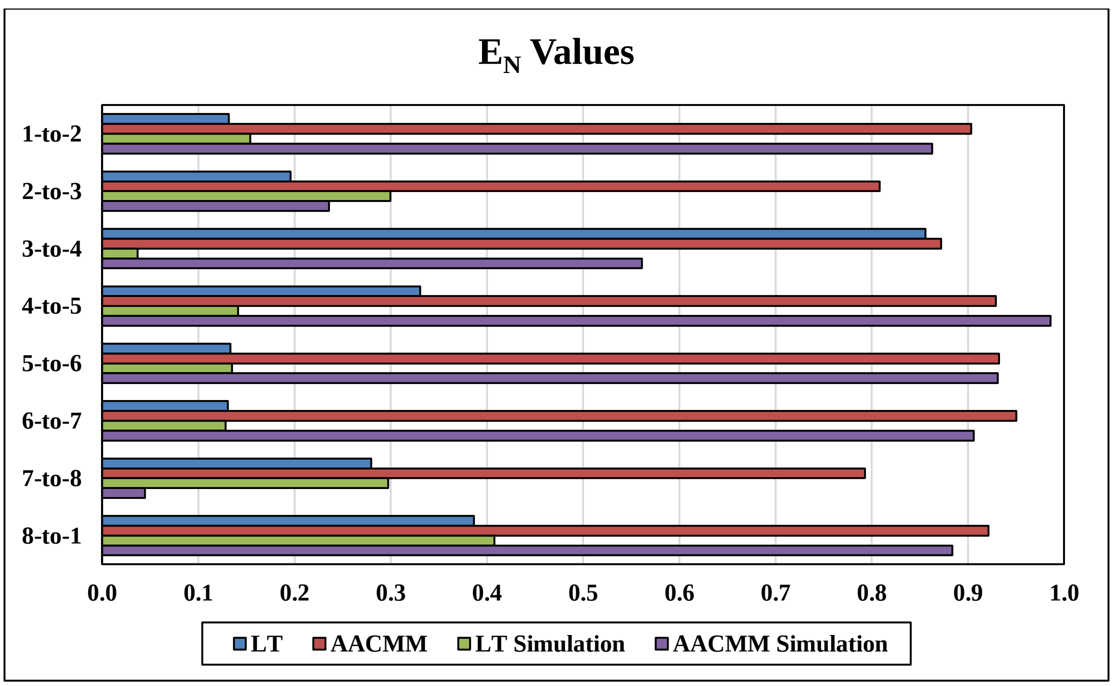

FIGURE 64: Rotor yoke E_N values, angles.

Lastly, a look at the results of the true position for the holes. FIGURE 65 shows the estimated results for the true position of the center hole. The bias in the laser tracker results between the two results is 8.2 µm, which is approximately 85% of the reference value! Similarly, the AACMM results are larger and has a larger bias of 9.4 µm or 98% of the reference value! These type of results are seen in all of the hole measurements. As for the expanded uncertainty, the laser tracker was estimated to be ±8.8 µm and the AACMM ±10.3 µm, which are near or larger than the reference values themselves. These are important pieces of information when looking at the performance comparisons. The rest of the results are in Appendix B, FIGURE 115, FIGURE 116 FIGURE 117, and FIGURE 118.

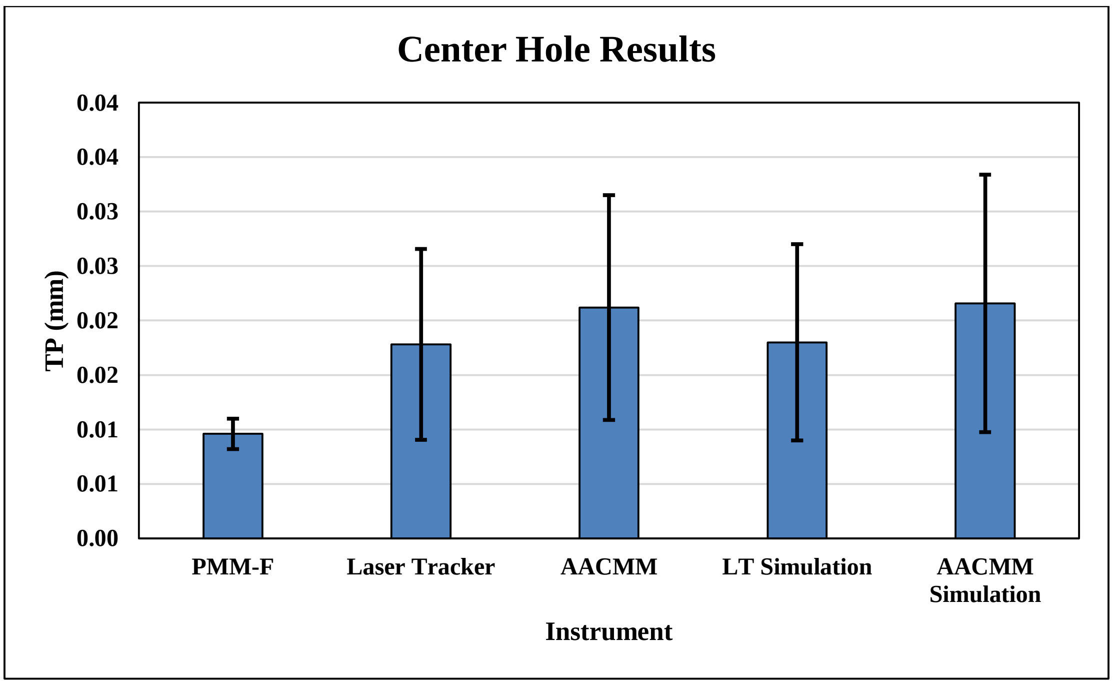

FIGURE 65: Measurement results for yoke true position.

When looking at the performance comparison, a majority of the E_N values are greater than the threshold of 1 for satisfactory measurement comparison. As is shown in FIGURE 66, 5 out of the 9 true position results shown at least one of the industrial measurements results to be unsatisfactory. As was mentioned earlier about the significance of the large bias values and smaller uncertainty, these results are directly related to the large

E_N values. Therefore, a conclusion to draw from this is for measurands that inherently have small values (i.e. true position, form error, etc.), determining the quality of the results by comparing to a reference set of data may result in unsatisfactory performance statistics if one is not able to estimate the measurement results and measurement uncertainty confidently.

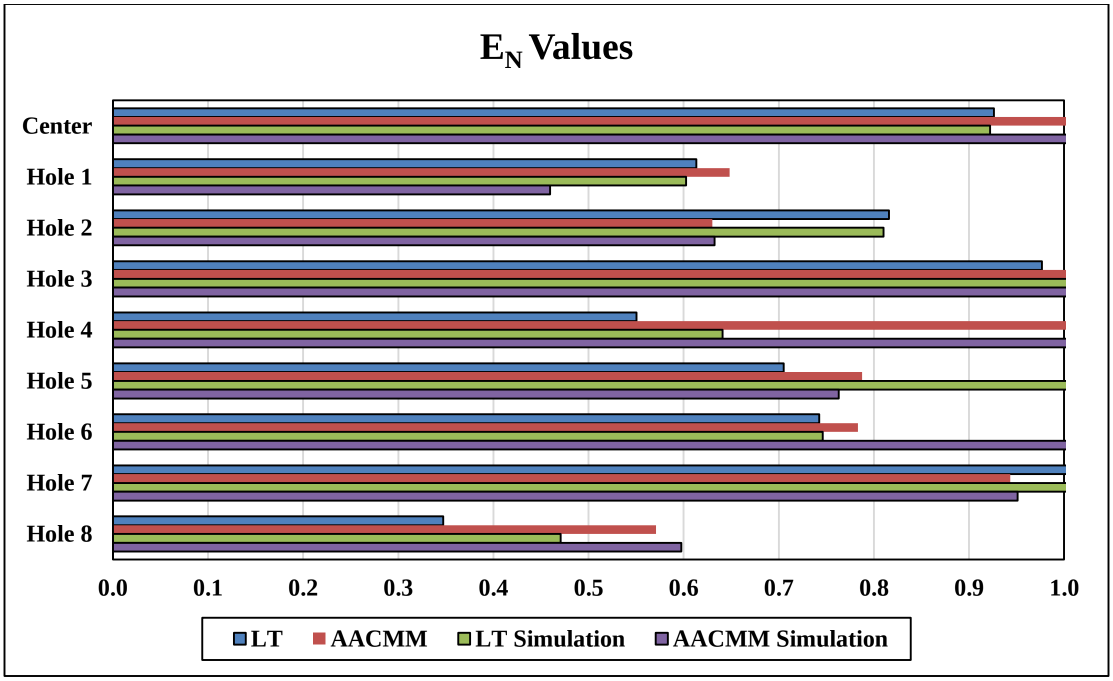

FIGURE 66: Rotor yoke E_N values, true position.

4.2.5 Flexible Artifact Industrial Measurements

Measurements of the flexible artifact were collected in two locations, the Large-scale Metrology laboratory with a laser tracker and on the shop floor of a motorsports laboratory with an AACMM. The temperature range in the Large-scale Metrology laboratory was 22°±2°C and is relatively-stable. A network of reference points were setup to create a "measurement volume" around the work-piece for the laser tracker measurements (FIGURE 71) and the part coordinate system was determined in the exact manner as the reference measurements. The left end-face was probed with 10 points and a plane was fitted to the data. Then, each location of the hole was determined depending on the instrument used. For the laser tracker, a 1.5” SMR was placed in each of the magnetic drift nest where a point was then collected. For the AACMM, a precision sphere was placed in the magnetic drift nest and 5 points were probed to find the center of the sphere. The sampling strategy for the machined flats was 12 points per plane, and the angles between the planes were calculated in Spatial Analyzer.

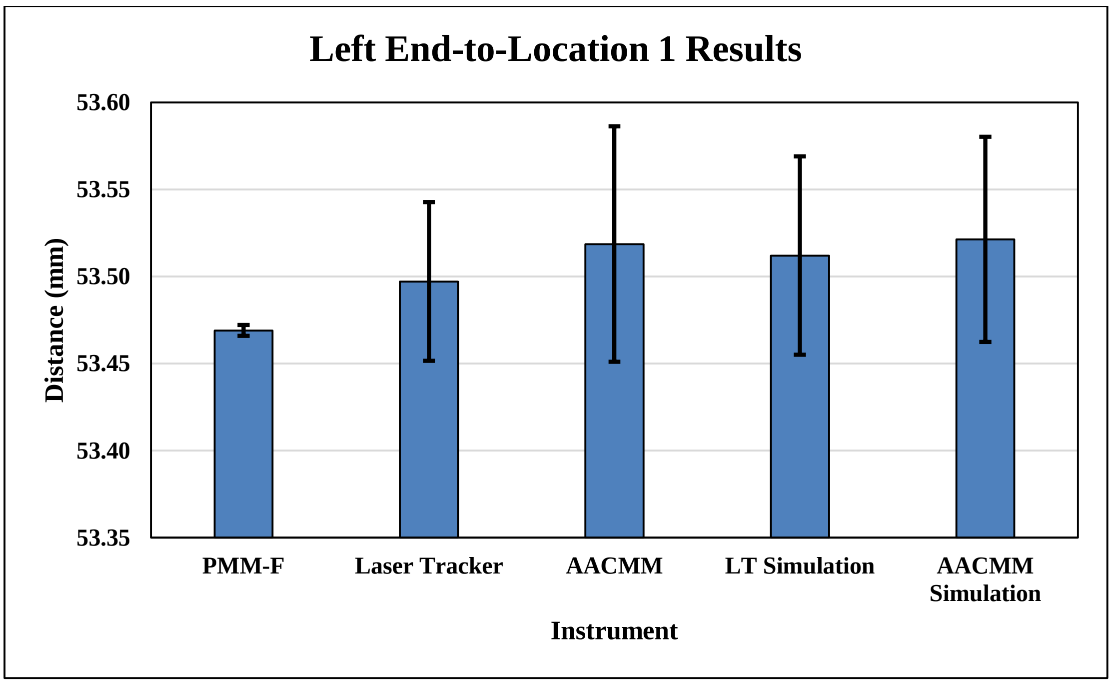

FIGURE 67: Measurement results for flexible artifact distances, L_1.

An example of the measurement results and uncertainty are shown in FIGURE 67, which are the results of the distance from the left end-face to the Location 1 of the work-piece (refer back to FIGURE 45). From the results, the laser tracker measurements showed a bias of 28.1 µm and an expanded uncertainty was estimated to be ±45.6 µm. As for the AACMM measurements, a bias of 49.6 µm was determined and an expanded uncertainty of ±67.6 µm. The E_N values of the measurands for the flexible artifact in FIGURE 68 shows satisfactory values thus making the measurement acceptable.

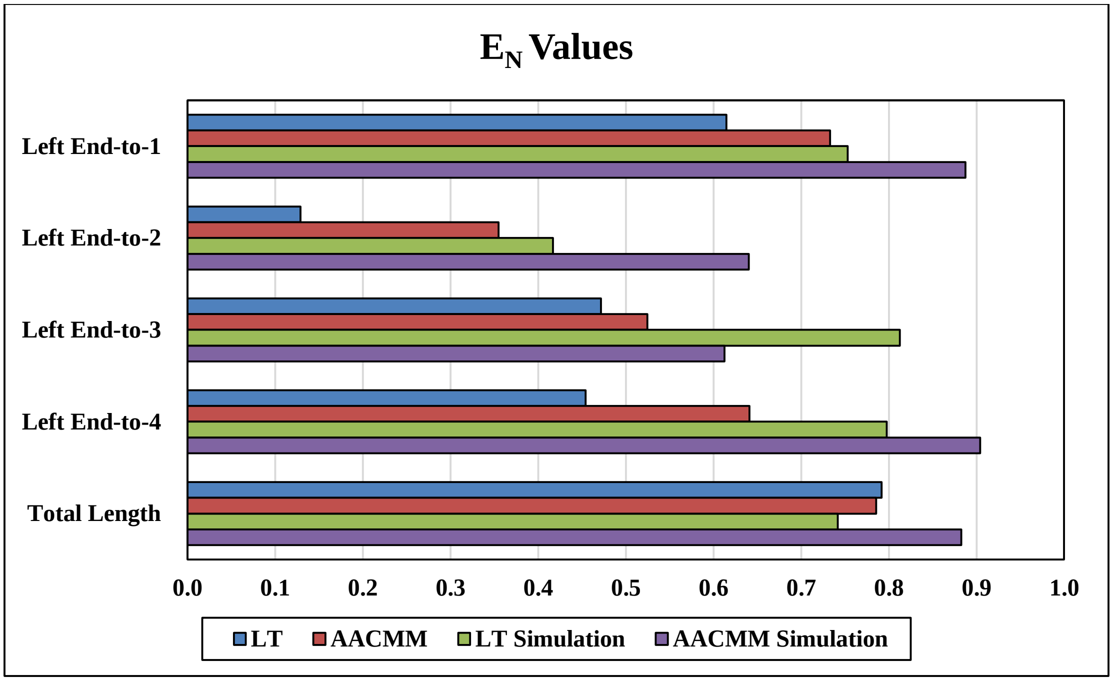

FIGURE 68: Flexible artifact E_N values, lengths.

For the measurement results of the angular orientations between the machined planes, FIGURE 69 above shows the results for the angle between the first and second machined flat. Both the laser tracker and AACMM measurements resulted in larger values, where the bias of the laser tracker measurements was 0.262° and an estimated expanded uncertainty of ±0.258°. As for the AACMM measurements, the bias was 0.288° with an estimated uncertainty of ±0.287°. For the complete data, see Appendix B, FIGURE 121 and FIGURE 122.

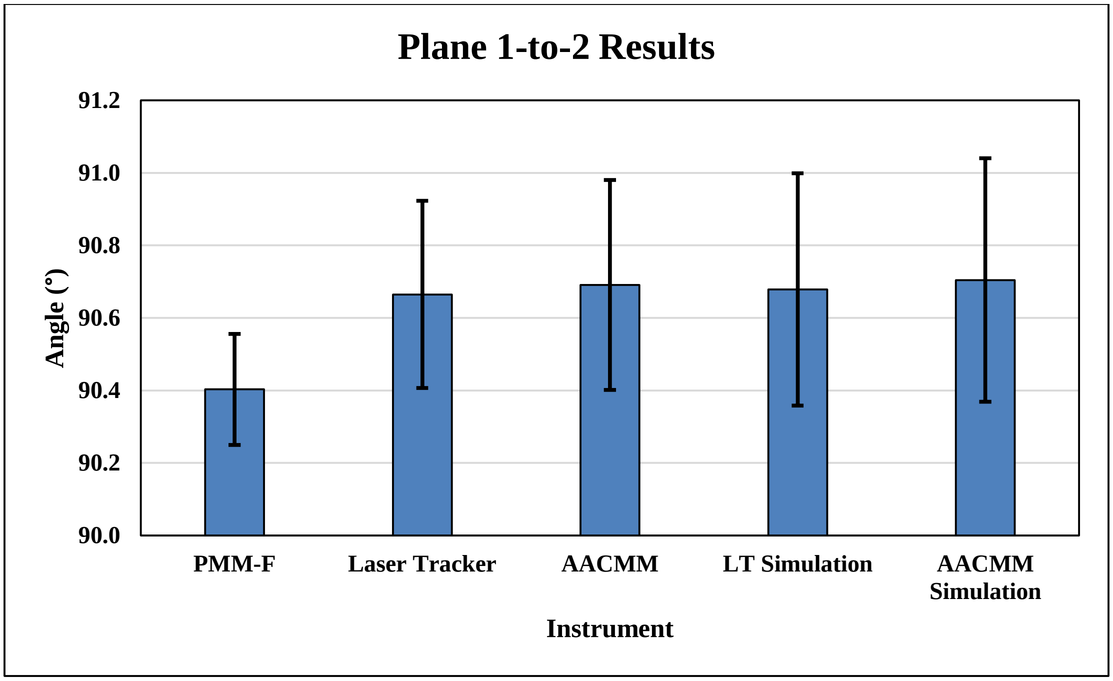

FIGURE 69: Measurement results for flexible artifact angle, $\boldsymbol{\varphi}_{\mathbf{12}}$.

For the E_N values, FIGURE 70 shows that all of the angular measurements on the work-piece compare with the reference measurements and are deemed acceptable. The angle between Plane 1 and Plane 2 had particularly large values. The machine surface does have some machining chatter which could lead to errors in the point coordinates, thus affecting the plane parameters used in determining the measurement uncertainty. Overall, the measurement results are good.

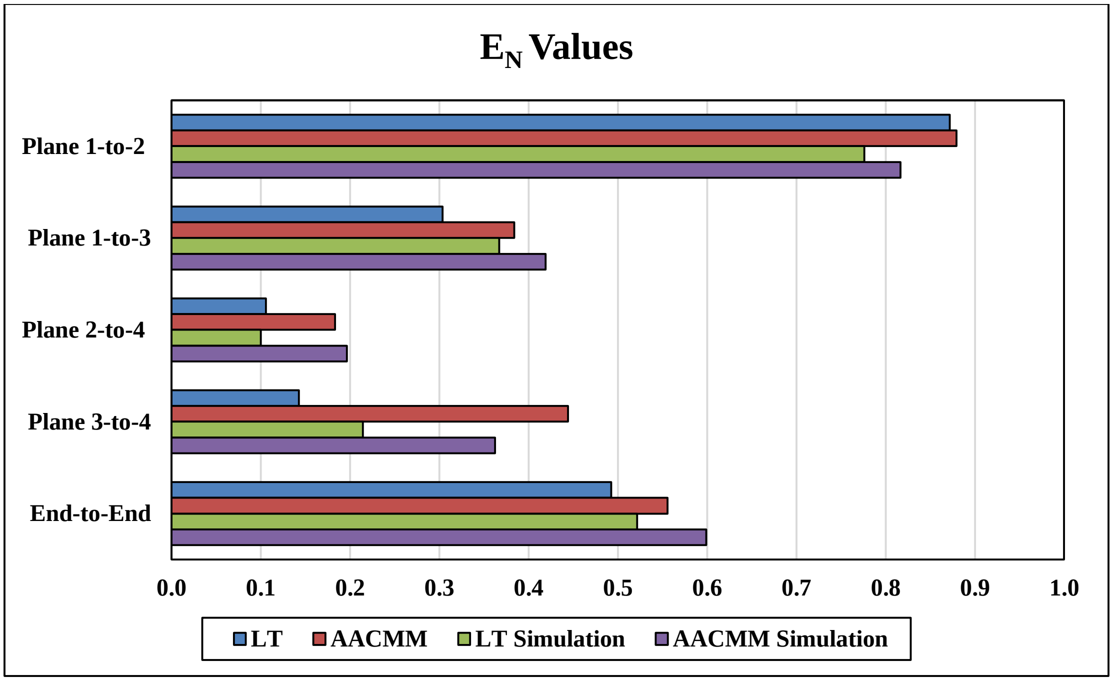

FIGURE 70: Flexible artifact E_N values, angles.

4.3 Sag Measurement Evaluation

The experimental testing and evaluation of the flexible artifact centerline sag is explained in this section. First the centerline measurements and then the length shortening error. For the centerline uncertainty evaluation, two sources of uncertainty were considered: the measurement process and the work-piece sensitivity (modulus of elasticity). For the work-piece, a range of $\Delta E = \pm 1 \times 10^{10}\ N/m$ was evaluated through a sensitivity analysis. As for the length shortening error, the measurement uncertainty was determined using a Monte Carlo simulation where a table of the parameter ranges is provided.

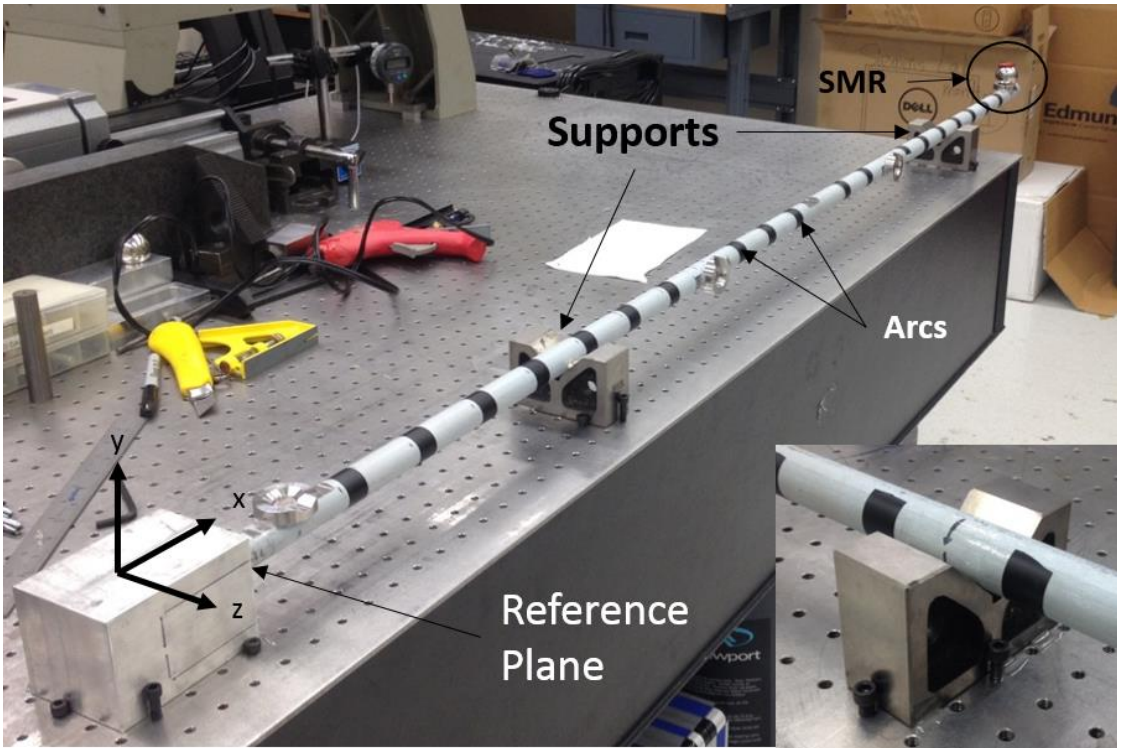

FIGURE 71: Experimental setup of flexible artifact: simply-supported.

4.3.1 Centerline Sag Measurements and Uncertainty Evaluation

The flexible artifact was first measured in a simply-supported setup as shown in FIGURE 71. A 1.5” SMR was placed on the attached SMR drift nest and then the bar was marked to best-control the measurement strategy. In doing this, a better estimation of the center points are calculated in the software which will be used to estimate the shape of the centerline from the multiple arc measurements. This same process was also performed when the work-piece was rotated 180° where a T-square was used to ensure a proper rotation (similar to FIGURE 72).

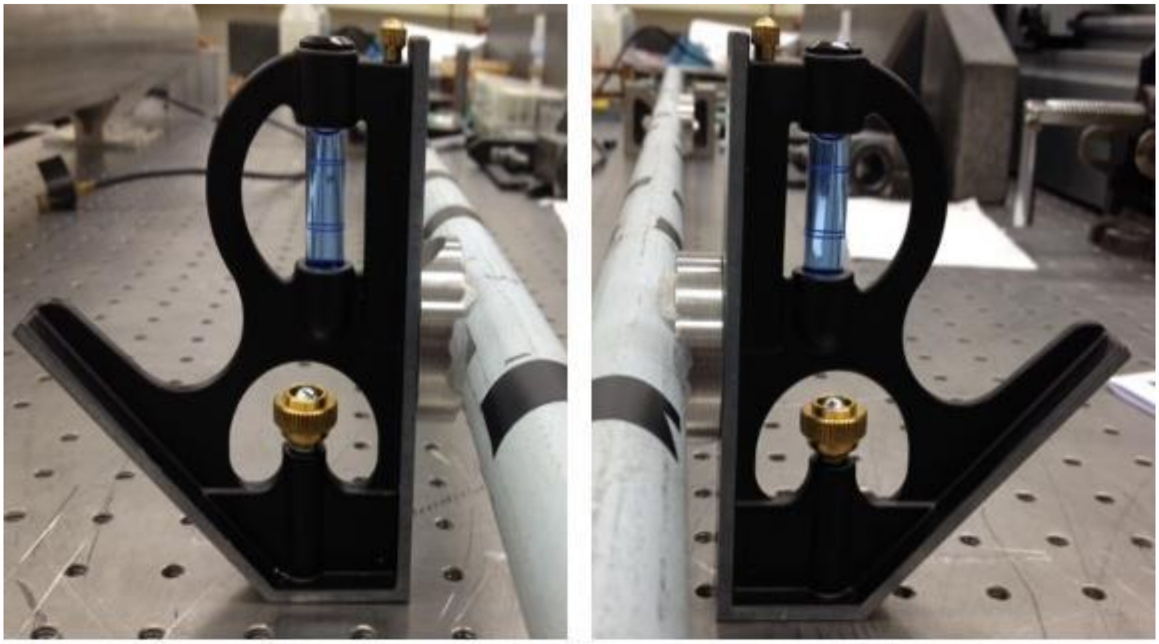

(A) (B)

FIGURE 72: Reversal alignment with T-square: (A) 0°; (B) 180°.

The measurements were taken with a Leica Absolute Tracker AT901-B and the data was collected using Spatial Analyzer. Each arc was measured with 5-6 points, where the center and radius were calculated using the default fitting algorithms (least-squares). FIGURE 73 shows a screenshot of the collected data points in Spatial Analyzer. After a circle was fit to each arc, a physical point was generated for each arc center, which represents a point on the centerline at a specific location in the *x*-direction. This entire process was performed four different times where the SMR was placed at each of the four different drift nest locations.

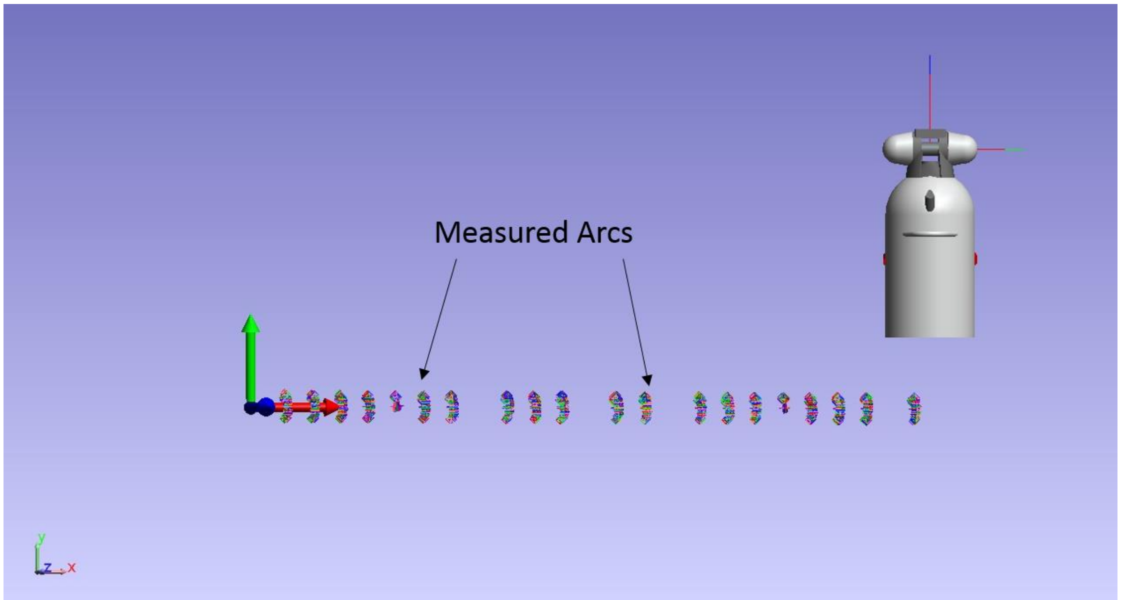

FIGURE 73: Spatial analyzer screenshot of data.

For the cantilever measurement setup, an aluminum block was fixed to the table to elevate the collet used in holding the work-piece as seen in FIGURE 74. The same measurement process and data analysis was performed on the cantilever measurements as that of the simply-supported measurements to determine the arc centers and radii. The arc measurement became increasingly sensitive the further away from the fixed end, as expected, so points were collected using a different measurement profile in the software. To combat the sensitivity issue of the arc measurements further away from the fixed end, the measurement profile *Stable Point to SA* was used. This measurement profile setting only allows a point to be collected when a stability criteria is met. For the all the arc measurements, the built-in default stability of 2 seconds was used.

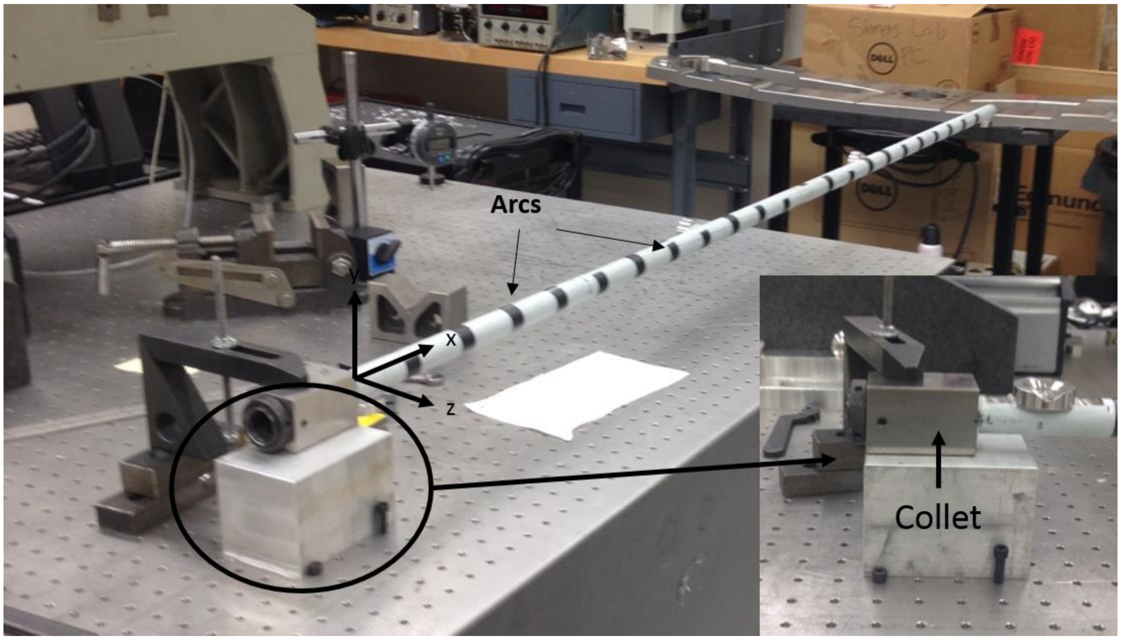

FIGURE 74: Experimental setup of flexible artifact: cantilever.

Processing the measurements yields the following results shown below in FIGURE 75 for the SMR located at the first drift nest. Initially, the measured results for the simply-supported case exhibited a tilt in the data which was caused by the optical table not being level so was corrected by subtracting out the tilt. Next, the uncertainty for each point was determined from the work-piece sensitivity and the uncertainty in the measurement of the arcs. Each individual point has an error bar that represents uncertainty with a 95% confidence. A majority of the point’s error bars overlap its respective predicted point which implies that the measured value range is within what was predicted thus making the measurement result acceptable. Noticeably, the uncertainty in the points further away from the reference end have larger variations which is the result work-piece deformation at the end from the manufacturing process. With the flexible artifact simply-supported, the effects from sag are minimized and thus have little influence on the measurement results, therefore, not influencing the measurement uncertainty very much. The results for when the SMR is located at the other three nest is found in Appendix C, FIGURE 123, FIGURE 124, and FIGURE 125.

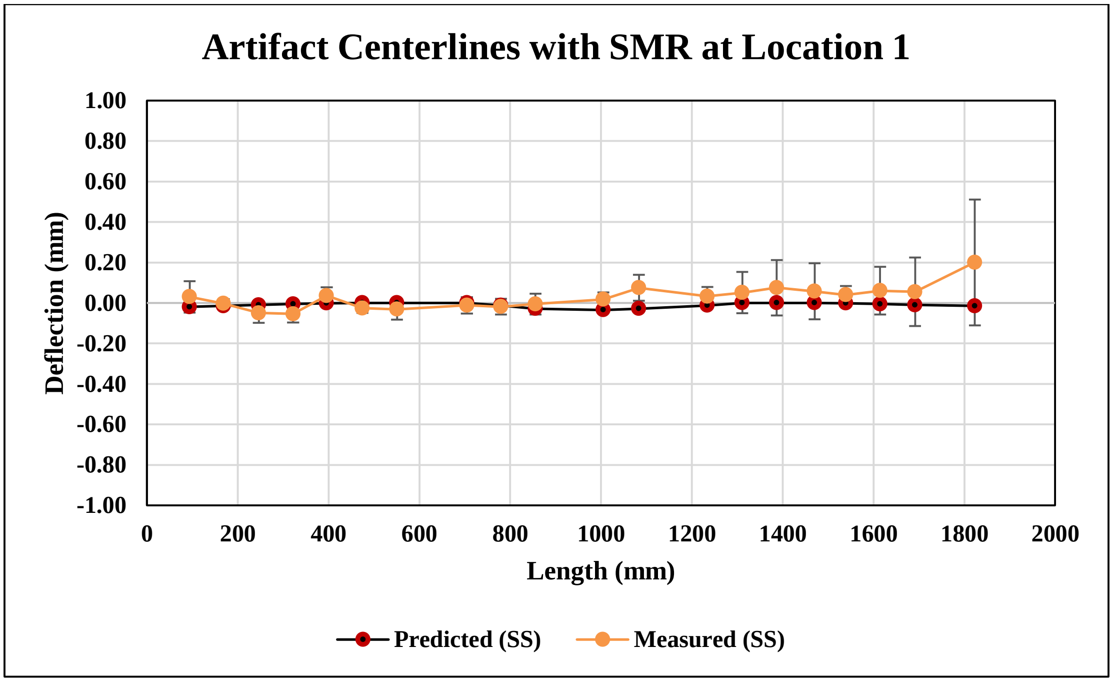

FIGURE 75: Centerline comparison: simply-supported.

The measurements for the cantilever case are performed in the same manner as those of the simply-supported measurements. After correction for the tilt in the optical table, a comparison between the measured and predicted centerlines show very good agreement with minor variation as seen in FIGURE 76. A maximum variation in the results was 0.3 mm at the furthest point from the end. The uncertainty in the measurements was estimated in the same manner as that of the simply-supported case where each individual point has an error bar that represents the uncertainty with a 95% confidence. However, the uncertainty becomes larger the further away the measurements are taken from the fixed end as the error bars become larger. This is directly the result from the influence of gravity on the work-piece. As was mentioned, the sag in the work-piece makes the measurement less-stable. Therefore, one can see the influence directly in the measurement results. The results for when the SMR is located at the other three nest is found in Appendix C, FIGURE 126, FIGURE 127, and FIGURE 128.

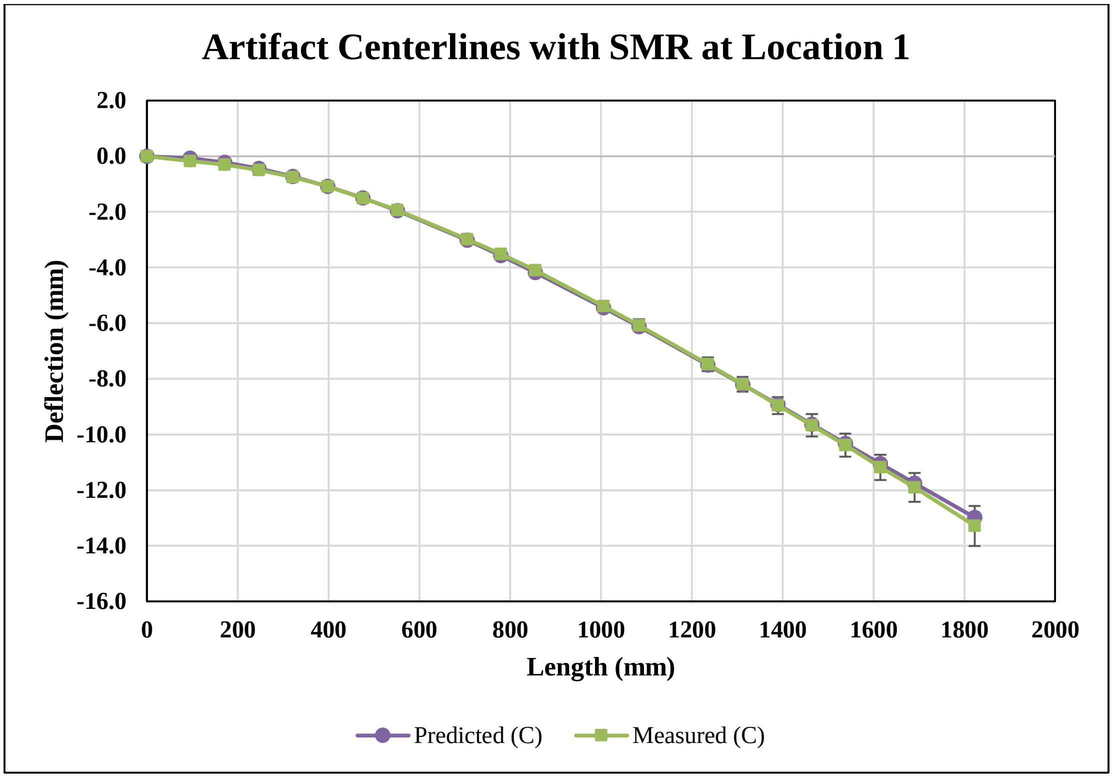

FIGURE 76: Centerline comparison: cantilever.

The model errors for the simply-supported case are shown in FIGURE 77. The errors are relatively-small and hover around zero. Furthermore, all the errors are contained within a 400 μm band with the largest variation in the results at the far-right end. At this portion of the artifact, the shape is deformed so the results of fitting a circle to the arc measurements are dependent on the points measured. From the results, it is confident to say that the centerline was modelled predicted and modelled very accurately.

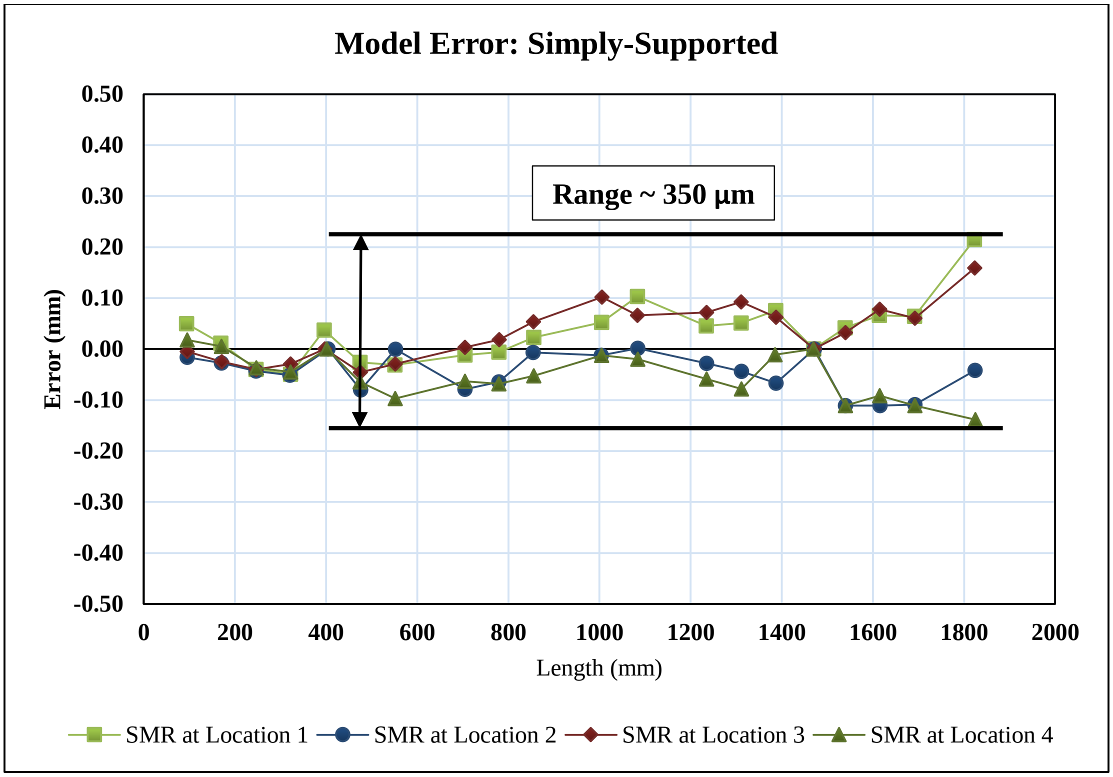

FIGURE 77: Model error for flexible artifact: simply-supported.

For the model errors of the cantilever setup, FIGURE 78 shows the results. The data trends almost in a parabolic manner which may be related to a systematic error such as the fixturing in the collet. However, all the errors lie within a 500 µm band and similarly the largest variation in the data again being at the far-right end. Overall, the results show that the centerline was modelled sufficiently well. From the results, it is confident to say that the centerline was modelled predicted and modelled accurately.

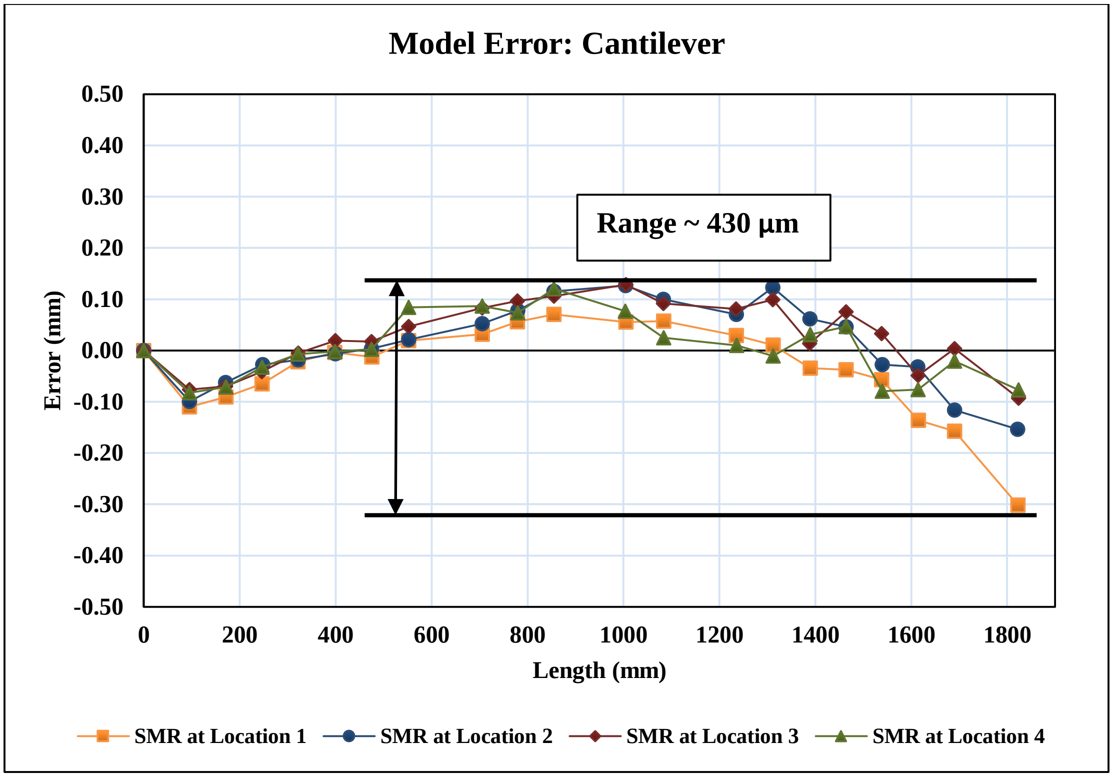

FIGURE 78: Model error for flexible artifact: cantilever.

4.3.2 Length Shortening Error Measurements and Uncertainty Evaluation

To experimentally determine the length shortening error, measurements of the SMR drift nest locations were taken in a cantilever setup (FIGURE 74) with a 1.5” SMR placed in each magnetic nest. Three measurements were taken at each of the four drift nest locations (FIGURE 79) and the results were averaged. Again, to reiterate that the measurement profile used for this set of measurements was the *Stable Point to SA* in the software. Getting stable points at the furthest distance (i.e. distance a_4 in the figure below) was always going to be the same problem as the centerline measurements since the work-piece was easily agitated with any minute force.

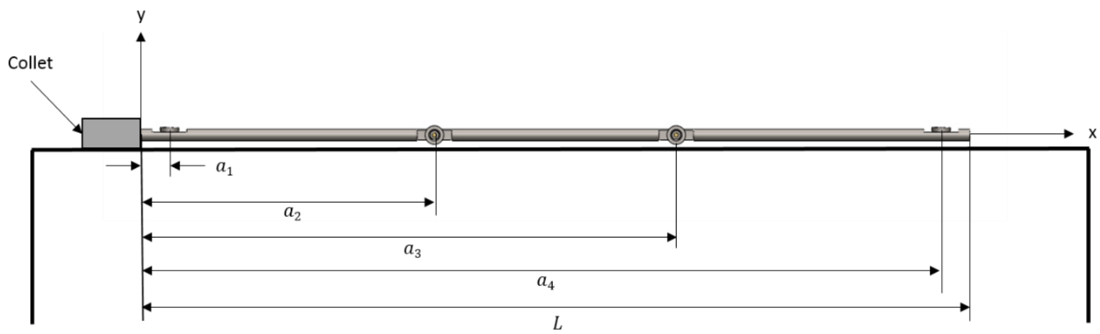

FIGURE 79: SMR drift nest locations.

The fixed artifact parameters used in processing the measurements were as follows: $W_1 = 72.63\ N$, $W_2 = 1.60\ N$, $E = 205\ GPa$, and $I = 2.04 \times 10^{-8}\ m^4$. Each of the measured parameters for a_1, a_2, a_3, a_4 and L were determined in the software for each particular case for the three different measurement cycles. Calculating the length shortening error for the reference, experimentally determined and simulated yielded the results shown in TABLE 15. Distance a_4 was always going to have the largest length shortening error but the experimental evaluation was needed for validation. As expected, distance a_4 had the largest length shortening error as well as the largest bias in the measurements at 28.2 μm between the reference and measured data. The simulated results (see FIGURE 80) matched up well with the measured results for the two closest distances (i.e. a_1 and a_2) however then matched closer to the reference measurements for the two further distances (i.e. a_3 and a_4). This is the result of the stability issues as the measurements are taken further away from the fixed end, the work-piece is more-sensitive to touch whether from probing or SMR placement.

TABLE 15: Length shortening error comparison.

Parameter	**Measurement of:**			
	$\Delta L(a_1)$	$\Delta L(a_2)$	$\Delta L(a_3)$	$\Delta L(a_4)$
Reference	-0.5730	-0.5969	-0.6142	-0.6287
Measured	-0.5743	-0.6023	-0.6245	-0.6569
Simulated	-0.5752	-0.6018	-0.6169	-0.6306

Estimating the uncertainty in measurements, ranges of input parameters were needed. Each of the measured parameters for a_1, a_2, a_3, a_4 and L were assumed normally distributed since each standard uncertainty was determined as the standard deviation from the multiple measurements. A systematic, uniform distribution was assumed for all the other parameters used in the measurement processing which are located in TABLE 16. The number of simulation trails was $n = 200{,}000$, which is suggested in Supplement 1 [95].

TABLE 16: Length shortening influences and standard uncertainties.

Input Quantity (units)	**Upper Bound (a_+)**	**Lower Bound (a_-)**	**Standard Uncertainty**
W_1 (N)	1.0	-1.0	1.15
W_2 (N)	0.1	-0.1	0.12
E (N/m^2)	10×10^9	-10×10^9	1.15×10^{10}
I (m^4)	40×10^{-10}	-40×10^{-10}	0.46×10^{-10}

The results in TABLE 17 show the measured length shortening results and the associated expanded uncertainties at 95% confidence. As expected, the measurement uncertainty increased the further away the measurements were taken from the fixed end. However, the results are still relatively minute in comparison to the calibrated distances, particularly the further away from the fixed end. Therefore, it is safe to assume that for this specific work-piece, the length shortening error has little effect and can be deemed negligible, even in the most-sensitive to bending cantilever setup.

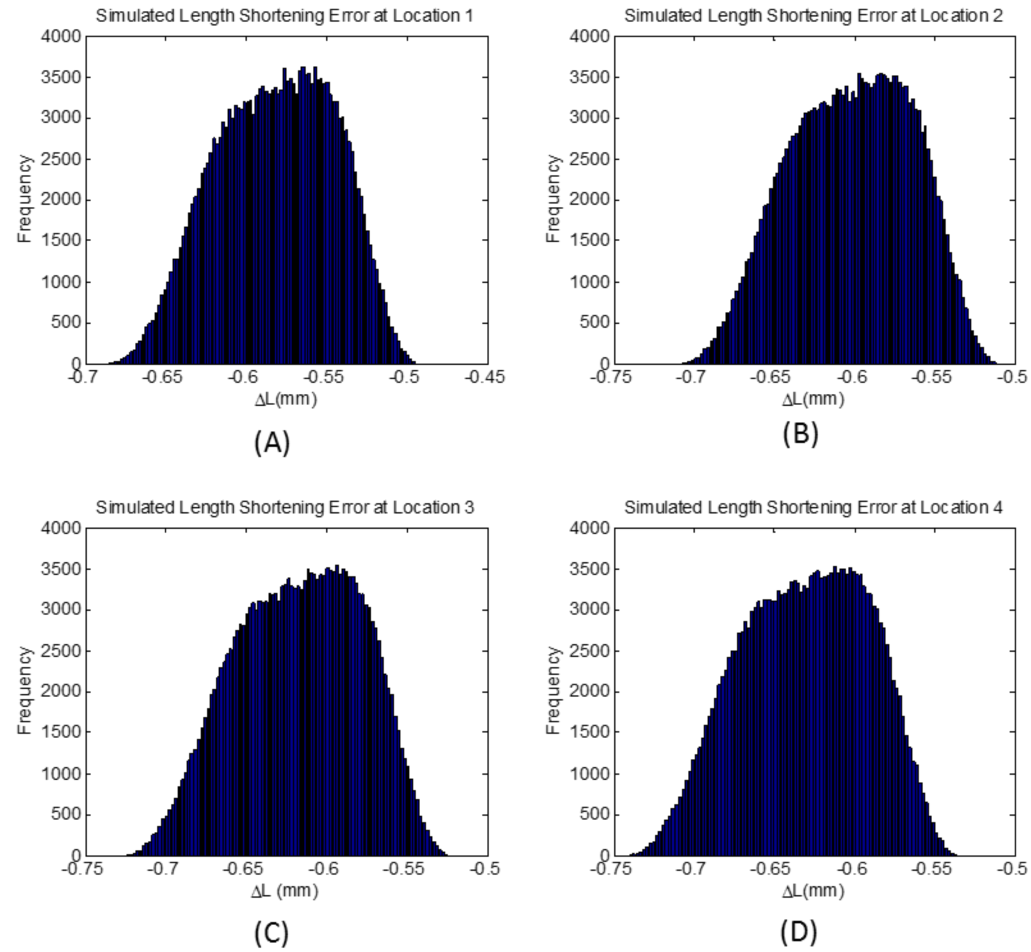

FIGURE 80: Simulated results: (A) a_1; (B) a_2; (C) a_3; and (D) a_4.

TABLE 17: Length shortening results and expanded uncertainty.

Parameter	**Measurement of:**		
	Best-Estimate		$\boldsymbol{U\ (k=2)}$
$\Delta L(a_1)$	-0.5743	$\pm$	0.0318
$\Delta L(a_2)$	-0.6023	$\pm$	0.0559
$\Delta L(a_3)$	-0.6345	$\pm$	0.0774
$\Delta L(a_4)$	-0.6569	$\pm$	0.0906

4.4 Non-uniform Temperature Evaluations

Experimental testing on the effects of non-uniform temperature distribution are described and evaluated. The work-piece used in the testing is the aluminum cylinder. Since aluminum has a high CTE, the results will be sensitive to the temperature distribution generated by the experimental heat source. The heat source used was 72” x 1” (1800 mm x 25 mm) silicone rubber heating tape with an adjustable thermostat control. The adjustable temperature range is specified at 50-425°F (10-218°C) from the manufacturer.

Before the experimental measurements, an FEA analysis was performed to determine the predictive deflections when the heat source was simulated over the specified surface area. As an example of the predictive deflection from the heat source, the FEA simulation for the temperature at T = 27°C is shown below in FIGURE 81. The figure shows the original shape when simply-supported and the deflected shape when the temperature is simulated. As one would expect, the geometry bows in a circular arc shape (negative) where the centerline between the supports is positive and the centerline on either end of the supports is negative. It should be noted that the effect from gravity in the model is neglected and the deflections are purely the results of the temperature distribution.

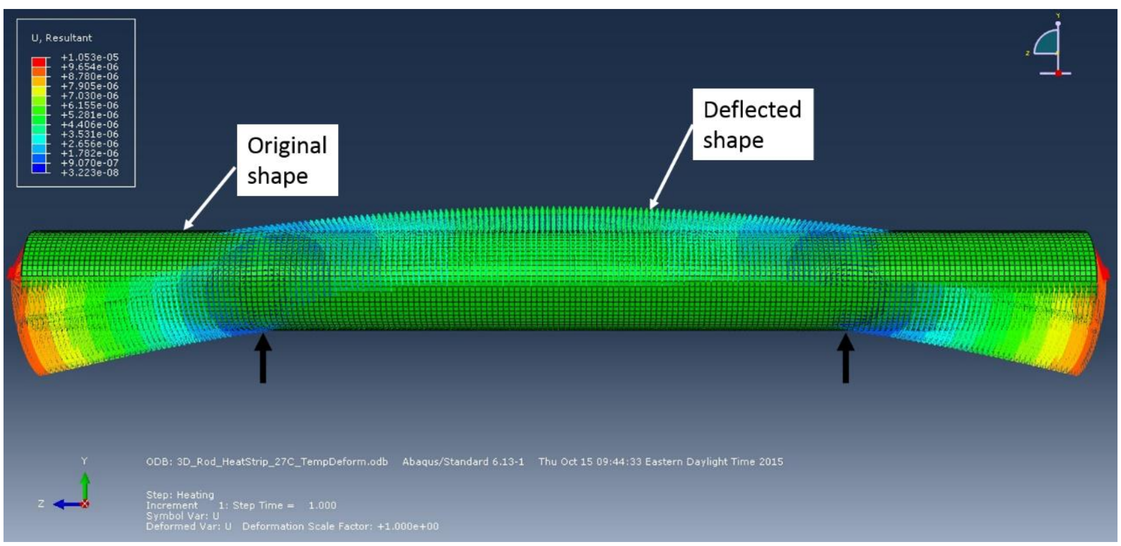

FIGURE 81: FEA results of the work-piece deflections at T = 27°C.

For the experimental testing, the setup is shown in FIGURE 82. The work-piece is mounted on two aluminum V-blocks at approximately the Gauss points (i.e. a distance of 0.212L from each end or a distance of 0.586L between the two supports) to minimize the effects from gravity on the neutral axis. Because of the large range of possible temperatures, it was easy to generate very high temperatures in small amounts of time thus becoming a safety hazard. To control the temperature variability, a temperature sensor was attached to the heat source and monitored to ensure that the temperature was not excessively high. A sensor is built in to the control knob to monitor the temperature of the work-piece for constant regulation of the heat. However, it still proved to be a challenge controlling the temperature to within a few degrees. Due to the complexity of controlling the temperature, only three temperature ranges on the heat tape were used for testing which were ~27°C, ~33°C and ~38°C. These temperatures fall into typical temperature ranges often seen in industrial environments.

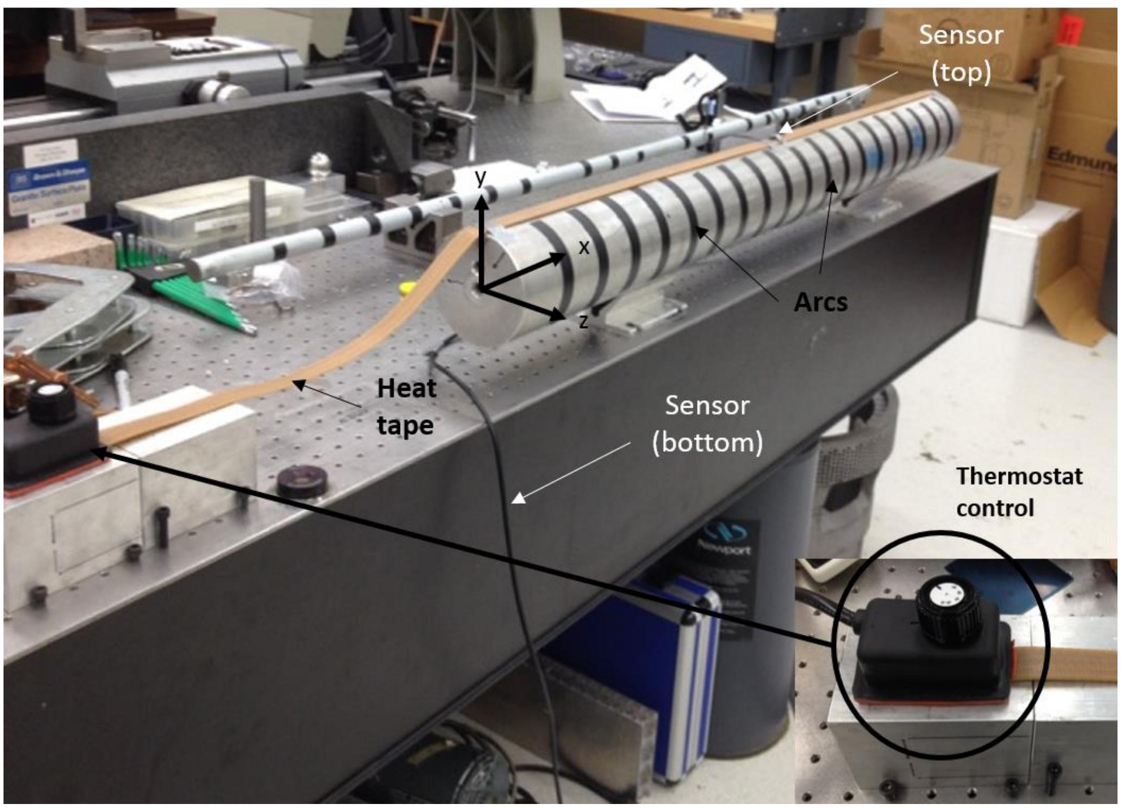

FIGURE 82: Experimental testing for temperature non-uniformity.

The measurements were taken with a Leica Absolute Tracker AT901-B and the data was collected using Spatial Analyzer. As seen in FIGURE 82, each arc was measured with 7 points, where the centers and radii were calculated using a least-squares algorithms. After a circle was fit to each arc measurement, a physical point was generated for each center point which represents a point on the centerline measured in the *x*-direction. Since the predictive model is based on the FEA algorithms, the data could not be normalized with the measured *x*-direction values so a point-to-point comparison was not possible. The results of the FEA predictions and experimental measurements for the first temperature are shown in FIGURE 83.

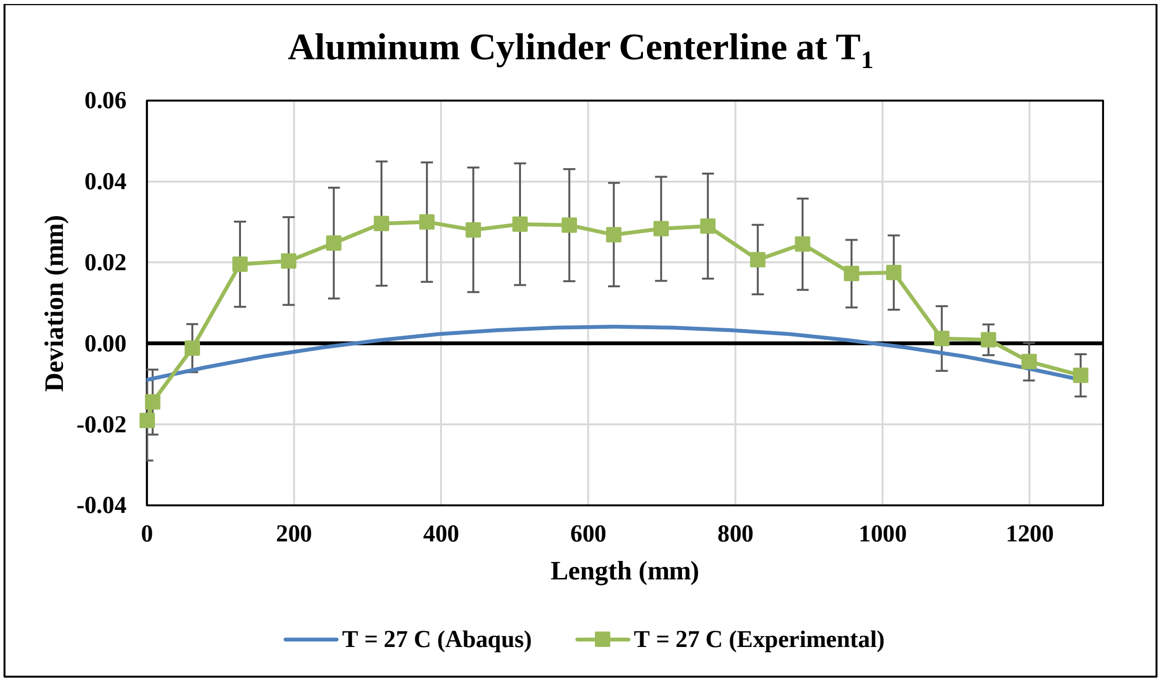

FIGURE 83: Cylinder centerline result for $T_1 \approx 27°C$.

From the measurement results in FIGURE 83, it appears that the data does trend in parabolic manner, similar to that of the predictive models but the values were much large. The range of predictive values was 13.2 µm whereas the measured values had a range of 37.8 µm, so a difference of 24.6 µm. In the beginning of the measurements, there is a sharp increase which could be related to the heat tape generating heat to meet the desired setting. The results do stabilize over the middle of the work-piece but tales off as the last of the measurements are collected. The entire measurement process took approximately 15 minutes to complete so it is possible that the results at the far right were collected when the heat source was not generating any heat or the work-piece was cooling down.

As was mentioned earlier, the uncertainty in the measurements was determined as the difference between the measured center point and the center point at T = 20°C from the reference measurements. Since both center points were at close, yet different *x*–direction values, the average between the two was used. Small in the beginning and the end, this is the results of the comparison to the calibrated centerline which showed minimal variation. Because of the large biases in the measurements at the middle of the part, the uncertainty was always going to be greater, where the largest value was ±15.4 μm at 95% confidence.

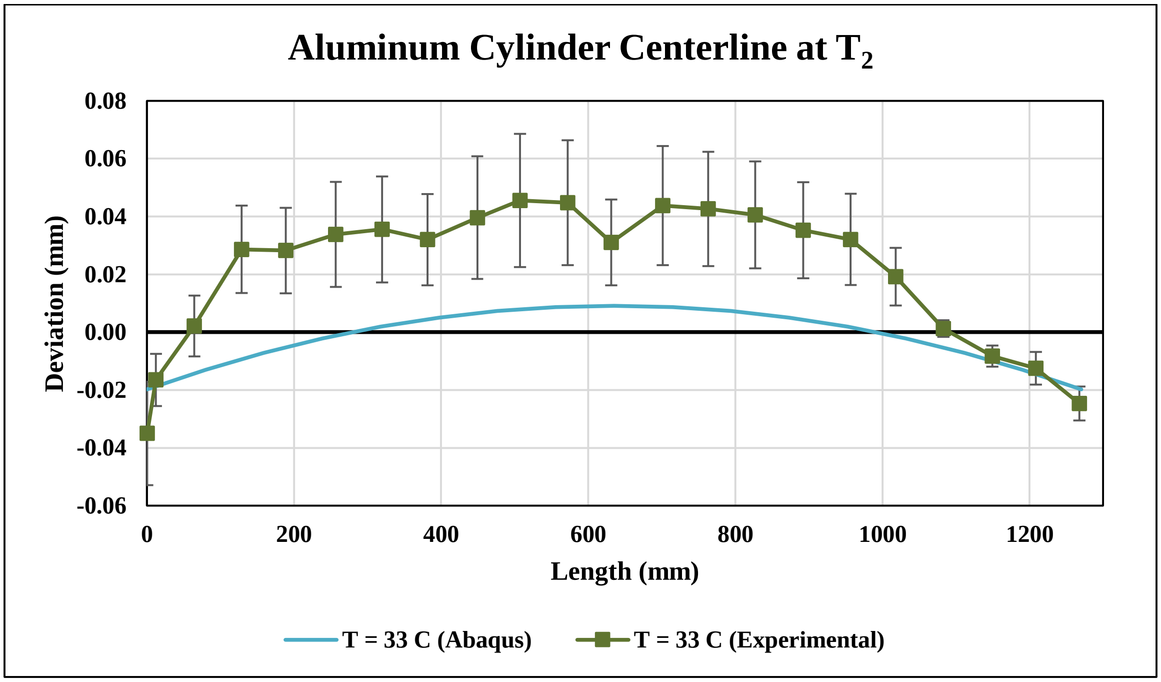

FIGURE 84: Cylinder centerline result for $T_2 \approx 33$°C.

For the measurements at a temperature of approximately 33°C, the same can be said about the measurements exhibiting large biases in relation to the FEA predictions as shown in FIGURE 84. The range of predictive FEA values was 28.9 μm, whereas the range of the measured values was 70.2 µm, hence a difference of 41.3 µm. Data had a similar trend to that of the first temperature tested, with a slight dip near the middle measurement. Because of the large biases, the uncertainty in the measurements over the section between the supports was much larger than that at the ends with the largest being ±23.1 µm at 95% confidence.

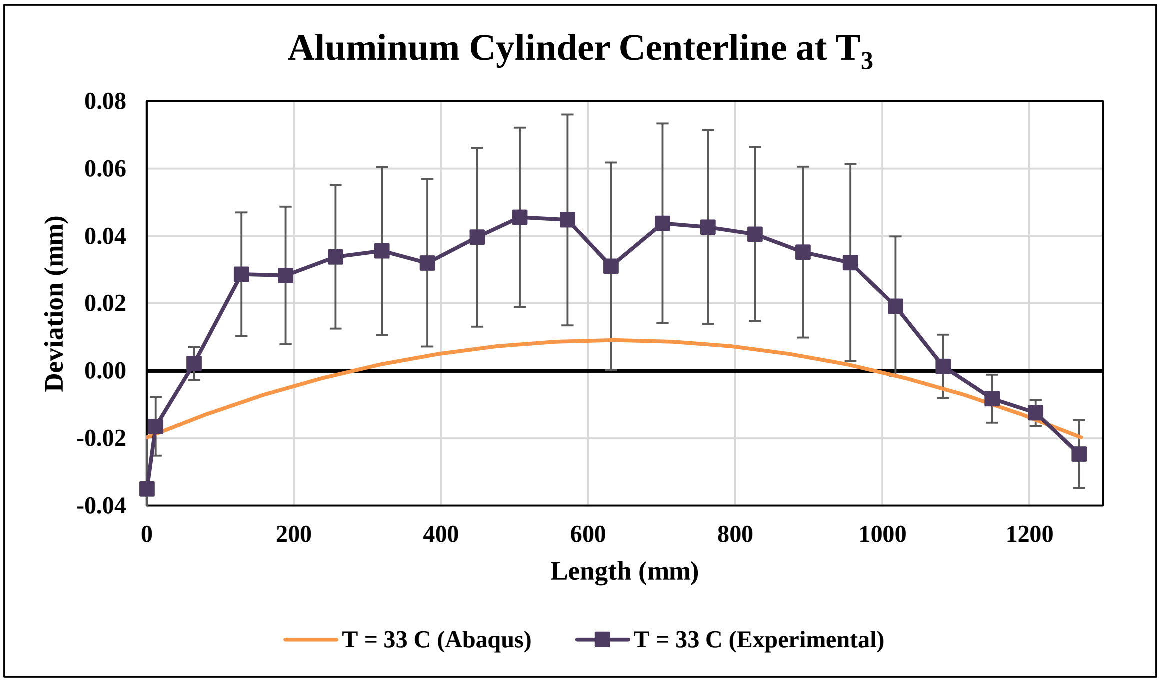

FIGURE 85: Cylinder centerline results for $T_3 \approx 38°C$.

As for the measurements at for the last temperature tested, FIGURE 85 shows the results. The range of predictive FEA values was 42 µm, whereas the range of the measured values was 105.5 µm, hence a difference of 63.5 µm. The largest uncertainty in any of the points was estimated to be ±31.3 µm at 95% confidence.

It was determined that the results from the experimental assessment generally overestimate FEA predictions and thus may not be a suitable experimental testbed to determine the influence from temperature non-uniformity on a set of measurements. Even with a simple geometry, estimating the measurement uncertainty proved to be more complicated than first thought. However, it is a baseline testbed to build on where better control of the heat source is priority number one, whether more experience is need in understanding or developing better methods to control the heat or if a better heat source is need. Overall, a good first step in experimental testing and heading towards a more adequate setup.

In all practicality, ensuring that the work-piece has thermally stabilized before measurements are taken is still the best course of action for industrial measurements. The randomness of temperature non-uniformity is always going to be a problem if not recognized from the start. Therefore, to get an accurate assessment of what non-uniformity in work-piece temperature does to simple geometries, FEA analysis is still the preferred method when it comes to this dilemma.

CHAPTER 5: CASE-STUDIES

As an application of the new methodology to determine the measurement uncertainty for industrial measurements, two case studies are described in this chapter. First, the measurement of an outside diameter on a throttle valve for a steam turbine and then the measurement of the centerline for a rotor body used in generator assembly. First an introduction to the current metrology processes as well as proposed alternative method to the measurements using a laser tracker. Then a detailed description of the work-piece measurand and the measurement strategy used to gather the measurements. Then a brief description of the measurement setup and environment. Finally the estimated measurement results with expanded uncertainty statements.

5.1 Steam Turbine Throttle Valve

The objective of the project was to investigate numerically controlled alignment, measurement and evaluation of the throttle valve component for steam turbines. Current measurement methods of the throttle valve component are done manually with a set of outside diameter micrometers (OD-micrometer), inside diameter micrometer (ID-micrometer) and a 1D probe with the use of a vertical boring machine (VBM) as the rotary table axis. The aim of the project is to compare and partial/complete replacement of the current metrology process using laser tracker technology.

Typically, the throttle valve is measured in two different orientations: vertical and horizontal. This is very manually intensive and time consuming. Using a laser tracker, a preferred method for the throttle valve measurement is in a horizontal position or “as shipped” position (see FIGURE 2). The reason for measuring in the horizontal position is for access to measurement in a bi-directional path along the central, symmetry axis, which eliminates the need to measure the throttle valve in the vertical direction (i.e. on the VBM). Overall, the goal was to reduce the metrology efforts for this project (~12 hours of measurement time and a high percentage of manual labor) to a range of 40-50% at an improved (or at a minimum equal) accuracy level and validated with a stated uncertainty estimation.

5.1.1 Measurand and Measurement Strategy

The throttle valve had multiple measurands of interest, both external and internal components, which are critical for alignment purposes with an assembly. The measurand in consideration here is an outside diameter known as the spigot outside diameter (FIGURE 86). The nominal diameter is 45.875” (1165.225 mm) and has a height from the compression stop face of 0.125” (3.175 mm). Although the measurand is a large diameter, the tolerance specification is a few thousandths of an inch so it is critical that the actual measurement results are known with confidence, hence the need for an uncertainty statement. With the measurands defined and the obstacle of the minimal surface area for probing identified, a measurement strategy was developed to best obtain the measurements with custom tooling while minimizing the influence on the measurements.

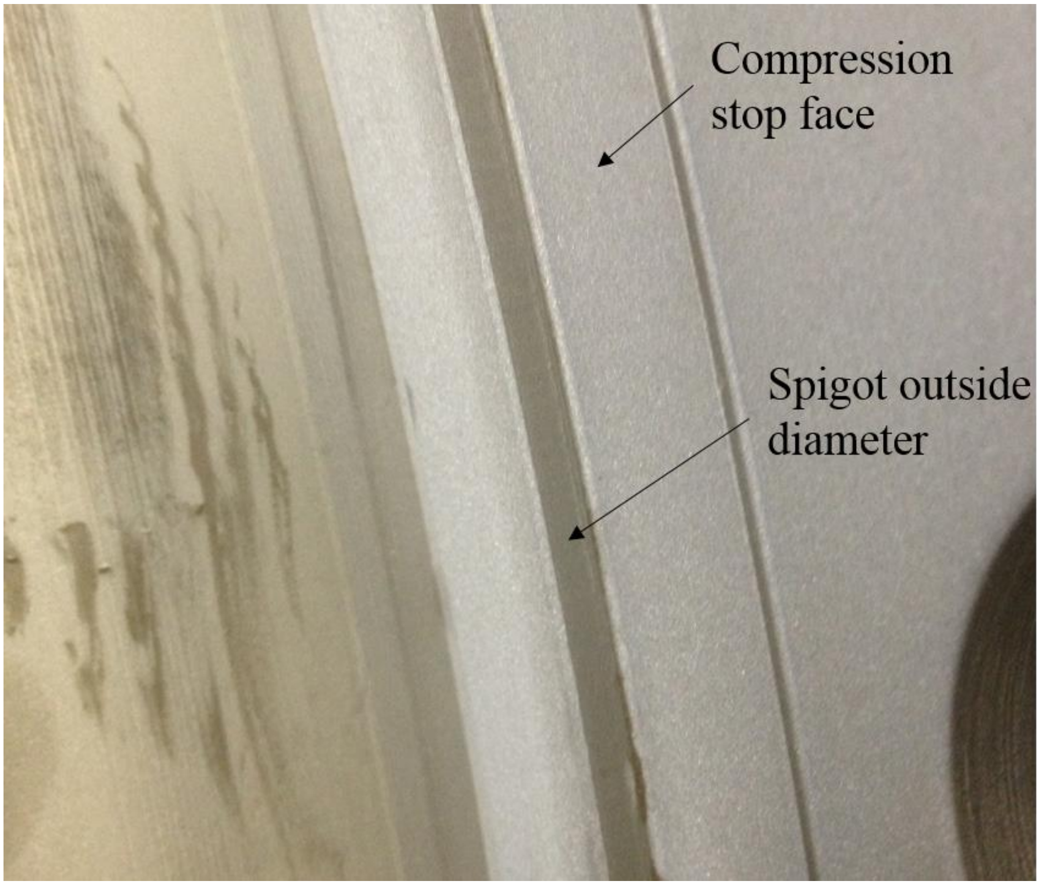

FIGURE 86: Spigot OD on throttle valve.

Since the measurand could not be measured from a single laser tracker location, the instrument was placed in different locations to measure the entire feature. As a results, the determination of the measurement uncertainty can be performed according to the multiple measurement strategies where randomization of the measurement process in effect randomizes the systematic errors. For each set of measurements, the instrument was moved to three different locations. The first location was to measure the reference points for the data fusion. Next, the instrument was moved to either side of the throttle valve to measure the spigot diameter as well as points used to determine the coordinate system, similar to the schematic in FIGURE 87.

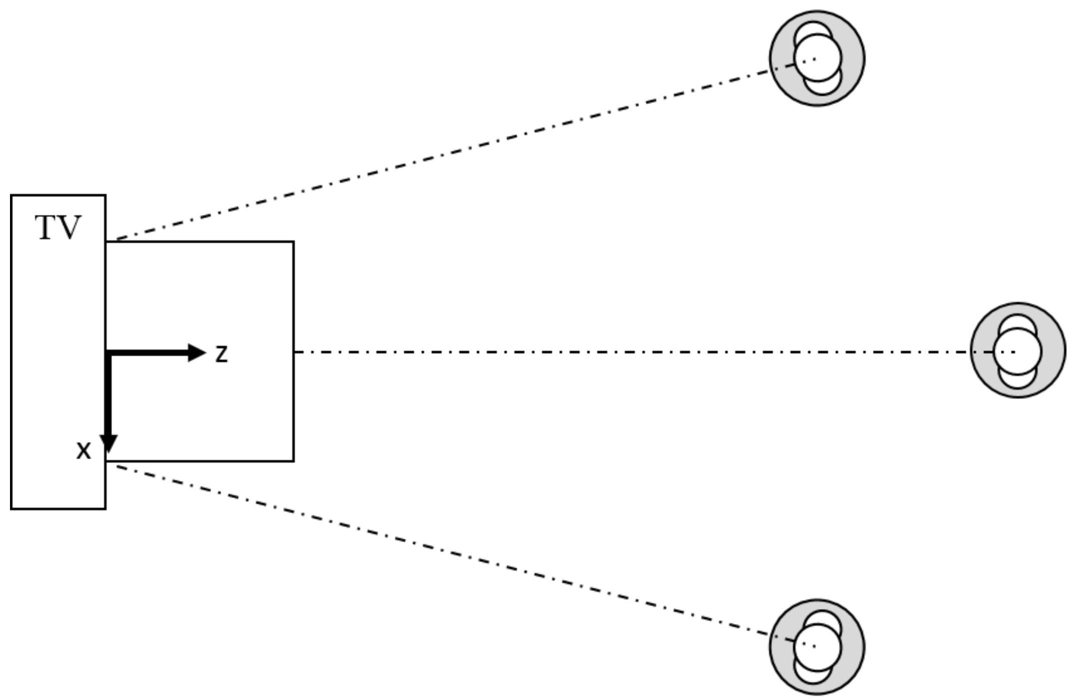

FIGURE 87: Laser tracker positions for measurement.

Since the measurements are manual, no defined sampling strategy was used other than to conscientiously ensure that an adequate number of points was taken on each side of the work-piece. To do this, the spigot diameter was marked with points at approximately every 8°-10° in an attempt to control the sampling strategy. As was mentioned earlier, the spigot outside diameter does not have much surface area to probe points and using a smaller SMR is an option but the influence from the operator will likely be greater with the awkwardness of holding the SMR against the surface. In an attempt to remedy this, an edge finder was modified with precision ground half-pins to ensure that there was only two points of contact and the measurements were stable, FIGURE 88. With the half-pin modifications, the data points were now an unknown distance away from the part surface so the modified edge-finder needed to be calibrated to determine the new point location.

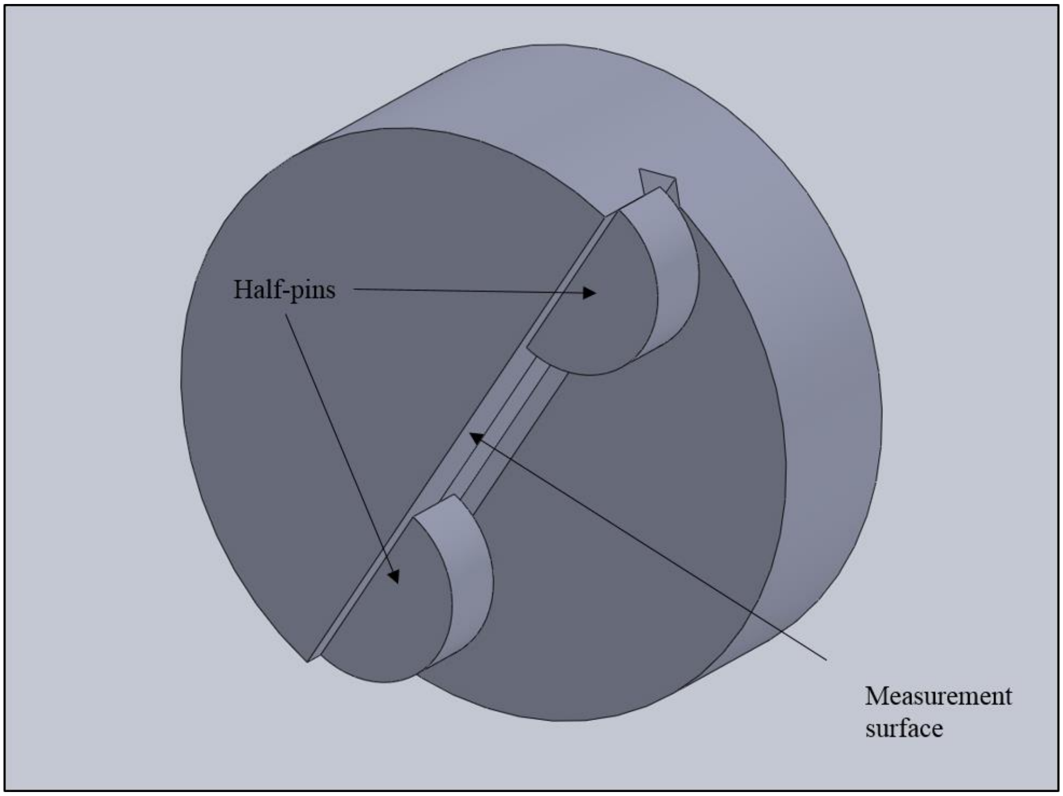

FIGURE 88: CAD model of modified edge finder.

Calculating the correction is a matter of basic trigonometry. From right-angle geometry, one can see the relationship between the geometry in FIGURE 89 and Eq. 69 as an application of the Pythagorean Theorem,

$$c = R_B + r_P = \sqrt{a^2 + b^2} \tag{69}$$

where $a = L/2$ and $b = R_B + \Delta$ as the two remaining sides. Therefore, substituting these side length into Eq. 69 and solving for Δ yields the correction for the modified edge finder or Eq. 70

$$\Delta = \sqrt{(R_B + r_P)^2 - (\frac{1}{2}L)^2} - R_B \tag{70}$$

Calibrated using a high accuracy CMM, a value of $\Delta = 0.24341"$ was determined with a difference from the theoretical value of 51 μin (1.3 μm).

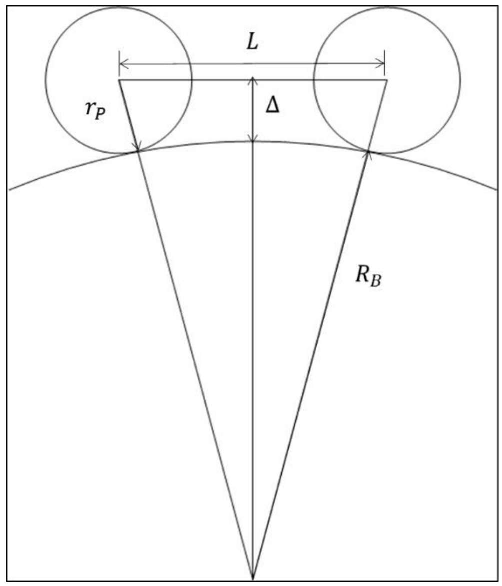

FIGURE 89: Correction for modified edge finder.

5.1.2 Measurement Environment and Setup

A shop floor temperature of 74°±4°F is maintained with suitable consistency throughout the entire steam turbine section. Work-pieces are soaked before any measurements are taken to minimize the effects from temperature and for thermal equilibrium throughout. Like any production environment, other extrinsic factors like dirt, grime, oil, etc. will affect the measurements so the work-piece was cleaned prior to measurement. Reference points were placed on the throttle valve itself and the tooling skid it rested on as both were large-mass objects and very rigid. Measurements of the reference points were performed before and after the measurement process to estimate the drift as well as the influence from the point stitching. The throttle valve was measured in a horizontal position, with the center at approximately "eye-level" of the laser tracker at a distance of approximately 15 ft away.

5.1.3 Measurement Results and Uncertainty Budget

An example of the laser tracker measurements are seen below in FIGURE 90 where one can see the reference points located on the throttle valve. Multiple measurements were collected over the course of six different visits where all the measurements were analyzed using least-squares fits to determine the spigot outside diameter. Each set of data was correct for the modified edge finder offset. For the thermally-induced contribution, the laser tracker has thermal compensation for its scales so only the CTE of the work-piece was needed, that is 7.2 ppm/°F for steel.

FIGURE 90: SA measurement of throttle valve.

For the uncertainty analysis, the sources and formulae introduced in Chapter 3 were used to determine the influence from each source. A reference value was determined using the current metrology process since the large-scale CMM capability was not yet available at the time the measurements were collected. The diameter had a large form error but this could be the result of the part being measured prior to manufacturing modifications such as skim-cuts to smooth out some of the mating surfaces when sent in for service repairs.

The form error therefore will contribute to the work-piece influence in the uncertainty measurements. Since the measurements were taken inside the “measuring volume”, and the laser tracker was outside the network of reference points, the influence from the data fusion was accounted for. Finally, the uncertainty from the modified tooling must be considered, which had minimal effect.

TABLE 18: Throttle valve spigot diameter uncertainty budget.

Source	Method	Distribution	Standard Uncertainty (in.)
Measurement Process	A	Normal	0.0016
Bias	B	Uniform	0.0013
Work-piece	B	Uniform	0.0028
Thermally-Induced	B	U-shaped	0.0022
Data Fusion	B	Uniform	0.0013
Tooling	B	Uniform	0.0012
Combined Standard Uncertainty, u_c			0.0045
Expanded Uncertainty at 95%, $U(k=2)$			0.0090

From the uncertainty budget of TABLE 18, the largest uncertainty source came from the work-piece itself where the form error was approximately 0.010”. Hence, the final result is stated as follows:

$$d_{spigot} = 45.877'' \pm 0.009''$$

where the best-estimate of the spigot diameter is the average of the six different visits and the expanded uncertainty at a 95% confidence level. This is an acceptable result since the range of values are within the specification value and specification tolerance limits from the drawing. Additionally, total measurement time was approximately 2 hours, start to finish, which came out to a reduction in effort of 50%, thus validating that the new metrology process was a viable alternative.

5.2 Generator Rotor Body

For this case study, the objective of the project was to develop new and improved processes used to mount and align generator rotors on a horizontal machine tool for the machining of slots on a rotor body. Also, to provide methods to measure slot spacing and conformance to design specifications. The goal is to develop a deterministic and non-iterative process that reduces manual operation time by at least 30% and ensures that the quality of the alignment is sufficient to allow feature tolerances on the work-piece to be achieved.

The current alignment process involves a series of iterative steps to align a rotor in a horizontal milling machine with the use of manual hand tools and an entire 8 hour shift. Each operator follows five steps to align the centerline of the rotor body (FIGURE 91) to the center of a non-adjustable set of auxiliary spindles. The rotor body sits on two pedestals that support a journal on each end (i.e. Exciter End (EE) and Turbine End (TE)) in a simply-supported manner. The pedestal on the EE side is non-adjustable. Additionally, a center support, in this case a hydraulic jack, is used to compensate for the sag of the rotor body (sag has been measured anywhere from 0.020” - 0.080” (0.5 mm – 2 mm) in multiple rotors) and aid in the manufacturing of centerline cuts. The focus of this case study is related to the alignment process where the centerline of the rotor as it passes a set of auxiliary spindles is investigated to determine the shape and confidence in the measurements in the form of an uncertainty estimate.

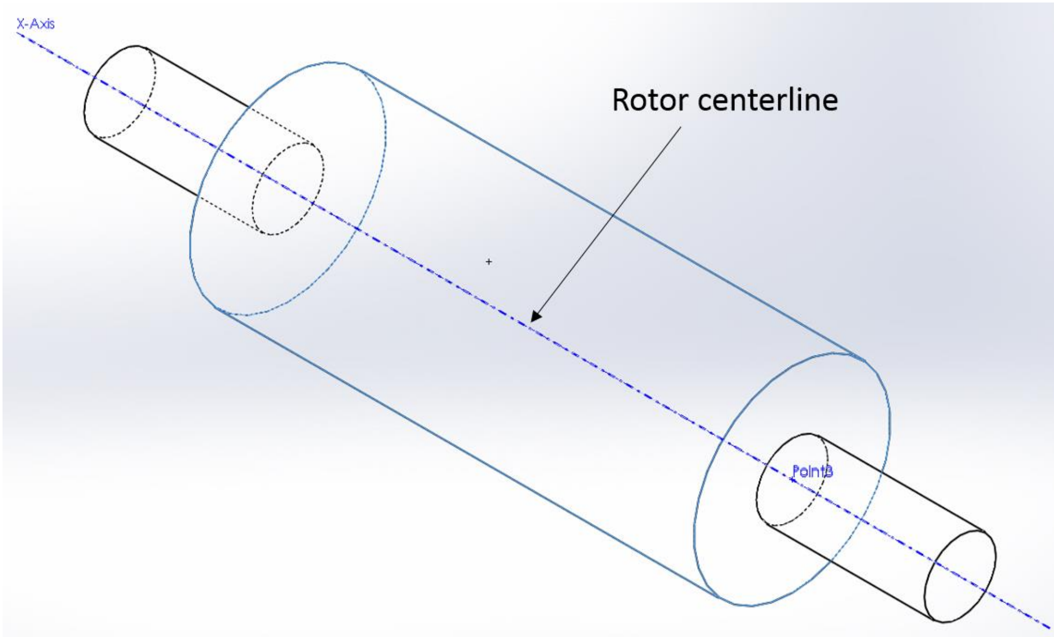

FIGURE 91: Centerline of the rotor.

5.2.1 Measurand and Measurement Strategy

The measurand is the centerline of the rotor body as it passes by the set of auxiliary spindles. Since the rotor is traversed along the *x*-direction, the measurement coordinate system must be set on a fixed location, therefore, it is located between the opposing sets of auxiliary spindles, as seen in FIGURE 92. The *y*-axis is the line constructed between the centers of the two spindles closest to the cutting wheels (i.e. spindles #1 and #5), the *x*-axis is the direction the table traverses and the *z*-axis is perpendicular to the table. To determine the *x*-axis direction, an SMR drift nest was attached to the rotor body and a spatial scan of data points were collected to construct a line.

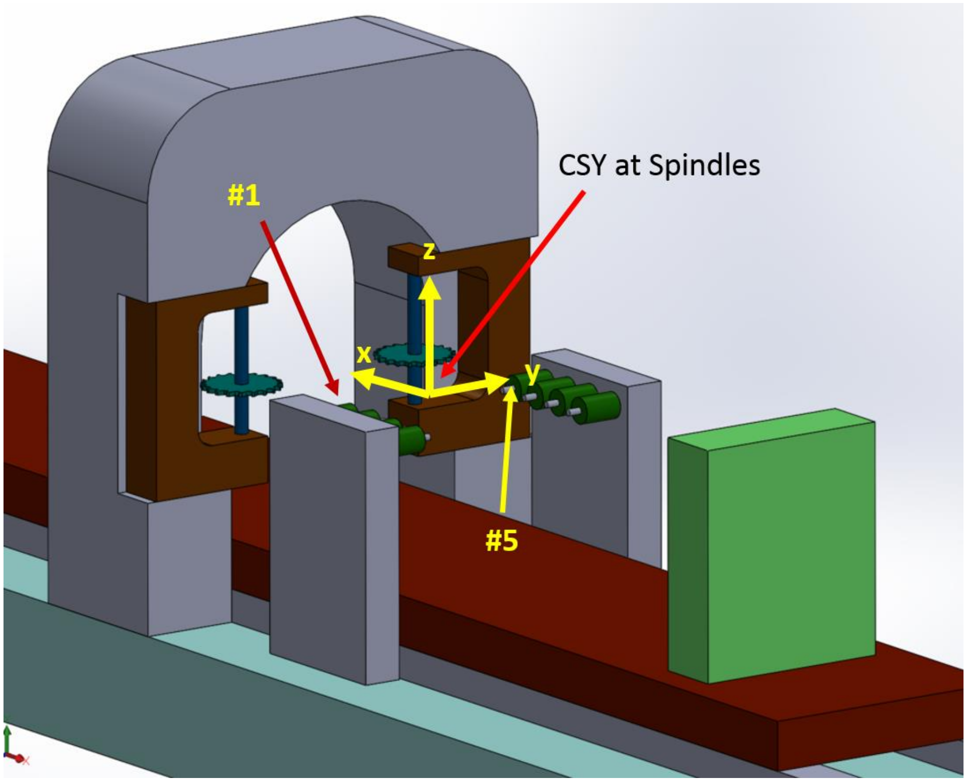

FIGURE 92: Slotter coordinate system.

Determining the centerline shape was done by measuring multiple arcs throughout the entire length of the rotor body as it passed by the auxiliary spindles, similar to what is shown in FIGURE 93. Measurements were first taken starting at the EE of the rotor and then at distances ranging between 36”- 72”, depending on where the previously measured arc was relative to the cutting wheels. A sampling density for each arc ranged anywhere from 10-20 points, depending on which section of the rotor body was measured (e.g. journals, barrel, etc.) To characterize the centerline thoroughly, measurements were taken on both sides of the rotor at approximately the same location in the *x*-direction so the opposing arc measurements resembled more of a semi-circle sampling pattern. Additionally, having two separate sets of measurements from both sides of the rotor allowed for the opportunity to compare whether the results from a single-sided measurement differed significantly from a measurement composed of two-sided data.

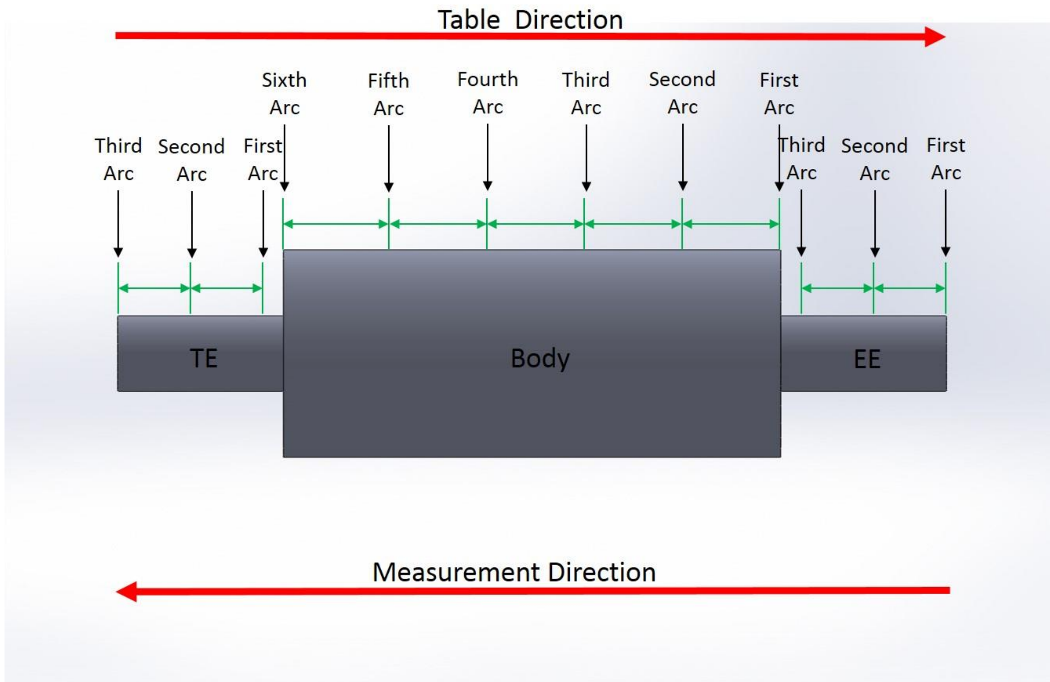

FIGURE 93: Measurement strategy of rotor body.

5.2.2 Measurement Environment and Setup

The shop floor thermal conditions are regulated at 74°±4°F with very good consistency throughout so ambient thermally-induced errors are minimized. Due to the material removal rate of the manufacturing process, copious amounts of cutting lubricant are used which leave the work area and rotor in less-than desirable measurement condition. Before setup and measurement are taken, all surfaces that are to be probed were cleaned to remove as much oil, grime and other particulates as possible. Also, any chip debris was removed using a high-pressure air hose. Great care was taken to ensure that these extrinsic factors were minimized to limit the influence on the measurements.

A network of reference points was strategically setup to minimize the effect of data fusion and drift from the relocation of the laser tracker as well as to capture any influences from the machine tool as the measurements were collected. The laser tracker was positioned *inside* the reference point network which should have minimal effect on the best-fit transformation error calculation. The physical location of the laser tracker was on top the auxiliary spindle bank which had a very rigid platform where the magnetic base of the laser tracker could be secured. FIGURE 94 shows a screenshot of what the measurement setup looked like in Spatial Analyzer as well as where the work-piece coordinate system is located.

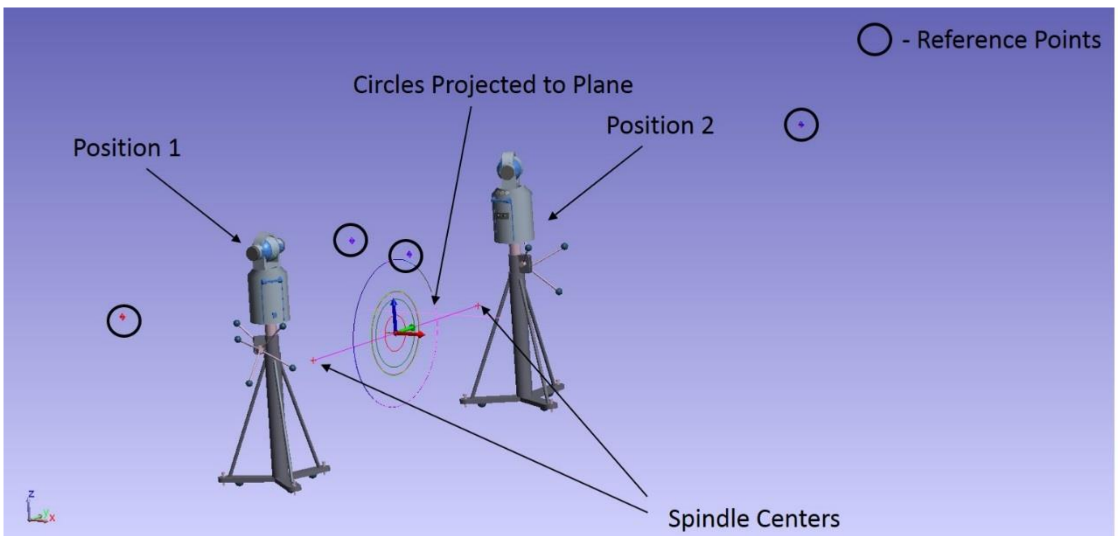

FIGURE 94: Measurement setup in spatial analyzer.

5.2.3 Measurement Results and Uncertainty

After completion of the measurements, each individual set of measurements was evaluated using a least-squares fit. A physical point of the center of each arc was generated in Spatial Analyzer, which represented a specific point on the centerline of the rotor at a location *x*. Upon plotting the measurement results, the centerline of the rotor exhibited a "banana shape" where the ends have the largest departure from zero as shown in FIGURE

95. This results was expected given the “simply-supported” nature of the alignment setup and the majority of the mass located in the rotor barrel. EE1 is the largest error and rightfully so with that part of the rotor free. TE3 is a fixed end which is attached to a horizontal indexer used to rotate the rotor for slot cutting, however there is still a noticeable error from the zero-centerline which is greater than 0.001” (25 μm). The centerline through the barrel of the rotor was relatively straight and did not show any effect from gravity. This can be attributed to the elimination of the sag when the center jacks are adjusted.

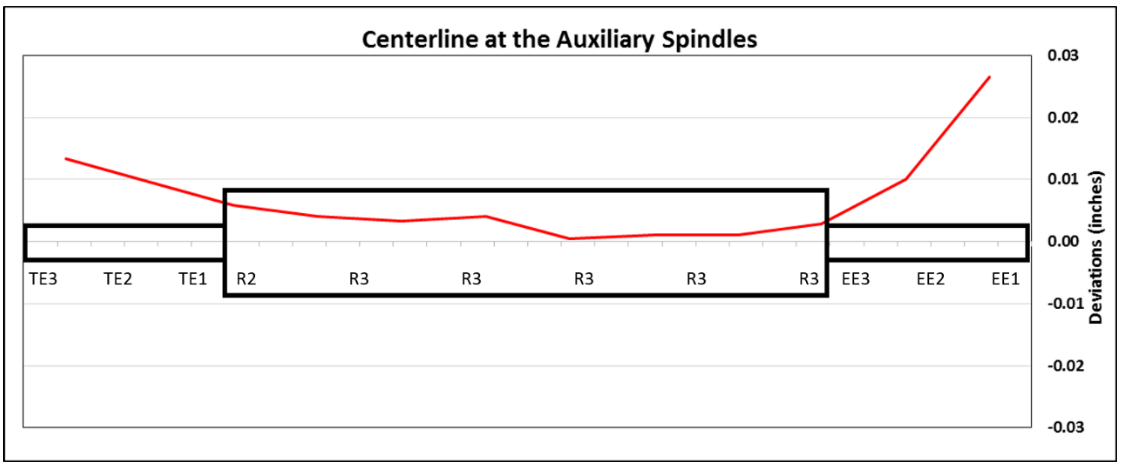

FIGURE 95: Shape of the rotor centerline at the auxiliary spindles.

When estimating the uncertainty in the measurements, the greatest source of error was in the measurement themselves. An additional influence considered is the data fusion error (i.e. point stitching) since the measurement results are a combination of the measurements from both sides of the rotor. As was mentioned earlier, this influence was small due to the laser tracker being positioned *inside* the network of reference points but a maximum error of 0.0006” (15 μm) was determined. Sag was already corrected and the temperature is assumed to expand uniformly since the material is a single piece of material. FIGURE 96 shows the uncertainty in each of the points measured where the error bars represent a 95% confidence level. The largest of the uncertainty estimates is 0.003” (75 μm) therefore it is concluded that the measurements of the centerline are accurately represented.

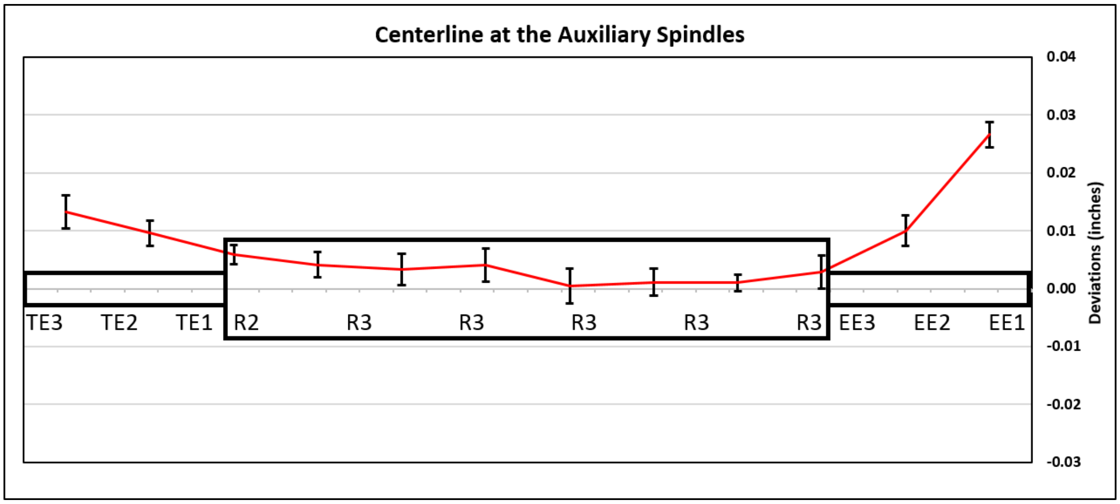

FIGURE 96: Uncertainty of the rotor centerline at the auxiliary spindles.

CHAPTER 6: CONCLUSIONS AND FUTURE WORK

6.1 Conclusions

A process was developed and implemented for evaluation methods used to determine the task-specific measurement uncertainty for industrial measurements. Primarily, the development of methods for assessment of the measurement uncertainty where the different construction of the instrument, operational environments and nature of the inspected work-piece were considered. A procedural view of the experimental evaluations was performed on multiple large-scale work-pieces, namely an aluminum cylinder, turbine exhaust muffler, invar ball-bar length standard, a helicopter rotor yoke and a flexible artifact.

Each was calibrated with a large-scale, high accuracy CMM. Next, each calibrated work-piece was re-measured using the available portable CMMs, where for the work in this dissertation were laser trackers and AACMMs, in typical industrial environments and conditions. After the completion of the measurements, expanded uncertainties were estimated for each of the measurands with 95% confidence and a comparison in the form of a performance statistic was calculated to determine if there was satisfactory agreement between the reference measurements and industrial measurements thus determining whether the industrial measurements were acceptable. It was shown that the process and evaluation methods developed in this work showed satisfactory comparisons with the reference measurements.

Agreement with measurands of length and size was unanimous throughout all of the work-pieces that had measurands of this nature, thus validating the methodologies. Angles showed good agreement, especially in the 2D case where the angle between two lines was the measurand. As for measurands such as form error and true positions, the results were mixed. If a large uncertainty was estimated or a poor estimate of the measurement result was determined, then the E_N value would be large and result in unsatisfactory comparison to the reference measurements. It seems that the best-course of action in consistently estimating the measurement uncertainties for measurands of these types with the highest confidence is through simulation.

Effects from extrinsic influences on the measurements were also investigated, in specific the effects of gravitational sag and non-uniform work-piece temperature. The effects from gravitational sag was investigated by measuring the centerline of a long, flexible artifact in both a simply-supported and cantilever setup. Predictive models of the centerline were developed using Euler-Bernoulli beam theory and comparisons with the measured values were carried-out. It was determined that the gravity had little effect on the simply-supported results as most of the uncertainty came from the measurement process. However, there was noticeable effect on the cantilever measurements as the uncertainty was greater the further away from the fixed end, as predicted. This is an example of uncertainty estimation for a very specific measuring task, where the fixturing method must be considered, as it influences the uncertainty.

Experiments were conducted on the aluminum cylinder in estimating the influence of non-uniform temperature distributions by introducing a heat source (heat tape) over a small surface area over the entire length of the work-piece. Since a predictive model is mathematically-intense, FEA predictions were used as a baseline for observing the effect of the heat source on the work-piece centerline. Comparing the FEA predictions to the experimental measurements showed similar shapes of the centerline but were biased. With the effort needed to control the heat generation, it was determined that this metric of testing was not ideal for larger work-pieces. Overall, FEA analysis is the preferred method for testing of the influence from non-uniformity in the work-piece temperature.

Two applications of the methodologies developed in this dissertation were discussed in the form of case-studies. Each measurand of work-piece in the case study was described in detail as well as how it was realized. Expanded uncertainty estimates with a 95% coverage were determined for each measurand.

6.2 Future Work

Further investigation into the measurement uncertainty of measurands such as form error and tolerances should be addressed with emphasis on the error sources that attribute to the measurement uncertainty to get a better understanding of the fundamental issues when addressing such measurands. Another investigation would be estimating the measurement uncertainties of measurands through the use of software, such as Metrosage Pundit/CMM which has the capability to model the entire CMM, probing system, measurement strategy, and some extrinsic factors. Another area would be on the effect from gravity on more complicated geometries seen in traditional industrial manufacturing such as turbine blades or airplane components. Also, more adequate testing or experiments to investigate the effect of work-piece temperature non-uniformity. Lastly, an investigation of the task-specific measurements and uncertainties of measurements taken with a laser scanner and high-density point clouds.

REFERENCES

[1] R. G. Wilhelm, R. J. Hocken and H. Schwenke, "Task-Specific Uncertainty in Coordinate Measement," *CIRP Annals - Manufacturing Technology,* vol. 50, no. 2, pp. 553-563, 2001.

[2] "ASME Y14.5-1994: Dimensioning and Tolerancing," American Society of Mechanical Engineering, 1994.

[3] "JCGM 200:2012 - International Vocabulary of Metrology - Basic and General Concepts and Associated Terms (VIM)," BIPM, 2012.

[4] "JCGM 100:2008 - Evaluation of Measurement Data - Guide to the Expression of Uncertainty in Measurement," BIPM, 2008.

[5] L. Kirkup and B. Frenkel, An Introduction to Uncertainty in Measurement Using The GUM, 1st ed., New York: Cambridge University Press, 2006.

[6] B. Taylor and C. Kuyatt, "NIST Technical Note 1297: Guidelines for Evaluating and Expressing the Uncertainty of NIST Measurement Results," NIST, 1994.

[7] R. J. Hocken and P. H. Pereira, Coordinate Measuring Machines and Systems, 2nd ed., CRC Press, 2011.

[8] H. Schwenke, W. Knapp, H. Haitjema, A. Weckermann, R. Schmitt and F. Delbressine, "Geometric Error Measurement and Compensation of Machines - An Update," *CIRP Annals - Manufacturing Technology,* vol. 57, no. 2, pp. 660-675, 2008.

[9] J. Bryan, "International Status of Thermal Error Research," *CIRP Annals - Manufacturing Technology,* vol. 39, no. 2, pp. 645-656, 1990.

[10] A. Weckerman, M. Knauer and H. Kunzmann, "The Influence of Measurement Strategy on the Uncertainty of CMM-Measurements," *CIRP Annals - Manufacturing Technology,* vol. 47, no. 1, pp. 451-454, 1998.

[11] L. Uriate, M. Zatarain, D. Axinte, J. Yague-Fabra, S. Ihlenfeldt, J. Eguia and A. Olarra, "Machine Tools for Large Parts," *CIRP Annals - Manufacturing Technology,* vol. 62, pp. 731-750, 2013.

[12] R. Edgeworth and R. Wilhelm, "Measurement Uncertainty Dure to Work-Piece Error Interaction with Sampling Period," in *Maching Impossible Shapes*, New York, Springer Science, 1999, pp. 196-200.

[13] B. Muralikrishnan and J. Raja, Computational Surface and Roundness Metrology, London: Springer, 2009.

[14] C. Porta and F. Waldele, "Testing of Three Coordinate Measuring Machine Evaluation Algortihms," PTB, 1986.

[15] T. Hopp and M. Levenson, "Performance Measures for Geometric Fitting in the NIST Algorithm and Evaluation Program for Coordinate Measuring Machines," *Journal of Research of NIST,* vol. 100, no. 5, pp. 563-574, 1995.

[16] C. Shakarji, "Least-Squares Fitting Algorithms of the NIST Algorithm Testing System," *Journal of Research of NIST,* vol. 103, no. 6, pp. 633-641, 1998.

[17] I. Lira, Evaluating The Measurement Uncertainty: Fundamentals and Practical Guidance, 1st ed., London: CRC Press, 2002.

[18] P. Lingard, M. Purss, C. Sona and E. Thwaite, "Length-Bar and Step-Gauge Calibration Using a Laser Measurement Sysem with a Coordinate Measuring Machine," *CIPR Annals - Manufacturing Technology,* vol. 40, no. 1, pp. 515-517, 1991.

[19] E. Trapet and F. Waldele, "The Virtual CMM Concept," *Advanced Mathematical Tools in Metrology II,* pp. 238-247, 1996.

[20] S. Phillips, B. Borchardt, D. Sawyer, W. Estler, D. Ward, E. Eberhardt, M. Levenson, M. McClain, B. Melvin, T. Hopp and Y. Shen, "The Calculation of CMM Measurement Uncertainty via The Method of Simulation by Constraints," in *American Society for Precision Engineering*, 1997.

[21] A. Balsamo, M. Di Ciommo, R. Mugno, B. Rebaglia, E. Ricci and R. Grella, "Evaluation of CMM Uncertainty Through Monte Carlo Simulation," *CIRP Annals - Manufacturing Technology,* vol. 48, no. 1, pp. 425-428, 1999.

[22] Z. Humienny, "State of Art in Standardization in GPS Area," *CIRP Journal of Manufacturing Science and Technology,* vol. 2, no. 1, pp. 1-7, 2009.

[23] E. Trapet, M. Calzada, P. Cimadomo, L. De Chiffre, F. Hartig, T. Hageney, K. Kniel, E. Prieto, T. Ristonen, E. Savio, D. Serciat, P. Skalnik, H. Tikka and V. Zeleny, "EASYTRAC Final Report," Unimetrik, Vitoria, Spain, 2004.

[24] D. Flack, "Measurement Good Practice Guide No. 130: Co-ordinate Measruing Task-specific Measreument Uncertainty," National Physical Laboratory, 2013.

[25] "ISO/TS 15530-1: Geometrical Product Specification (GPS) - Coordinate Measuring Machines (CMM): Techniques for Evaluation of the Uncertainty of Measurement - Part 1: Overview and Metrological Characteristics," ISO, 2013.

[26] "ISO/TS 15530-2: Geometrical Product Specification (GPS) - Coordinate Measuring Machines (CMM): Techniques for Evaluation of the Uncertainty of Measurement - Part 2: Use of Multiple Measurement Strategies in Measurement of Artifacts," ISO (Unpublished), 2007.

[27] E. Trapet, E. Savio and L. De Chiffre, "New Advances in Traceabilty of CMMs for Almost the Entire Range of Industrial Dimensional Metrology Needs," *CIRP Annals - Manufacturing Technology,* vol. 53, no. 1, pp. 433-438, 2004.

[28] E. Savio, N. Hansen and L. De Chiffre, "Approaches to the Calibration of Freeform Artefacts on CMMs," *CIRP Annals - Manufacturing Technology,* vol. 51, no. 1, pp. 433-436, 2002.

[29] E. Savio and L. De Chiffre, "An Artefact for Traceable Freeform Measurements on Coordinate Measuring Machines," *Precision Engineering,* vol. 26, no. 1, pp. 58-68, 2002.

[30] "ISO/TS 15330-3: Geometrical Product Specification (GPS) - Coordinate Measuring Machines (CMM): Techniques for Evaluation of the Uncertainty of Measurement - Part 3: Use of Calibrated Workpieces or Measurement Standards," ISO, 2011.

[31] S. Camignato and L. De Chiffre, "A New Mehod for Thread Calibration on Coordinate Measuring Machines," *CIRP Annals - Manufacturing Technology,* vol. 52, no. 1, pp. 477-450, 2003.

[32] "ISO/TS 15530-4: Geometrical Product Specification (GPS) - Coordinate Measuring Machines (CMM): Techniques for Evaluation of the Uncertainty of Measurement - Part 4: Evaluating Task-Specific Measurement Uncertainty Using Simulation," ISO, 2008.

[33] F. Aggogeri, G. Barbato, E. Barini, G. Genta and R. Levi, "Measurement Uncertainty Assessment of CMMs by Simulation and Planned Experimentation," *CIRP Journal of Manufacturing Science and Technology,* vol. 4, no. 1, pp. 51-56, 2011.

[34] J. Kruth, N. Van Gestel, P. Bleys and F. Welkenhuyzen, "Uncertainty Determination for CMMs by Monte Carlo Simulation Intergrating Form Deviations," *CIRP Annals - Manufacturing Technology,* vol. 58, no. 1, pp. 463-466, 2009.

[35] J. Beaman and E. Morse, "Experimental Evaluation of Software Estimates of Task-specific Measurement Uncertainty for CMMs," *Precision Engineering,* vol. 34, no. 1, pp. 28-33, 2010.

[36] "ASME B89.4.19-2006: Performance Evaluation of Laser-Based Spherical Coordinate Measuring Machines," American Society of Mechanical Engineers, 2006.

[37] "ASME B89.4.22-2004: Methods for Performance Evaluation of Articulated Arm Coordinate Measuring Machines," American Society of Mechanical Engineers, 2004.

[38] "VDI/VDE 2617-9: Accuracy of Coordinate Measuring Machines - Charateristics and Their Reverification - Acceptance and Reverification Tests for Arrticulated Arm Coordinate Measuring Machines," Verlag des Verenis Deutcher Ingenieure, 2009.

[39] "VDI/VDE 2617-10: Accuracy of Coordinate Measuring Machines - Charateristics and Their Reverification - Acceptance and Reverification Tests Laser Trackers," Verlag des Verenis Deutcher Ingenieure, 2011.

[40] P. Tullar, J. Grant, J. Patten and R. Hocken, "Error Modeling and Correction of a Laser Tracker," UNC-Chalotte, Charlotte, 1990.

[41] R. Loser and S. Kyle, "Alignment and Field Check Procedure for the Leica Laser Tracker LTD 500," in *Boeing Large-scale Optical Seminar,* Seattle, 1998.

[42] B. Muralikrishnan, D. Sawyer, C. Blackburn, S. Phillips, B. Borchardt and W. Estler, "ASME B89.4.19 Performance Evaluation Tests and Geometric Misalignments in Laser Trackers," *Journal of Research of the National Institute of Standards and Technology,* vol. 114, pp. 21-35, 2009.

[43] B. Hughes, A. Forbes, A. Lewis, W. Sun, D. Veal and K. Nasr, "Laser Tracker Error Determination Using a Network of Measurement," *Measurement Science Technology,* vol. 22, no. 4, 2011.

[44] J. Conte, J. Santolaria, A. Majarena, A. Brau and J. Aguilar, "Identification and Kinematic Calculation of Laser Tracker Errors," *Procedia Engineering,* vol. 63, pp. 379-387, 2013.

[45] J. Yang, G. Li, J. Wu, J. Gong, J. Wang and M. Zhang, "Efficient Methods for Evaluating Task-specific Uncertainty in Laser Tracking Measurements," *Journal of Metrology, Society of India,* 2015.

[46] M. Puttock, "Large-scale Metrology," *CIRP Annals - Manufacturing Technology,* vol. 27, no. 1, pp. 351-356, 1978.

[47] W. Estler, K. Edmundson, G. Peggs and D. Parker, "Large-Scale Metrology - An Update," *CIRP Annals - Manufacturing Technology,* vol. 51, no. 2, pp. 587-609, 2002.

[48] M. Rubeo, "A Feasibility Study on the Application of Laser Tracking Interferometers for Machine Tool Error Mapping (Thesis)," The University of North Carolina at Charlotte, Charlotte, 2014.

[49] S. Sandwith, "Thermal Stability of Laser Tracking Interferometer Calibration," in *SPIE, Three-Dimensional Imaging, Optical metrology and Inspection V*, Boston, 1999.

[50] U. Mutilba, G. Kortaberria, A. Olarra, A. Gutierrez, E. Gomez-Acedo and M. Zubieta, "Performance Calibration of Articulated Arm Coordinate Measuring Machine," *Procedia Engineering,* vol. 63, pp. 720-727, 2013.

[51] J. Santolaria, J. Aguilar, J. Yague and J. Pastor, "Kinematic Parameter Estimation Technique for Calibration and Repeatability Improvement of Articulated Arm Coordinate Measuring Machines," *Precision Engineering,* vol. 32, no. 4, pp. 251-268, 2008.

[52] J. Santolaria, A. Brau, J. Velazquez and J. Aguilar, "A Self-centering Active Probing Technique for Kinematic Parameter Identification and Verification of Articulated Arm Coordinate Measuring Machines," *Measurement Science and Technology,* vol. 21, no. 5, 2010.

[53] J. Sladek, K. Ostrowska and A. Gaska, "Modeling and Identification of Errors of Coordinate Measuring Arms," *Measurement,* vol. 46, pp. 667-679, 2013.

[54] R. Furutani, K. Shimojima and K. Takamasu, "Parameter Calibration for Non-Cartesian CMM," *VDI Berichte,* pp. 317-326, 2004.

[55] D. Ye, R. S. Che and Q. Huang, "Calibration for Kinematic Parameters of Articulated CMM," in *Second International Symposium on Instrumentation Science and Technology*, 2002.

[56] X. Li, B. Chen and Z. Qiu, "The Calibration and Error Compensation Techniques for an Articulated Arm," *Measurement*, vol. 46, pp. 603-609, 2013.

[57] H. Hamana, M. Tominaga and M. Ozaki, "Calibration of Articulated Arm Coordinate Measuring Machine Considering Measuring Posture," *International Journal of Automated Technology,* vol. 5, pp. 109-114, 2010.

[58] F. Romdhani, F. Hennebelle, M. Ge, P. Jullion, R. Coquet and J. F. Fontaine, "Methodology for the Assessment of Measuring Uncertainties of Articulated Arm Coordinate Measuring," *Measurement Science and Technology,* vol. 25, 2014.

[59] J. Santolaria, J. A. Yague, R. Jimenez and J. Aguilar, "Calibration-based Thermal Error Model for Articulated Arm Coordinate Measuring Machines," *Precision Engineering,* vol. 33, pp. 476-485, 2009.

[60] B. Muralikhrishnan, M. Ferrucci, D. Sawyer, G. Gerner, G. Lee, C. Blackburn, S. Phillips, P. Petrov, Y. Yakovlev, A. Astrelin, S. Milligan and J. Palmateer, "Volumetric Performance Evaluation of a Laser Scanner Based on Geometric Error Model," *Precision Engineering,* vol. 40, pp. 139-150, 2015.

[61] D. Lichti, "Error Modelling, Calibration and Analysis of an AM-CW Terrestrial Laser Scanner," *ISPRS Journal of Photogrammetry & Remote Sensing,* vol. 61, pp. 307-324, 2007.

[62] J. Chow, D. Lichti and W. Teskey, "Accuracy Assessment of the FARO Focus and Leica HDS6100 Panoramic-type Terrestrial Laser Scanners Through Point-based and Plane-based User Self-calibration.," in *Proceedings of the FIG Working Week*, Rome, 2012.

[63] M. Abbas, D. Lichti, A. Chong, H. Setan and Z. Majid, "An On-site Approach for the Self-calibration of Terrestrial Laser Scanner," *Measurement,* vol. 52, pp. 111-123, 2014.

[64] M. Polo, A. Felicisimo, A. Villanueva and J. Martinez del Pozo, "Estimating the Uncertainty of Terrestrial Laser Scanner Measurements," *IEEE Transaction on Geoscience and Remote Sensing,* vol. 50, no. 11, 2012.

[65] T. Nguyen and X. Liu, "Analysis of Error Sources in Terrestrial Laser Scanning," Joint ISPRS Workshop, 2011.

[66] "ISO 10360-2: Geometrical Product Specification (GPS) - Acceptance and Reverification Tests for Coordinate Measuring Machines (CMM) - Part 2: CMMs Used for Measuring Linear Dimensions," ISO, 2009.

[67] "ISO 10360-4: Geometrical Product Specification (GPS) - Acceptance and Reverification Tests for Coordinate Measuring Machines (CMM) - Part 4: CMMs Used in Scanning Mode," ISO, 2000.

[68] "ISO 10360-5: Geometrical Product Specification (GPS) - Acceptance and Reverification Tests for Coordinate Measuring Machines (CMM) - Part 5: CMMs Using Single and Multiple Stylus Contacting Probing Systems," ISO, 2010.

[69] A. Weckenmann, M. Knauer and T. Killmaier, "Uncertainty of Coordinate Measurements on Sheet-metal Parts in the Automotive Industry," *Journal of Materials Processing Technology,* vol. 115, pp. 9-13, 2001.

[70] "ISO/TR 16015:2003 - Geometric Product Specification (GPS) - Systematic Errors and Contributions to Measurement Uncertainty of Length Measurement due to Thermal Influences," ISO, 2003.

[71] W. Knapp, "Circular Test for Three-Coordinate Measuring Machines and Machine Tools," *Precision Engineering,* vol. 5, no. 3, pp. 115-124, 1983.

[72] H. Pahk and J. Kim, "Development of Computer Integrated Systems for Error Diagnosis of a CMM Using Calibrated Mechanical Artefacts," *International Journal of Manchine Tools and Manufacture*, vol. 33, no. 6, pp. 773-790, 1993.

[73] E. Morse and H. Voelcker, "Technical Feature: A Tale of Two Tails," vol. 3, no. 46, 1996.

[74] M. Abramowitz and I. Stegun, Handbook of Mathematical Functions with Formulas, Graphs and Mathematical Tables, New York: Dover Books on Mathematics, 1965.

[75] F. Arenhart, G. Donatelli and M. Porath, "An Experimental Method for Assessing the Contribution of the Production Process Variations to the Task-specific Uncertainty of Coordinate Measurements," *Measurement,* vol. 45, pp. 507-519, 2012.

[76] P. Muller, J. Hiller, J. Dai, J. L. Andreasen, H. Hansen and L. De Chiffre, "Estimation of Measurement Uncertainties in X-ray Computed Tomography Metrology Using the Substitution Method," *CIRP Journal of Manufacturing and Science,* vol. 7, pp. 222-232, 2014.

[77] D. Montgomery and G. Runger, Applied Statistics and Probability for Engineers, Hoboken: Wiley & Sons, 2006.

[78] R. Leach, "Calibration, Traceability and Uncertainty Issues in Surface Texture Metrology," NPL, Teddington, 1999.

[79] F. Hartig and M. Krystek, "Correct Treatment of Systematic Errors for the Evaluation of Measurement Uncertainty," in *Proceedings of 9th International*

Symposium on Measurement Technology and Intelligent Instruments, Saint Petersburg, 2009.

[80] Y.-L. Shen and N. Duffie, "Uncertainties in the Acqusition and Utilization of Coordinate Frames in Manufacturing Systems," *CIRP Annals - Manufacturing Technology,* vol. 40, no. 1, pp. 527-530, 1991.

[81] T. Dorion, "20 C - A Short History of the Standard Reference Temperature for Industrial Dimensional Measurements," *Journal of Research of the National Institute of Standards and Technology*, vol. 112, no. 1, 2007.

[82] D. Swyt, "Uncertainties in Dimensional Measurements Made at Nonstandard Temperatures," *Journal of Research of the National Institute of Standards and Technology,* vol. 99, no. 1, pp. 31-44, 1994.

[83] J. Kruth, P. Vanherck, C. Van den Bergh and B. Schacht, "Interaction Between Workpiece and CMM During Geometrical Quality Control in Non-standard Thermal Conditions," *Precision Engineering,* vol. 26, pp. 93-98, 2002.

[84] "ANSI B89.6.2 - 1973: Temperature and Humidity for Dimensional Measurements," American Society of Mechanical Engineers, 1973.

[85] F. Incropera, D. Dewitt, T. Bergman and A. Lavine, Introduction to Heat Transfer, 5th ed., Wiley, 2007.

[86] B. Chakravarthy, H. Cherukuri and R. Wilhelm, "Prediction of Soakout Time Using Analytical Models," *Precision Engineering,* vol. 26, pp. 15-23, 2002.

[87] D. Sawyer, B. Parry, S. Phillips, C. Blackburn and B. Muralikhrishnan, "A Model for Geometry-dependent Errors in Length Artifacts," *Journal of Research of the National Institute of Standards and Technology,* vol. 117, pp. 216-230, 2012.

[88] S. Phillips, B. Borchardt, T. Doiron and J. Henry, "Properties of Free-standing Ball Bar Systems," *Precision Engineering,* vol. 15, no. 1, pp. 16-24, 1993.

[89] H. Stahl, "Metrology of Large Parts," in *Handbook of Optical Dimensional Metrology,* Boca Raton, CRC Press, 2012, pp. 239-262.

[90] R. C. Hibbeler, Mechanics of Materials, Upper Saddle River: Pearson Prentice Hall, 2007.

[91] W. Young, Roark's Formulas for Stress and Strain, 6th ed., New York: Mcgraw-Hill, 1989.

[92] C. J. Evans, R. J. Hocken and W. T. Estler, "Self Calibration: Reversal, Redundancy, Error Separation and Absolute Testing," in *Annals of CIRP*, 1996.

[93] R. B. Hetnarski and M. R. Eslami, Thermal Stresses - Advanced Theory and Applications, Springer , 2009.

[94] F. Pavese and A. Forbes, Data Modelling for Metrology and Testing in Measurement Science, Boston: Birkhäuser, 2009.

[95] "JCGM 101:2008 - Evlauation of Measurement Data - Supplement 1 to the "Guide to the Expression of Uncertainty in Measurement" - Propagation of Distributions Using a Monte Carlo Method," BIPM, 2008.

[96] "ISO/IEC 17043: Conformity assessment - General requirements for proficiency testing," ISO, 2010.

[97] E. Oberg, F. Jones, H. Horton, H. Ryffel and C. McCauley, Machinery's Handbook, New York: Industrial Press, 2012.

APPENDIX A: LENGTH SHORTENING ERROR DERIVATION

The length error due to bending can be modelled as the difference between the calibrated length and the horizontal projection of the elastic curve. To determine the deflection equation of the, two cantilever models from Appendix A are considered: (i) a uniform, distributed loading $w(x)$ which will mimic the deflection of the artifact due to its own weight, and (ii) a concentered load P at any point which will mimic the weight of the SMR or precision sphere, depending on the measurement instrument being used. The total deflection can then be modelled using the superposition principle or Eq. A.1 below,

$$y(x) = y_{bar}(x) + y_{sphere/nest}(x) \quad \text{(A.1).}$$

Once all the deflection models have been determined, the superposition principle, Eq. A.1 can be used to model the total deflection of the flexible artifact or Eq. A.2

$$y(x) = -\left[\frac{W_1}{24EIL}(x^4 - 4Lx^3 + 6L^2x^2) + \frac{W_2}{6EI}(-x^3 + 3ax^2 + 3a^2x - a^3)\right] \quad \text{(A.2).}$$

Now, taking the derivative with respect to the x-axis is calculated using Eq. A.3 as follows where it has been simplified with a common denominator,

$$\frac{dy}{dx} = \frac{-1}{6EIL}[W_1(x^3 - 3Lx^2 - 3L^2x) - W_2(3Lx^2 + 6aLx - 3a^2L)] \quad \text{(A.3).}$$

Next, substituting the result of Eq. A.4 into Eq. 62 yields the following,

$$\Delta L = -\frac{1}{2}\int_{0}^{L} \left[\frac{-1}{6EIL}[W_1(x^3 - 3L^2x + 3Lx^2) - W_2(3Lx^2 + 6aLx - 3a^2L)]\right]^2 \quad \text{(A.4)}$$

where after integrating from 0 to L and simplification one gets Eq. A.5 or the length shortening error from bending,

$$\Delta L = \frac{-L}{5040E^2I^2}[L^4(507W_1^2 + 497W_1W_2 + 126W_2^2) - aL^3(1302W_1W_2 + 630W_2^2) - a^2L^2(945W_1W_2 - 420W_2^2) + a^3W_2^2(1260L + 630a)] \quad \text{(A.5).}$$

APPENDIX B: INDUSTRIAL MEASUREMENT RESULTS

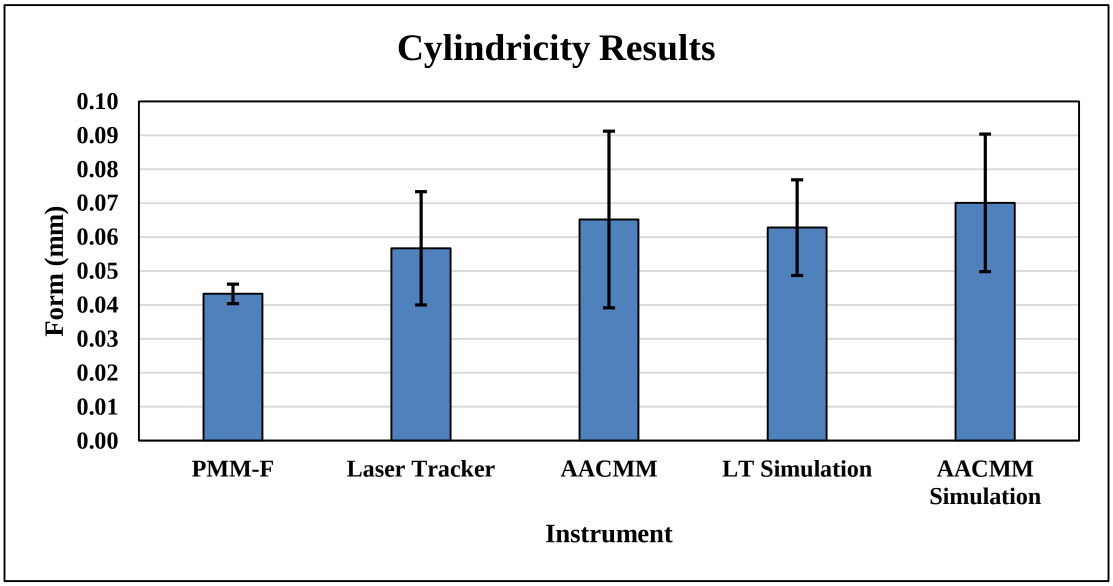

FIGURE 97: Measurement results for the aluminum cylinder cylindricity.

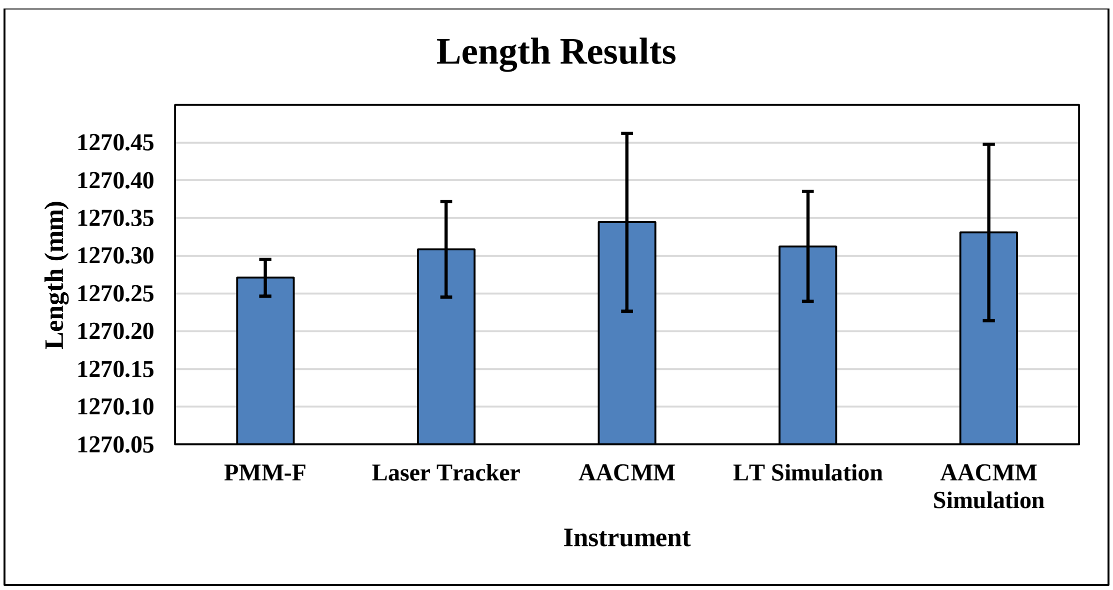

FIGURE 98: Measurement results for the aluminum cylinder length.

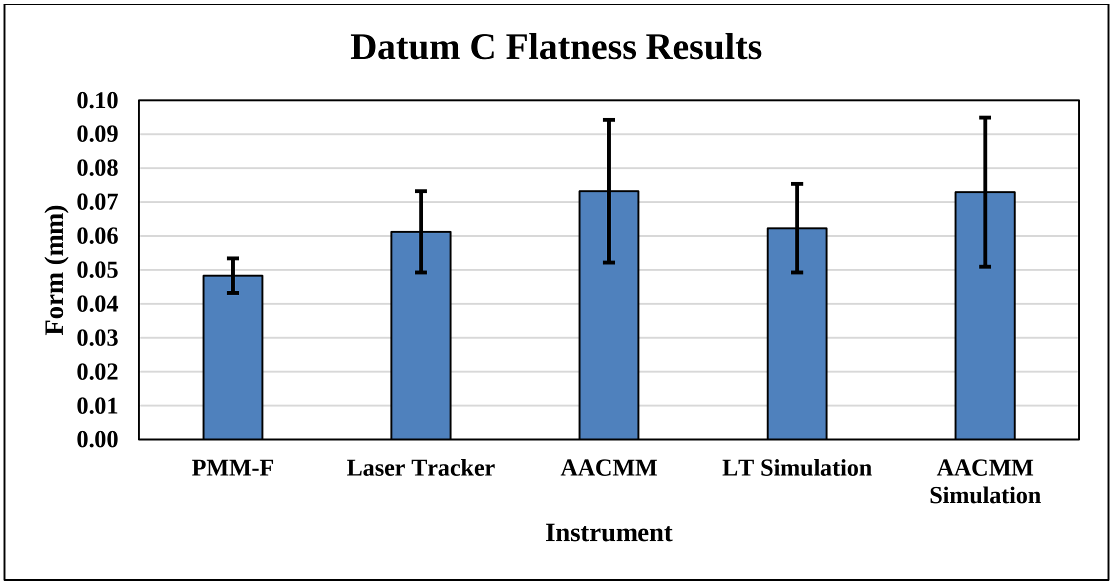

FIGURE 99: Measurement results for the muffler flatness.

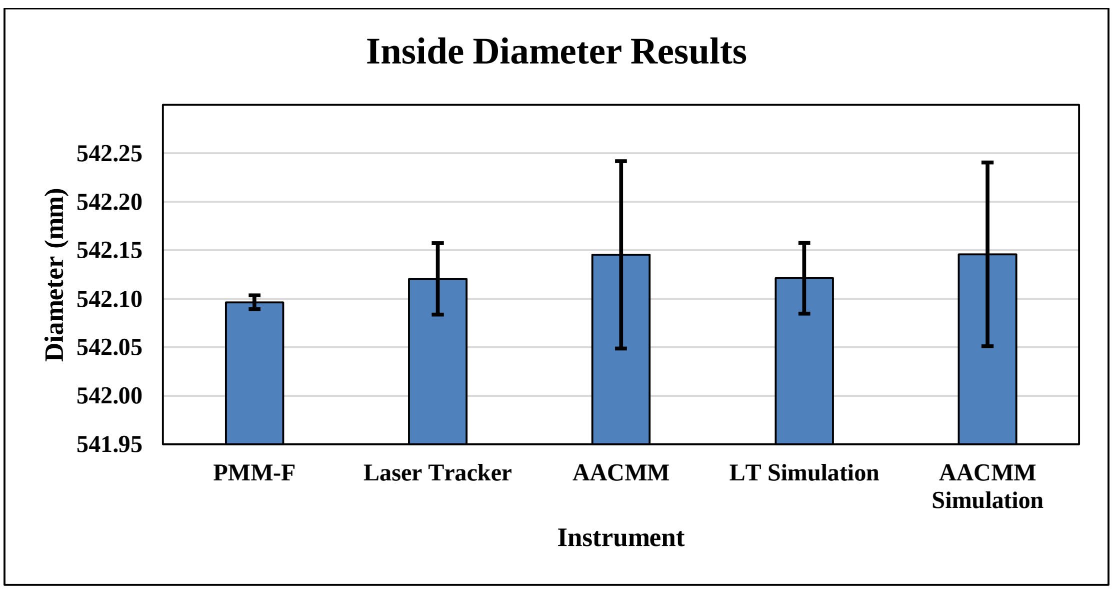

FIGURE 100: Measurement results for the muffler inside diameter.

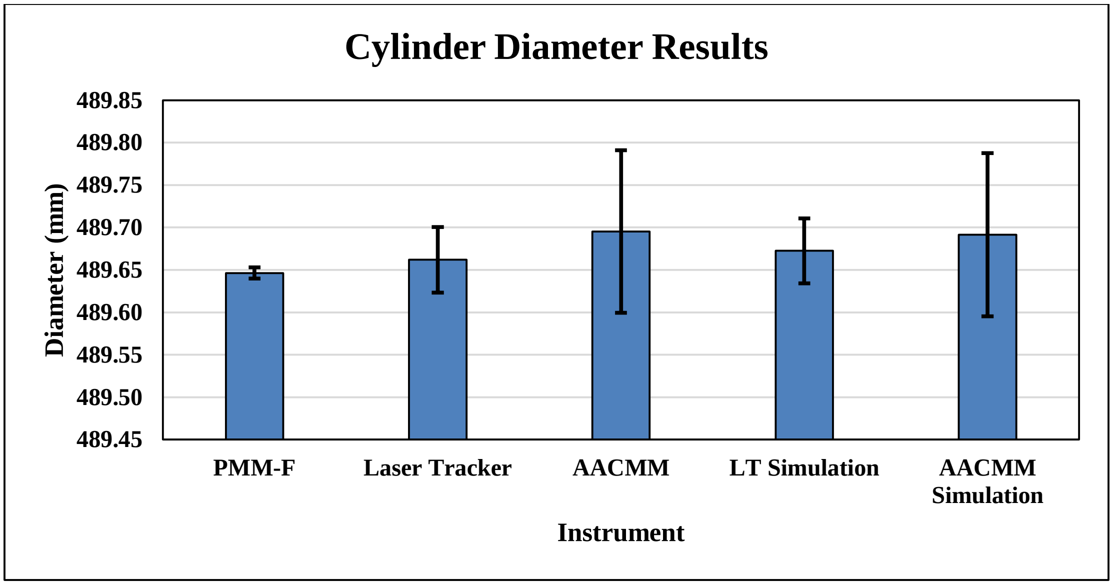

FIGURE 101: Measurement results for the muffler cylinder diameter.

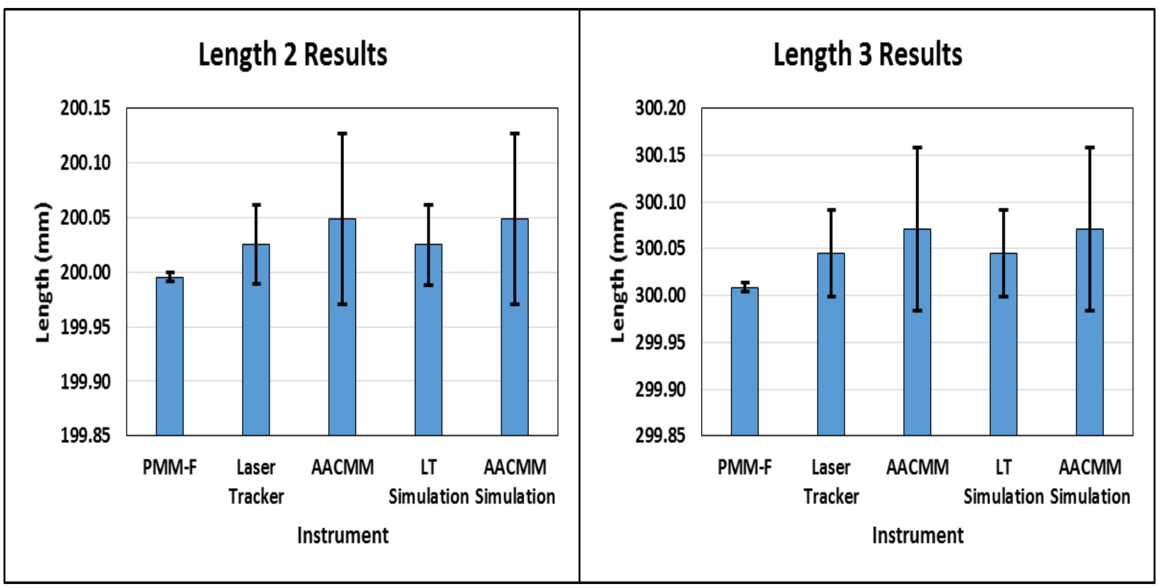

FIGURE 102: Measurement results for the ball-bar, lengths 2 and 3.

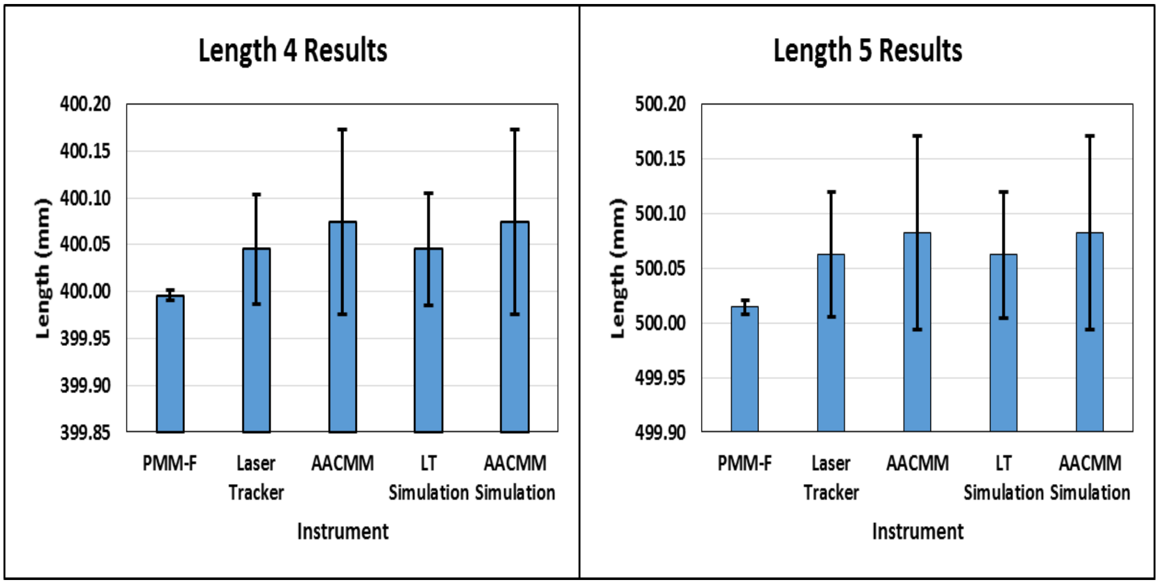

FIGURE 103: Measurement results for the ball-bar, lengths 4 and 5.

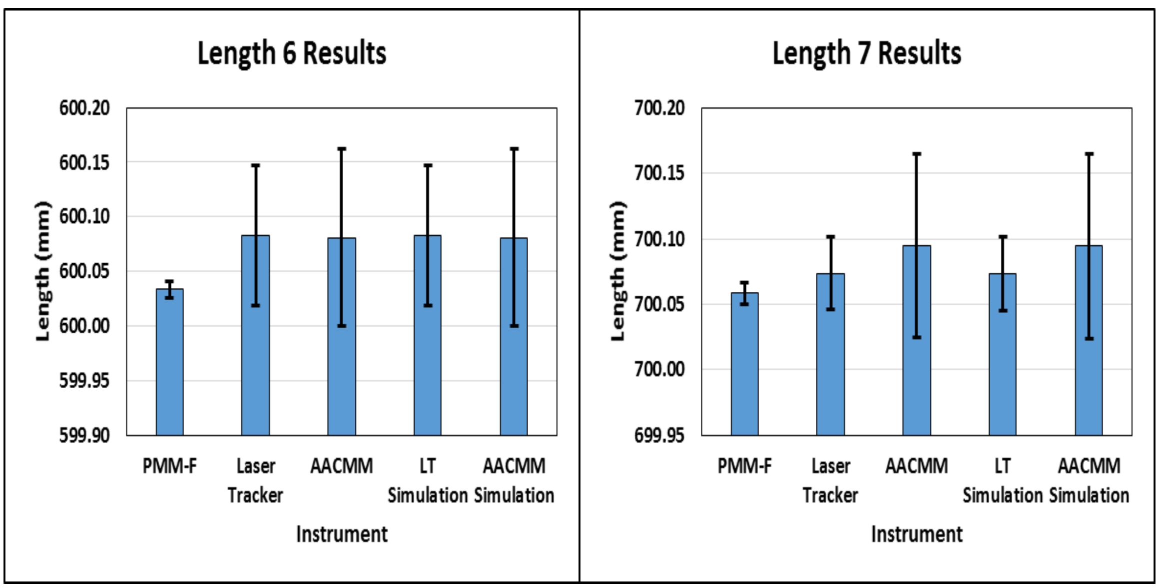

FIGURE 104: Measurement results for the ball-bar, lengths 6 and 7.

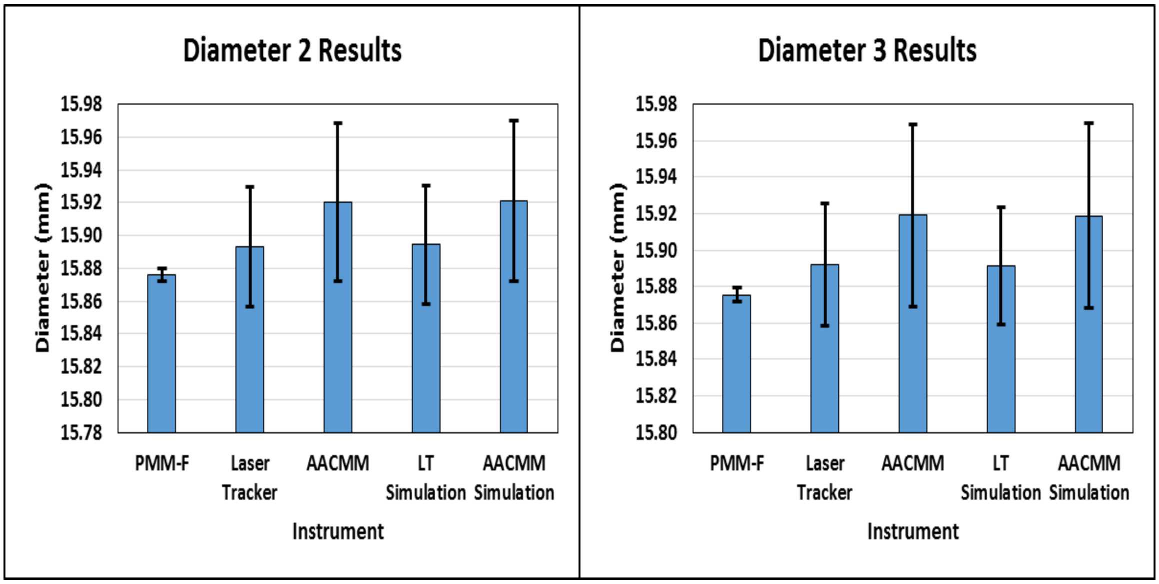

FIGURE 105: Measurement results for the ball-bar, diameters 2 and 3.

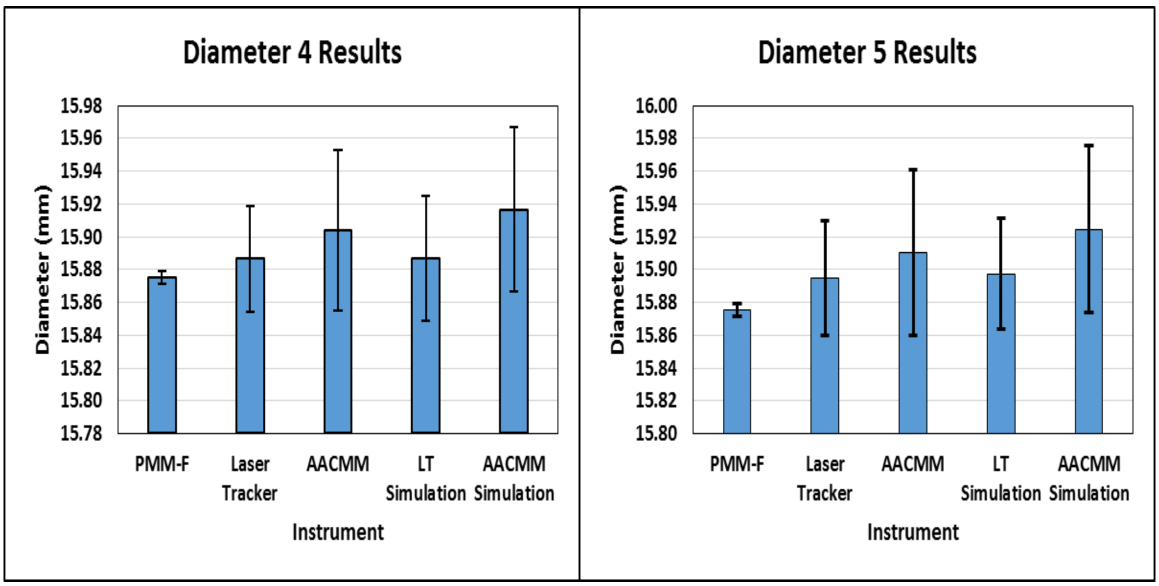

FIGURE 106: Measurement results for the ball-bar, diameters 4 and 5.

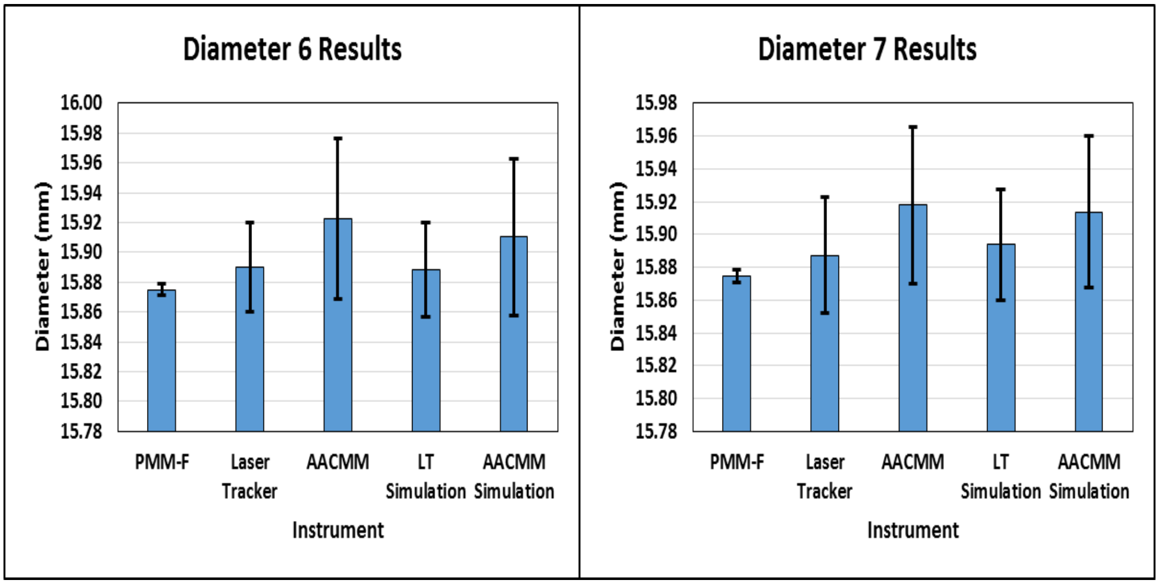

FIGURE 107: Measurement results for the ball-bar, diameters 6 and 7.

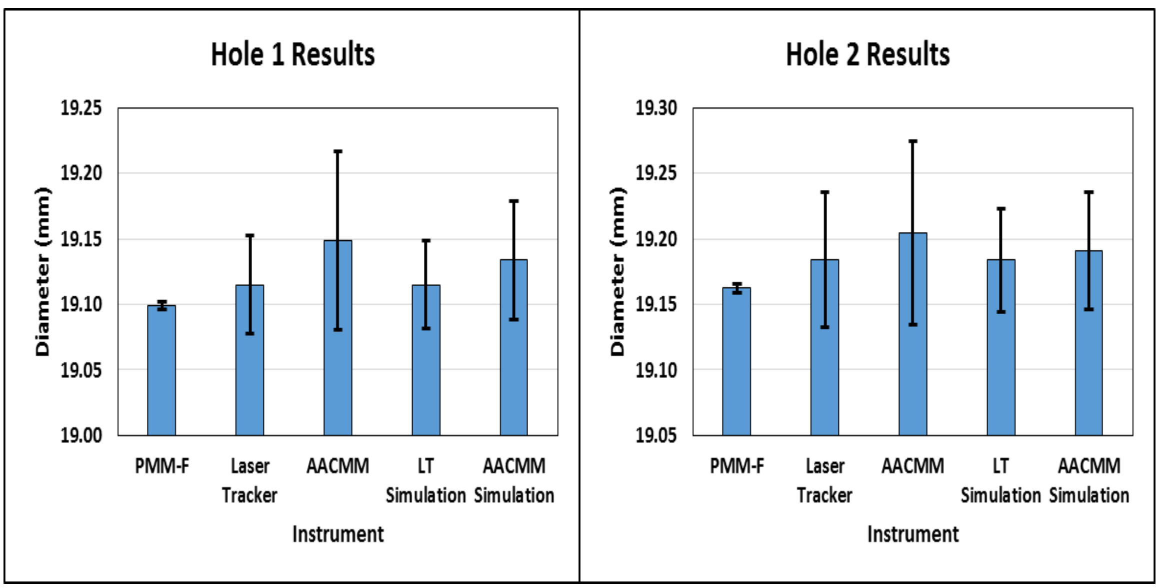

FIGURE 108: Measurement results for rotor yoke diameters, 1 and 2.

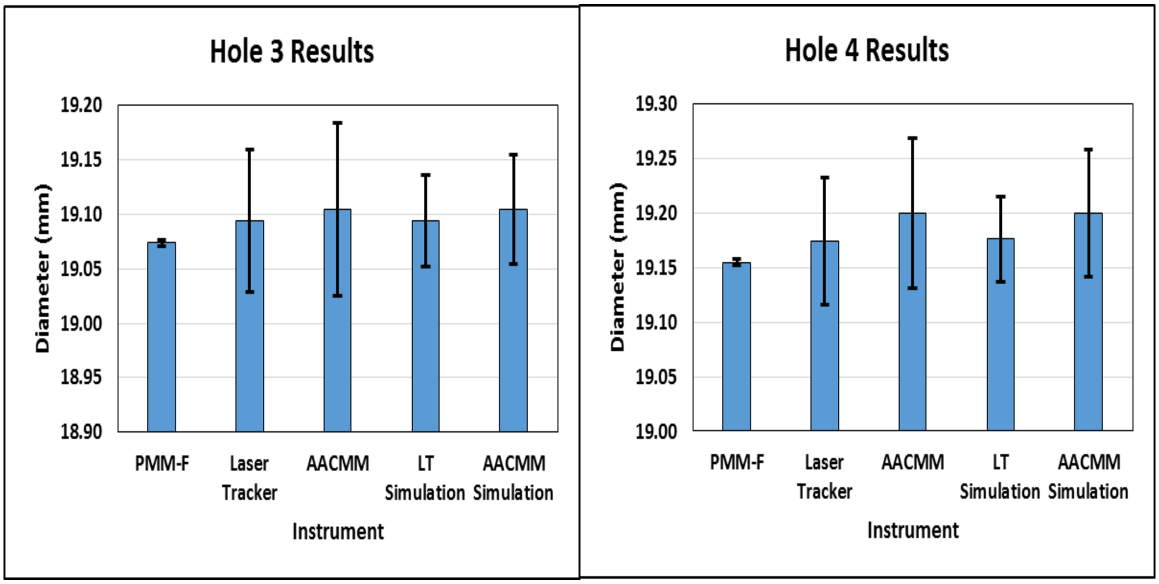

FIGURE 109: Measurement results for rotor yoke diameters, 3 and 4.

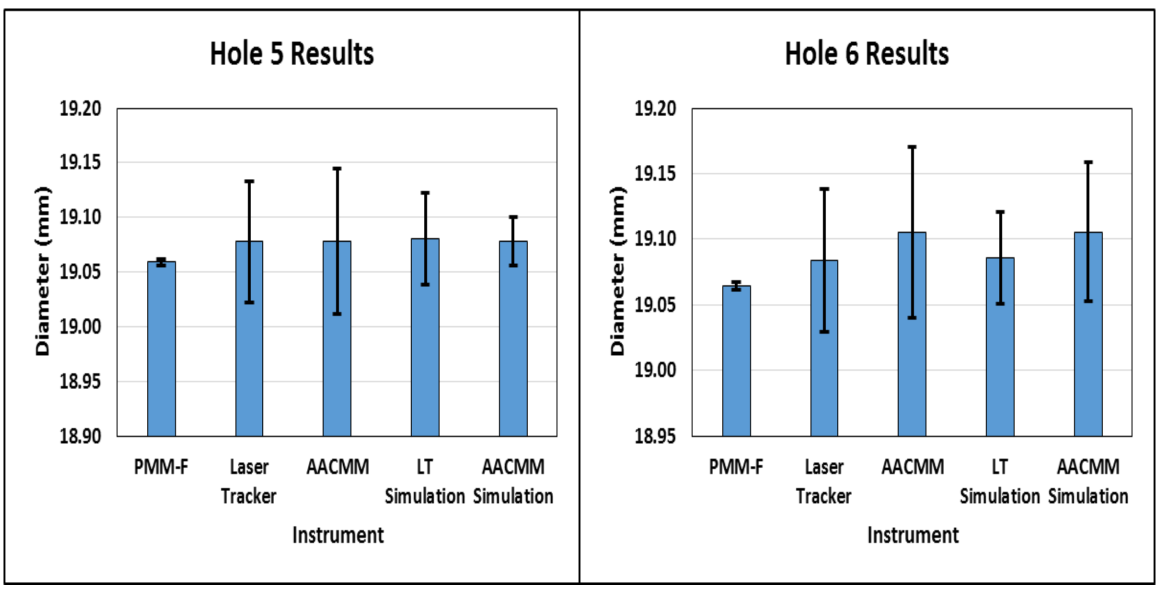

FIGURE 110: Measurement results for rotor yoke diameters, 5 and 6.

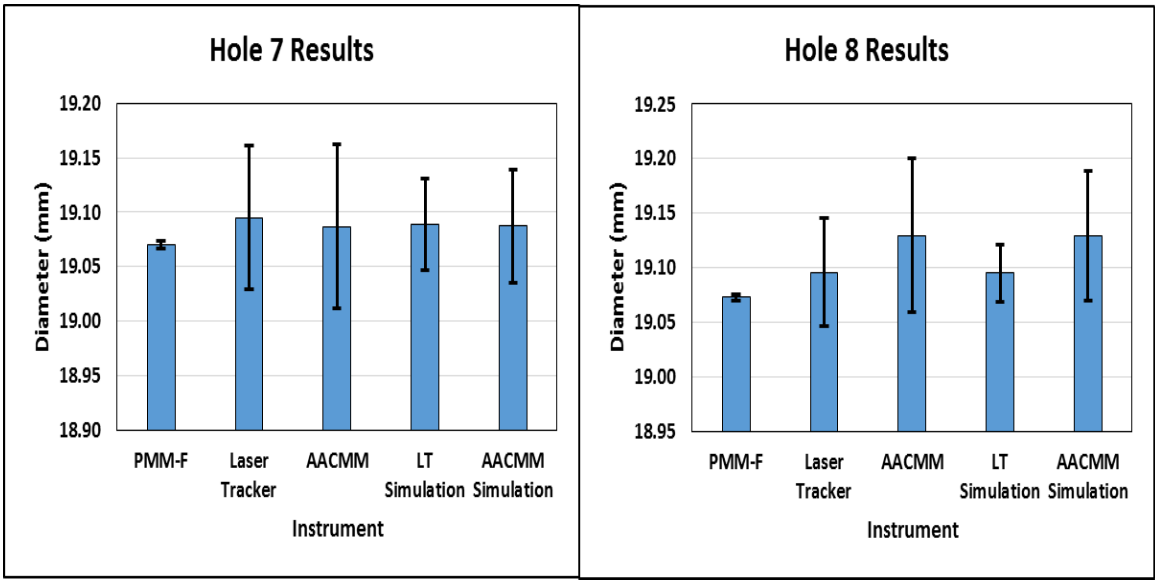

FIGURE 111: Measurement results for rotor yoke diameters, 7 and 8.

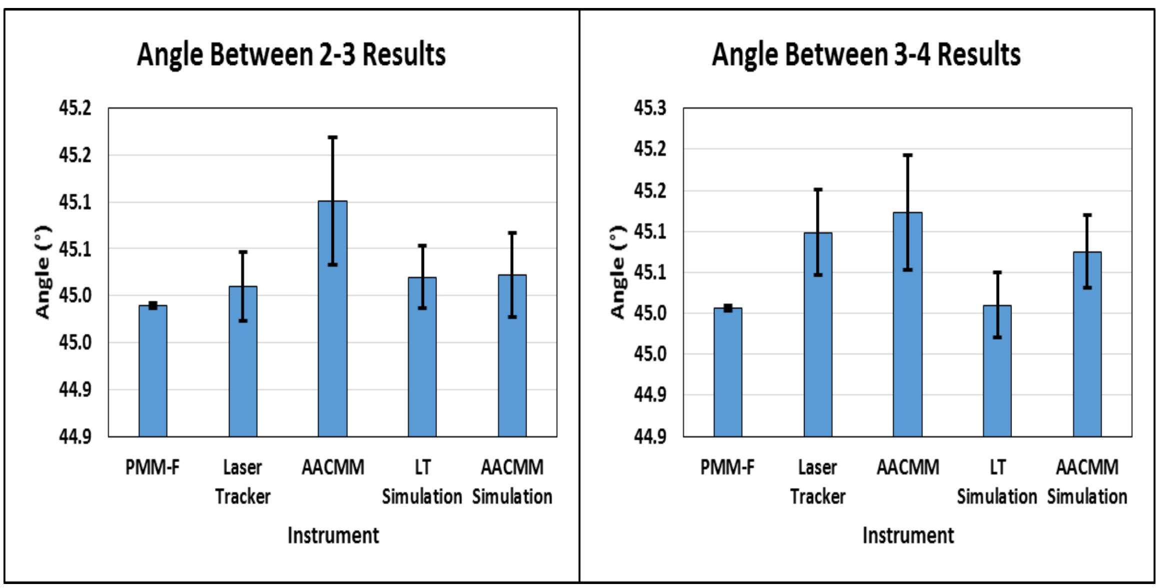

FIGURE 112: Measurement results for rotor yoke angles, 2/3 and 3/4.

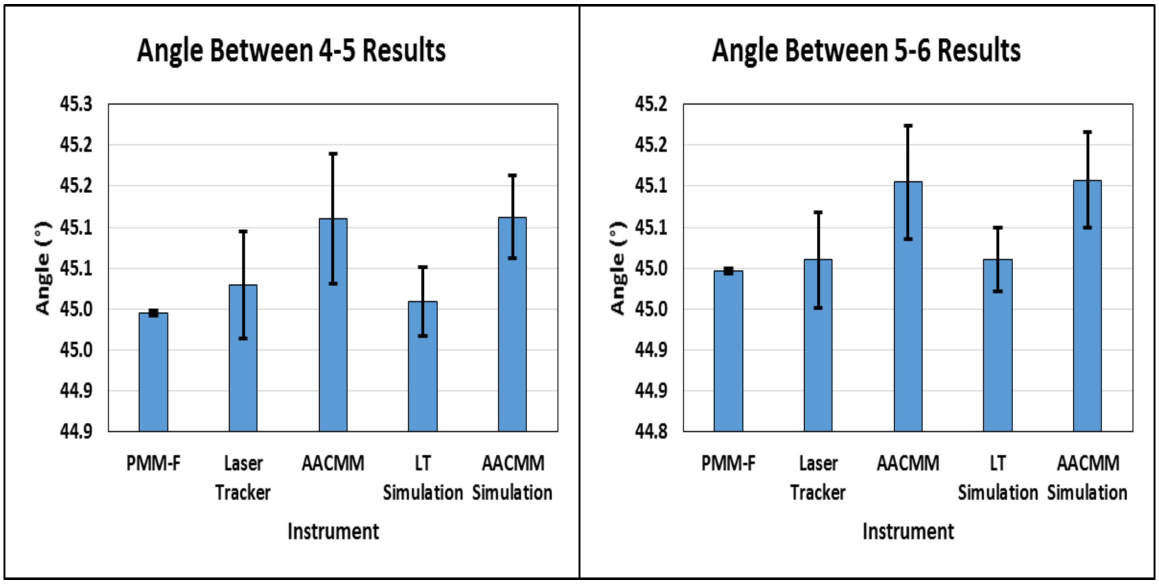

FIGURE 113: Measurement results for rotor yoke angles, 4/5 and 5/6.

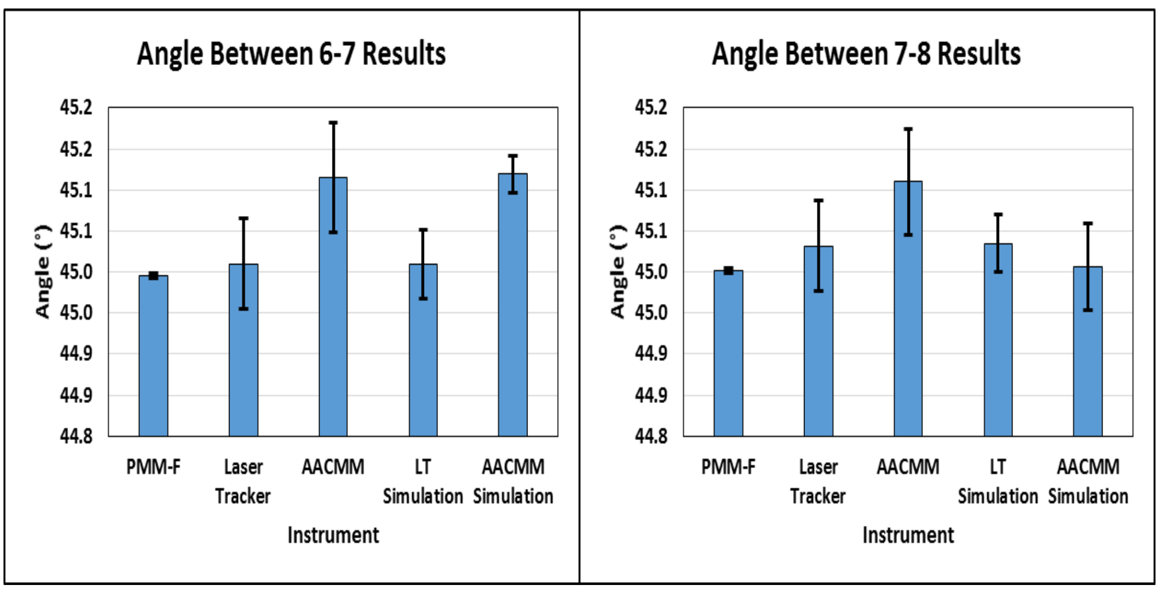

FIGURE 114: Measurement results for rotor yoke angles, 6/7 and 7/8.

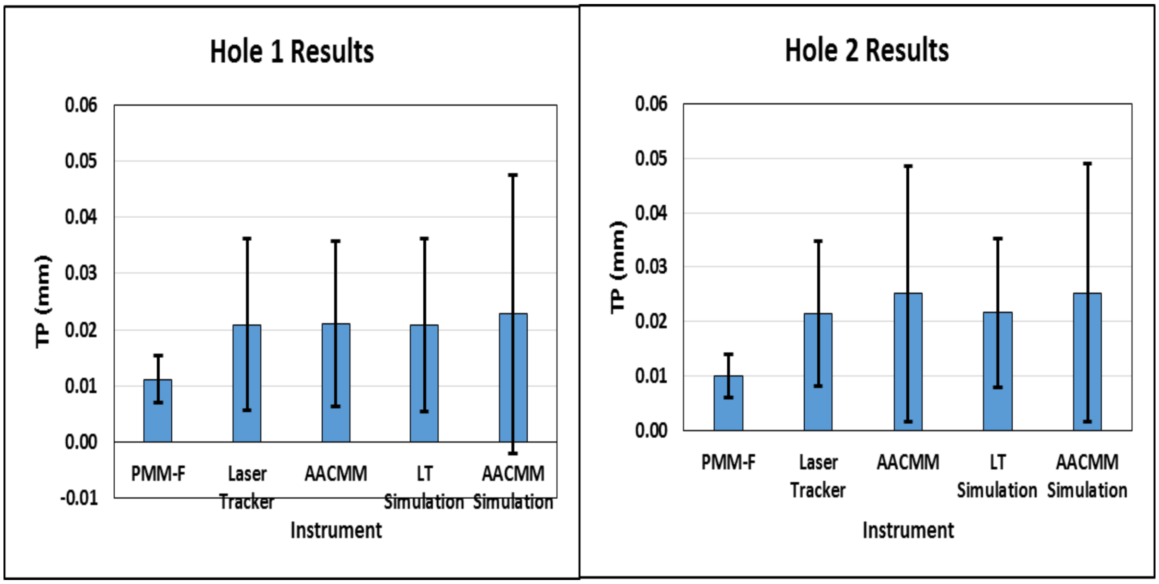

FIGURE 115: Measurement results for rotor yoke positions, 1 and 2.

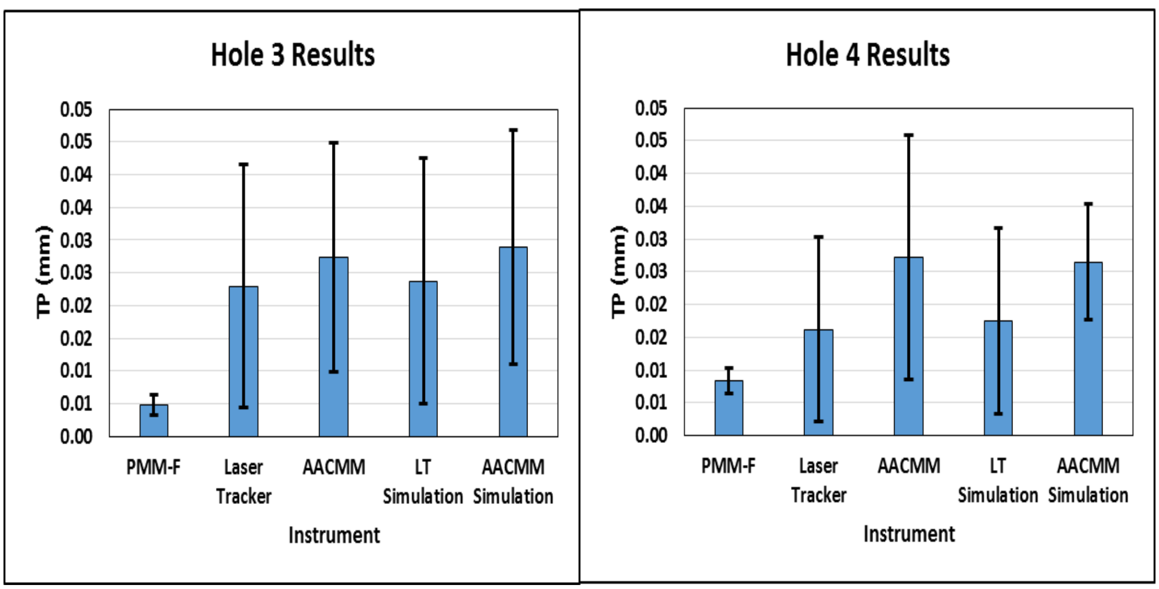

FIGURE 116: Measurement results for rotor yoke positions, 3 and 4.

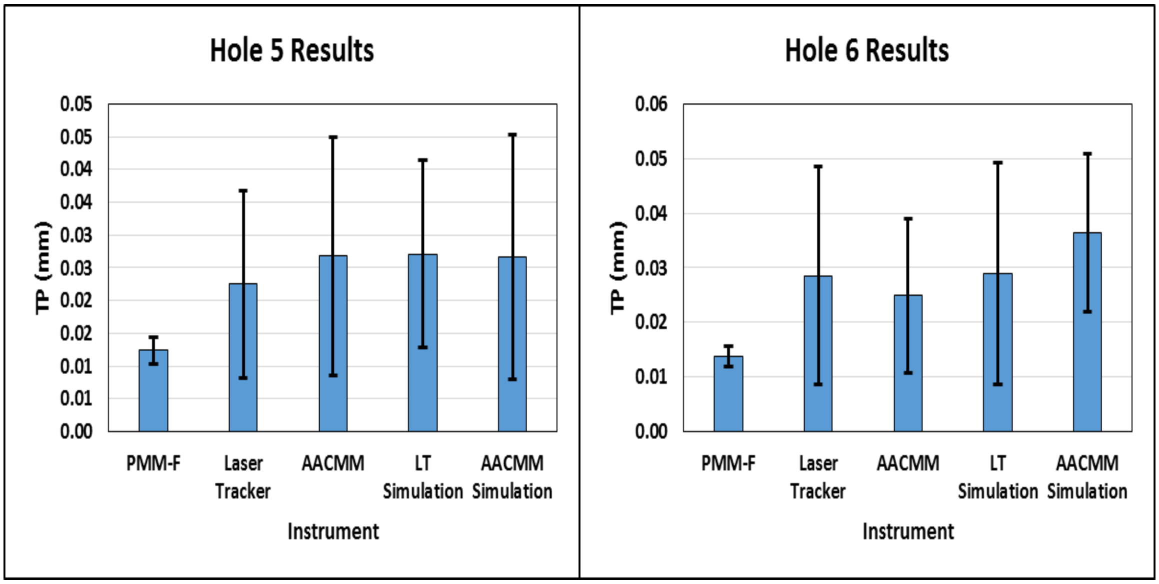

FIGURE 117: Measurement results for rotor yoke positions, 5 and 6.

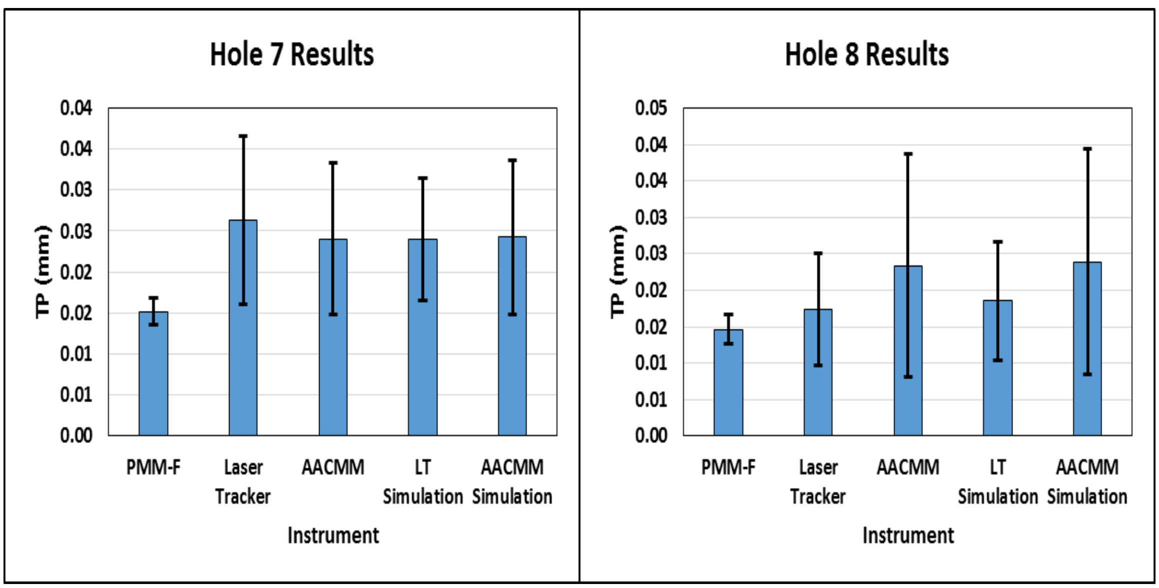

FIGURE 118: Measurement results for rotor yoke positions, 7 and 8.

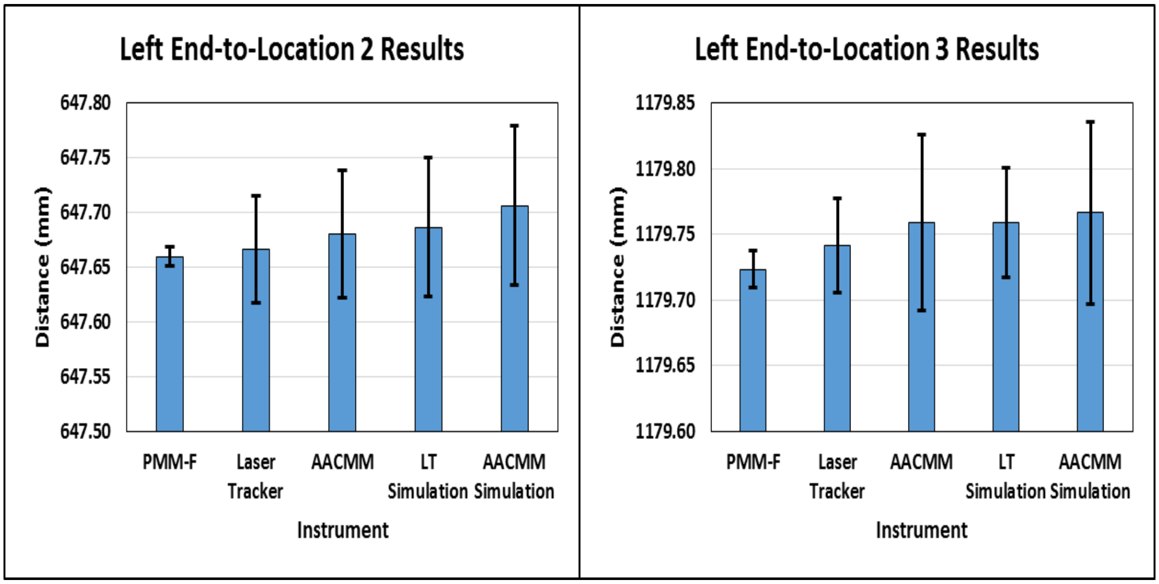

FIGURE 119: Measurement results for flexible artifact, lengths 2 and 3.

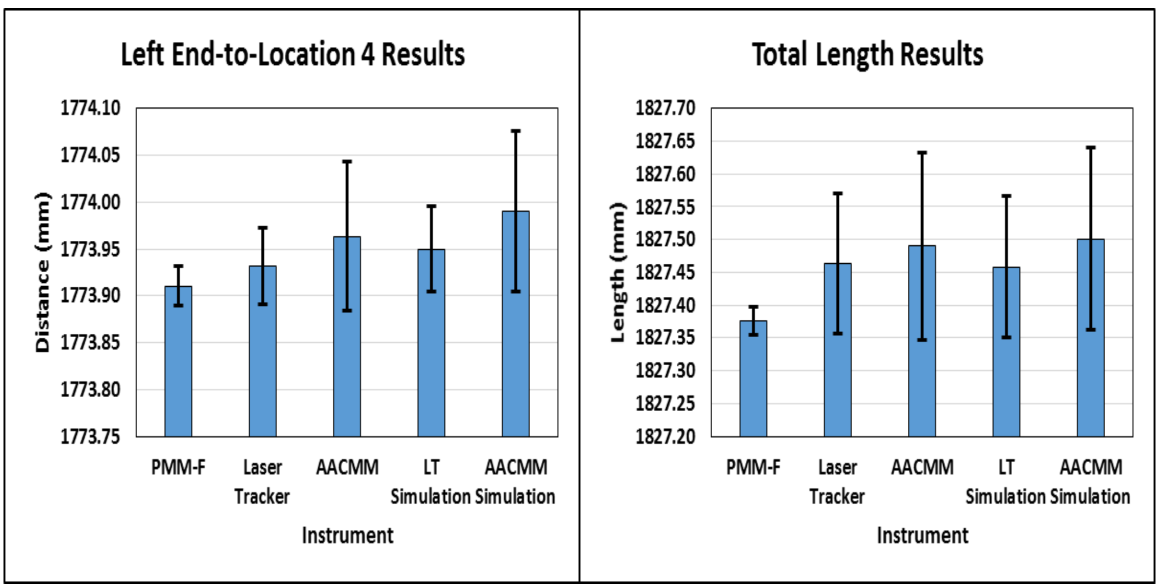

FIGURE 120: Measurement results for flexible artifact, lengths 4 and 5.

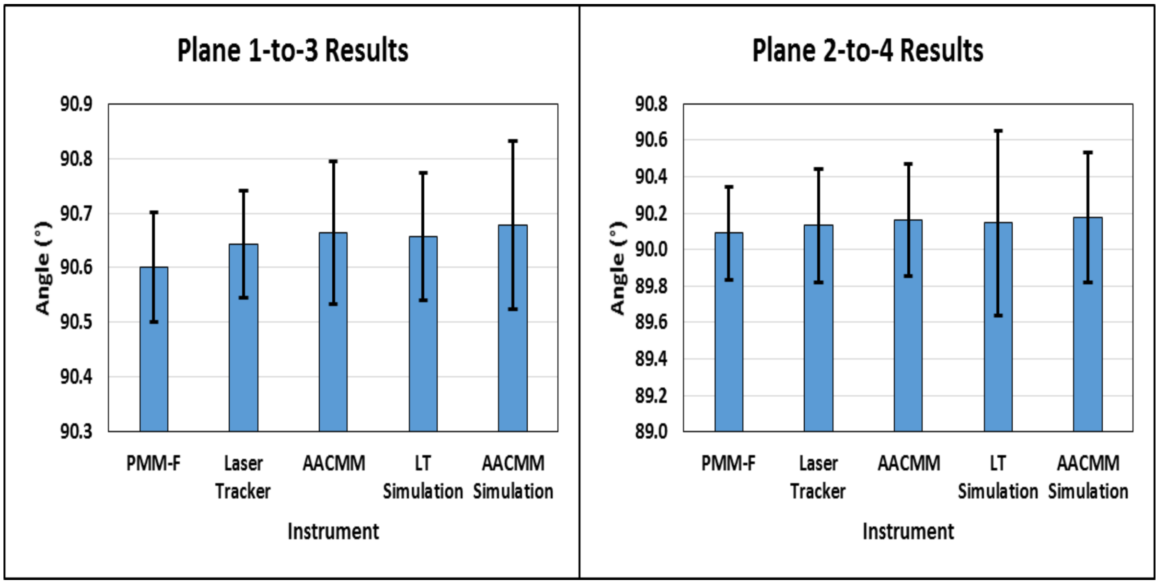

FIGURE 121: Measurement results for flexible artifact, angles 1/3 and 2/4.

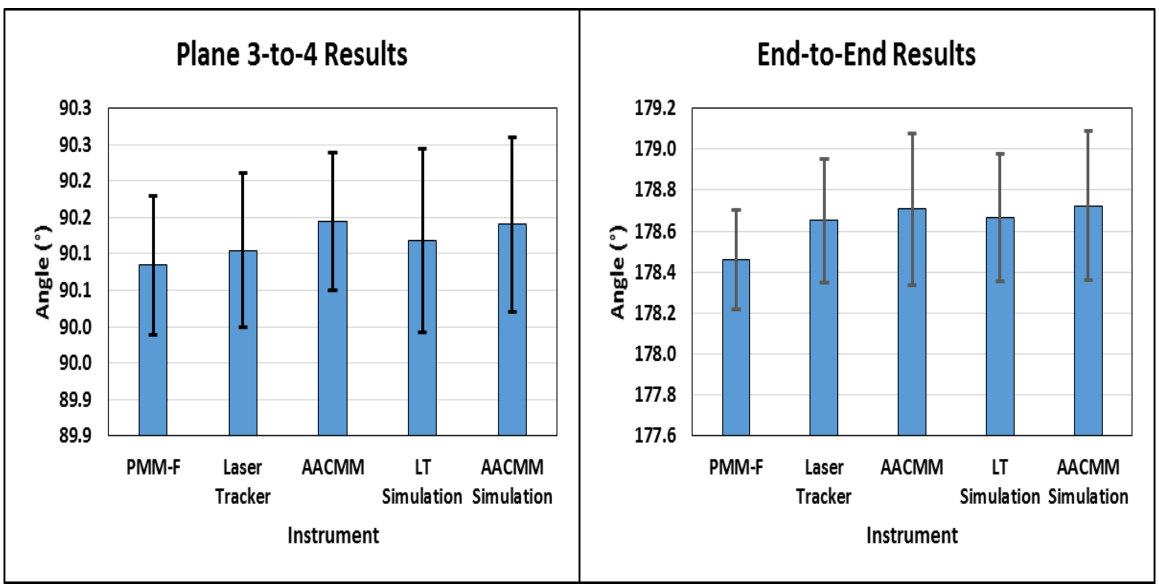

FIGURE 122: Measurement results for flexible artifact, angles 3/4 and //.

APPENDIX C: CENTERLINE SAG MEASUREMENT AND UNCERTAINTY

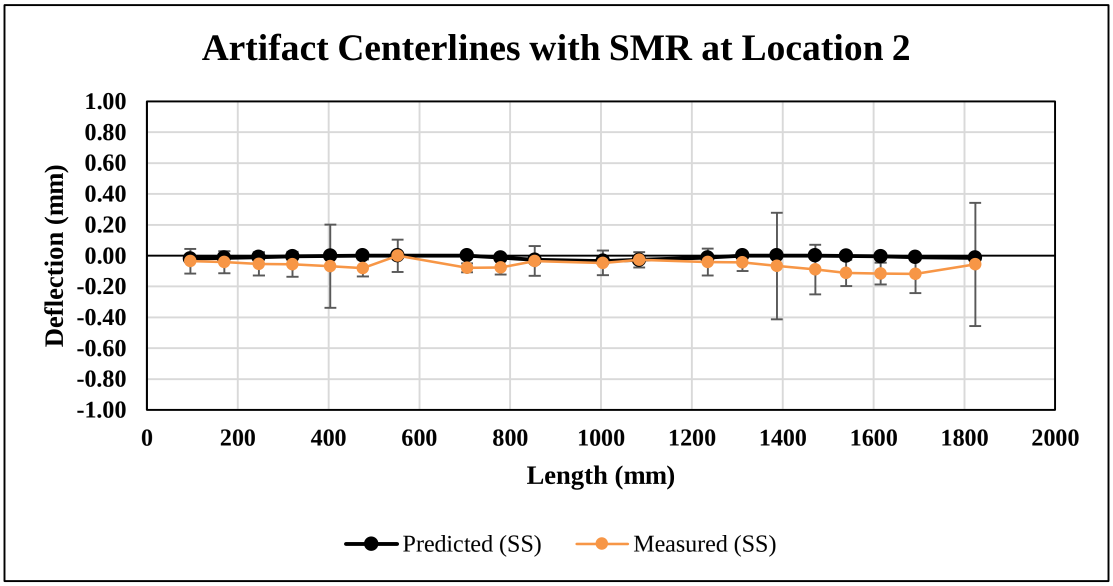

FIGURE 123: Centerline (SS) results for load at location 2.

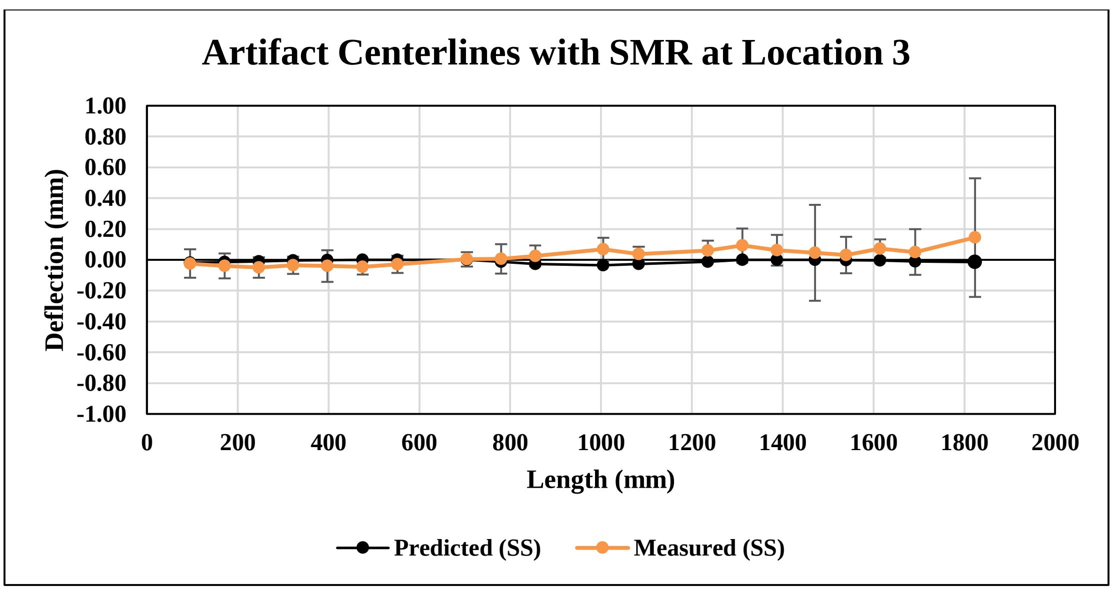

FIGURE 124: Centerline (SS) results for load at location 3.

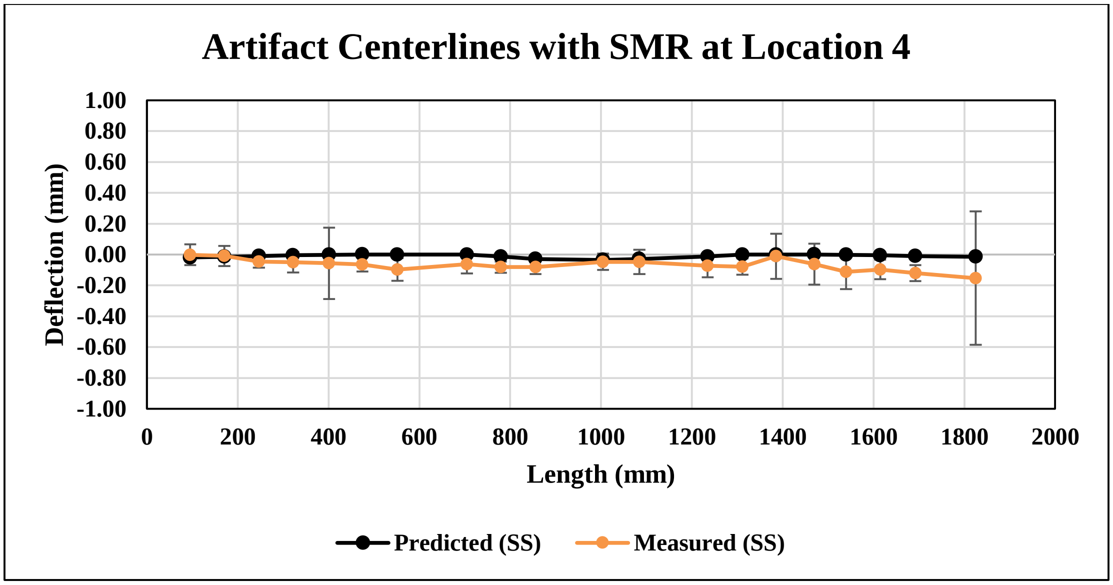

FIGURE 125: Centerline (SS) results for load at location 4.

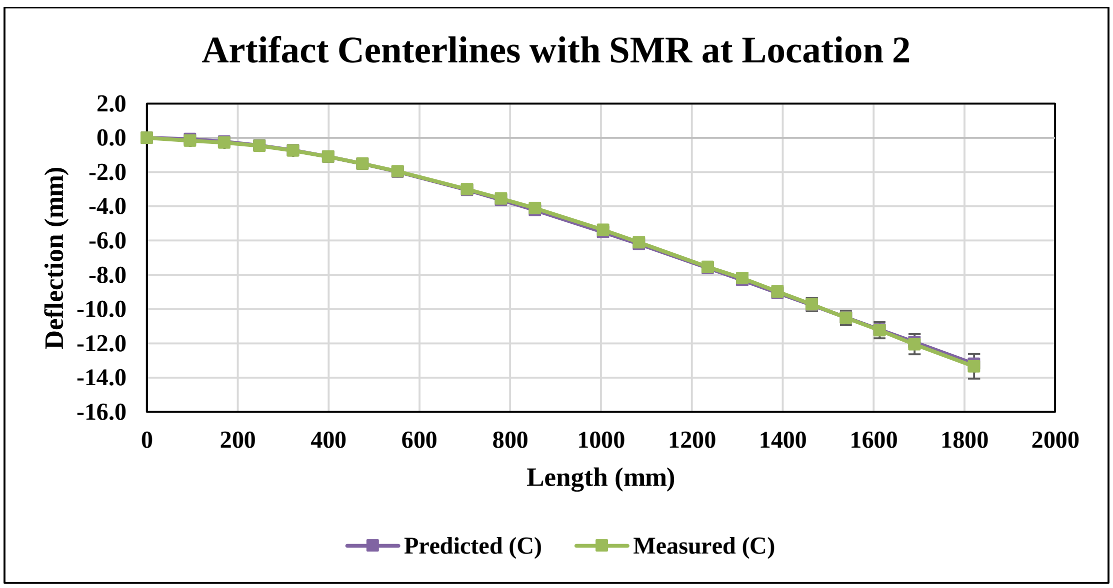

FIGURE 126: Centerline (C) results for load at location 2.

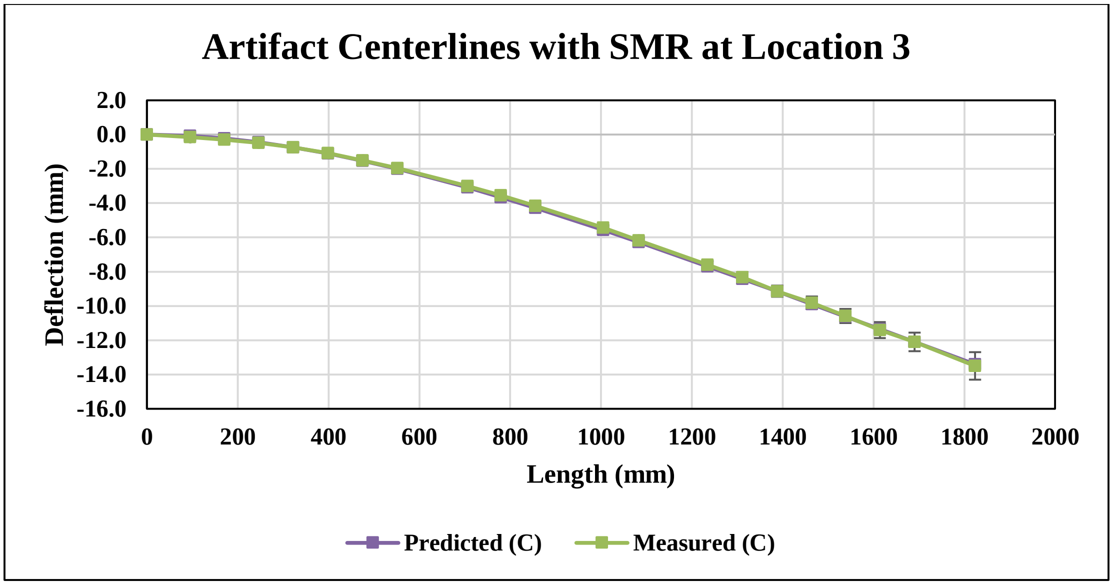

FIGURE 127: Centerline (C) results for load at location 3.

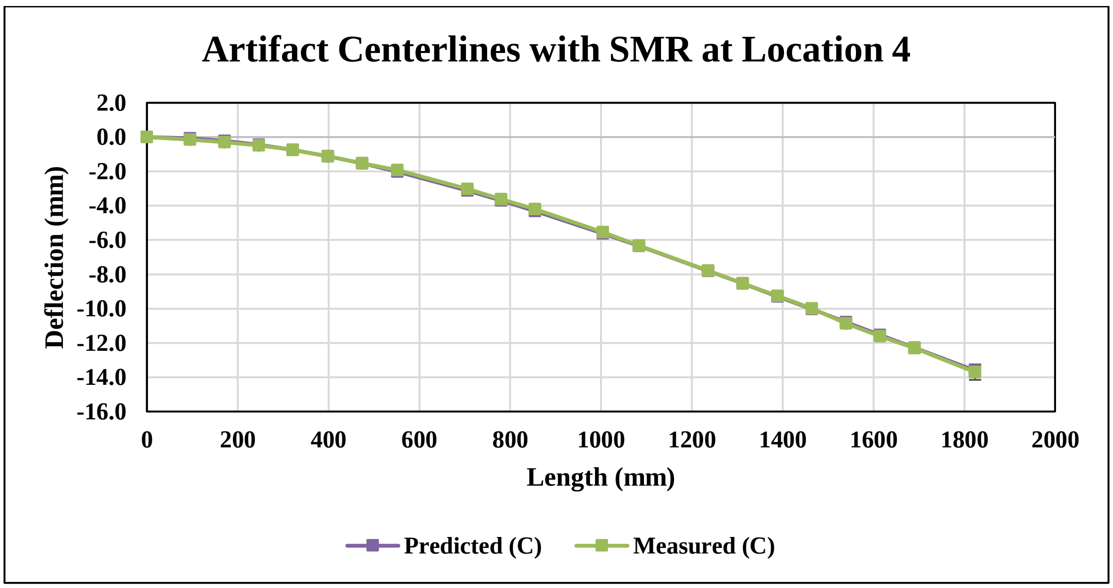

FIGURE 128: Centerline (C) results for load at location 4.